Techniques to Minimize the Dosimetric Impact of Intrafractional Motion with Improved Treatment Accuracy and Efficiency on a C-arm Medical Linear Accelerator

by

Cody M. Church

Submitted in partial fulfillment of the requirements

for the degree of Doctor of Philosophy

at

Dalhousie University

Halifax, Nova Scotia

July 2022

TABLE OF CONTENTS

LIST OF TABLES

LIST OF FIGURES

ABSTRACT

Mechanical and algorithmic advances in the field of linac-based radiation therapy have enabled for increasingly complex, and personalized therapies to irradiate disease with a high-dose technique known as stereotactic radiosurgery (SRS). This technique is highly conformal, places stringent tolerances on patient alignment, and requires a steep dosimetric fall-off beyond the target volume to ensure surrounding tissues receive minimal dose. To ensure optimal treatment, several techniques are employed, namely: (1) Use of image guidance to ensure accurate patient positioning (*e.g.* pre-treatment cone-beam computed tomography); (2) Use of immobilization devices (*e.g.* invasive frames or non-invasive thermoplastic masks) that fixate the patient to the treatment couch during therapy. Despite these efforts, intra-fraction motion on the order of several millimetres or degrees can occur that could impact target coverage, and dose received to healthy tissues. This work aims to quantify the dosimetric impact of motion during radiosurgery and develop two methodologies for addressing motion: 1) megavoltage (MV) imaging with region of interest (ROI) apertures to detect and correct for motion with couch translations. 2) Dynamic couch trajectories to minimize treatment distances during delivery which could improve treatment efficiency, potentially minimizing the magnitude and/or frequency of motion.

This thesis presents a series of three manuscripts pertaining to the topics mentioned above. The first manuscript explores three variables, namely, aperture size, target size, and intrafractional motion, when assessing delivery quality for the treatment of small targets. The second investigation introduces a methodology for generating control point-specific optimal apertures to be used for MV imaging; these apertures conform to anatomical sites which allow for sub-mm positional verification while also reducing imaging dose. The third manuscript explores the potential efficiencies gained by treating at a shortened, virtual isocentre in previously treated clinical cases.

These manuscripts form the basis for methodologies and strategies to improve treatment efficiency, and fidelity with planned treatments. These techniques are motivated by evidence that intrafractional motion during SRS can have clinically significant detriments. These works demonstrate an embodiment of dynamic, trajectory radiotherapy where multiple axes of a linac engage in coordinated motion during therapy.

LIST OF ABBREVIATIONS AND SYMBOLS USED

TV	Target volume
SRS	Stereotactic radiosurgery
SRT	Stereotactic radiotherapy
3D	Three-Dimensional
TN	Trigeminal neuralgia
GK	Gamma Knife®
AVM	Arteriovenous malformation
CT	Computed tomography
MRI	Magnetic resonance imaging
IR-GRE	Inversion recovery gradient echo
TSE	Turbo-spin-echo
ISRS	International Stereotactic Radiosurgery Society
AVM	Arteriovenous malformation
RTOG	Radiation Therapy Oncology Group
AAPM	American Association of Physicists in Medicine's
TG	Task Group
WL	Winston Lutz
EPI	Electronic portal image
CK	CyberKnife®
SAD	Source-to-axis-distance
MLC	Multileaf collimator
HDMLC	High-definition multileaf collimator
BEV	Beams-eye-view
3D-CRT	Three dimensional conformal radiation therapy
DCA	Dynamic conformal arc
IMRT	Intensity-modulated radiation therapy
DAO	Direct aperture optimization
DMPO	Direct Machine Parameter Optimization
IMAT	Intensity Modulated Arc Therapy
VMAT	Volumetric Arc Therapy
WBRT	Whole brain radiation therapy
MU	Monitor unit
MBSRS	Elements™ Multiple Brain Mets SRS
$\mathbf{V_{xGy}}$	Volume receiving x Gy or more
GI	Paddick gradient index
SIDCA	Single isocentre dynamic conformal arc
MIDCA	Multiple isocentre dynamic conformal arc
$\mathbf{CI_{RTOG}}$	Radiation Therapy Oncology Group conformity index
kV	Kilovoltage
MV	Megavoltage
DRR	Digitally reconstructed radiograph

EPID	Electronic portal imaging device
CBCT	Cone beam computed tomography
AP	Anterior-posterior
RL	Right-left
LR	Left-right
IR	Infrared Marker
BRW	Brown-Roberts-Wells
CRW	Cosmon-Roberts-Wells
GTC	Gill-Thomas-Cosmon
TPS	Treatment planning system
SBRT	Stereotactic body radiation therapy
OAR	Organ at risk
V_x	Volume receiving x% of prescription dose
FFF	Flattening filter free
ROI	Region-of-interest
D_{max}	Maximum dose
SSD	Source-to-surface-distance
RF	Radiofrequency
XML	Extensible Markup Language
DICOM	Digital Imaging and Communications in Medicine
IEC	International Electrotechnical Commission
vSAD	Virtual source-to-axis-distance
CNR	Contrast-to-noise-ratio
MC	Monte Carlo
CPE	Charged particle equilibrium
CSDA	Continuous slowing down approximation
AAA	Analytical Anisotropic Algorithm
AXB	Acuros XB
LBTE	Linear Boltzmann transport equation
OF	Output factor
FWHM	Full width at half-maximum
LCPE	Lateral charged particle equilibrium
SDD	Source-to-detector-distance
CDF	Cumulative distribution function
MI	Mutual information
VIM	Ventralis intermedius
D_{mean}	Mean dose
PTV	Planning target volume
DVH	Dose volume histogram
D_x	Dose received by x% of the volume
DOCA	Distance-of-closest-approach

CHAPTER 1. INTRODUCTION

The aim of radiation therapy is to deliver a lethal dose of radiation to a target volume (TV) while minimizing dose to normal tissue. External beam radiation therapy involves directing high-energy radiation (e.g, 4 – 20 MeV for electrons, 1 – 20 MeV photons, up to 150 – 250 MeV for protons.) in a targeted manner towards a delineated target within a patient's body.[1] Several different diseases are treated with radiation therapy and are further addressed in Section 1.1. The primary disease considered in this thesis is cancer, which is a disease that is characterized by the uncontrolled replication of abnormal cells which can develop into benign or malignant lesions that may spread to locations in the body that differ from their origin.[2] Cancer is one of the leading causes of death in every country worldwide.[3] There is a 19% higher incidence rate in men, and a 43% higher death rate in men when compared with women.[4] While there is a variance across treatment sites, and cancer staging, approximately 50% of patients will receive radiation therapy at some point during the management of their disease.[5]

1.1 STEREOTACTIC RADIOSURGERY

Stereotactic radiosurgery (SRS) is a highly targeted form of radiation therapy which delivers a large therapeutic dose in one single session.[6-8] When protracted over the course of a few fractions (typically three or five) it takes on the name of stereotactic radiotherapy (SRT). The hallmark of SRS is a conformal dose distribution with a rapid dosimetric fall-off beyond the TV.[9] An important distinction between conventional radiation therapy and

SRS is the mechanism by which a biological response is elicited. In conventional radiation therapy (2 Gy per fraction, where Gy = Gray, the unit of dose), a fraction of the cells in the lesion are killed by means of DNA damage. There is not enough damage to kill all tumour cells, thus subsequent treatments are needed for full eradication. The most important aspect of this treatment scheme (multiple treatments with low doses – compared with SRS) is the time allocated for the repair and repopulation of the surrounding healthy tissue.[2] In SRS/SRT therapies where doses are ablative,[10-12] indirect cell death appears to be a consequence of vascular damage, which can ultimately lead to cell death.[13] Due to the magnitude of the large doses delivered with SRS, sub-millimetre positional accuracy is required as to minimize dose to surrounding healthy tissue.[9,14]

Radiosurgery is a technique that was first invented by Lars Leskell and Borje Larsson in 1951 for the non-invasive treatment of intracranial lesions inaccessible to surgical resection.[7] The technique relied on earlier work by Leskell in 1949 where they developed a frame for the three-dimensional (3D) localization of anatomical sites within the cranium; this process is referred to as stereotaxy.[15] The frame establishes a polar coordinate system by fixating to the skull and allowing for the precise determination of points within the frame with respect to angle, depth, and anterior-posterior extent. Early work utilized stereotaxy with orthovoltage X-rays (200 kVp) for the treatment of trigeminal neuralgia (TN).[16] The lack of beam penetration of low energy x-rays limited the utility of this type of beam for therapeutic applications. Thus, the technique of SRS evolved to utilize deeper penetrating gamma rays from a Co-60 source (E_{avg} = 1.25 MeV, $T_{1/2}$ = 5.26 years) for delivering therapeutic radiation.[17] An adaptation of this methodology, called the

Gamma Knife ® (GK), utilized a hemispherical array of 179 Co-60 sources to create highly conformal dose distributions for radiosurgery, and was first used in Stockholm in 1968 for treating arteriovenous malformations (AVMs) and acoustic neuromas.[6] The modern GK system, the GK Icon™ is manufactured by Elekta (Elekta AB, Stockholm, Sweden). It shapes complex dose distributions with up to 192 sources by combining contributions from circularly shaped beams with cones (physical cone diameters of 4 mm, 8 mm, and 16 mm), from eight different sectors around the cranium with varying exposure times.[18]

1.2 IMAGING FOR RADIOSURGERY

The quality of treatment plans for radiosurgery has vastly improved with the invention of computed tomography (CT) in 1972 as it provided a 3D volumetric image for visualization of targets and normal structures.[19] The CT-data in conjunction with contrast-enhanced magnetic resonance imaging (MRI, used for soft tissue delineation due to superior soft tissue contrast) is routinely used for defining the extent of TVs in linac radiosurgery.[20] Common 3D MRI of the cranium utilizes gadolinium contrast-enhanced T1-weighted inversion recovery gradient echo (IR-GRE)[21] as well as 3D-turbo-spin-echo (TSE)[22]. Gadolinium is taken up by the tumor and provides visual contrast with MR imaging by effectively changing the relaxation time of the tumor environment relative to the background (normal tissue); its efficacy (with respect to improved tumor contrast) is a function of its physiochemical properties,[23] doseage,[24] timing of administration,[25,26] and magnetic field strength.[26] Paulson *et al.* found that MRI simulation scanning resolutions for stereotactic planning to be 1.0 x 1.0 x 2.0 mm^3 amongst seven clinical institutions in the Elekta 'Atlantic' consortium.[27] No general consensus for the use of immobilization

systems during MRI was found by Paulson *et al.*[27]; scanning without thermoplastic immobilization systems improves the signal to noise ratio in the brain,[28] however, this could lead to uncertainties when registering to CT imaging.[29,30] Geometric distortions can occur in MR-image as a result of: nonlinearity of the magnetic field produced by the gradient coils[31] (which implement the imaging protocol via a pulse sequence), inhomogeneity of the main magnetic field,[32] patient-induce magnetic field perturbations,[33] as well as pulse sequence choices.[34]

1.3 INDICATIONS FOR RADIOSURGERY

A variety of different functional, benign, and malignant indications are treatable by SRS. Meningiomas are slowly growing benign[35] or malignant[36] neoplasms originating from arachnoidal cap cells within the dural sinus and can cause impaired vision, personality changes, headaches, and seizures.[37] Prescription doses of 14 Gy have been reported with local tumour control rates of up to 93% at 10 years.[38] Acoustic neuromas (vestibular schwannomas) are slow-forming benign indications that develop in the vestibular portion of the inner ear and cause hearing loss, vertigo, tinnitus, and disequilibrium.[39] The International Stereotactic Radiosurgery Society (ISRS) recommends a dose of 11 to 14 Gy in a single fraction,[40] and control rates of 99% have been reported for 5-year longitudinal studies.[41-43] An arteriovenous malformation (AVM) is a shunt between cerebral veins and arteries which can disrupt oxygen circulation through the brain.[44] Maximal obliteration was determined to occur when the indication is covered by approximately 25 Gy by Flickinger *et al*. in a 3 to 11 year follow up study of 351 AVM cases.[45] Alternative dosing regimens

for large AVMs have incorporated staged deliveries where geometrically distinct segments of the lesion are treated over separate SRS sessions.[46] Obliteration rates with staged deliveries have been shown to reach 42%[47] to 71%[48] with low rates of adverse reactions (6% to 13%). Pituitary adenomas are growths on the pituitary gland and represent 10 to 20% of all intracranial lesions;[49] doses vary between centres and cases but typically fall within the region of 10 to 18 Gy.[50,51] Trigeminal neuralgia is functional indication stemming from a disruption in the function of the trigeminal nerve. Its therapy is ablative in nature with doses ranging from 60 to 97 Gy as determined from a systematic review of the literature by the ISRS.[52]

Gliomas are the most commonly occurring type of primary malignant lesion of the brain which encompasses 35-45% of all primary brain tumors.[53,54] Brain metastases occur as secondary malignancies in 20 to 40% of all cancer patients;[55] with 30 to 60% of brain metastases being owed to primary lung lesions.[56] The Radiation Therapy Oncology Group (RTOG) defined the maximum tolerated doses, and sizes by single-fraction SRS with primary brain tumors such as gliomas, and recurrent lesions like brain metastases in a retrospective analysis of 156 patients. They found that the maximum treatable tumor sizes (in diameter) were ≤ 20 mm, 21–30 mm, and 31–40 mm with a maximum tolerated dose of 24 Gy, 18 Gy, and 15 Gy, respectively.[57] Dose escalation is viable for lesions ≤ 20 mm, but is to be implemented at the discretion of the clinician.[58,59] Modifications to the RTOG 90-05 guidelines have been suggested for dose reduction in cases where there are five or more lesions.[60]

1.4 SRS THERAPY TREATMENT UNITS

Over the past several decades the stereotactic technique at its core remains unchanged, but the means by which it is implemented has seen many changes in the hands of different commercial vendors. Following the development of the GK system, several commercial entities made innovations to reproduce its radiosurgical capabilities with a medical linear accelerator (linac). Medical linacs are often gantry mounted systems that, in ideal conditions, rotate around a single point in space referred to as isocentre. In reality, the coincidence of the rotational axes of the linac (gantry, collimator, treatment table), referred to as the mechanical isocentre, forms a spherical volume due to excursions of ideal motions along each axis.[61] The American Association of Physicists in Medicine's (AAPM) Task Group (TG) 142 report recommends that the coincidence between mechanical and radiation isocentre should not exceed ± 1.0 mm.[14] While QA tests are not explicitly defined within the TG-142 document, various different investigations have devised techniques to assess the coincidence between mechanical and radiation isocentre. The Winston Lutz (WL) test, formulated by Lutz and Maleki in 1988, involves the irradiation of a sheet of radiographic film at four cardinal gantry angles (0°, 90°, 180°, 270°) which have been mounted on a mechanism that is fixed to the head of the gantry.[62] Proximal to the film is a metal ball bearing that is mounted to the end of the treatment table (the WL phantom) which has been aligned to mechanical isocentre.[62] The difference between the radiographic shadow created by the ball bearing and the center of the field indicates the magnitude of coincidence.[62] Extensions of this technique with additional irradiation angles,[63] 3D

mathematical localization algorithms,[64] and electronic portal imaging (EPI)[65] have been developed.

Radiation therapy with a linac is delivered either from a series of fixed gantry positions, or while rotating around the patient as demonstrated in Figure 1. The first attempts at radiosurgery with a C-arm linac was in 1982 by Betti *et al.*[66] A C-arm linac is one in which the x-ray generation and delivery system rotates in one single plane around isocentre. These first systems used 6 MV to 10 MV x-ray beams with externally mounted circular collimation systems referred to as stereotactic cones.[67] Some centres still make use of stereotactic cones which have sizes ranging from 4 to 45 mm.[68]

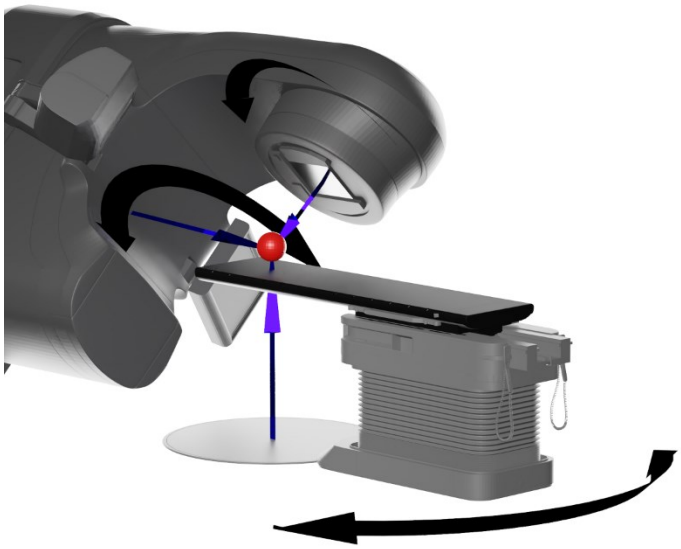

Figure 1: A conventional C-arm linac and its rotational axes that would ideally intersect a single point in space. In reality, the isocentre is defined by an ellipsoidal volume as depicted by the ellipse in the diagram.

An alternative linac design was conceived in 1994 with the manufacturing of a Robotic-arm-mounted linac known as the CyberKnife® (CK) system by Accuray (Accuray Inc. Sunnyvale, CA, USA). The CK system was invented by a neurosurgeon, John Adler along with several engineering colleagues at Stanford University.[69] It differs from conventional C-arm linacs in that it utilizes an X-band wave-guide (9.3 GHz) for production of the its treatment beam, and it has access to slightly more than half of 4π space for treatment angles. The collimation system of the CK was initially based on

tungsten cones ranging from 5 to 60 mm. An updated version used a dynamic cone-based collimation system with twelve tungsten pieces (two stacks of six) was made and can produce an effective circular field with a maximum diameter of 60 mm at an 80 cm source-to-axis-distance (SAD); this system is referred to as Iris™. Today, modern CK systems utilize a high-definition multi-leaf collimator (MLC) which contains 41 pairs of 0.9 mm thick (along beamline) tungsten leaves which have a projected width of 2.5 mm at 80 cm SAD.[70,71] A demonstration of the three commercially available SRS units is shown in Figure 2.

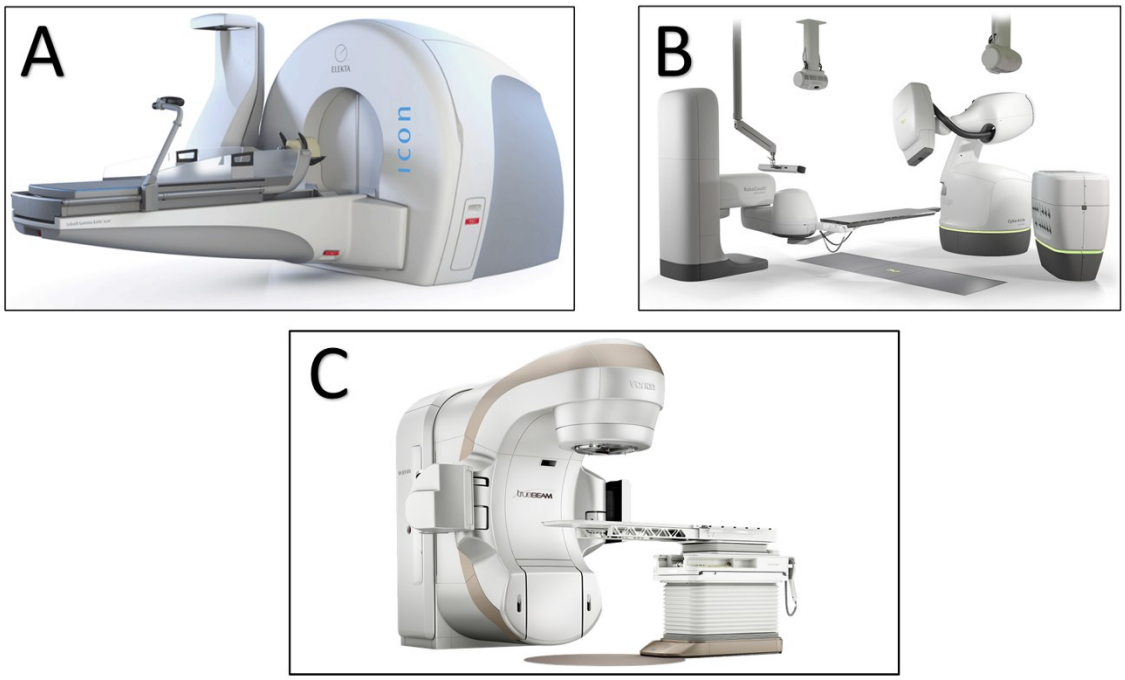

Figure 2: Therapy units available for radiosurgery. (A) The Gamma Knife® Icon system by Elekta (Elekta AB, Stockholm, Sweden). (B) The CyberKnife® M6 system by Accuray (Accuray Inc. Sunnyvale, CA, USA). (C) The Truebeam by Varian (Varian Medical Systems Inc., Palo Alto, CA).

C-arm linacs have also featured similar improvements to the internal, tertiary collimation system (MLC) beyond externally mounted stereotactic cones. The Clinac® system manufactured by Varian (Varian Medical Systems Inc., Palo Alto, CA) was the first to introduce an internal MLC system which used 26 leaf pairs with a 1.0 cm projected leaf width at 100 cm SAD. The next iteration of MLCs by Varian, known as the Millenium™ MLC, increased the number of leaf pairs to 60 and increased the resolution of the central 28 leaves to 5 mm.[71] Brainlab (Brainlab AG, Munich, Germany) developed the m3 micro-MLC, an externally mounted MLC to further increase the resolution of the leaves to a projected 3.0 mm at 100 cm SAD.[72] The newest linacs designed by Varian utilize a high-definition MLC referred to as the HDMLC, which includes 60 pairs of leaves with a 2.5 mm width projected at 100 cm SAD for the central 28 leaf pairs and 5 mm for the outer leaves.[73]

1.5 DELIVERY TECHNIQUES

Beyond the mechanical limitations of the collimation hardware utilized by a therapeutic unit, a variety of delivery techniques can also be employed to achieve dosimetric conformity. The simplest of these is a conformal fitting procedure, where the collimation system is positioned to match the projection of a delineated target for each beams-eye-view (BEV) as demonstrated in Figure 3B; this technique is referred to as 3D conformal radiation therapy (3D-CRT). This methodology can be used to deliver static ports or during arc-based therapies where radiation is delivered continuously as the gantry rotates. This is called dynamic conformal arc therapy (DCA) where the MLC (and

sometimes the jaws) are dynamically positioned to maintain the changing projection of the TV for each BEV.

Increased computational capacity has allowed for more complex approaches to treatment planning with the use of optimization procedures[74,75]; where "optimization," in the context of treatment planning for radiation therapy, refers to shaping the dose distribution as dictated by choices of the clinician. Clinically, forward-planning optimization involves perturbing the numerous degrees-of-freedom for treatment (*e.g,* gantry angle, beam weighting, fluence pattern, additional fields with field-in-field[76]) to achieve a desired dose distribution, whereby the perturbations are typically derived from anecdotal experiences of the clinician. Conversely, inverse-optimization defines dosimetric goals or constraints (*e.g,* criteria for dose to some percentage of the target and dose limits for normal tissues) along with their relative importance (determined by the planner). The optimizer proposes a series of fluence intensity patterns (or aperture shapes depending on the optimization technique), and a dose distribution is calculated. The deviation of each dosimetric goal from the ideal value is converted into a cost and summed across all dosimetric goals to represent the cost function, where each cost is weighted by its relative importance. This process is repeated numerous times with each iteration using perturbation to the fluence patterns to minimize the cost function (or commonly referred to as the objective function).[77,78] In the seminal paper by Brahme *et al*.,[79] the use of intensity modulated radiation beams for a series of fields in rotational delivery was developed to produce homogenous dose distributions in complex target shapes. This technique was later paired with inverse optimization to achieve conformal avoidance of normal tissue and is

known as intensity-modulated radiation therapy (IMRT).[80] To create treatments with this method, each intensity pattern (shaped by the MLC) for each BEV is subdivided into hundreds of individual beamlets. The weighting of the individual beamlets is iteratively perturbed until plan quality improves no further either using the step-and-shoot,[81] or sliding window technique.[82] A subsequent optimization step follows the optimization of the distribution where a leaf-sequencing algorithm translates the intensity distribution into a set of MLC apertures.[81] Alternative algorithms exist which synchronously optimize leaf-sequencing and aperture intensities known as direct aperture optimization (DAO),[83] or Direct Machine Parameter Optimization (DMPO)[84] by the Pinnacle planning system (Philips Radiation Oncology Systems, Milpitas, CA) and is based upon the principle of DAO.

Another embodiment of an IMRT-style delivery is one where the in an arc-based delivery where the gantry rotates, and the MLC moves while radiation is being delivered. The first commercial implementation of this technique is intensity-modulated arc therapy (IMAT), now commonly referred to as volumetric arc therapy (VMAT).[85,86] The advantage of VMAT delivery is increased therapeutic efficiency while maintaining or improving dosimetric outcomes.[87-92]

The CK and GK systems cannot produce arc-based deliveries, thus, they employ a slightly different version of this treatment methodology by adding the dosimetric contributions from individual "shots" (fixed couch/gantry angle combinations for CK and individual source positions with GK).[93,94] When compared with GK, conformity with the MLC (C-arm linac or CK MLC) has been shown to be non-inferior.[95-98]

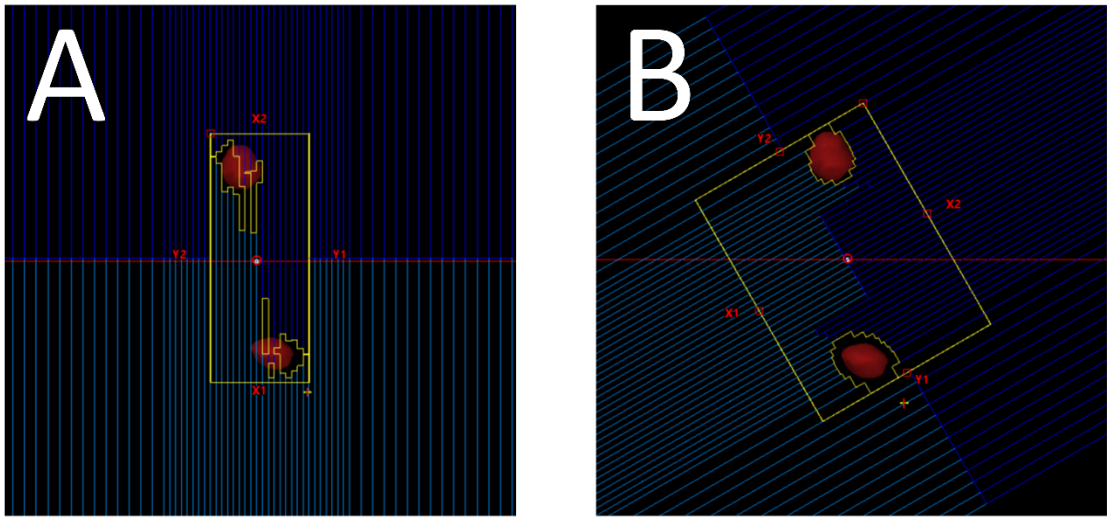

Figure 3: Example of fitting achieved with intensity modulated therapy with complex aperture pattern shaped by the multileaf collimator to shield surrounding tissue in (A). Example of conformally fitting with a multileaf collimator to two lesions in (B).

For many centres, treatments of secondary malignancies in the brain utilizes whole-brain radiation therapy (WBRT) in conjunction with SRS and/or surgical resection.[99-104] The efficacy and safety of adjuvant therapy of SRS with WBRT was retrospectively evaluated by multiple clinical trials by the RTOG.[105] Some investigations have explored the feasibility of treating multiple metastases with SRS alone; Yamamoto *et al*. found that the treatment of five to ten metastases with SRS was noninferior to the treatment of two to four metastases and ongoing trials are exploring the treatment of five to fifteen metastases.[106] The use of SRS in place of WBRT for treating multiple metastases is a treatment paradigm which is continually evolving as WBRT has been shown to cause

neurocognitive decline.[107,108] An ongoing clinical trial is exploring possible improvements with WBRT by adopting a hippocampal avoidance strategy when comparing to treatments with SRS alone for patients with five to 20 cranial lesions.[109]

The superiority of intensity-modulated therapies or conformal arc therapies for the treatment of multiple lesions remains as a point of contention within the field of radiation therapy. In general, the necessary monitor units (MUs) are higher for VMAT plans due to aperture modulation during delivery. To create DCA plans for multiple lesions different methodologies have been developed such as the Elements^{TM} Multiple Brain Mets SRS (MBSRS) by Brainlab (Brainlab AG, Munich, Germany) which treats subsets of the total number of lesions using specific arcs.[110-114] With respect to plan quality, conflicting evidence has been shown in the literature. Velten *et al*. found that VMAT produced a better homogeneity index (0.16 versus 0.24 ± 0.07 for DCA with MBSRS) and conformity index (0.8 ± 0.08 versus 0.71 ± 0.08 for DCA with MBSRS) whereas the V_{10Gy} was higher (13.5 ± 6.64 cc versus 9.26 ± 4.57 cc for DCA with MBSRS), where V_{10Gy} is the volume receiving 10 Gy or more.[88] Hofmaier *et al*. found that conformity was similar (median of 0.75 for DCA MBSRS versus 0.73 VMAT) with better healthy brain sparing for DCA (V_{10Gy} median of 3.2 cc versus 4.9 cc for VMAT) and lower MUs (median 4569 versus 5840 for VMAT).[110] Liu *et al*. found better conformity with VMAT based upon the RTOG definition (closer to unity is better; VMAT = 1.21, MBSRS = 1.38, $P < 0.0001$) with lower volumes receiving 12 Gy or more ($V_{12Gy)}$ and volumes receiving 8 Gy or more (V_{8Gy}) (median: $V_{12Gy, VMAT}$ = 19.2 cc, $V_{12Gy, MBSRS}$ = 23.7 cc; P = 0.0001; V_{8Gy}, VMAT = 44.1 cc, $V_{8Gy, MBSRS}$ = 53.6 cc; P = 0.024).[115]

For the average cranial lesion, treatments with linacs usually take approximately 15 – 20 minutes per isocentre.[116] Thus, treating cases with multiple lesions, each with a separate isocenter, could lead to long treatment times. The use of a single isocentre for treating multiple lesions simultaneously is an attractive option due to the inherent gains in treatment efficiency. Clarke *et al.* evaluated the feasibility of treating three brain metastases simultaneously with three non-coplanar arcs and found that treatment plans were comparable with multiple-isocentre plans with smaller V_{12Gy} for lesions that were close together.[117] Clarke *et al.* also investigated plan quality when treating up to five lesions with single isocentre-VMAT and found that 2 to 4 arcs was sufficient to produce clinically acceptable plans with a median Paddick conformity index of 0.86 and a mean Paddick gradient index (GI) of 3.34 ± 0.42.[95] Huang *et al*. explored plan quality metrics between single isocentre DCA (SIDCA), multiple isocentre DCA (MIDCA) and VMAT. They found the RTOG conformity index (CI_{RTOG}) to be best with VMAT when treating with a single isocentre (1.15 ± 0.09 versus 1.38 ± 0.12 for SIDCA) whereas the GI was worse (4.34 ± 0.46 versus 3.97 ± 0.51 for SIDCA, $p < 0.01$); they also found a substantial reduction in delivery time when treating with a single isocentre (52% for SIDCA and 46% with VMAT when compared to MIDCA).[89]

When treating small indications (less than 0.5 cc) stereotactic cones have historically been the standard to create small, conformal dose distributions. But, with the refinement of the MLC as mentioned in section 1.4, treating without the need for the externally mounted cone systems has become feasible. Popple *et al.* introduced a virtual cone technique in which two pairs of opposed MLC leaves with a small gap between the

leaves are used to shape the treatment field. In addition, the technique delivers a given arc twice with orthogonal collimator angles to create a dose distribution comparable to that of a stereotactic cone.[118] The virtual cone technique has been demonstrated with thalatomy of the nucleus ventralis intermedius (VIM),[119] dorsal nerve root ganglion ablation,[120] and trigeminal nerve ablation.[121] The treatment of small targets such as the trigeminal nerve have also been demonstrated with 18-21 static conformal fields shaped by the HDMLC.[122]

1.6 MOTION MANAGEMENT AND IMMOBILIZATION FOR SRS

For intrafractional (either inter-arc or intra-arc) image guidance, kilovoltage (kV) and megavoltage (MV) imaging options can be used on a C-arm linac. Positioning with individual kV or MV images is referred to as monoscopic imaging where images are compared with digitally reconstructed radiographs (DRRs) from the patient's CT data set to derive necessary corrections in set-up positioning. On a conventional linac, the kV imaging system (x-ray generator and detector) is mounted orthogonally to the central axis of the treatment beam as shown in Figure 4. The ability to perform image guidance with respect to the treatment beam is inherently limited by the coincidence of the kV imaging isocentre and radiation isocentre. Guidance documents suggest this should be limited to a maximum of ± 1.0 mm.[14] The MV imaging system uses a target within the head of the linac at the same location as the treatment beam target and its detector, known as the electronic portal imaging device (EPID), is mounted along the central axis of the beam (referred to as BEV imaging), also shown in Figure 4. Use of MV imaging for registration with DRRs usually necessitates image pre-processing due to a dissonance with DRRs later addressed

in Section 2.4.[123,124] The inherent limitation of MV imaging when compared with kV imaging is inferior contrast, spatial resolution,[125] and larger imaging dose.[126,127] Borsavage *et al*. investigated the use of a sintered diamond target for the 2.5MV imaging beam in a Varian TrueBeam Linac (Varian Medical Systems Inc., Palo Alto, CA) and reported enhanced contrast-to-noise-ratios (CNR) of approximately 16% to 19% in cortical bone when compared with the commercial 2.5 MV beam.[128] Similar results were seen by Parsons *et al.* with the modeling of a 2.35 MV carbon beam using Monte Carlo (MC).[129]

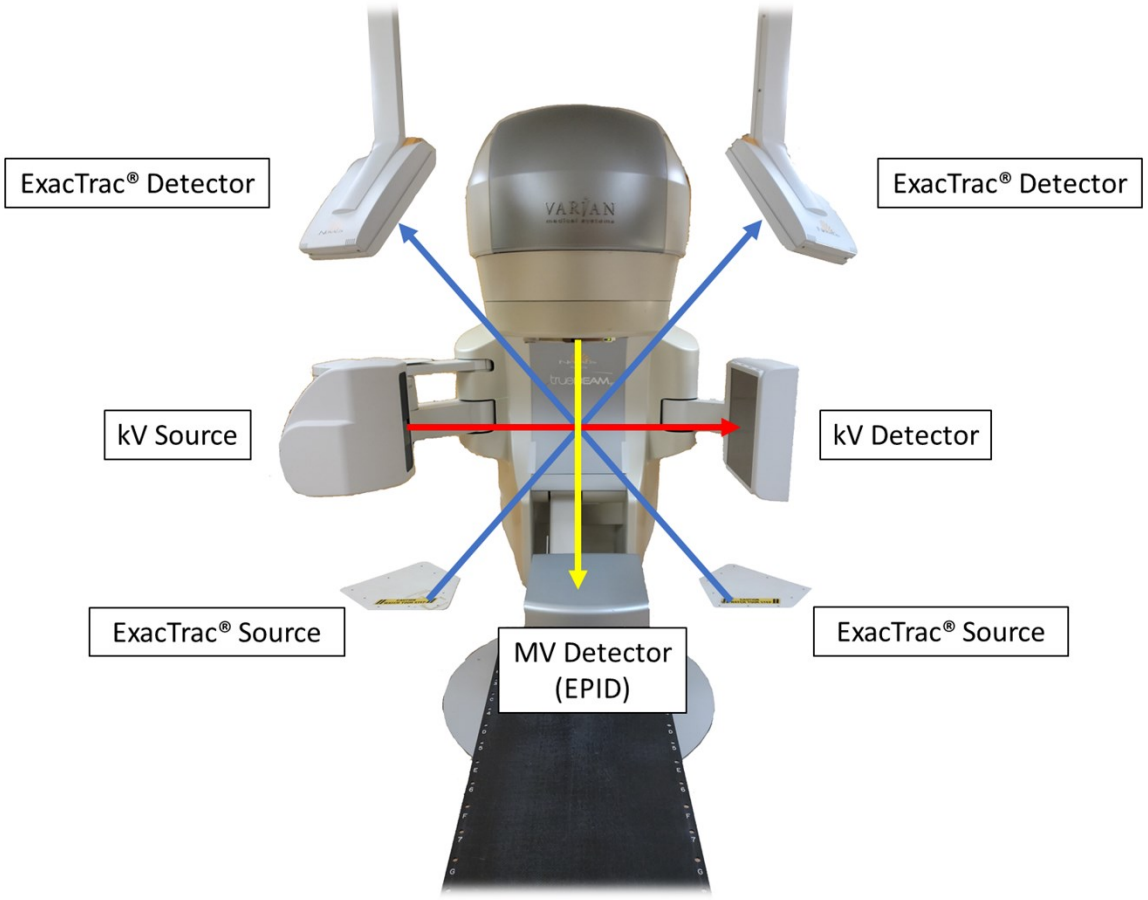

Figure 4: Monoscopic and stereoscopic imaging available on C-arm linac. Stereoscopic imaging shown with the Exactrac® system (Brainlab AG, Munich, Germany). Blue arrows indicate the ray-line direction of stereoscopic imaging, red arrows for kV imaging and yellow for MV imaging.

In a clinical setting, monoscopic imaging is rarely used alone. Instead, pairs of orthogonal images (kV/kV or MV/MV or kV/MV) or kV cone beam computed tomography (CBCT) is used to perform image guidance. Inter-arc CBCT is usually not utilized as it is slower and may not be necessary, given the rigid relation between a brain tumor and the skull. Most commonly, a pair of orthogonal images is used, with one being from the

anterior-posterior (AP) view and another being from the right-left (RL) or left-right (LR) view. In this format, 2D-3D registration is implemented by iteratively applying transformations to one image set and calculating a similarity metric (to assess registration) in both images. Using coordinate system transformations as demonstrated by Fu and Kuduvalli,[130] 2D-3D registration is achievable for any combinations of imaging view-points. One such implementation of this technique is with externally mounted stereoscopic systems such as those used by the CK platform[131] as well as the ExacTrac® system (Brainlab AG, Munich, Germany) as shown in Figure 4.[132] The limitation of the deploying 2D-3D registration to derive positional corrections for all six degrees-of-freedom for motion (translations and rotations about each principle axis) is that out-of-plane rotations can not be directly quantified; e.g, for two orthogonal images in the AP and RL view, a roll correction would be impossible to directly assess. Jans *et al.* investigated the coupling of perceived rotations and translation with orthogonal AP and LR MV/MV images and found that with clinical set-up errors less than 0.7 mm (translation), registration errors could be no better than $\pm 0.2^{o}$.[133]

There exist commercially available systems which do not utilize ionizing radiation for positional tracking, namely: optical surface imaging with speckled-light patterns and infrared (IR) marker tracking. Optical surface imaging works by projecting a known pattern onto the skin of the patient and extracts features from said pattern to derive 3D information such as the AlignRT system (Vision RT, London, UK) system. While this method possesses the ability to capture near continuous monitoring information (up to 60 frames per second), it suffers from ghosting,[134] as well as false positives and false negatives in the

case of skin monitoring.[135] IR marker tracking monitors the position of a reflective marker; for the GK system, a marker is placed on the tip of the nose during therapy and is imaged at 20 Hz, its position is monitored relative to its initial position that is established in the pre-treatment CBCT.[136] The limitation of this technique is that the tip of the nose is susceptible to deformations and rotations of the cranium, and thus does not necessarily represent positional deviations at the target site.[137,138] The IR marker tracking method is also available on C-arm linacs such as with the Varian Real-time Position Management system (Varian Medical Systems Inc., Palo Alto, CA), which monitors IR markers on a block which sits on the patient's chest during therapy. The limitation of this technique is that it assumes a correlation between the markers and the tumors motion during respiration.[139]

During delivery of radiosurgery, substantial effort is taken to ensure fidelity with planned positioning. To that end, minimizing motion while radiation is being delivered is of paramount importance. Historically, frame-based systems have been used to immobilize the patient by rigidly fixating to the patients skull.[140,141] Leskell's original stereotactic frame was improved upon through the introduction of the Brown-Roberts-Wells (BRW) and Cosmon-Roberts-Wells (CRW) frames which could be used in modern clinical workflows with CT and image guidance.[142,143] Rigid frame-based systems suffer from several drawbacks including slipping,[140] risk of bleeding and infection at the screw site,[144] as well as added stress and anxiety for the patient, oncologist, planner, and neurosurgery staff for treatment delivery coordination as treatment must be completed within the day. Frame-based systems have evolved into various manifestations such as the Gill-Thomas-

Cosmon (GTC) frame which and utilizes a bite-mould system for immobilization and can be utilized for fractionated radiosurgery.[145] This system however does obstruct the beam path for some treatments making it unsuitable.[146] Newer frames such as the PinPoint frame (Aktina Medical, Congers, NY, USA) have incorporated sophisticated bite-mould systems with integrated vacuum suction that improves contact and loses pressure when the patient moves.[135] A modern trend is towards the use of a frameless immobilization system with a thermoplastic mask which conform to the patient's facial features.[29,135,144,147-150] This system allows for fractionated therapy, is non-invasive, demonstrates improved patient comfort,[151] and easily usable in radiosurgical work-flows.

As mentioned above in Section 1.1 the stereotactic coordinate system is one that allows for the localization of anatomical sites (typically the TV) by utilizing affine-transformations to relate coordinate spaces during stereotaxis, namely: the anatomical coordinate system and the coordinate system of the frame.[152] The information described below is unique to medical linacs as it pertains to the device used for delivery in this thesis. To define a stereotactic coordinate system, CT or MR simulation can be implemented with a localizer box over the stereotactic frame (which is intrinsically linked to the coordinate system of the frame[153] or frameless-based immobilization system through mechanical fastening) or with other commercially available systems like the BrainLab frame (Brainlab, Inc, Westchester, IL).[154] The localizer boxes house various configurations of radio-opaque bars that relate anatomical locations to the coordinate system of the frame,[155] or in the case of the Brainlab system, relates the positions of the IR markers on the frame to the isocentre of the planning data set.[154]

When using a conventional stereotactic frame, alignment of the patient on the treatment unit can be achieved by using the localizer box (which will have the isocentre location defined in the treatment planning system (TPS) mapped to the faces of the localizer).[153] When thermoplastic mask systems are used, such as the BrainLab ExacTrac® system (Brainlab, Inc, Westchester, IL), patients are initially aligned to isocentre by IR-guidance which is then followed by some subsequent form of imaging (*e.g,* stereoscopic imaging).[154] To verify the coincidence of the ExacTrac® system with the radiation isocentre of the auxiliary system, a calibration is conducted before every treatment. A series of alignment tests are conducted with an IR-phantom and WL-phantom using the IR-alignment system in conjunction with either stereoscopic imaging,[156] kV imaging,[154] or MV imaging[157]

1.7 CURRENT LIMITATIONS OF SRS

Despite the combined efforts of image guidance and immobilization systems to minimize positional errors during treatment delivery, intrafractional motion can still occur. The magnitude, and frequency of motions observed during cranial radiosurgery has been explored in the literature for all manner of commercially available immobilization systems. Babic *et al*. explored translational and rotational intrafractional motions by comparing pre-treatment CBCT to one taken post-treatment for a variety of frame-based systems; they found that the patients using CRW frame had a mean 3D error of 0.30 ± 0.21 mm while the patients using the non-invasive GTC frame had 0.54 ± 0.76 mm.[158] The non-invasive PinPoint frame reduced 3D errors to 0.45 ± 0.33 mm and reduced the frequency of errors

exceeding 1.5 mm from 5% with the GTC frame to 0% with PinPoint frame.[158] Jursinic observed that the BRW frame allowed for an average motion of 0.93 ± 0.22 mm as determined with optical imaging tracking a fiducial plate with AlignRT (Vision RT, London, UK).[159]

Frameless systems are becoming increasingly more common for radiosurgery and SRT due to ease of use, and improved patient experience. Quality, and tightness-of-fit will impact the performance of immobilization, which is largely dictated by patient tolerance.[160,161] Using the BrainLab (Elekta AB. Stockholm Sweden) thermoplastic mask, Gaevert *et al.* quantified intrafractional motion with a post-treatment kV X-ray images (occurring 14.6 ± 3.9 minutes on average after set-up imaging) for 40 patients receiving SRS and found a mean 3D error of 0.58 ± 0.42 mm with motions reaching up to 1.8 mm and 1.55°.[162] Performing a similar assessment with 104 patients receiving radiosurgery, Lewis *et al.* quantified translation motion with kV images at two time points during therapy as shown in Figure 5; they found the maximal average motion at the first time point (0.79 ± 0.45 mm) and saw maximal 3D-displacement of 3.64 mm.[163] Comparisons between frameless thermoplastic immobilization systems and frame-based systems by Carminucci *et al*. found a significantly higher variance of intrafractional motion with the frameless system ($p < 0.05$).[164] Ramakrishna *et al.* similarly compared these two immobilization systems and found a larger proportion of patients exhibiting motions greater than or equal to 1.0 mm with the frameless mask-based system (22% compared to 3% for the frame-based system).[144] The magnitude, and frequency intrafractional motion during within thermoplastic masks has been shown to increase with increasing treatment time.[137,165-168]

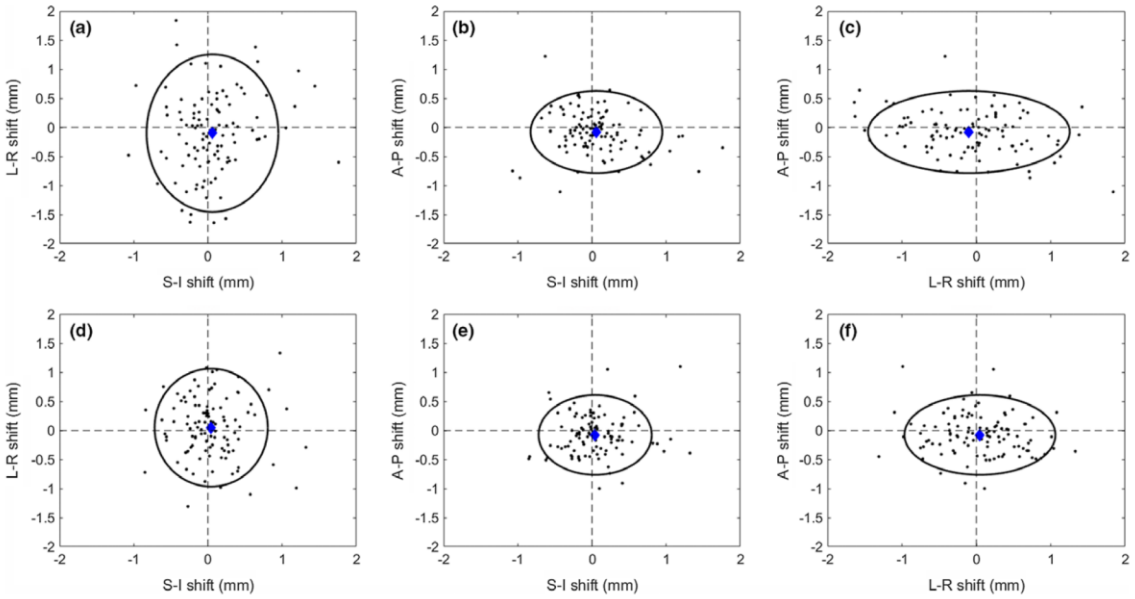

Figure 5: Translational intrafractional motion within a thermoplastic mask derived from kV images at two time points during therapy in the left-right (LR), anterior-posterior (AP) and superior-inferior (SI) direction. (a-c) were derived at the first imaging time point, (d-f) were derived from the second time point. Images from Lewis *et al.*[163]

Motion during treatment has the potential to negatively impact normal tissue dose constraints, as well as compromise therapeutic coverage. Guckenberger *et al.* calculated dose distributions in 72 patients with brain metastases while simulating intrafractional motion (translations and rotations) derived from post-treatment CBCT; they found that each simulated millimetre (3D-vector) of motion resulted in a 10% and 6% reduction of the Paddick conformity index and coverage index respectively.[169] Wang *et al.* investigated

the dosimetric impact of simulated intrafractional motion on 20 patients receiving stereotactic body radiation therapy (SBRT) for spinal metastases; they found that 13 out of 20 patients exhibited a max dose increase greater than 25% to organs at risk (OAR) with a 2.0 millimetre shift along the AP axis, and up to an approximately 10.0% decrease in the target volume receiving 95.0% of the prescription dose (V_{95}).[170] The treatment of multiple lesions simultaneously with a single isocentre is also highly sensitive to translational and rotational errors. Roper *et al.* performed a retrospective dosimetric analysis of rotational errors on 50 SRS cases with multiple metastases and found that TV, and distance from isocentre were predictors for compromises to target coverage as demonstrated in Figure 6, where the probability of coverage (determined by V_{95}) is shown to decrease in a complex manner as a function of distance of target from isocentre and TV size.[171] Similar results were determined by Minniti *et al*. when simulating intrafractional motion as determined from post-treatment ExacTrac™ images on patients receiving SIDCA; where 90.0% of targets with a V_{95} less than 95.0% had a volume less than 0.4 cc, and were located 3.9 mm or more from isocentre.[172]

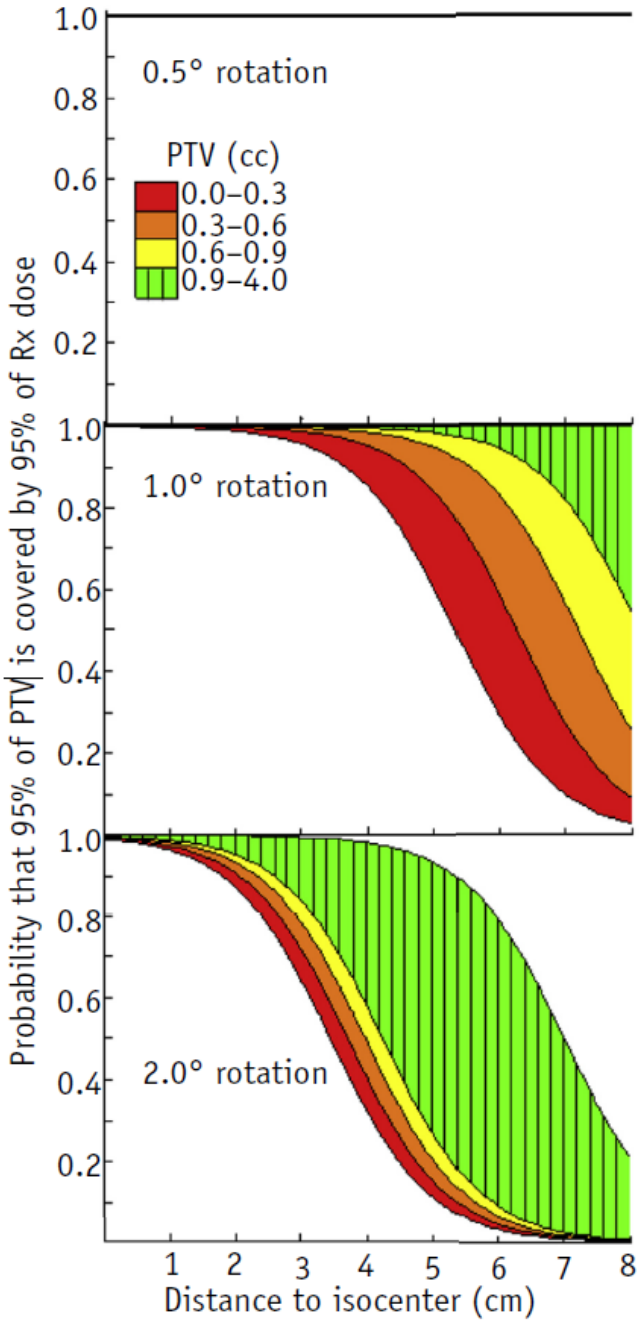

Figure 6: The probability that 95.0% of the planning target volume (PTV) will be covered by 95.0% of the prescription dose (Rx) as function distance from isocentre. The data is estimated from Generalized Estimating Equations logistic regression and is segmented for ranges of PTV sizes. The top plot for 0.5% indicates ideal circumstances where a 0.5° rotation would not impact any target size range for distances up to 8.0 cm from isocentre. Image from Roper *et al.*[171]

1.8 RESEARCH OBJECTIVES

As motion during therapy is unavoidable and has been shown to increase for long treatment times, the efficiency of treatment delivery is of significant importance, particularly in SRS. Manufacturers have recognized the importance of treatment efficiency and have made great strides to maximize the efficiency of treatment delivery by means of hardware improvements, such as the flattening-filter-free (FFF) beams which increase dose-rate, and software/algorithms improvements, such as Elements^{TM} Multiple Brain Mets SRS by Brainlab (Brainlab AG, Munich, Germany).

This thesis investigates two novel strategies for improving the fidelity between planned and delivered radiosurgery by means of improved treatment efficiency, as well as a motion correction strategy for cranial SRS workflows. The improvements in treatment efficiency would come from the manipulation of the movable axes of a C-arm linac during radiation delivery, in particular, the implementation of couch trajectories in which the distance from the radiation source to the target (isocentre) is shortened for unique combinations of treatment couch and gantry angle (defined as a control point). Shortening the distance of the radiation source to isocentre would lead to increases in the effective dose-rate at the target, which in turn would necessitate the delivery of fewer MUs to produce the same dosimetric outcome. The improvements in treatment efficiency by means of delivery at a shortened-isocentre must be achievable without dosimetric compromises for the intended TV as well as the surrounding tissues. Detecting and correcting for motion that could occur during therapy would be achieved with control point-specific couch motions derived from MV-imaging.

The work in this thesis explores questions pertaining to motion during cranial radiosurgery: 1) What are the dosimetric consequences for SRS-magnitude motions and for what target sizes do they compromise plan quality in a virtual cone treatment setting? 2) Can we detect SRS-magnitude motion with MV control point-specific imaging and correct for these positional errors with couch motions? 3) Can we implement couch trajectories to improve treatment efficiency and are there dosimetric consequences associated with these motions? These questions are explored in a series of three manuscripts as follows:

Manuscript 1 is presented in Chapter 4. This manuscript addresses the first research question by exploring the dosimetric consequences of simulated SRS-magnitude intrafractional motion while treating small spherical targets (less than or equal to 1.0 cm in diameter) with a virtual cone. Dose metrics for the TV as well as the surrounding normal tissue are explored for various target sizes, aperture sizes and types of motion. Relationships between these variables for clinical decision making is discussed within.

Manuscript 2 is presented in Chapter 5. This manuscript addresses the second research question by exploring the possibility of detecting SRS-magnitude motions with control point-specific MV region-of-interest (ROI) imaging using a 3D printed skull phantom. The investigation establishes a methodology for creating ROI imaging plans for cranial SRS which minimize registration errors without the need for user intervention. The characteristics of the apertures produced from this algorithm are explored. While simulating intrafractional motion on a Varian TrueBeam STx Linac, positional accuracy is

evaluated when using the ROI imaging plans to detect and correct for motion when imaging the 3D printed skull.

Manuscript 3 is presented in Chapter 6. This manuscript addresses the third research question by exploring the potential gains in treatment efficiency and plan quality when delivering at a shortened, virtual isocentre with couch trajectories. In this work, clinically delivered SRS plans for patients with one to three lesions are converted from a delivery at standard isocentre (100 cm SAD) to a shortened virtual isocentre. For each control point, the isocentre is shortened with an intent to deliver at distance of closest approach while avoiding collisions of the linac with the patient and/or treatment couch. Plan metrics for the TV(s), as well as OARs are explored. A delivery efficiency analysis is calculated for each of the plans based upon the velocity limits of the axes of the linac. A subset of the SRS plans are mapped to a cranial SRS phantom with an insertable holder for radiochromic film and ion chamber. The plans are delivered at a standard isocentre, and a virtual isocentre in Developer Mode. Gamma analysis and absolute dose measurements are compared to the planned dose distributions as a function of target size, and distance of target from isocentre.

The second chapter of this thesis describes the theoretical and algorithmic considerations pertaining to the experimental and modelling methodology used to conduct the investigations presented. The third chapter addresses the explicit methodologies utilized to conduct the work in Chapters 4-6 which are otherwise not addressed within each respective chapter. The seventh chapter summarizes the main findings from the manuscripts presented in this thesis and discusses the natural progression of future work.

CHAPTER 2. THEORETICAL CONSIDERATIONS

2.1. MEDICAL LINEAR ACCELERATOR

A medical linear accelerator is a device that generates high-energy x-rays by directing relativistic electrons into a target (often composite Copper (Cu) or Tungsten (W)). For the work in this thesis, the 6 MV FFF beam is exclusively used for all treatment deliveries. Commonly, flattened beams are referred to by their energy, e.g, 6MV beam; and FFF beams are similarly identified by 6 MV FFF. This photon beam has a maximum dose (D_{max}) at 1.5 cm depth in water, with a relative dose of 64.2% at 10 cm depth for a 10 x 10 cm^2 field at 100 cm source-to-surface distance (SSD). The beam has a maximum dose-rate of 1400 MUs per minute, where 1.0 MU is equivalent to 1.0 cGy at 95 cm SSD, 5 cm depth in water.[173] Other beam energies are available such as 10 MV, 15 MV, and 10 MV FFF but these are not considered in this work. Accelerators are able to change energies by changing the power transferred to the electrons within the accelerating waveguide.[174,175] Sometimes this can be coupled with the change of target. For the imaging performed in this thesis, the 2.5 MV imaging beam was used which does use a different target than the clinical treatment beam.

2.1.1. Beam Generation

The information from this section is taken from Karzmark and Morton[176] as well as Mayles *et al*.[177] To produce x-rays, several different systems can be used. Varian utilizes a

dispenser cathode which dispenses barium to the surface of the cathode,[178] where a kilovoltage potential difference across the cathode heats up the filament causing electrons to "boil" off via thermionic emission. These electrons are injected into an accelerating wave guide with a speed approximately equal to 20% of the speed of light. Radiofrequency (RF) pulses with a power in the range of 2.5 to 5 MW generated by either a magnetron or klystron are directed towards the wave guide with a frequency of 2.856 GHz for S-band linacs or 8 to 12 GHz for X-band linacs. The waveguide is a structure that accelerates and bunches electrons through interaction with the oscillatory electromagnetic wave produced from the RF power source. Two structures have been used, a traveling waveguide and a standing waveguide. The electrons leave the waveguide with speeds close to the speed of light and are steered by bending magnets. Different manufacturers have implemented different configurations of bending/steering to direct the electron beam towards the target; Varian uses a gradient magnetic field system to bend the beam 270^{o}, whereas Elekta has used a 112.5^{o} slalom bending system. The redirected electrons are incident on a "target" where bremsstrahlung photons are produced. The combination of electron energy and target material ensure that the photons are preferentially forward directed towards the patient.

After photons are produced, the beam can pass through a flattening filter which has a few effects: 1) it flattens the beam profile to be within 3% across the region defined by the inner 80% of the aperture at 90 cm SSD, 10 cm depth in water; this is accomplished by using a conical flattening filter that produces monotonically decreasing beam attenuation as a function of radial distance from the central axis. 2) A consequence of this filter design

is a radial dependence of the beam spectrum, with a harder beam being found on the central axis due to the preferential attenuation of low energy photons resulting from passing through the thickest region of the filter.[179] 3) Change the relative dose at a reference depth compared with un-flattened beams. The presence of the filter significantly reduces the dose rate compared to unfiltered beams. Ancillary components (dual ion chambers) downstream of the flattening filter stage are organized in a feedback loop configuration with the beam steering components above the target. The ion chambers monitor the beam output as well as the radial and transverse beam profile which is actively used to update the radiation beam during treatment delivery. Several components after the target are utilized to shape the radiation beam leaving the linac head (primary collimator, Jaws, MLC). A schematic representation the main beam-generating components of a medical linear accelerator is shown in Figure 7 where other notable components have been excluded for clarity including cooling, the pulse modulator cabinet, and voltage delivery.

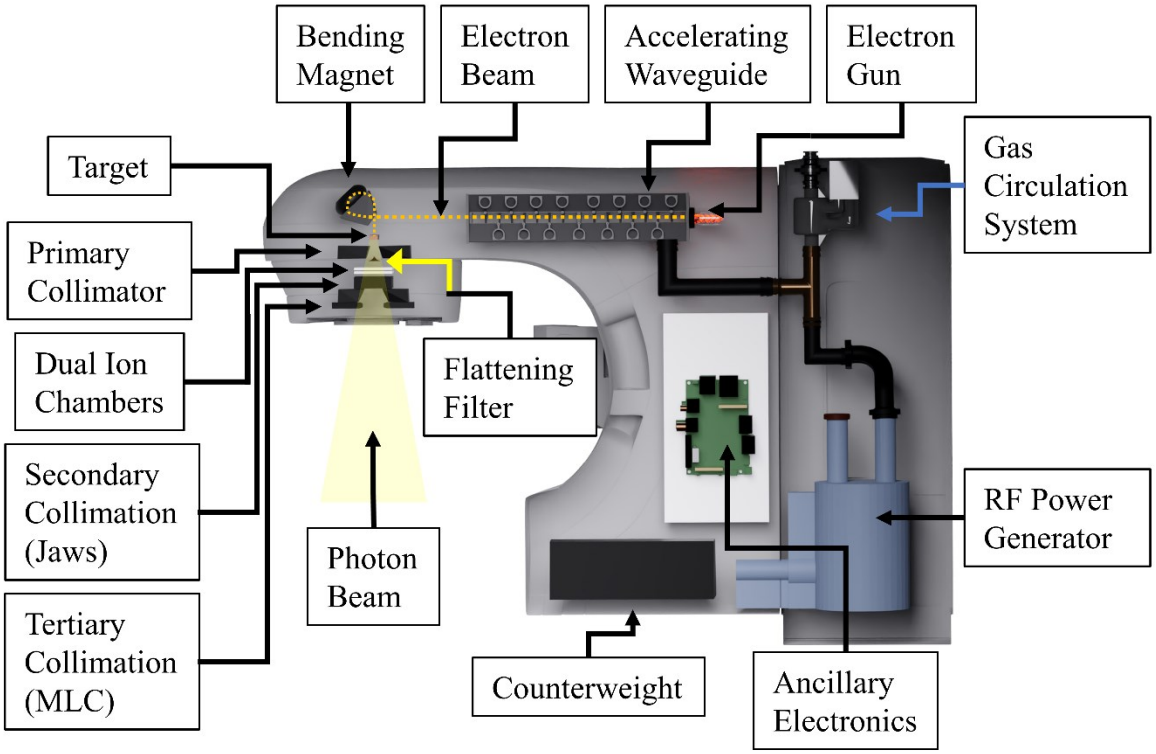

Figure 7: Schematic representation of the beam-generating components of a C-arm linac.

2.2. INTERACTIONS IN MATTER AND DOSE CALCULATION

2.2.1. Photon Interactions

When a monoenergetic pencil beam of photons is incident on a material, the beam is attenuated, and the incident number of photons, N_i is reduced by:

$$\mathrm{N} = N_i e^{-\mu x} \quad \textbf{(1)}$$

where μ is the attenuation coefficient of the material. The attenuation coefficient is dependent upon the elemental composition of the material and the density, ρ. There are tabulated values of the attenuation coefficient divided by the density, μ/ρ, and these are referred to as the mass attenuation coefficients. The coefficient, μ/ρ, is composed of the sum of all mass attenuation coefficients for the probabilistic interactions that a photon can undergo in a material. In human tissue, there are four common interactions that can occur within diagnostic (25 – 150 keV) and therapeutic (300 keV – 20 MeV) energy range, namely: Rayleigh scattering, the photoelectric effect, Compton scattering, and pair-production. Descriptions of these interactions can be found elsewhere.[180] The predominant interaction (in tissue) within the diagnostic energy range is the photoelectric effect, and the predominant interaction in the therapeutic range (for the 6xFFF treatment beam utilized in this work) is Compton Scattering.

The mass attenuation coefficient of the Compton interaction is effectively independent of atomic number as it reduces to $\sigma_c \propto \frac{Z}{A} \sim 0.5$ for most atoms. Thus, the probability of a Compton interaction occurring in materials with different atomic numbers is effectively the same. Given that the electron density of atoms contained within tissue does not vary significantly (as tissues are by-and-large not ionically charged), very little contrast is seen between different materials with MV imaging, as much of the photon energy spectrum is in the therapeutic range, primarily participating in Compton interactions. In contrast when using kV imaging (diagnostic energy range), the $\approx Z^3$ dependence of the photoelectric effect exhibits a much larger relative difference in the

interaction cross-section between materials, giving a much larger contrast. The mass attenuation coefficients of tissue and bone as defined by ICRU – 44[181] is shown in Figure 8.

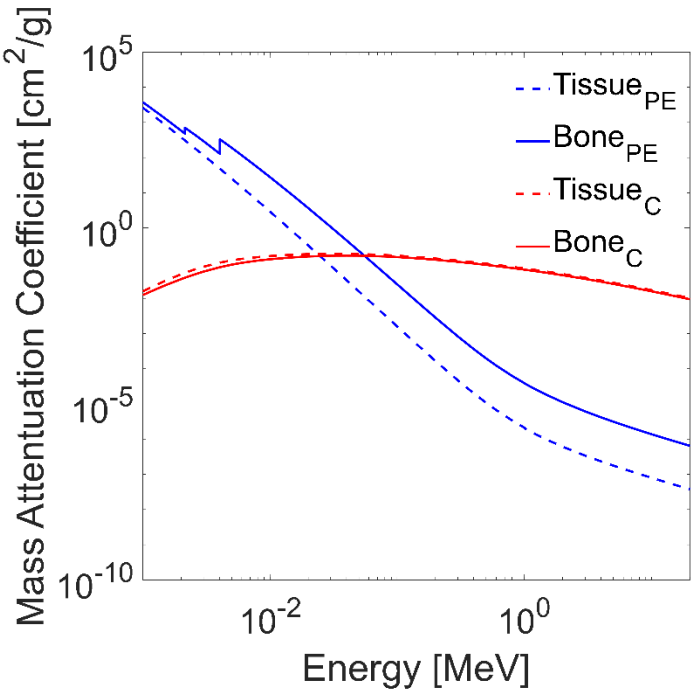

Figure 8: Mass attenuation coefficients as a function of energy for tissue (ICRU-44) and cortical bone (ICRU-44). Subscript PE denotes the photoelectric cross section and subscript C denotes the Compton cross section.

2.2.2. Electron Interactions

In this section, the information presented will focus on the motion of electrons through a material, as they are the primary source of dose from an incident photon beam. When electrons pass through a material, they go through several different interactions that cause them to lose energy. Energy loss per unit distance for these interactions is quantified by stopping power, commonly represented as the mass stopping power, $\left(\frac{dT}{\rho dx}\right)_{Tot}$, which is the sum of two contributions, the mass collisional stopping power, $\left(\frac{dT}{\rho dx}\right)_{c}$, and the mass radiative stopping power, $\left(\frac{dT}{\rho dx}\right)_{r}$.

The mass collisional stopping power is the result of the large number of collisional events in which a moving electron loses energy via Coulombic interactions with every charged particle in a medium. This interaction is separated into two types of events, namely, *soft* or *hard* collisions, and are distinguished by the proximity of the trajectory of the electron in relation to the atom radius, a, shown in Figure 9,

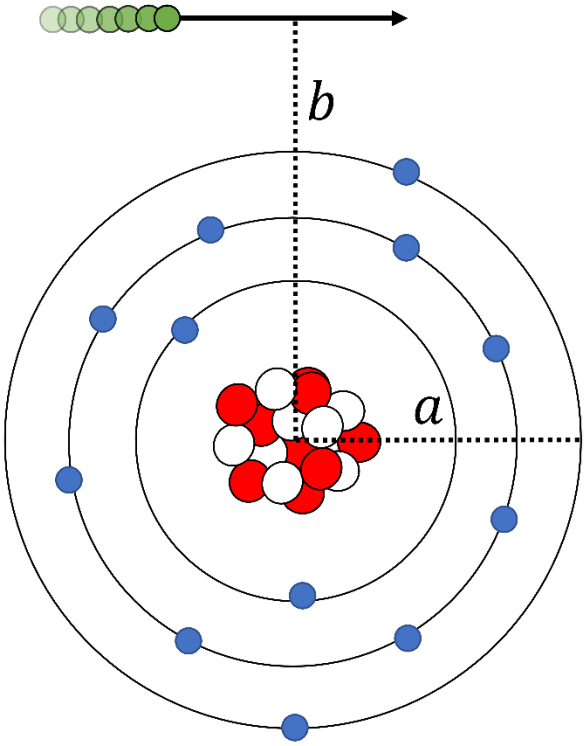

Figure 9: Electron interaction where a moving electron (green) passes by an atom with an atomic radius, a, with a proximity, b, referred to as the impact parameter.

where, b, is referred to as the impact parameter. A *soft* collision is one where an electron passes by the atom at a large distance, $b \gg a$, whereby the interaction of the Coulombic force field of the electron transfers momentum, and thus, energy to the atom.[182] A *hard* collision is one where the electron passes by at a distance on the order of the atomic radius, $b \approx a$; which results in the ejection of an orbital electron, referred to as a delta (δ) ray.[182] To describe the energy lost by the electron undergoing these interactions, Bethe[183] combined the contributions from *soft* and *hard* collisions based upon the Møller cross section for electrons.[184]

The mass radiative stopping power describes the energy loss of an electron that passes closes to the nucleus, $b < a$, and is described by Attix.[180] This interaction results in the production of bremsstrahlung photons from the deceleration of the electron via Coulombic interactions with the electric field of the nucleus. Up to 100% of the energy of the electron can be transferred from the energy stored in the electric field of the electron to the bremsstrahlung photon[185].

As stated earlier, dose deposition in a material is the result of energy transferred from moving electrons that were set in motion by incident photons. The dose deposited at some depth, x, can be calculated with the differential charged-particle fluence spectrum, Φ_x (calculation of this spectrum is discussed in the context of treatment planning systems in 3D later within Section 2.2.4.1 with symbol, Ψ^e), and used to determine dose with:

$$D = 1.602 \times 10^{-10} \left[\frac{Gy}{\frac{MeV}{g}}\right] \int_0^{T_{max}} \Phi_x(T) \left(\frac{dT}{\rho dx}\right)_c dT \qquad \textbf{(2)}$$

This calculation makes two assumptions about dose deposition: 1) Photons produced by electron interactions with the nuclear field will not deposit dose locally (instead, via subsequent interactions which set in motion other secondary electrons). 2) Charged particle equilibrium (CPE) exists,[180] allowing for the exclusion of dose owed to δ-ray production.

2.2.3. Monte Carlo

Analytically describing the progression of photon interactions, radiative losses, and coulombic interactions as electrons inelastically collide with other electrons from an incident photon beam leads to complex integro-partial differential equations.[186] These equations are computationally intractable to solve, even with approximations. Thus, the MC dose calculation framework has been developed to model the transport of photons and electrons in a material. The algorithmic premise behind the technique involves sampling probability distributions of stochastic processes with a random number generator. Essentially, the MC process uses random numbers to follow the history of a simulated particle, by determining where in space an interaction takes place, the type of interaction that takes place and the geometric-, as well as energetic- after-products of that interaction are. The are two inherent limitations of MC methods to accurately simulate radiation transport: 1) The data utilized to determine the outcome of individual interactions (*e.g*, cross-section data for each interaction, as well as approximations that go into sampling probability distributions) are derived from an amalgamation of theoretical and experimental measures. The limitations of these various interaction types have been discussed at length in the EGSnrc[187] and EGS4[188] manuals. 2) The MC method simulates a finite number of user-defined histories, N, which is intimately related to the convergence of the system to analytical solutions of the Boltzmann equations (which describes radiation transport). The number of histories is representative of a partial sampling of the stochastic nature of radiation transport; thus, quantities that are derived from MC simulations are subject to statistical uncertainty which are proportional to $N^{-1/2}$.[187]

In the following, the MC approach for simulating radiation transport as employed by Kawrakow *et al*. will be introduced following a generalized history of a photon as it progresses through a MC simulation.[189] The first required action is to determine the distance to the next interaction, x, by sampling the cumulative probability distribution function which describes the probability of an interaction occurring with:

$$x = -\frac{\ln(1-r)}{\mu} \tag{3}$$

Where $\boldsymbol{\mu}$ is the linear attenuation of the material, and $\boldsymbol{r}$ is randomly generated number between 0 and 1. At the depth of the interaction, the next algorithmic step is to determine the type of interaction that will occur. A mentioned prior in Section 2.2.1, given that the attenuation coefficient is the sum of the possible interaction coefficients (Rayleigh scattering, Compton, photoelectric, pair-production) a stepwise function can be constructed for random sampling with, $\boldsymbol{r}$, to determine interaction type with:

$$\begin{aligned}
&\{Rayleigh \,|0 \le r < \frac{\sigma_R}{\mu} \qquad r \in [0,1)\} \\
&\{Photoelectric \,|\frac{\sigma_R}{\mu} \le r < \frac{(\sigma_R+\tau)}{\mu} \qquad r \in [0,1)\} \\
&\{Compton \,|\frac{(\sigma_R+\tau)}{\mu} \le r < \frac{(\sigma_R+\tau+\sigma)}{\mu} \qquad r \in [0,1)\} \\
&\{Pair\ Production \,|\frac{(\sigma_R+\tau+\sigma)}{\mu} \le r < 1 \qquad r \in [0,1)\}
\end{aligned} \tag{4}$$

Once an interaction is determined, the kinematics of the problem, *i.e,* the resulting angle(s) and energies of the particle(s) following the interaction is determined by decomposing the

differential cross-sections of the respective interaction into a probability density function which can be sampled with a random number.

Following a photon interaction, which produces a secondary charged particle (electrons will be considered for simplicity), the history of the charged particle will be followed until it loses all of its energy. As shown by Podgorsak,[185,190] a 10 MeV electron can undergo up to 10^6 interactions in oxygen before slowing down. To fully simulate every interaction an electron would participate in would be too computationally expensive; thus, an approximation referred to as the condensed history technique was developed by Berger.[191] The concept of the technique is to combine the small-effect electron interactions which result in small angular deflections and energy losses into large steps to make the process more computationally feasible. Energy loss between electron path-steps (between "catastrophic" interactions) is approximated by the continuous slowing down approximation (CSDA) which is governed by stopping powers.[192] The small-angular deflections along an electrons path within the condensed history technique are modelled by several small-angle theories.[183] The electron's history will be simulated with few larger-steps by sampling a probability distribution describing its energy losses, and trajectory through a medium. The condensed history technique is an approximation in which its representation of full electron-transport is dictated by a "step-length" parameter, to which this parameter has been shown to create artifacts at boundaries between different media.[193] At each interaction site (*i.e* the "catastrophic" event), an interaction type is selected based upon the step-wise function describing the cross sections of possible events (similar to photons) and the outcome of each interaction is determined from sampling the differential

cross section of each interaction type; for *hard* collisions the Møller cross section is sampled, for bremsstrahlung interactions the Bethe-Heitler cross sections are sampled.[194]

2.2.4. Treatment Planning System

Calculating the absorbed dose from radiation produced by a medical linear accelerator is a complicated process that requires transporting a radiation beam through two different stages. In the first stage, the radiation beam is transported through the beam-shaping components of the linac which contain high atomic number materials for shielding. In the second stage, the collimated radiation beam is incident on a patient geometry where a dose deposition calculation is performed. This final step is affected by various intricacies such as tissue heterogeneities and obliquities through the curvature of different material interfaces. To simplify this process, a clinical treatment planning software (in which there are several different versions produced by different vendors) is utilized to approximate the various radiation transport scenarios mentioned above with algorithms and experimentally verified data repositories. For Chapter 6, the Eclipse integrated treatment planning system (TPS; Varian Medical Systems, Inc., Palo Alto, USA) was used and will be introduced below.

Monte Carlo simulations of radiation transport through the up-stream components of the linac before the collimation system (*e.g,* target, primary collimator, flattening filter, etc.) are conducted to generate a photon beam model for dose calculation in the TPS. The configuration of the input model is based upon feedback from measured clinical data. The

components of the beam model include: the photon energy spectrum, the mean radial energy with respect to the central axis, and the beam intensity profile which is unit-specific. The phase space simulates the treatment beam with four separate models: 1) The primary photon source resulting from bremsstrahlung photons produced in the target. 2) The extra focal source resulting from photons that are produced from interactions in the components of the accelerator head. 3) Electron contamination source which would represent dose deposited within the build-up region that does not come from source 1 or 2. 4) Photons scattered from the wedge – when a wedge is being used. Eclipse currently comes equipped with two dose calculation engines, namely: the Analytical Anisotropic Algorithm (AAA)[195-197] and the Acuros XB advanced dose calculation (AXB)[198-200]. Both algorithms will be briefly described below.

2.2.4.1. Analytical Anisotropic Algorithm (AAA)

Prior to dose calculation the TPS divides the material data of the dose-deposition volume (clinically the patients' CT scan) into voxels (volume pixel in 3D) which are divergent, aligning with divergence of the treatment beam; the voxels are then assigned with the mean electron density of the local medium, $\rho(x, y, z)$. The treatment beam is subdivided into finite beamlets, β, which are incident on the dose-deposition volume to derive an energy distribution, E_β, for each beamlet using a 3D pencil beam convolution superposition:

$$E_\beta(\tilde{X},\tilde{Y},\tilde{Z}) = \Phi_\beta * I_\beta(z,\rho) * \iint_{(u_i,v_i)\in Area(\beta)}^{u_f,v_f} \kappa(u-x,v-y,z,\rho)dudv \qquad \textbf{(5)}$$

where $(\tilde{X},\tilde{Y},\tilde{Z})$ is the calculation point relative to the beamlet coordinate system (X,Y,Z), and Φ is the fluence of the beamlet. The photon scatter kernel, $\kappa(x,y,z,\rho)$, defines the absorbed energy at location (x,y,z) with respect to the beamlet derived from MC pencil beam scatter kernels. The energy deposition function, $I_\beta(z,\rho)$, models photon beam attenuation throughout the material. This function is polyenergetic and is created from a superposition of MC-modeled monoenergetic beams – thus, the relative contribution of each $I_\beta(z,\rho)$ depends on the incident photon energy spectrum. For each photon source mentioned above, this operation is performed independently.

The AAA algorithm handles tissue heterogeneities between the incident beamlet, and the calculation point, $(\tilde{X},\tilde{Y},\tilde{Z})$, by scaling I_β and κ with the concept of radiological path-scaling:

$$z' = \int_0^z \frac{\rho(x,y,t)}{\rho_{water}}dt \qquad \textbf{(6)}$$

For example, in the presence of heterogeneities, $I_\beta(z,\rho)$ used in equation (5) becomes:

$$I_\beta(z,\rho) = I_\beta(z') * \frac{\rho(x,y,z)}{\rho_{water}} \qquad \textbf{(7)}$$

To adequately handle the impact of heterogeneities on the scatter kernel, β, the kernel is first collapsed to the depth dimension, z and is pre-emptively deconvolved with the energy deposition function before calculating equation (5) with:

$$I'_{\beta}(z) = I_{\beta} \otimes \ inv(\kappa_z\ (z)) \quad \textbf{(8)}$$

Where $\otimes$ denotes the convolution operator and $\kappa_z\ (z)$ is the photon scatter kernel which has been modified with radiological scaling. At the end of the calculation, a dose distribution is determined by superposing all energy distributions from each source and multiplying by the ratio of the electron densities in the material with respect to water.

2.2.4.2. Acuros XB (AXB)

The Acuros XB dose calculation engine solves the linear Boltzmann transport equation (LBTE) numerically; it assumes that radiation only interacts with the matter it is passing through and not with other radiation sources/interactions. It utilizes the same machine model as the AAA algorithm (comprising of the same four source components). Differing from the AAA algorithm, AXB directly models different radiation interactions in matter; to do this, the voxelized dose calculation volume is converted into a mass-density grid (derived from the imaging data set with the CT calibration curve) and the chemical composition of each material is used to calculate the photon cross section:

$$\sigma = \frac{N_a \rho}{M} \sum_i \widetilde{\sigma_\iota} \quad \textbf{(9)}$$

where ρ is the mass density, M is the mass of the atom in the voxel, and $\widetilde{\sigma_\iota}$ is the cross section for each photon interaction (Rayleigh scattering is excluded).

Dose to the medium is calculated in four sequential steps: 1) Transport the beam model into the dose calculation volume. 2) Calculated the scattered photon fluence. 3)

Calculate the scattered electron fluence. 4) Calculate the dose. Analytically, the AXB algorithm is solving the time-independent coupled Boltzmann equations which take the form:

$$\begin{aligned} \hat{\Omega} \cdot \vec{\nabla}\Psi^{\gamma} + \sigma_t^{\gamma}\Psi^{\gamma} &= q^{\gamma\gamma} + q^{\gamma} \\ \hat{\Omega} \cdot \vec{\nabla}\Psi^{e} + \sigma_t^{e}\Psi^{e} - \frac{\partial}{\partial E}(L\Psi^{e}) &= q^{ee} + q^{\gamma e} + q^{e} \end{aligned} \quad \textbf{(10)}$$

where $\hat{\Omega}$ is the directionality function in spherical coordinates. The parameter Ψ^{x}, is the angular fluence where x denotes the photon (γ) fluence or the electron (e) fluence. The parameter q^{xx}, is the scattering source where xx denotes the photon-photon $(\gamma\gamma)$ scattering source of photons resulting from photon interactions, the electron-electron (ee) scattering source of electrons resulting from electron interactions, or the photon-electron (γe) scattering source of electrons resulting from photon interactions. The parameter q^{x}, is the extraneous source from a point source P, where x denotes the photon (γ) or electron (e) source. The parameter σ^{x}, is the cross section where x denotes the photon (γ) or electron (e) cross sections and σ_t denotes the total cross section. The parameter L, denotes the restricted collision and radiative stopping power.

Steps 1-3 in the AXB algorithm numerically derives the final angular electron fluence ,Ψ^{e}, through various discretizations of geometries, limitations of scattering models as well as cutoffs for energy deposition conditions. Once the angular electron fluence ,Ψ^{e}, is derived, the dose in every voxel within the medium is calculated with:

$$D(x,y,z) = \int_0^{E_{max}} dE \int_{4\pi} d\widehat{\Omega} \frac{\sigma_{ED}^e(\vec{r},E)}{\rho(\vec{r})} \Psi^e(\vec{r},E,\widehat{\Omega}) \quad \textbf{(11)}$$

where σ_{ED}^e is the macroscropic electron energy deposition cross section, and E_{max} is the maximum energy of the input beam phase space model.

2.3. DOSIMETRY

Dosimetry refers to the determination of an absorbed dose in a material with some measurement apparatus. In a clinical setting, published protocols (*e.g,* TG-51[173]) can be used to accurately quantify the dose output of a linac under a prescribed set of reference conditions (more on this below). With knowledge of the dose delivered by the linac, it is then possible to cross calibrate other dosimetry systems (*e.g,* film, other ion chambers) to permit the translation of a measured signal (optical density or integrated charge) into dose in conditions other than reference conditions. This chain of cross calibration is critically important in the setting of small field dosimetry (see Section 2.3.1) where some detectors used for clinical reference dosimetry are simply not appropriate for small field dosimetry measurements.

The modern protocol for reference dosimetry was established in TG-51 where the dose to liquid water, D_w^Q, for a given treatment beam quality, Q, is calculated with:

$$D_w^Q = Mk_Q N_{D,w}^{60Co} \quad \textbf{(12)}$$

where M, is the corrected measurement of the ion chamber, k_Q is the chamber-specific quality conversion factor that was calculated by Muir and Rogers[201] using egs++[202] and $N_{D,w}^{60Co}$ is the absorbed-dose calibration factor that is obtained under reference condition with a ^{60}Co radiation beam determined by an accredited standards laboratory. When establishing reference dosimetry in clinical practice, the measurement M, necessitates several correction factors:

$$M = P_{ion}P_{TP}P_{pol}M_{raw} \tag{13}$$

where P_{ion} is a correction factor to adjust for incomplete ion collection owed to ions of opposite charges recombining before reaching the collecting electrode;[203] P_{ion} exhibits non-linear behaviour for pulsed beams,[204] has a dose per pulse dependency,[173] and is defined as:

$$P_{ion} = \frac{1 - \frac{V_H}{V_L}}{\frac{M_H}{M_L} - \frac{V_H}{V_L}} \tag{14}$$

where V_H is the high operating voltage (typically -300V), M_H is the raw measurement at V_H, V_L is the low operating voltage (typically -150V) and the corresponding raw measurement is M_L. The temperature-pressure correction, P_{TP}, corrects for changes in gas density within the active volume of the ion chamber from reference conditions (T = 22.0^o C, and P = 760 mmHg) defined as:

$$P_{TP} = \left(\frac{273.15 + T}{295.15}\right)\left(\frac{760}{P}\right) \tag{15}$$

where T is the temperature in Celsius, and P, is the pressure in mmHg. The polarity correction factor, P_{pol}, adjusts for several variables including: 1) Current induced within the collecting electrode from incident radiation interacting within the electrode;[205] 2) Extracameral current arising from ionizations outside of the collecting volume;[206] 3) Distortions in the electric field between the guard electrode and the collecting electrode.[207]

2.3.1. Small-field Dosimetry

In Chapter 6 small-field dose measurements are quantified and require special consideration. Small fields create complex dosimetric conditions where the penumbrae (defined approximately by the measured distance between 80% to 20% dose level for lateral beam profile) of opposing components in the collimation system (*e.g,* opposing MLC leaf pair) overlap causing a drop in measured output, and increase in radiation field size as determined by the full width at half-maximum (FWHM: defined by the difference in physical extent between the 50% dose levels for a lateral beam profile). To delineate what constitutes a small-field, the definition described in TRS-483 will be used.[208] Dosimetrically, a small-field is one where at least one of three physical conditions are met: 1) There is a loss of lateral charged particle equilibrium (LCPE). This condition occurs when the half-width of the beam is smaller than the maximum range of the electrons that are set in motion from interactions of photons within the beam. 2) There is an occlusion of the spot-size of the bremsstrahlung photon fluence distribution within target indicated in Figure 10 by the collimation system. An investigation by López-Sánchez *et al*. found that

the mean focal spot-size projected at isocentre (100 cm SAD) was 1.56 ± 0.02 mm for three separate Varian TrueBeam linacs installed over three years.[209] 3) The detector size exceeds the dimensions of the beam; this condition being intimately related to the volume averaging effect and perturbation of the charged particle fluence.

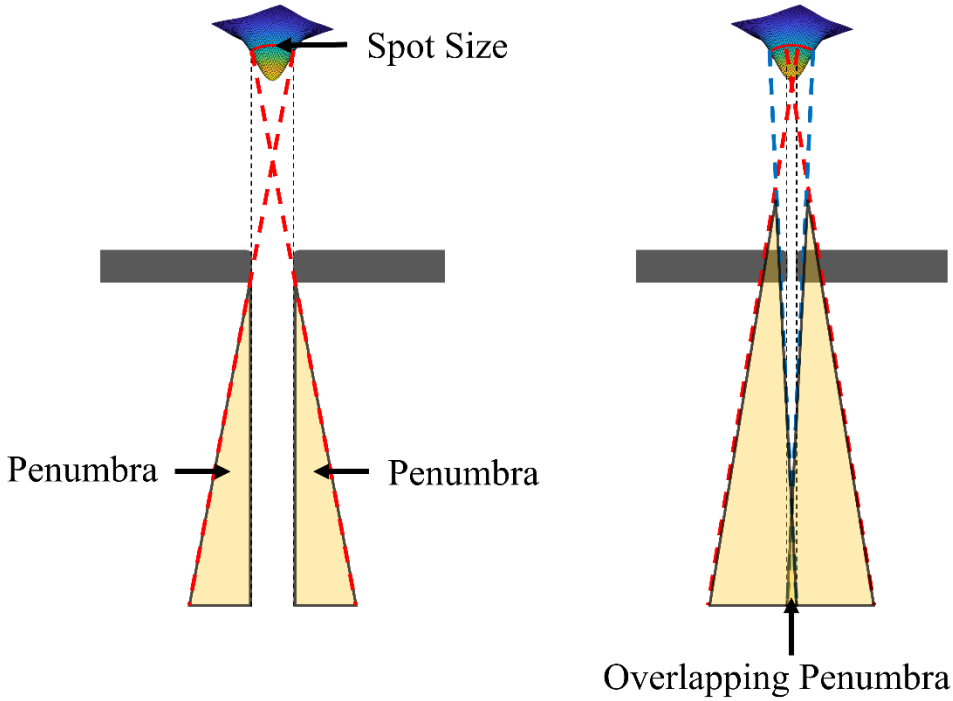

Figure 10: Demonstration of a measurement of the maximum output region (indicated by dotted black lines) for a regular sized field (left) and small field (right) where the spot size of the bremsstrahlung photon fluence spectrum has been occluded by the collimation system, causing the dosimetric penumbra of the opposing collimation components overlap. Figure reproduced from TRS-483.[208]

2.3.2. GafChromic™ Film Dosimetry

In this work, EBT3 GafChromic™ film (Ashland Advanced Materials, Bridgewater, NJ, USA) was used to measure dose distributions due to its potential for high spatial resolution. An additional benefit of GafChromic film is its near tissue-equivalence as well as little to no energy dependence.[210,211] EBT3 film consists of two symmetric layers of 120 μm of a polyester sandwiching a ~28 μm of a proprietary substrate which contains di-acetylenes (active monomer) that upon irradiation,[212] initiates a polymerization reaction that darkens the film .[212,213] Film dosimetry is particularly sensitive to scanner response and film orientation,[214] as well as post-irradiation darkening time.[215]

The dosimetric response of GafChromic film has historically been determined from the change of its optical density when compared to a measurement of its optical density prior to irradiation. Optical density by definition is the logarithm of the inverse transmission measured in the scanning process. The outcome of this measurement is affected by: 1) The absorption spectra of the film which is function of the irradiation and manufacturing condition for the film. 2) The emission spectra of the densitometer (lightbulb in the scanner). 3) The sensitivity spectrum of the sensor in the scanner.[210,216] Modern practices have adopted the determination of dose by directly measuring the pixel value with a flat-bed scanner and comparing this to a calibration protocol under reference conditions (discussed further in Section 3.3).

2.4. IMAGING ON A MEDICAL LINEAR ACCELERATOR

As discussed in Section 1.6, the importance of imaging in radiotherapy is to verify patient position both before and during treatment. While a modern linac has a kV imaging system orthogonally mounted to the treatment beam, this section focuses on MV imaging with the 2.5 MV beam of the Varian TrueBeam® STx linac. The impetus for imaging with the 2.5 MV beam is that it provides positional information with respect to the BEV, and it produces images with higher contrast than ones acquired with the 6 MV treatment beam. Higher contrast with the 2.5 MV beam is the result of a softer energy spectrum. Parsons *et al.* reports that approximately 22% of the photons in the 2.5 MV beam fall within the diagnostic energy range, compared with less than 1% with the 6 MV beam.[129] The normalized energy spectra for the 2.5 MV and 6 MV beam are shown in Figure 11. As mentioned in Section 2.1.1, changing of the photon beam spectrum relies on the adjustment of the incident electron energy, and target. The production of the 2.5 MV beam relies on an incident electron beam with a nominal energy of 2.5 MeV as well as a target change to 2 mm of a copper alloy.[217] Due to proprietary reasons, exact information on the operational parameters of the waveguide during the production of the 2.5 MV are not available to describe the production of the 2.5 MeV electron beam. In other works by Parsons *et al*., a tuning of the gun high voltage, and grid-voltage was required to adjust beam current to practical levels with an in-house low-Z target which produced a 1.9 MV or 2.35 MV beam.[218] However, it is not publicly known if these operational changes are needed with 2.5 MV imaging beam by Varian.

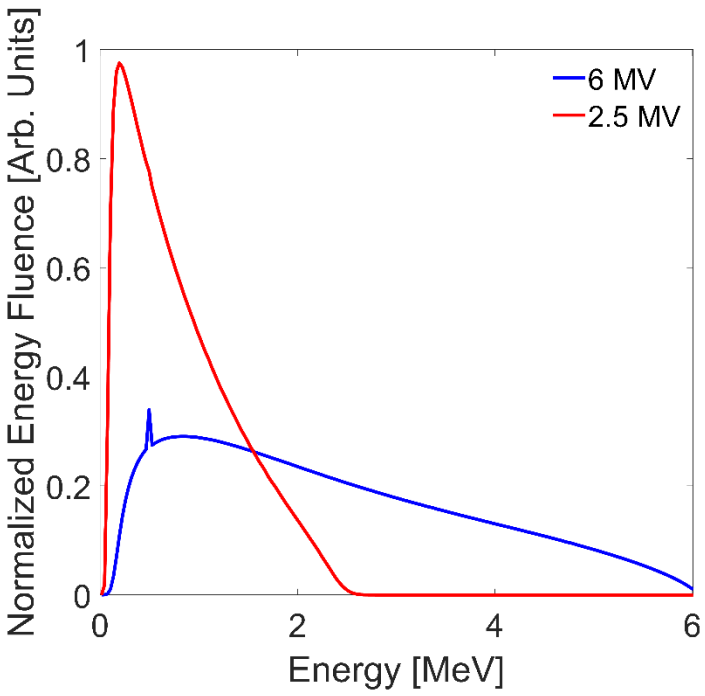

Figure 11: The relative spectral distributions of the 2.5 MV imaging beam[129] and the 6 MV treatment beam[219] that have been normalized by their respective integrated energy spectra.

The EPID for the Varian TrueBeam® STx linac utilizes the aS1000 MV imaging panel and was used extensively in Chapter 5. The aS1000 has physical dimensions of 40 x 30 cm^2 with a pixel area of 1024 x 768 pixels (0.392 x 0.392 mm^2 physical pixel size) and can be moved along central axis from 95 to 180 cm source-to-detector distance (SDD). The imaging panel consists of a stacked design where the first layer is a 1 mm sheet of copper which creates a cascade of secondary electrons (from the incident photons). The electrons travel into a scintillating sheet of 134 mg/cm^2 gadolinium oxysulphide phosphor

material creating visible light photons. This is followed by a layer amorphous silicon on a grid (each pixel) consisting of a light sensitive photodiode and a thin film transistor connected to the data readout lines.[220] Gräfe *et al*. found that the 6MV and 2.5MV imaging beam exhibited a strong correlation ($r^2 \sim 0.99$) in detected positional shifts with a WL phantom.[217] Using the Leeds phantom, the discernible resolution of the high-contrast portion of the phantom was found to be 1.4 lp/mm (line-pair per mm) with the 2.5MV beam and 2 lp/mm with a 80 kV, 0.8 mAs beam; none of the line-pairs were discernible with the 6 MV beam.[217,221]

2.4.1. Digitally Reconstructed Radiograph

In patient position verification tasks, acquired images must be compared to a reference image for the purpose of evaluating the degree of positional similarity. In the case of planar imaging applications, this is typically accomplished by comparing an acquired image to a DRR. A commonly used method to generate a DRR has been described by Siddon,[222] where the radiological path is calculated through a 3D volume of linear attenuation coefficients as depicted in the illustration shown in Figure 12. In the text below, the algorithmic formalism for calculating the radiological path for a given ray-line will be introduced.

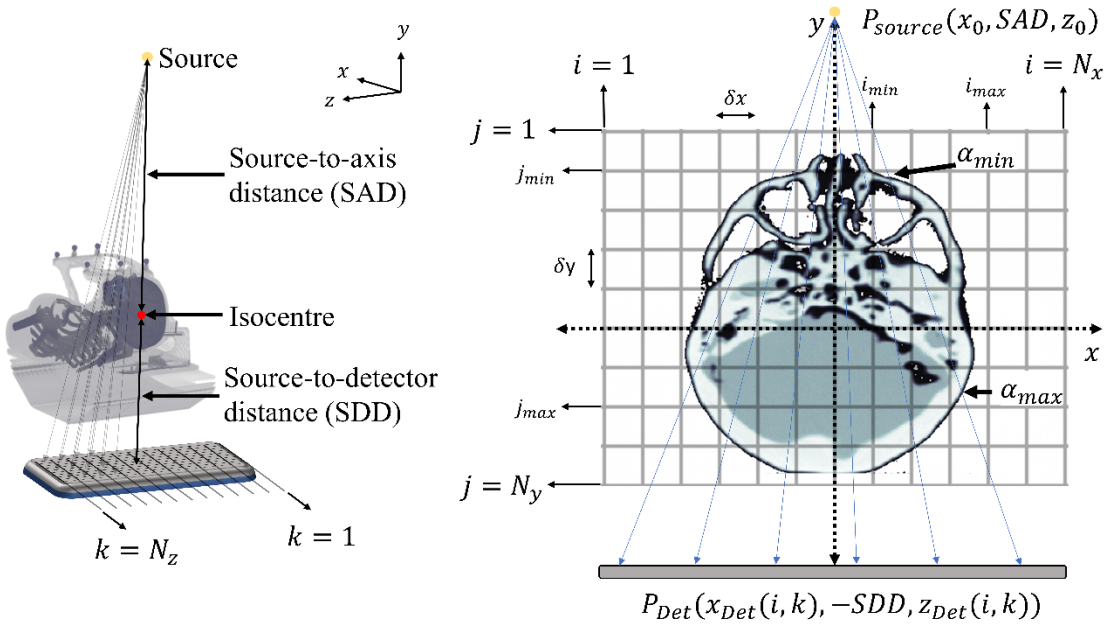

Figure 12: A pictorial demonstration of Siddon's Method[222] for calculating the radiological pathlength through a 3D array where the voxels describe the linear attenuation coefficient of the material. (Left) Shows ray-tracing through the 3D volume to the pixels of the detector plane. (Right) Shows ray-tracing in one 2D plane.

A parametric equation can be used to describe the ray-line from the source, P_{source}, to a detector element, P_{Det} with:

$$P_{\beta}(\alpha) = P_{\beta,source} + \alpha * (P_{\beta,Det} - P_{\beta,source}) \quad \textbf{(16)}$$

where β describes the x, y, or z dimension of point P, and α is parameter that has value of zero at P_{source} and a value of one at P_{Det}. Within the 3D volume, the planes along each dimension can be described with:

$$P_{\beta,plane}(\eta) = P_{\beta,plane}(1) + (\eta - 1) * \delta_{\beta} \qquad (\beta = 1, \dots, N_{\beta}) \quad \textbf{(17)}$$

where η is the i^{th}, j^{th}, or , k^{th} index in the 3D volume, δ_β is the distance in the β dimension, and N_β is the number of pixels in the β dimension. The parametric values, α_{min} and α_{max} shown in in Figure 12, represent the intersection, and exit of the ray passing through the 3D volume respectively and are determined with:

$$\begin{aligned} \alpha_{\beta,min} &= \min\left[\alpha_\beta(1), \alpha_\beta\left(N_\beta\right)\right] \\ \alpha_{\beta,max} &= \max\left[\alpha_\beta(1), \alpha_\beta\left(N_\beta\right)\right] \\ \alpha_\beta(\eta) &= \frac{P_{\beta,plane}(\eta) - P_{\beta,source}}{P_{\beta,Det} - P_{\beta,source}} \end{aligned} \tag{18}$$

From equation (17), only certain planes will have parametric values in the range of α_{min} and α_{max}; these planes with have indices η_{min} and η_{max} in the 3D volume and are given by:

$$\begin{aligned} \eta_{\beta,min} &= N_\beta - \frac{P_{\beta,plane}\left(N_\beta\right) - \alpha_{min} * \left(P_{\beta,Det} - P_{\beta,source}\right) - P_{\beta,source}}{\delta_\beta} \\ \eta_{\beta,max} &= 1 - \frac{P_{\beta,source} - \alpha_{max} * \left(P_{\beta,Det} - P_{\beta,source}\right) - P_{\beta,source}}{\delta_\beta} \end{aligned} \tag{19}$$

The set of all parametric values for each ray-plane intersection is defined by merging the sets of parametric values for each dimension which are in ascending order:

$$\{\alpha\} = \left\{merge[\alpha_\beta(\eta_{min})], merge[\alpha_\beta(\eta)], merge[\alpha_\beta(\eta_{max})]\right\} \tag{20}$$

where η_{max} across all β dimensions is given by:

$$\eta_{max} = \left[\sum_{\beta=1}^{3}(\eta_{\beta,max} - \eta_{\beta,min} + 1)\right] + 1 \quad \textbf{(21)}$$

Sequential terms in the set $\{\alpha\}$ represent the intersection of the ray with consecutive voxels along its path and the distance travelled by the ray across said voxel is given by:

$$d_{ray}(m) = \|P_{Det} - P_{source}\| * [\alpha(m) - a(m-1)] \quad \textbf{(22)}$$

The total radiological path for a given ray line is then calculated with:

$$R = \sum_{m=2}^{N} \mu\big(\eta(m)\big) * d_{ray}(m) \quad \textbf{(23)}$$

Where N is the number of elements in the set $\{\alpha\}$, and $\eta(m)$ for a given dimension β is defined as:

$$\eta_{\beta}(m) = 1 + \frac{P_{\beta,source} + \left[\frac{\alpha(m) + \alpha(m-1)}{2}\right] * \left(P_{\beta,Det} - P_{\beta,source}\right) - P_{\beta,plane}(1)}{\delta_{\beta}} \quad \textbf{(24)}$$

An example of a DRR calculated with the process described above is depicted in Figure 13.

Figure 13: A digitally reconstructed radiograph produced using Siddon's method[222] from the computed tomography data set of the 3D printed skull used in Chapter 5.

2.4.2. Image Registration

Registration in the context of this work refers to the spatial alignment of anatomical features between image data from the same, or different imaging modality. To achieve a co-registration between to image sets (I_{moving}, I_{target}), there exists a transformation, $\mathcal{T}$, that maps I_{moving} to I_{target} via:

$$\boldsymbol{\mathcal{T}: \; I_{moving} \mapsto I_{target} \;\; \Leftrightarrow \;\; \mathcal{T}(I_{moving}) = I_{target}} \qquad \textbf{(25)}$$

This notation implies that $\mathcal{T}$ is a spatial transformation. For the explicit utilization of image registration in this work, $\mathcal{T}$ represents a rigid transformation which is composed of translational and/or rotational motions that map I_{moving} to I_{target}. Other transformations,

such as affine (which includes shearing/scaling), as well as deformable registration exist, but, do not serve much utility in this work as registration is confined to the alignment of a rigid body (the skull). The spatial mapping, $\mathcal{T}$ is determined by an iterative optimization process which explores the solution space (possible translations and/or rotations) of the registration problem. With each iteration, a similarity metric between the two imaging data sets would be quantified to inform and guide the optimization process. There are numerous similarity metrics that are available such as the sum of squared intensity differences,[223] the correlation coefficient,[224] or mutual information by the joint entropy between images (discussed later in Section 3.4).[225] An inherent limitation of registration in medical imaging (for the purposes of patient positioning) is that geometric distortions of the imaging data can be present which will impact the validity of derived transformations. These distortions are dependent on the underlying physics of specific the imaging modality.[226] For example, with CT acquisitions, scaling or skew distortions can arise from a tilt in the gantry during the procedure,[227] or pincushion distortions can arise from the curvature of the input phosphor of the imaging panel.[228]

2.5. RELEVANCE TO THESIS RESEARCH

The concepts addressed in this chapter were presented due to their relevance to the various measurements, calculations, and simulations performed in this thesis. Addressing radiation transport in matter is necessary as much of this work relies of the fundamental physics behind the interactions of radiation with matter. In Chapter 4 and Chapter 6, dose

calculations are performed with MC, MATLAB, and the Eclipse TPS (AAA and AXB). The MC method, and the AXB dose calculation engine explicitly model radiation interactions with various approximations, while the AAA algorithm, and the in-house MATLAB dose calculation algorithm employ model-based dose deposition behaviours in tissues to approximate the deposition of dose in a material from MC data. Understanding the underlying physics of radiation transport is helpful to contextualize how each dose calculation method diverges from explicit modelling of all radiation interactions in tissue. Addressing the probability of individual photon interactions, specifically the photoelectric effect and Compton scattering, as it pertains to imaging, is necessary to understand the utility of MV imaging conducted in Chapter 5.

In the final manuscript presented in this thesis, Chapter 6, dosimetry is quantified with two different dosimeters, namely, an ion chamber and GafChromic ™ film for the purposes of dose-verification. The fundamentals of ion chamber dosimetry, and the nuances of how to conduct dosimetry in the presence of a small field were addressed to properly quantify treatment dose linac. GafChromic™ film dosimetry was addressed for the determination of an experimental dose distribution with planar SRS dose measurements. Comparing experimental planar dose-distributions to calculated 3D dose distributions was addressed with the theoretical background of the gamma analysis.

CHAPTER 3. RESEARCH METHODS

3.1. MEDICAL LINEAR ACCELERATOR OPERATION

3.1.1. Developer Mode

Various sections in this thesis utilize Varian Developer Mode on a TrueBeam™ STx platform. In this mode, motion along any axis (couch, gantry, collimator) is permittable during irradiation, as well as any form of clinically available imaging. To communicate with the linac in Developer Mode, an Extensible Markup Language (XML) dialect was created by engineers at Varian referred to as SetBeam XML. Treatments designed in the XML schema serve as instructions for the linac during delivery. The information in a SetBeam XML script is discretized into control point-specific instructions where all axes-of-motion (including collimation by Jaws and MLC), as well as MUs per control point is specified. For imaging control points, the type of imaging, position of the imager, and the amount of MUs per image is specified. Between adjacent control points, with dynamic motion, MU delivery is linearly interpolated. The speed at which linac motion (and MU delivery) proceeds between controls points is dictated by the slowest moving axis such that the endpoints of all motion (and MU delivery) are completed in synchrony. The maximum speed of each movable axis is shown in Table 1.

Table 1: Velocity limits for XML delivery in the Varian Developer Mode.[229]

Axis	Maximum Velocity
MLC Leaf	2.5 cm/s
Gantry Rotation	6.0 Degrees/s
Couch Rotation	3.0 Degrees/s
Couch Vertical	2.0 cm/s
Couch Lateral	4.0 cm/s
Couch Longitudinal	8.0 cm/s
Jaws	2.4 cm/s
Dose Rate	1400 MU/min

To generate the XML files used for imaging and delivery in this work, a plan was initially made in Eclipse (Varian Medical Systems, Inc., Palo Alto, USA) and all information contained within the Digital Imaging and Communications in Medicine (DICOM) data set was exported. The RT Plan DICOM was imported in MATLAB (The MathWorks, Inc., Natick, Massachusetts, U.S.A.) and all plan information was converted into control point-specific instructions in the XML schema with a custom in-house script. The coordinate system used in the Eclipse (and seen on the treatment console) utilizes the Varian International Electrotechnical Commission (IEC) scale, which differs from the DICOM (IEC 61217) and the Developer Mode coordinate system. Therefore, for each unique couch-gantry angle combination, the geometry of each movable axis (couch rotation, translation, and gantry rotation) was transformed using the relationships depicted in Figure 14.

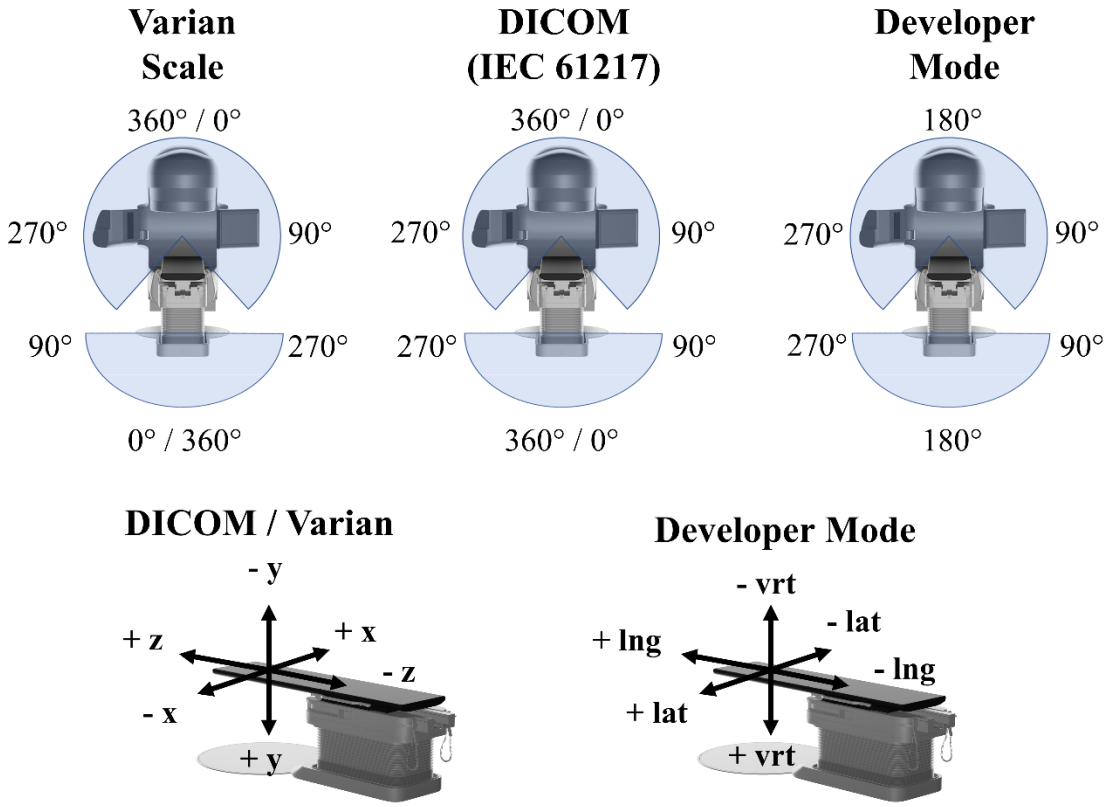

XML couch translations (vrt, lat, lng) for a given isocenter position (x, y, z)

$$-y \leftrightarrow +vrt \qquad -x \leftrightarrow -lat \qquad -z \leftrightarrow -lng$$

$$+y \leftrightarrow -vrt \qquad +x \leftrightarrow +lat \qquad +z \leftrightarrow +lng$$

Figure 14: Coordinate transforms between Eclipse (Varian IEC) coordinates, DICOM (IEC 61217) coordinates, and Developer Mode coordinates. Isocentre position in the Eclipse treatment planning system was used as a surrogate for defining couch translations. The accompanying transformations between isocentre coordinates and Developer Mode couch positions are shown.

3.1.2. Virtual Isocentre Trajectories

A virtual isocentre is defined as a point within the anatomy that lies on the central beam axis for every control point, though not necessarily at the same distance from the linac target. In this work, the couch top is moved with linear translations to shorten the treatment distance during treatment delivery, as shown in Figure 15. To implement couch trajectories at a variable SAD in this work for dose calculation in the Eclipse TPS, translations to isocentre are calculated in the DICOM coordinate frame. The calculation first converts the couch and gantry angle from DICOM coordinates into Developer Mode coordinates. The required shift to translate isocentre to a virtual position, $Shift_{iso}$, for gantry angle, θ, and couch angle, **φ** is calculated with:

$$Shift_{iso}(\theta, \phi) = vSAD * \begin{bmatrix} -\sin(\theta)\cos(\phi) \\ -\sin(\phi)\sin(\theta) \\ -\cos(\theta) \end{bmatrix} \quad \textbf{(26)}$$

Where $vSAD$ is a virtual SAD. The new virtual isocentre, V_{iso}, would then be calculated with the original isocentre position, O_{iso}, defined in the RT plan DICOM using:

$$V_{iso} = O_{iso} - Shift_{iso} \quad \textbf{(27)}$$

To implement couch trajectories on the linac with a virtual isocentre, the isocentre shift calculated in equation (26) is applied to initial couch positions using the coordinate transforms depicted in Figure 14.

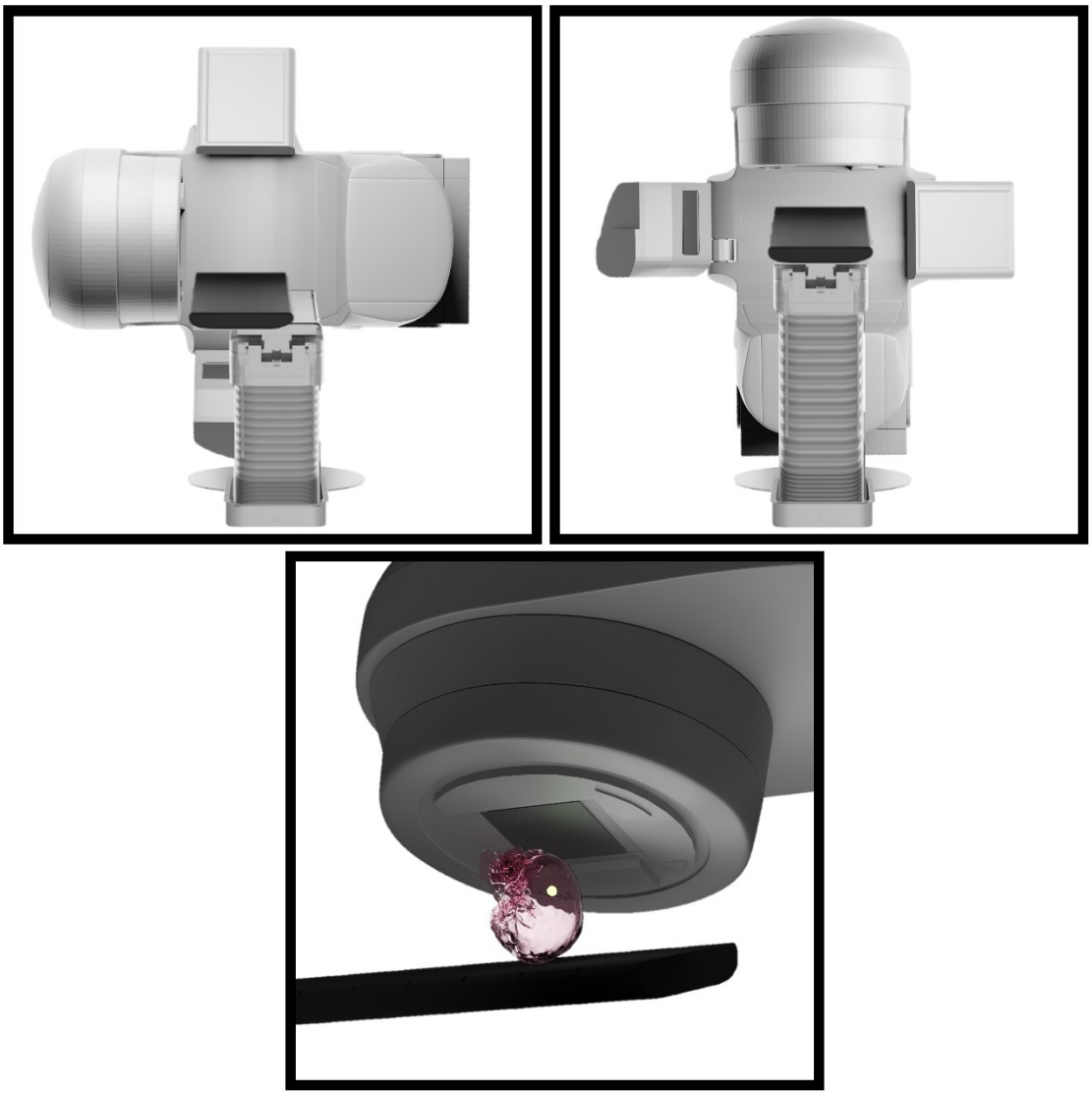

Figure 15: Virtual isocenter trajectories with a shortened treatment distance involve moving the couch top closer to the gantry head during radiation delivery. A virtual isocentre is a point within the anatomy (depicted by the green target in the bottom subplot) that is intersected by the radiation beamline.

3.2. DOSE CALCULATION

3.2.1. Monte Carlo

In this work, dose calculations were completed in the EGSnrc system with the use of the BEAMnrc[230] and DOSXYZnrc[231] user codes and their specific uses are described in Sections 4.4.1 and 5.4.5. To conduct a simulation, phase space files from gold-beam data were used that had been scored directly above the jaws.[232] A phase space file contains information of all particles crossing a plane. For a given particle this information includes: particle type, particle weight, direction cosines, position, and energy. The phase space files used in this work were generated by VirtuaLinac (Varian Medical Systems, Inc., Palo Alto, CA), and includes all particles that have been transported through the components upstream of the jaws. Varian does not release proprietary information about these components within the Truebeam, thus this was the only option for simulations. A model of the Varian TrueBeam™ STx system was designed in the BEAMnrc system with the XY Jaws and the HD120MLC. A custom in-house script was used to convert RT plan DICOM files into '.egsinp' and '.sequence' files which describe the linac model geometry, beam data, collimation geometries, gantry and couch angles via transformations described by Zhan *et al.*[233] To calculate dose in medium for a continuous delivery (emulating a RapidArc™ delivery) SOURCE-21 was used in DOSXYZnrc and is described by Lobo *et al*.[234] SOURCE-21 makes use of the '.sequence' files which describe the positioning of the jaws and MLC leaves on a control point-specific basis. In addition to a description of the geometry, the '.sequence' file also contains beam-weighting for each control point, where

the weighting is analogous to the 'CumulativeMetersetWeight' parameter within the RT plan DICOM structure; albeit, the sum of all weightings in the '.sequence' must add to unity across all arcs.

3.2.2. MATLAB

In Chapter 4 dose calculations of simulated treatment deliveries are achieved by superposing a MC-derived dose kernel in MATLAB. A dose kernel, D_{κ}, was created in MC by delivering a MLC-shaped beamlet to a water sphere with a beam-angle orientation of $[0°, 0°, 0°]$ for the gantry, collimator, and couch angle respectively in Eclipse coordinates. In MATLAB rotational operators were used to rotate the beam along a given axis:

$$R_x(\theta) = \begin{bmatrix} 1 & 0 & 0 \\ \cos(\theta) & -\sin(\theta) & 0 \\ \sin(\theta) & \cos(\theta) & 0 \end{bmatrix}$$
$$R_y(\theta) = \begin{bmatrix} \cos(\theta) & 0 & \sin(\theta) \\ 0 & 1 & 0 \\ -\sin(\theta) & 0 & \cos(\theta) \end{bmatrix} \quad \textbf{(28)}$$
$$R_z(\theta) = \begin{bmatrix} \cos(\theta) & -\sin(\theta) & 0 \\ \sin(\theta) & \cos(\theta) & 0 \\ 0 & 0 & 1 \end{bmatrix}$$

where θ is an arbitrary angle of rotation. To replicate simultaneous rotations of the couch, gantry, and collimator, these rotational operators were applied sequentially using the imwarp function in the order given:

$$D_{\kappa,MATLAB}\,\widehat{\Omega}(\theta_G,\theta_{Col},\theta_{Cu}) = R_y(\theta_{Cu})R_y(\theta_G)R_z(\theta_{Col}) * D_{\kappa,MC} \quad \textbf{(29)}$$

Where $\widehat{\Omega}(\theta_G,\theta_{Col},\theta_{Cu})$ is the orientation of delivery for gantry angle θ_G, collimator angle θ_{Col}, and couch angle, θ_{Cu}. The imwarp function utilizes 3D cubic-splines to interpolate the input 3D matrix after rotation.[235] For a given arc-arrangement, the total dose is then calculated by summing the dose-kernel from all beam-angle orientations.

3.3. DOSE MEASUREMENTS

3.3.1. Ion Chamber

For measurements conducted in Chapter 6, a PTW Semiflex Ionization Chamber 31010 (PTW, Freidburg, Germany) was utilized due to clinical availability, and correction factors derived from Table 26 in TRS-483[208] were applied to all raw measurements (a description of how correction factors were derived can be found in Section 6.4.6.1). To convert measurements with the PTW 31010 into a dose, an output factor (OF) calibration curve was cross-calibrated at a field size of 5 x 5 cm^2 with an OF calibration curve (up to reference field size conditions with a 10 x 10 cm^2 field size) for an Exradin A12 ion chamber (Standard Imaging, Middleton, WI, USA) with a process known as "daisy-chaining". Where the OF for a given field size of interest, FS_i, is defined by:

$$OF(FS_i) = \frac{M_{FS_i}}{M_{ref}} \quad \textbf{(30)}$$

Each measurement was corrected with the factors introduced above. An OF is quantity that is determined by the scattering conditions in which the measurement is acquired and is defined by:

$$OF(FS) = S_c(FS)S_p(FS) \tag{31}$$

where S_c is the collimator scatter factor owed to photon scatter within components inside the head of the linac. The phantom scatter factor S_p is the ratio of dose rate for a given field size, FS, at reference depth conditions to the dose rate at the same depth with reference field size conditions. Thus, the dose to an ion chamber for an arbitrary field, FS_i, size at reference depth is calculated with:

$$D_w(FS_i) = OF(FS_i) * P_{ion}P_{TP}P_{pol}M_{raw}(FS_i) \tag{32}$$

Measurements during treatment delivery were acquired with the PTW 31010 inserted into the MAX-HD SRS anthropomorphic phantom (Integrated Medical Technologies, Troy, NY, USA) as shown in Figure 16 and were converted into a dose using equation **(32)** where P_{ion} and P_{pol} had field-size and dose-rate dependent correction described in 6.4.6.1.

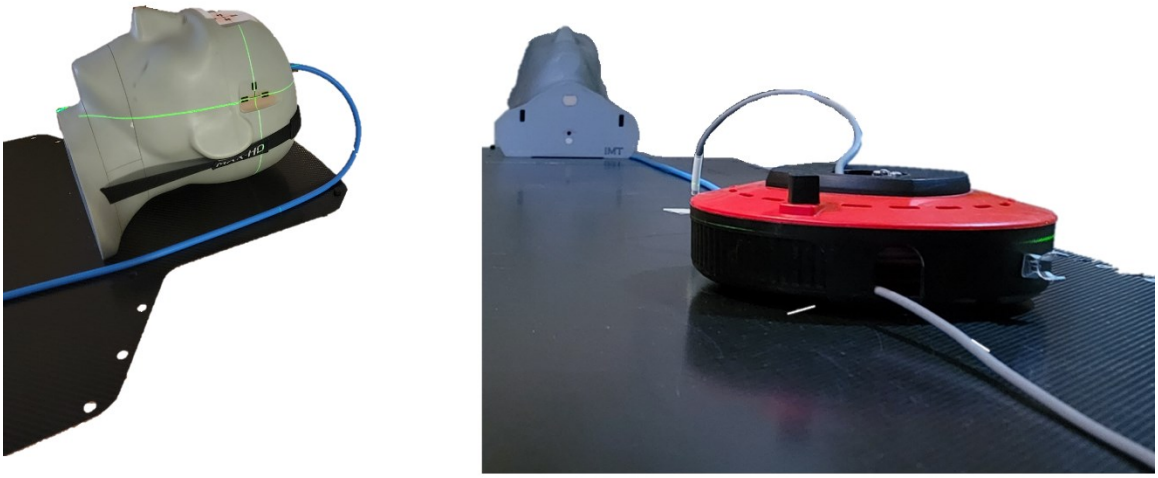

Figure 16: Irradiation set up for ion chamber measurements with the MAX-HD anthropomorphic phantom (Standard Imaging, Middleton, WI, USA) used in Chapter 6. The electrometer is out of frame in the treatment console area.

3.3.2. GafChromic™ Film

When utilizing film for absorbed dosed dose measurements in Chapter 6, a consistent irradiation and read-out process was implemented when measuring dose and calibrating the films. Prior to irradiation, all films were cut with straight edge and marked for orientation (up-down, and rotational orientation). Films were kept in a darkened envelope in transport to the linac for dose delivery. The dose-response of the box of film was initially calibrated by delivering incrementally higher doses from 0 to 2000 cGy to a 2 x 2 cm^2 film in reference conditions. The films were stored in a dark envelope, in a sealed box for 12 hours to cure prior to scanning. For scanning, an EPSON EXPRESSION 10,000 XL scanner (Epson, Suwa, Japan) was used with a 48-bit colour depth and resolution of 72

dpi. The scanner bulb was warmed up by implementing five total-bed pre-scans prior to scanning the film. A template guide was used to align the film in the center of the scanner bed and the films were scanned along the same orientation of the beamline axis of delivery.

Images of the calibration films were brought into MATLAB and decomposed into the red, green, and blue channels for films with increased absorbed dose; the mean pixel value in a 1 x 1 cm^2 area was extracted for each colour channel and was fit with the function:

$$Pixel\ Value = \frac{a + Db}{c + D} \tag{33}$$

Where D is the dose delivered to the respective film and a, b and c were parameters determined with nonlinear least squares fitting. For each new sheet of film used (within the same box) two 2 x 2 cm^2 films were cut and one was irradiated with 200 cGy; these films were used to scale the calibration curve derived in (33). To scale the calibration curve, a new fit was recalculated by: 1) forcing the zero-dose calibration film to match the film-sheet-specific zero dose calibration film, 2) scaling the non-zero dose pixel values of each colour channel based upon the percent difference between the original raw measurement and the film-sheet-specific 200 cGy calibration film. A visual representation of this procedure is shown in Figure 17.

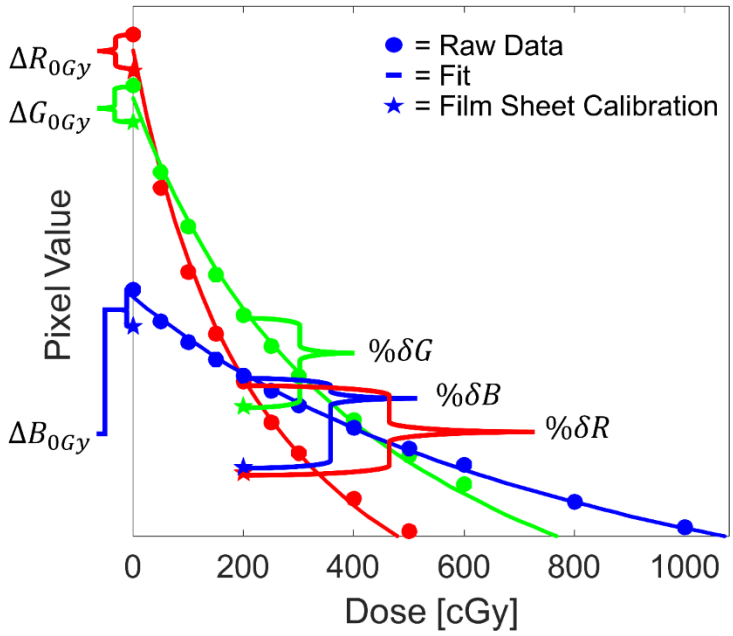

Figure 17: Film calibration procedure, where the individual red (R), green (G), and blue (B) colour channels have been fit independently. To scale the fit of the original raw calibration data, the zero-dose calibration film of the raw data was forced to match the film-sheet-specific zero dose calibration film via ΔX_{0Gy}, where X is the (R, G, or B channel). For all non-zero doses, the values were scaled by the percent difference between the original raw measurement, and the film-sheet-specific 200 cGy calibration film with, $\%\delta X$. All film sheet calibration doses (indicated by stars) were exaggerated for illustrative purposes.

To convert films scans into doses in this work, the triple-channel film dosimetry algorithm by Mayer *et al.*[236] was used as it has been shown to have improved gamma pass-rates over single-channel film dosimetry and to reduce the lateral scanner artifact.[237] The triple-channel algorithm by Mayer *et al.*[236] calculates a dose, D, for the pixel of the scanned film with indices i and j by:

$$D(i,j) = \frac{D_{avg}(i,j) - RS(i,j)\dfrac{\sum_{k=1}^{3} D_k(i,j)\dfrac{\partial D_k}{\partial PV}_k(i,j)}{\sum_{k=1}^{3}\dfrac{\partial D_k}{\partial PV}_k(i,j)}}{1 - RS(i,j)} \quad \textbf{(34)}$$

where $D_{avg}(i,j)$ the average dose across all colour channels given by:

$$D_{avg}(i,j) = \frac{1}{3}\big(D_R(i,j) + D_G(i,j) + D_B(i,j)\big) \quad \textbf{(35)}$$

where R, G, and B are the red, green, and blue colour channels respectively. The relative slope of the colour calibration curve (described later in Section 3.3.2) is given by:

$$RS(i,j) = \frac{1}{3}\frac{\left(\sum_{k=1}^{3}\dfrac{\partial D_k}{\partial PV}_k(i,j)\right)^2}{\sum_{k=1}^{3}\dfrac{\partial D_k}{\partial PV}_k(i,j)} \quad \textbf{(36)}$$

where $\frac{\partial D_k}{\partial PV_k}$ is the derivative of the dose-calibration curve for the kth colour channel with respect to the pixel value (PV) of the kth colour channel.

For absorbed dose measurements with film in Chapter 6, films were cut and prepared with an in-house film punch for insertion in the MAX-HD phantom in the coronal plane with the included film holder as shown Figure 18.

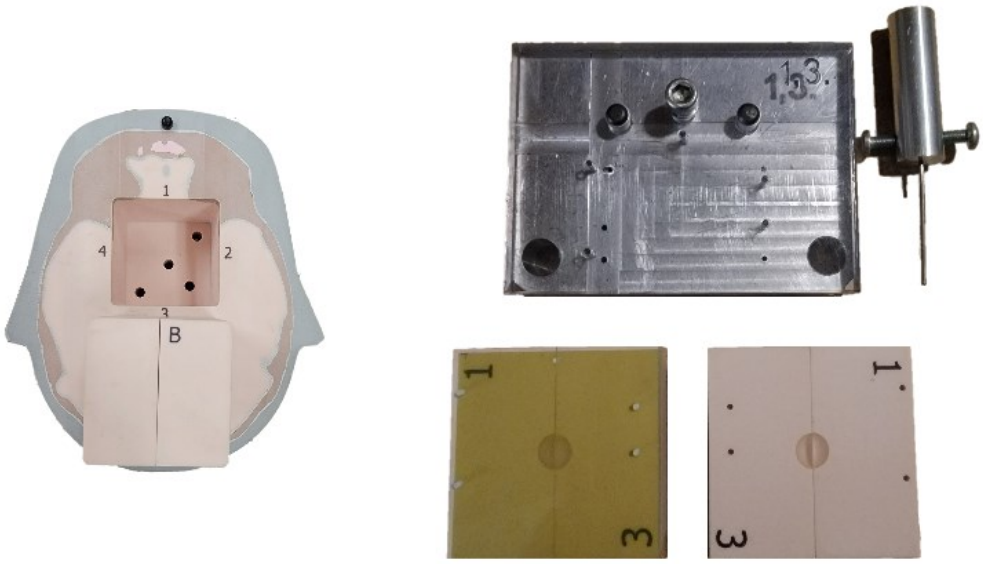

Figure 18: Film punch and film-holder for use with the MAX-HD anthropomorphic phantom (Standard Imaging, Middleton, WI, USA) used in Chapter 6.

Post irradiation, films were scanned using the procedure described above. Scanned film images were then imported into MATLAB and converted into a dose using triple-channel film dosimetry using the algorithm[236] described above in Section 2.3.2.

To compare measured film doses to calculated doses in Eclipse, a 2D-3D gamma analysis was performed using the methodology described by Low *et al*.[238] First, a median filter in 5 x 5 pixel neighbourhood was applied to the film dose. Then, the Eclipse dose distribution was interpolated to the same resolution as the film dose using tricubic interpolation. The film dose was rigidly registered (translations and rotations) to the Eclipse dose (at the film plane) using mutual information (MI) described later in Section 3.4. Using

a distance threshold (δr) of 1.0 mm, and a dose threshold (δD) of 5.0%, for each measured dose pixel at location (i_m, j_m) in the film-plane, the gamma value (γ) was calculated in a 5.0 x 5.0 x 5.0 mm^3 search region ($\mathbb{R}$) using:

$$\gamma_{\mathbb{R}}(i_c, j_c, k_c) = \sqrt{\left(\frac{D_{Eclipse}(i_c, j_c, k_c) - D_{film}(i_m, j_m)}{\delta D}\right)^2 + \left(\frac{\vec{r}_{calc}(i_c, j_c, k_c) - \vec{r}_{film}(i_m, j_m, 0)}{\delta r}\right)^2} \quad \textbf{(37)}$$

where (i_c, j_c, k_c) are the pixels being tested in the Eclipse dose matrix, with the k^{th} dimension being normal to the film-plane. The Eclipse dose is $D_{Eclipse}(i_c, j_c, k_c)$, and the position of the calculated dose is $\vec{\boldsymbol{r}}_{\boldsymbol{calc}}(i_c, j_c, k_c)$. The final gamma value Γ from the search region $\mathbb{R}$ was determined with:

$$\Gamma(i_m, j_m) = min\{\gamma_{\mathbb{R}}\} \forall \{\vec{r}_{calc}\} \quad \textbf{(38)}$$

where $\forall$ represents all test points in the Eclipse dose distribution. A $\Gamma \leq 1$ indicates a passing value while $\Gamma > 1$ indicates a failing value. A pictorial demonstration of the calculation process is shown in Figure 19.

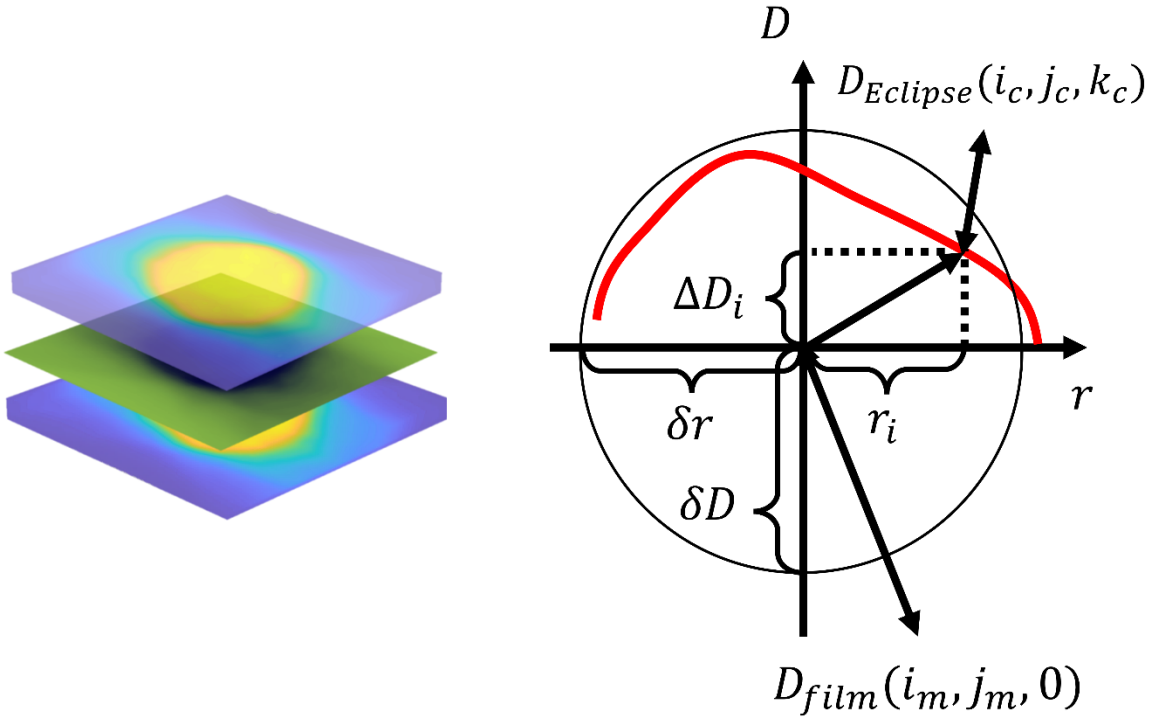

Figure 19: (Left) A pictorial representation of the setup for a 2D-3D gamma analysis between a measured dose with EBT3 GafChromic™ film and a calculated dose with the Eclipse treatment planning system (Varian Medical Systems Inc., Palo Alto, CA). (Right) A geometrically collapsed representation of the parameters used for the gamma evaluation criteria in equation (37). The red line represents the collapsed dose distribution from the Eclipse dose matrix, $D_{Eclipse}$. The dose difference between the film, D_{film} and $D_{Eclipse}$ is given by ΔD_i. The vector distance from the measured D_{film} and the calculated $D_{Eclipse}$ is given by r_i

3.4. IMAGE PROCESSING AND REGISTRATION

Using the formalism described above in section 2.4.1, DRRs were calculated in MATLAB and compared with images acquired with the 2.5 MV beam. Direct comparison between DRRs and images with the EPID are inherently difficult due a few factors: 1)

DRRs are generated with a calculation of the radiological path through the imaging volume; equation (23) utilizes the linear attenuation coefficients within the volume which have been interpolated from a Hounsfield unit (units of the CT imaging data set) calibration curve for 60 keV monoenergetic photons. 2) Siddon's method[222] does not model photon interactions within the imaging volume, thus ignoring the impact of patient scatter on the DRR appearance. The choice of 60 keV for DRR generation was intended to be representative of a typical photon energy from the scan used to generate the CT images. To minimize the impacts difference in image content between measured EPID images and calculated DRRs, image pre-processing was conducted in two steps using the methodology outlined in Jans *et al*.[133]:

1) Unsharp masking of the image to filter low frequency noise out of the image. This was achieved by subtracting a blurred version of the image and then adding the mean value of the original image to all pixels. The blurred image was created by applying a gaussian filter with a kernel width that was half of the size of the image width and a Gaussian width of one-sixteenth of the image width.
2) Histogram equalization between the EPID image and the DRR was achieved by first converting the histogram content of each image into a cumulative distribution function (CDF). Subsequently, a CDF for a gaussian distribution with a width of $\sigma = 0.2 * Dynamic\ Range$ was created. The pixel information in each image was mapped to the gaussian distribution using the procedure

depicted in Figure 20. This process results in each image having pixels values in the same range of 0 to N.

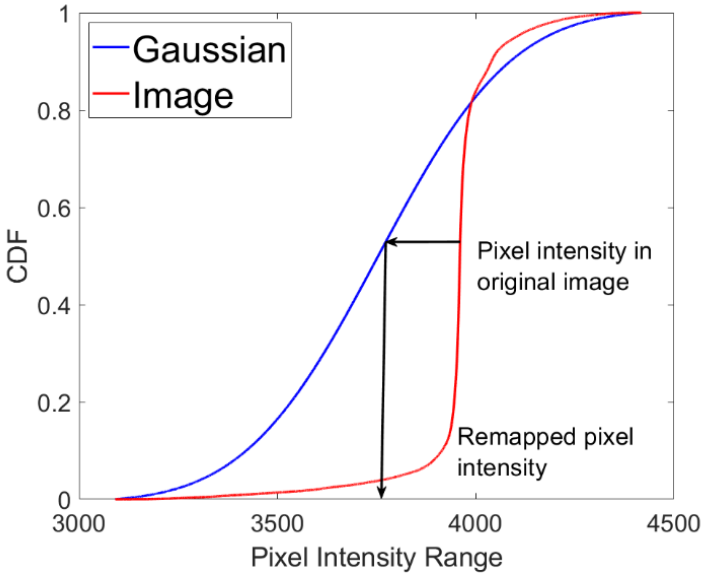

Figure 20: Histogram equalization procedure by mapping pixel values from the cumulative distribution function of an image to a pre-set gaussian distribution.

To derive the translational corrections to align the two images, MATLABs built-in imregtform function was used. The configuration of the registration algorithm (where all pixels are used in the calculated) reduces the similarity metric for image comparison to MI as introduced formalism introduced by Shannon.[225] To determine the MI between two images, $MI(EPID, DRR)$, a probability distribution function is constructed from the histogram of each image (p_{EPID} and p_{DRR}), as well as a joint probability distribution function between the two images ($p_{EPID,DRR}$); the MI is then calculated with:

$$MI(EPID, DRR) = -\sum_{i=1}^{N} p_{EPID}(i)\log\left(p_{EPID}(i)\right) + \sum_{j=1}^{N} p_{DRR}\,(j) log\left(p_{DRR}(j)\right) + \sum_{i=1}^{N}\sum_{j=1}^{N} p_{EPID,DRR}(i,j)\log\left(p_{EPID,DRR}(i,j)\right) \quad \textbf{(39)}$$

where N is the number of possible pixel values in each image. To guide the registration process, the one plus one evolutionary optimizer was used.[239] Briefly, the algorithm perturbs the MI calculated in equation (39) by translating the EPID image; through each iteration, the perturbation space is adapted by updating a gaussian probability distribution function describing the solution space in the local search region.

3.5. RELEVANCE TO THESIS RESEARCH

The purpose of the sections presented in this chapter was to elaborate on the methodologies that were not included in the manuscripts presented in chapters 4-6; as submission of these manuscripts for publication require that they contain less detail due to length constraints. While the experimental and algorithmic considerations were addressed in the preceding chapters, a large proportion this thesis utilized a programmatic implementation of the theories and equations which has not been addressed. The explicit computational formalism and syntax required to deploy these topics would be dependent upon the data structures, and programming language used, and thus was outlined in this document.

CHAPTER 4.MANUSCRIPT 1: INVESTIGATING THE IMPACTS OF INTRAFRACTION MOTION ON DOSIMETRIC OUTCOMES WHEN TREATING SMALL TARGETS WITH VIRTUAL CONES

4.1 PROLOGUE

This manuscript explores the dosimetric impact of treating small lesions intended for radiosurgery with small treatment apertures during simulated intrafractional motion. It is an application of the methodologies presented in Sections 3.1.2 and 3.2.2 where simulated motion traces are an embodiment of a virtual isocentre trajectory during treatment delivery. This section serves as an explorative investigation to assess if SRS magnitude motions have clinically significant dosimetric impacts; thus, motivating the investigations in Chapter 5 and Chapter 6. The aim of this work is to provide clinicians with an understanding of how treatment outcomes are impacted in the multivariate problem (aperture selection, target size, magnitude of motion).

This manuscript was published in the Journal of Applied Clinical Medical Physics:

"Church C, Parsons D, Syme A. Investigating the impacts of intrafraction motion on dosimetric outcomes when treating small targets with virtual cones. *J Appl Clin Med Phys*. 2021; 22(8): 60 – 71."[240]

4.2 ABSTRACT

Purpose: Intrafraction patient motion is a well-documented phenomenon in radiation therapy. In stereotactic radiosurgery applications in which target sizes can be very small and dose gradients very steep, patient motion can significantly impact the magnitude and positional accuracy of the delivered dose. This work investigates the impact of intrafraction motion on dose metrics for small targets when treated with a virtual cone.

Materials and Methods: Monte Carlo simulations were performed to calculate dose kernels for treatment apertures ranging from 1 x 2.5 mm^2 to 10 x 10 mm^2. The phantom was an 8.2 cm diameter sphere and isotropic voxels had lengths of 0.25 mm. Simulated treatments consisted of 3 arcs: 1 axial arc (360° gantry rotation, couch angle 0°) and 2 oblique arcs (180° gantry rotation, couch angle $\pm$ 45°). Dose distributions were calculated via superposition of the rotated kernels. Two different collimator orientations were considered to create a virtual cone: i) each treatment arc was delivered twice, once each with a static collimator angle of ± 45°, and ii) each treatment arc was delivered once, with dynamic collimator rotation throughout the arc. Two different intrafraction motion patterns were considered: i) constant linear motion and ii) sudden, persistent motion. The impact of motion on dose distributions for target sizes ranging from 1 to 10 mm diameter spheres was quantified as a function of the aperture size used to treat the lesions.

Results: The impact of motion on both the target and the surrounding tissue was a function of both aperture shape and target size. When a 0.5 mm linear drift along each dimension occurred during treatment, targets ≥ 5 mm saw less than a 10 % decrease in coverage by the prescription dose. Smaller apertures accrued larger penalties with respect to dosimetric

hotspots seen in the tissues surrounding the target volume during intrafraction motion. For example, treating a 4 mm sized target that undergoes 2.60 mm (3D vector) of continuous linear motion, the D_5 in the concentric shells that extend 1, 2, and 3 mm from the surface of the target was 39%, 24%, and 14% smaller respectively when comparing the delivery of a larger aperture (6 x 10 mm^2) to a smaller aperture (2 x 5 mm^2). Using a static collimator for shaping a virtual cone during treatment minimized the dosimetric impact of motion in the majority of cases. For example, the volume that is covered by 70% or more of the prescription dose is smaller in 60.4% of cases when using the static collimator. However, the volume covered by 50, and 30% or more of the prescription dose is larger when treating with a rotating collimator, but the clinical significance of this finding is unknown.

Conclusions: In this work, the dosimetric trade-offs between aperture size and target size when irradiating with virtual cones has been demonstrated. These findings provide information about the tradeoffs between target coverage and normal tissue sparing that may help inform clinical decision making when treating smaller targets with virtual cones.

4.3 INTRODUCTION

Highly conformal treatments of small cranial lesions utilize a technique known as SRS which aims to achieve sub-mm target localization in all three spatial dimensions.[9] Compared with conventionally-fractionated treatments, single-fraction SRS and few-fraction SRT are characterized by large doses per fraction, high dose conformity, and strict patient positioning tolerances.[241] Several approaches have been developed to deliver these treatments, including VMAT and stereotactic cones. In comparison to VMAT, cones have

demonstrated better conformity for smaller TVs (4 mm in diameter) when treating spherical lesions.[242,243] For certain indications such as TN where targets sizes become sufficiently small and dose limitations on surrounding tissues are stringent,[244] circular stereotactic cones are most commonly used for treatment delivery.[245]

Recent literature has demonstrated that a combination of collimator rotations and apertures shaped by the MLC, referred to as a virtual cone, are capable of shaping dose distributions comparable to stereotactic cones for small targets. Popple *et al.* aimed to create spherical dose distributions for the purpose of treating a small target like the trigeminal nerve with a virtual cone and found that performing an arc-based delivery with a 2.1 x 5 mm^2 aperture using two arcs with orthogonal collimator angles, produced a dose distribution comparable to a 4 mm stereotactic cone defined at the 50% isodose line.[118] Additional preliminary work with virtual cones investigated the treatment of functional disorders (e.g. thalamotomy of the VIM), which coupled high-resolution fMRI and SRS to delineate and ablate the VIM.[119] They found that a delivery with a fixed-MLC position and series of non-coplanar arcs can deliver a spherical dose distribution comparable to a 4 mm SRS shot with a cone. Another study using virtual cones for dorsal nerve root gangle ablation therapy alluded to the potential of reducing treatment times (and therefore intrafraction motion) when using virtual cones, but did not quantify the dosimetric impact of intrafraction motion with virtual cones.[120] They found that the shape of the 60 Gy isodose surface was appropriate for the ablative doses used in therapy, and that the dose limits on surrounding organs at risk were satisfied. Furthermore, the conformity of the spherical dose

profile shaped by virtual cones and arc arrangement eliminated the need for inverse planning and could be used as a standard template for most patients.

Historically, framed-based systems were used for immobilization during SRS treatments, but many centers have moved away from invasive immobilization techniques in favor of non-invasive, thermoplastic mask-based methods.[140,141,167,246] However, mask-based systems have been shown to allow larger intrafractional positioning errors that increase in magnitude with increasing treatment time.[163,165,247] There have been several studies that have investigated the magnitude of detected motion within different thermoplastic mask systems and imaging modalities. Using Brainlab frameless masks and imaging with the Brainlab ExacTrac stereoscopic X-ray system, Gevaert *et al.* reported the 3D displacement from intrafraction motion to be 0.66 to 3.16 mm.[162] Similarly, Bichay *et al.* found 3D displacements of 0.4 to 3.23 mm using a Civco mask, and aligning orthogonal images to DRRs.[166] Tryggestad *et al*. showed that set-up errors could range from 2.1 – 2.7 mm with four different thermoplastic masks.[29] Using GK-specific thermoplastic masks, and imaging an IR motion marker on the nose, MacDonald *et al*. found 3D-errors owed to intrafraction motion up to 2.5 mm.[137] While the literature reports that the majority of patients experience sub-mm motions, it is important to remember that pre-treatment imaging modalities for SRS typically have 1 mm tolerances; which, in conjunction with patient motion, could lead to larger errors (> 1 mm).

The dosimetric impact of motion is highly dependent upon the type of motion experienced during treatment, the magnitude of motion, and the treatment site. Previous literature has assessed the dosimetric impact of intrafraction motion on TV coverage when

treating vertebral columns with SBRT. When treating with IMRT, Kim *et al*. found that there was a ± 1% median change in dose received to 95% (D_{95}) and 90% (D_{90}) of the TV, the D_{max}, and mean dose (D_{mean}) for 8/9 subjects; whereas the dose received to 0.1% ($D_{0.1}$), 0.5%($D_{0.5}$), 1%($D_{1.0}$), and D_{max} for the surrounding organs at risk (OAR) differed by -14% to 38%.[248] Similar impacts of motion (simulated by shifts in one dimension at a time) were shown by Wang *et al*. with IMRT where a ± 2 mm shift in a given dimension resulted in a reduction of up to 17.9 % to the volume receiving 95% of the prescription dose (V_{95}), though the majority of cases had changes of ≤ 5%; D_{max} to surrounding OAR differed by approximately (-15) – (+50)%.[170] Using VMAT Ong *et al*. found that a 2 mm shift for 30s during therapy could result in a 13% increase of the maximum dose (D_{max}) to the spinal cord.[249] For cranial indications, and for TN in particular, the planning target volume (PTV) volumes can be an order of magnitude smaller with much more stringent tolerances on positioning due to the TV abutting sensitive structures. For example, the prescription volume for TN can range 0.001 – 0.05 cc. (effective spherical radius: 0.6 – 2.3 mm), and can reside an average of 2 mm away from the pons which is a radiologically sensitive structure.[250] Therapeutic situations such as these necessitate PTV margins to be as small as possible. However, Guckenberg showed that using a 0-mm PTV margin on cranial lesions could result in a 40% reduction in the conformity index when intrafraction motion occurs.[169]

There have been several bodies of work to investigate dosimetric impact of motion when treating larger targets (> 0.52 cc) with MLC-based VMAT,[170-172] but there remains a gap in the literature for investigating the dosimetric impact of treating with virtual cones.

This study aims to investigate the impact of intrafraction motion when treating small cranial targets with a virtual cone. Various motion traces were investigated for increasing degrees of linear drift, and sudden large motions. None of the previously published studies have investigated the dosimetric consequences of motion in a virtual cone-based treatment delivery and previous studies related to virtual cones have restricted their analysis to a limited number of treatment apertures. Results of this study provide insight into the robustness of both target dose metrics and surrounding tissue doses when the planning conditions (no motion) differ from the treatment delivery conditions (motion) as a function of target size and treatment aperture size. Such information will be of value to clinicians seeking to understand the risk-reward balance of highly conformal treatment apertures.

4.4 MATERIALS AND METHODS

4.4.1 Monte Carlo Simulation

Dose kernels were created with the EGSnrc MC system.[187] To simulate a dose kernel, a phase-space from the treatment head of the TrueBeam STx platform for a 6 MVFFF beam was provided by Varian Medical Systems through 54 phase space files (~69 Gb) that was validated down to a field size of 1x1 cm^2.[219] The phase space was scored above the jaws at 73.3 cm from isocentre, and was used an input for SOURCE-21 containing a linac model with the jaws, HDMLC, and Mylar exit window within BEAMnrc.[230] The MLC-defined aperture was incident on an 8.2 cm diameter water sphere phantom in DOSXYZnrc,[231] with material composition defined by ICRU 521 pegs4 data

file, with a 0.25 mm isotropic voxel size. To keep voxel dose uncertainty < 5% within the size aperture defined at the nominal isocentre (100 cm SAD), 10^8 histories were used. Prior to applying the simulated dose kernels to dose-delivery calculations, a Gaussian filter with a sigma of 1.2 was applied to smooth out the dose kernel. A total of 19 dose kernels were created from different apertures and are mentioned in Section 4.4.3, and Table 2.

MC simulations of a full treatment delivery with simulated intrafraction motion (Section 4.4.2 and 4.4.4) were conducted with two apertures sizes (2 x 5, and 4 x 10 mm^2) incident on an 8.2 cm water sphere with a 0.5 mm resolution. The simulations were conducted with a target residing in the center of the sphere, as well as targets residing 2, and 3 cm off-axis. These simulations were then compared with the superposition methodology described in Section 4.4.2 to quantify the impact of non-central target locations.

4.4.2 Simulating treatment delivery

Treatments modeled in this study consisted of a set of 3 arcs: a 360° axial arc (couch angle = 0°) and 2 partial arcs (180° rotations) with the couch at ± 45°. Dose distributions were calculated via superposition of the MC-derived dose kernels described previously. To simulate the delivery, each arc was modeled as a series of discrete control points with 10° of gantry rotation between each control point. The kernel was rotated to account for the motion of the gantry, couch, and collimator. Rotations and translations were implemented in MATLAB utilizing tricubic interpolation.

4.4.3 Aperture Size and Orientation

In total, 19 different apertures shaped by a model of the NDS120HD MLC (Varian Medical Systems Inc., Palo Alto, CA) were analyzed. Although stereotactic cones can reach diameters of several centimetres (e.g. BrainLAB offers stereotactic cones ranging from 4 – 30 mm),[251] this study focuses on creating dose distributions that would be comparable to plans created by stereotactic cones < 10 mm in diameter. The geometric properties of the apertures studied in this work are listed in Table 2. A virtual cone was created by implementing two different arc deliveries: 1) Static Collimator: For each arc geometry in the treatment listed in Section 4.4.2, the arc was delivered twice; once each with the collimator at ± 45°. 2) Dynamic Collimator: For each arc geometry, the arc was delivered once with the collimator rotating 180° throughout delivery. For the axial arc, the collimator was rotated 0 – 180° for half of the arc, and 180 – 0° for the rest of the arc.

Table 2: MLC-shaped treatment apertures.

# of MLC leaves used	Gap between leaves (mm)	Effective Area (cm^2)
1	1	0.025
	2	0.050
	3	0.075
2	1	0.050
	2	0.100
	3	0.150
	4	0.200
	5	0.250
3	2	0.150
	3	0.225
	4	0.300
	5	0.375
	6	0.450
	7	0.525
4	2	0.200
	4	0.400
	6	0.600
	8	0.800
	10	1.0000

4.4.4 Simulating Intrafraction Motion

To approximate positioning errors owed to intrafraction motion, six different motion traces were simulated as shown in Figure 21. Three of the traces mimicked a continuous linear drift until the phantom was offset by 0.5, 1.0, and 1.5 mm in all three dimensions which resulted in a 3D-offset of 0.87, 1.73, and 2.60 mm, respectively, (defined as $\boldsymbol{L}_{0.5\ mm}, \boldsymbol{L}_{1.0\ mm}, \boldsymbol{L}_{1.5\ mm}$, respectively). The other three traces emulated a sudden large shift of 2 mm along each dimension (3D-offset of 3.46 mm) at different time points during treatment, and persisted throughout treatment. These time points were chosen to occur at: ¼, ½, and ¾ of the way throughout treatment and were defined as $\boldsymbol{S}_{1/4}$. $\boldsymbol{S}_{1/2}$, and $\boldsymbol{S}_{3/4}$, respectively.

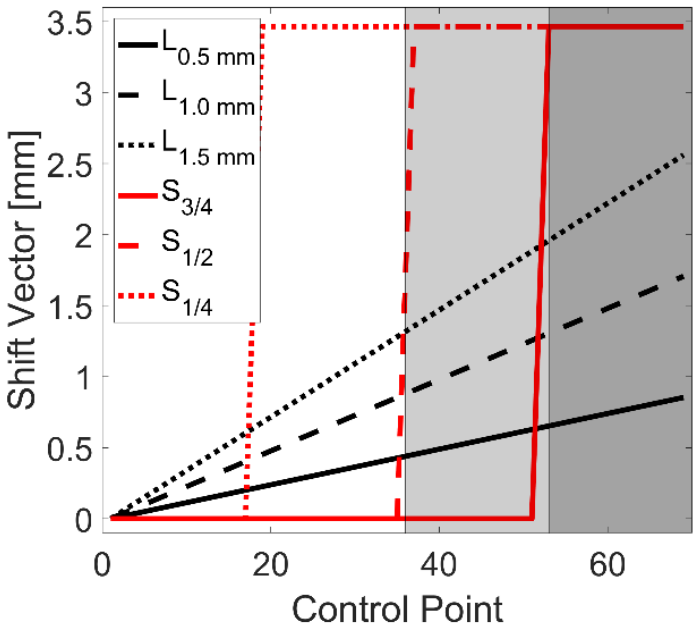

Figure 21: Movement traces for different intrafraction motion patterns. $L_{0.5\ mm}$, $L_{1.0\ mm}$, $L_{1.5\ mm}$, represent linear motion up to 0.5, 1.0, and 1.5 mm in each dimension respectively. $S_{1/4}$, $S_{1/2}$, $S_{3/4}$, represents a linear motion of 2 mm in each dimension at ¼, ½ and ¾ of the way through treatment respectively. The shaded regions represent the first co-planar arc and the two non-coplanar arcs in order from left to right.

The spherical nature of the simulated phantom and the central location of the target meant that the dose kernel was spatially invariant. When implementing shifts of the dose kernel (caused by simulated target motion), spatial invariance was lost. To account for this, an approximation was used by calculating the intersection of the central ray for a given beam with the water sphere and applying an inverse square weighting correction based upon the magnitude of the proximal or distal shift of the ray along the beamline (assuming the entire field receives a homogenous correction).

4.4.5 Dosimetric Analysis

For treatment simulations that did not involve motion, for each aperture size, a dose volume histogram (DVH) was calculated for target sizes ranging from 1 to 10 mm in diameter. For each TV, the dose matrix was normalized such that 99% of that TV was covered by the prescription dose (which will be defined as D_{99}). For simulations where motion was present, the distributions were not renormalized to achieve the same coverage. The effective output of the linac at each control point was preserved (i.e. the equivalent of delivering the same number of MU for both the no-motion and motion cases) to facilitate evaluation of the impact of motion on delivered dose. To evaluate the dose received by the volume abutting the target, three concentric spherical shells, each with a 1 mm thickness were created around the TV.

To evaluate the dosimetric impact of motion, the ratio of the Paddick conformity indices was calculated for the case of motion to the case without motion[252]:

$$R_C = \frac{\frac{TV_M^2}{PIV_M}}{\frac{TV_{NO}^2}{PIV_{NO}}} \quad \textbf{(40)}$$

Where TV_M refers to the volume within the target covered by the prescription dose for the case of motion, PIV_M is the prescription isodose volume for the case of motion; both of these parameters are determined using the prescription isodose in the case of no motion. TV_{NO} refers to the volume within the target covered by the prescription dose for the case of no motion, PIV_{NO} is the prescription isodose volume for the case of no motion. A value

of unity would indicate that the conformity index for the case of motion is equivalent to the case without motion.

To evaluate the steepness of the dose gradient for different plans, the GI was calculated by conventional means[252]:

$$GI = \frac{V_{50}}{V_{100}} \quad \textbf{(41)}$$

Where V_{50} is the volume receiving 50% of the prescription dose, and V_{100} is the volume receiving 100% of the prescription dose. For this analysis, the dose distributions were normalized such that the prescription dose was defined as 100%.

4.5 RESULTS

4.5.1 Effect of Aperture Size on Target Coverage

The impact of different sized apertures on target coverage is demonstrated by the black lines in Figure 22 for the static collimator case. In Figure 22.A, a single target size (5 mm) is considered while changing the size of the aperture. For all other target sizes not shown in Figure 22.A, the same trend of larger aperture sizes producing steeper dose volume histograms within the TV, as well as in the surrounding concentric shells is seen. Analogous data are shown in Figure 22.B, where a fixed field size of 6 x 10 mm^2 is used to treat various target sizes. For illustrative purposes, the doses received by the third concentric shell around the target have been included in the figures. The GI as a function

of target size and aperture size is shown in Figure 22.C. where all target size and aperture size pairings that result in a maximum dose (D_{max}) ≥ 200% have been blacked-out as they were considered unlikely choices for clinical application. For any given aperture size, delivering to a larger target size results in a reduction of the GI. In general, there is a trend of increasing GI as a function of effective aperture area. When implementing the dynamic collimator, the GI is up to 6.3% smaller when compared with the static collimator. However, only meaningful differences (≥ 2% smaller compared to static collimator) are seen in 26.5% of target size and aperture combinations when implementing the dynamic collimator.

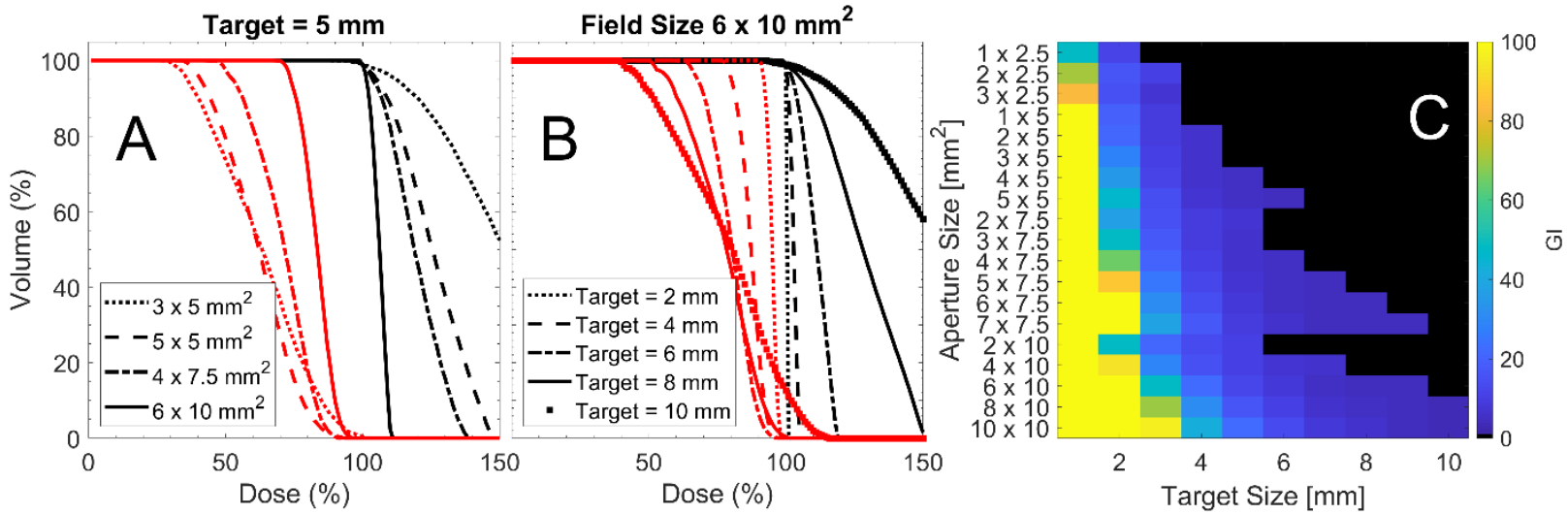

Figure 22: (A) Dose volume histogram for a fixed target size with various aperture sizes. Black lines represent dose to the target, red lines represent dose to the 3rd shell around the target. (B) Dose volume histogram for a fixed aperture size with various target sizes. Black lines represent dose to the target, red lines represent dose to the 3rd shell. (C) GI calculated for all field sizes and target sizes, black tiles represent a case where the maximum dose within the target was ≥ 20

In Table 3 the minimum dose received by 100% of a volume (D_m), and the dose received by 5% of a volume (D_5) are shown for a fixed target size with varying aperture sizes. This table is representative of the trends seen within the data, which is that larger apertures (effective area) produce lower D_5 at the expense of delivering a higher D_m to the surrounding concentric shells.

Table 3: Dose metrics described as a percentage of the prescription dose for the treatment of a 5 mm target with the static collimator case. Plans were normalized such that D_{99} was 100% of the prescription dose. D_m is the minimum dose received by 100% of the volume for the respective volume indicated. D_5 is the dose received by 5% of the volume for the respective volume indicated.

Metric	Aperture Size								
	1 x 2.5 mm^2	1 x 5 mm^2	3 x 5 mm^2	5 x 5 mm^2	3 x 7.5 mm^2	5 x 7.5 mm^2	7 x 7.5 mm^2	2 x 10 mm^2	6 x 10 mm^2
D_5, PTV	397	257	201	145	157	121	109	175	110
D_m, 1st Shell	54	59	59	69	71	82	91	72	90
D_5, 1st Shell	176	144	131	113	114	106	103	119	103
D_m, 2nd Shell	39	40	39	48	54	65	79	60	80
D_5, 2nd Shell	142	118	109	97	100	97	98	105	98
D_m, 3rd Shell	29	28	26	31	39	48	65	50	67
D_5, 3rd Shell	118	98	90	82	86	87	92	93	92

4.5.2 Effect on Collimator Orientation

The impact of collimator rotation throughout gantry motion is depicted in Figure 23 for various circumstances. In Figure 23.A. a collimator size of 4 x 5 mm^2 is used to irradiate a 5 mm spherical target. Differences between the static and dynamic collimator deliveries were minimal for both the TV and the surrounding shells. However, as shown in Figure 23.B, when irradiating with a dynamic collimator and a 1 x 5 mm^2 aperture, a smaller D_5 is observed for the 1st, 2nd, and 3rd shells. The V_{50} for the dynamic collimator case is 96.7, 74.2, and 56.4%, while the V_{50} for the static collimator case is 103.9, 81.1, and 62.6% for the 1st, 2nd, and 3rd shell respectively. The dynamic collimator creates a lower D_5 for 82.4% of the aperture/target size combinations where the D_5 differed by more than ± 2 % between the dynamic collimator and the static collimator; one of these cases is represented in Figure 23.C when treating a 7 mm target. The arbitrary choice of a 2% threshold was used to highlight meaningful differences between the static and dynamic collimator deliveries as much of the data exhibited much smaller differences.

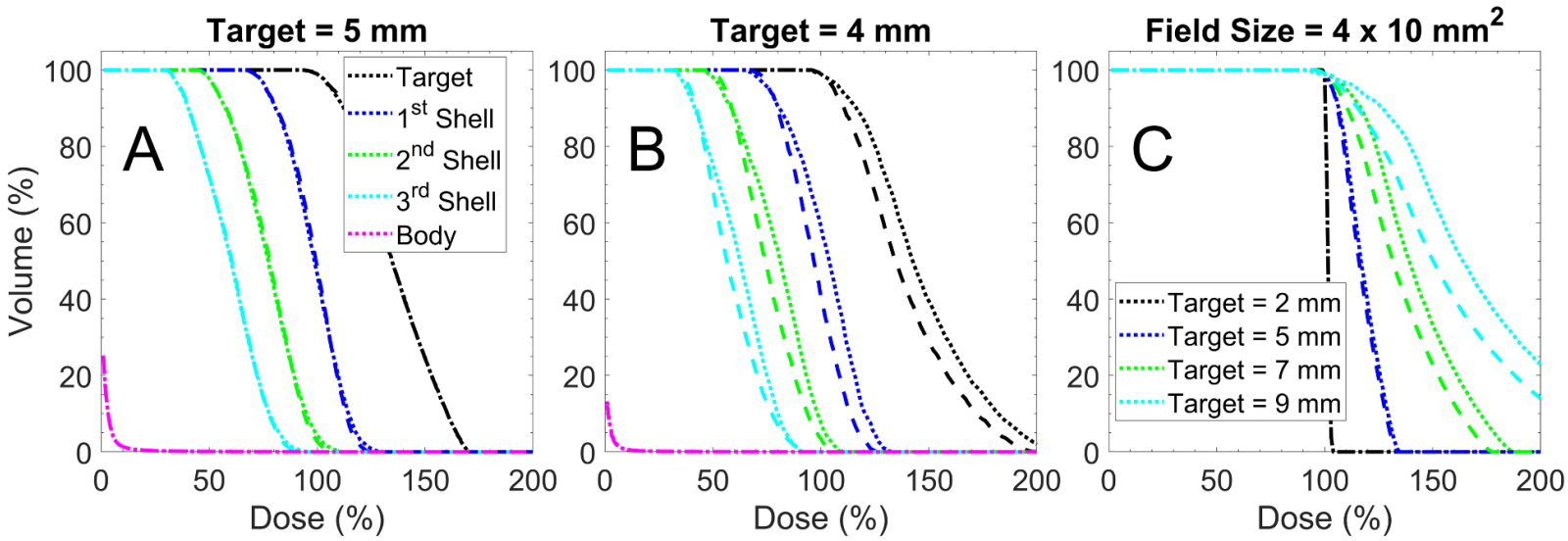

Figure 23: Impact of collimator orientation during delivery. (A) Dose volume histogram where target is a 5 mm sphere and aperture size is 4 x 5 mm^2. Dotted lines represent the static collimator case, dashed lines represent the dynamic collimator case. (B) Same plot characteristics as (A) but the delivery was performed to a 4 mm target with an aperture size of 1 x 5 mm^2. (C) A dose volume histogram for different target sizes with a fixed field size. Line definitions are the same as in (A).

Figure 24 depicts the absolute volumetric differences between the volumes receiving 30 and 10% or more of the prescription isodose defined as V_{30}, V_{10} for the dynamic collimator compared to the static collimator. Blacked out tiles represent cases deemed to be clinically infeasible as they possess a $D_{max} > 200\%$. Volumes < 0 cc indicate a smaller volume for the rotating collimator case. The magnitude of volumetric differences for V_{70} is -4.31×10^{-2} to 5.98×10^{-2} cc, and -3.26×10^{-2} to 7.72×10^{-2} for V_{50} (data not shown). The majority of cases for V_{30}, and V_{10} have volumetric differences $< \pm 0.1$ cc (97.3 and 76.7%, respectively). The dynamic collimator case produces smaller relative volumes in 60.4, 44.1, 41.4 and 50.5% of clinically feasible cases for V_{70}, V_{50}, V_{30}, and V_{10}, respectively.

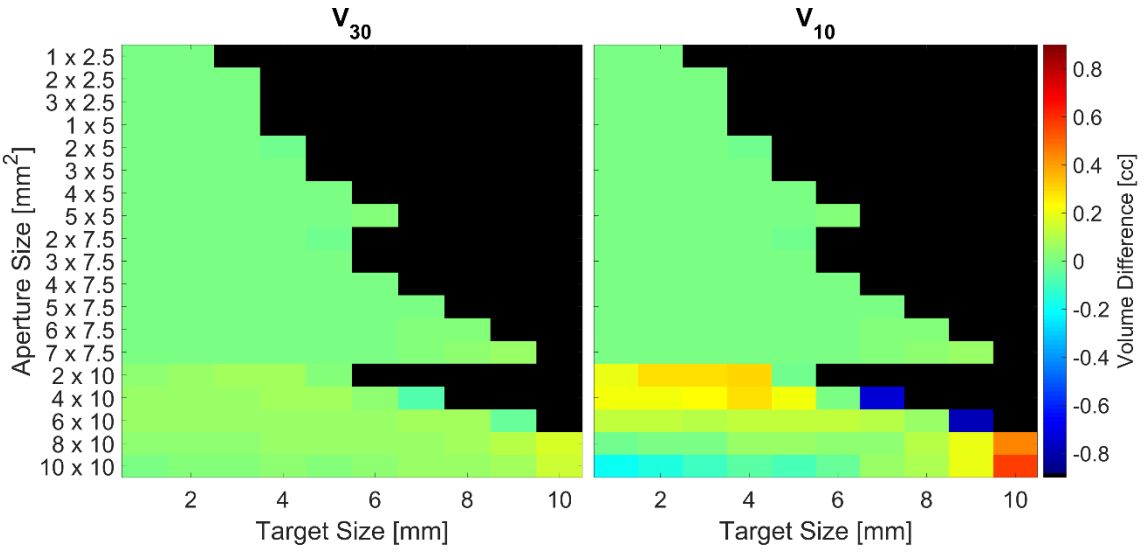

Figure 24: The absolute volumetric differences between the volumes receiving 30 and 10 % or more of the prescription isodose defined as V_{30} and V_{10} respectively for the different collimator deliveries. Volumes < 0 cc indicate a smaller relative volume for the dynamic collimator case. Blacked out tiles represent plans that delivered a $D_{max} >$ 200%.

4.5.3 Impact of motion on dosimetry

A visualization of the dosimetric impact of a linear motion ($L_{1.0\,mm}$) during treatment when irradiating a 3 mm sized target with a 2 x 5 mm^2 aperture is shown in Figure 25. The volume within the target receiving the prescription dose is reduced by 26.3%, but when the same motion is implemented with a 4 mm sized target, the volume receiving the prescription dose is only reduced by 11.0%. The hottest fraction of the target, represented by D_5, is also reduced by motion, but by a smaller amount: 177.8% (no motion) vs 170.6% (with motion) for the 3 mm target, and 133.8% (no motion) vs 139.6% (with motion). When $L_{1.0\,mm}$ motion is present, the dose wash area is reduced to 86.6, 84.5, and 84.3% in the axial, sagittal, and coronal planes along isocentre respectively when compared with a delivery without motion. An alternative visualization is shown in Figure 26, where profiles are taken along the three orthogonal planes about isocentre when treating with a 2 x 5 mm^2 aperture with $L_{1.0\,mm}$ motion. It is evident that the dose intended for the TV can been pushed away and the shape of the dose distribution has changed.

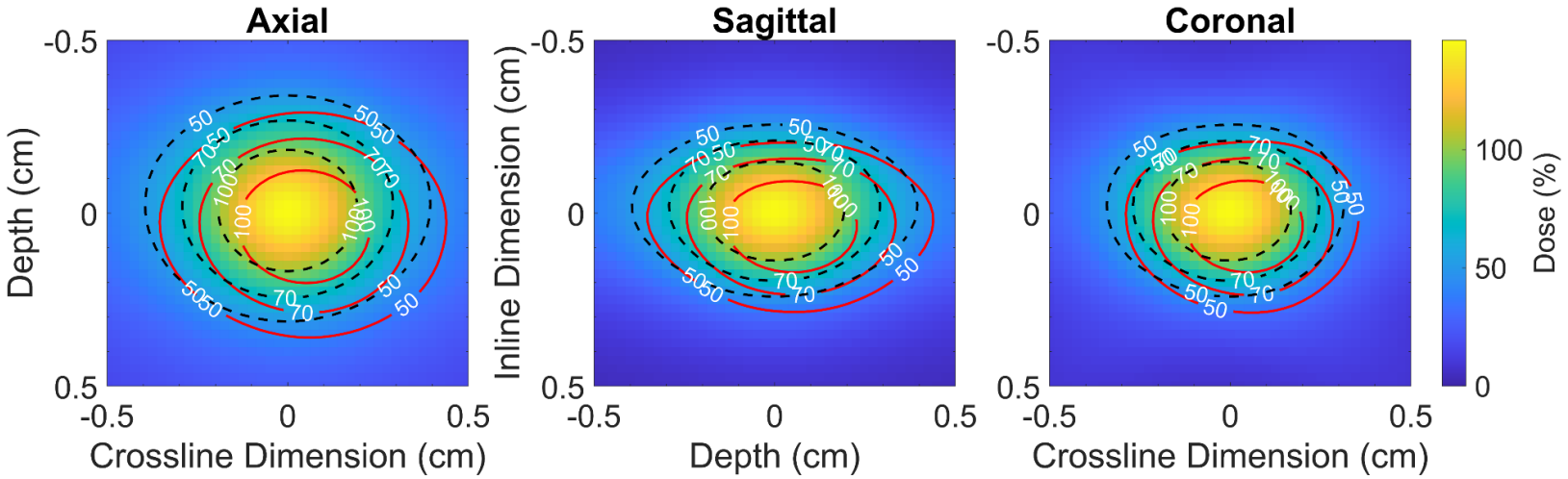

Figure 25: Dose map for a delivery with a 2 x 5 mm^2 aperture with the static collimator case. The black-dashed contour line represents delivery without motion and red lines represents with the same delivery characteristics but the phantom has been linearly moved 1.0 mm along each dimension by the end of treatment.

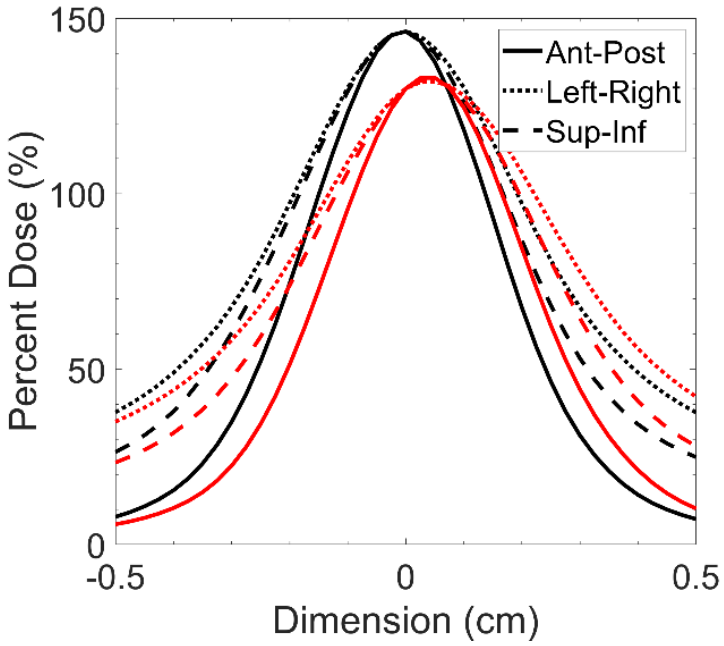

Figure 26: Dose profiles extracted along the three orthogonal axes intersecting isocentre for dose distributions when treating 3 mm spherical target with a 2 x 5 mm^2 aperture with 1.0 mm of linear motion along each axes. Black lines represent the case without motion, red lines represent the case with motion.

Analyzing the DVHs for two representative cases with the static collimator case; the dosimetric trade-offs for different aperture sizes when intrafraction motion is present can be evaluated. In Figure 27.A. and Figure 27.B. these trade-offs become apparent for an irradiation of a 4 mm target irradiated with a 2 x 5 mm^2, and 6 x 10 mm^2 sized field, respectively. As is shown above in previous sections, irradiating with a smaller field has the potential to produce a sharper dose gradient as the surrounding concentric shells receive less dose. However, when intrafraction motion is present, small field sizes result in larger relative increases to the hotspots in the surrounding shells of tissue. In the example of Figure 27, the increase in the D_5 for the smaller aperture (2 x 5 mm^2) in the 1st, 2nd, and 3rd

concentric shell was 39%, 24%, and 14% larger respectively when compared with the delivery using the larger aperture (6 x 10 mm^2). While treating with a larger aperture minimizes the relative penalties of intrafraction motion, this comes at the expense of delivering a larger integral dose to the surrounding tissues.

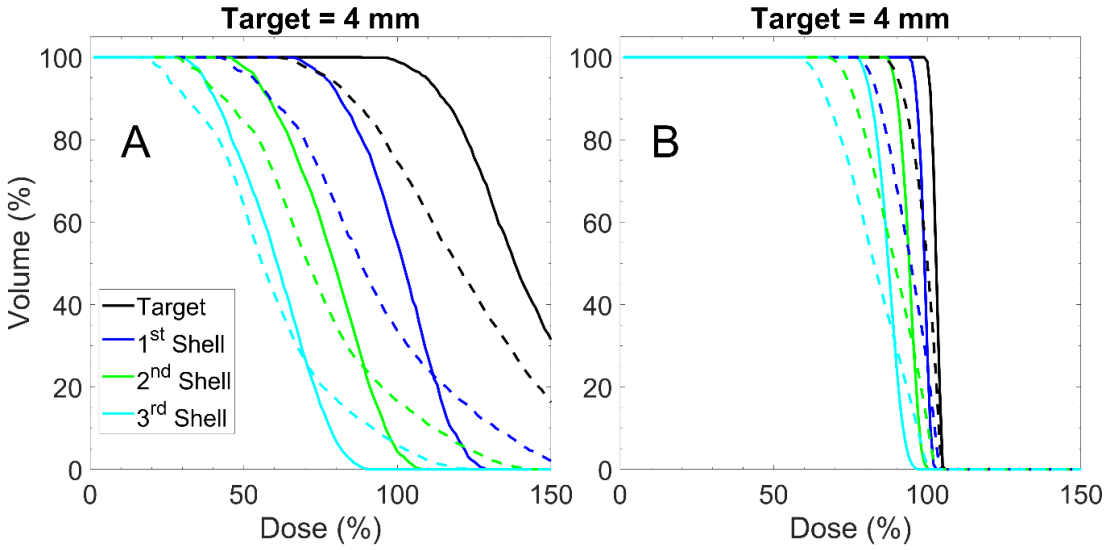

Figure 27: Dose volume histogram depicting impacts of motion for when the phantom has been moved linearly 1.5 mm along each dimension during treatment. (A) Represents an irradiation of a 4 mm sized target with a 2 x 5 mm^2 field size. (B) Represents an irradiation of a 4 mm sized target with a 6 x 10 mm^2 field size. Each delivery was performed with the static collimator case. The solid lines represent delivery without motion and the dashed lines represent delivery with motion.

The dosimetric impact of motion on targets that reside off-axis are visualized in Figure 28 where isodose lines for a full MC treatment delivery with simulated motion (shown in white) are shown with isodose lines for the same treatment delivery using the proposed superposition methodology outlined in Section 4.4.2 (shown in black). The isodose lines for the different MC deliveries appear virtually on top of each other for the

treatment of a central target, a target 2 cm off-axis, and a target 3 cm off-axis. The isodose lines have been shifted for comparison with the dose distribution of the central target. In comparison to a delivery performed with the superposition methodology, D_5 is -0.07 %, 2.72 %, and 5.16 % different for the MC delivery with the target centered, 2 cm, and 3 cm off-axis respectively. Similarly, the differences in V_{100} are less than 8×10^{-4} cc for the three target locations when simulating a delivery with MC.

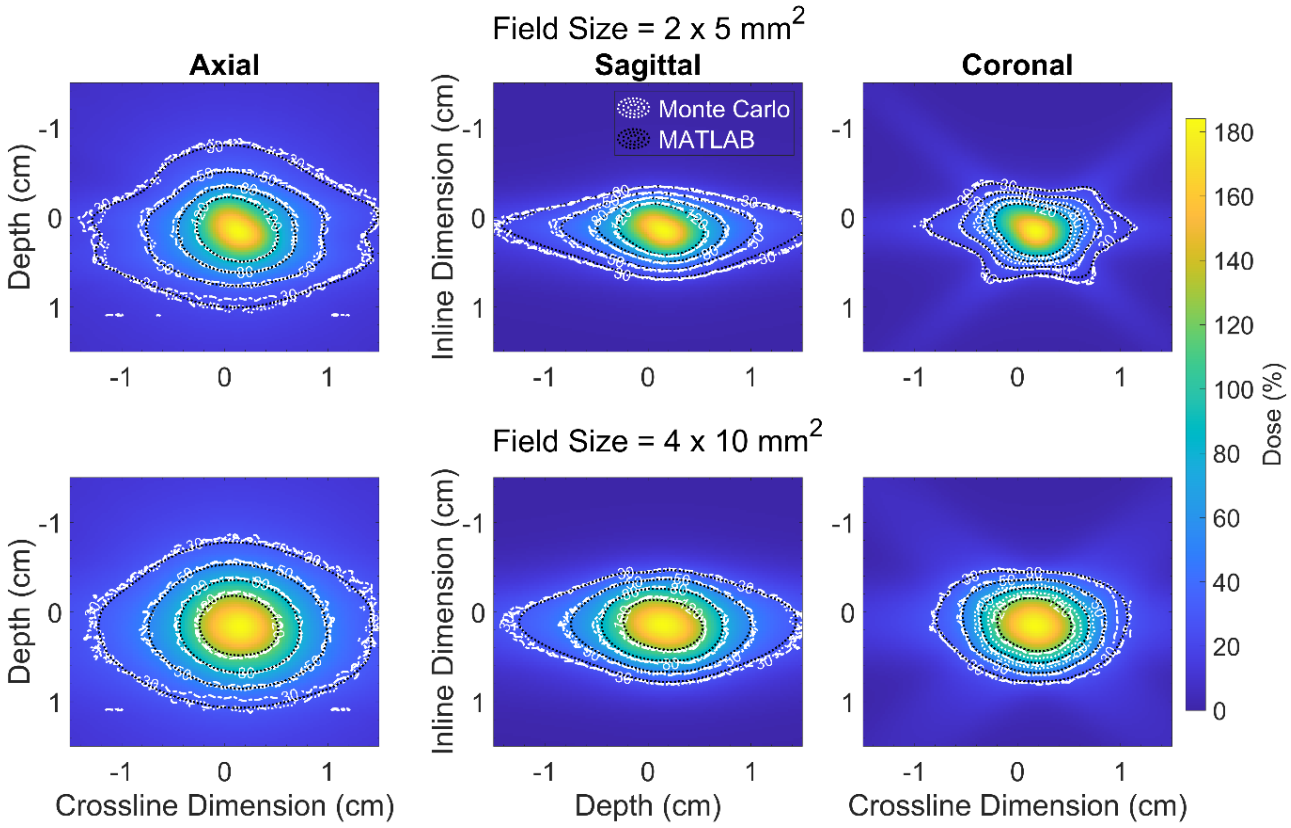

Figure 28: Isodose lines from dose distributions produced in Monte Carlo (white), and MATLAB (black) when simulation a sudden 2 mm shift ¼ of the way throughout treatment ($S_{1/4}$). The isodose lines are overlayed on top of a dose wash produced using the MATLAB superposition methodology outlined in Section 4.4.2. There are three white lines in the plot indicating the isodose lines for a central target (dotted), a target 2 cm off-axis (dashed), and a target 3 cm off-axis (dashed-dotted). The lines all occupy effectively the same spaces, indicating that the off-central location of targets is not playing a significant role in altering the dose distribution in these target locations.

In Figure 29 the R_C is shown for all field sizes and each different type of motion trace. Predictably, the magnitude of conformity loss increases with increasing magnitude of linear drift. A similar trend is observed for the large shifts that occur at different time points, where earlier shifts producing larger losses of conformity. Interestingly, for the case of large shifts occurring at set time points in Figure D, E, and F, there is a trend of worsening conformity with increasing effective aperture area. The average R_C for the different cases of motion are summarized in Table 4.

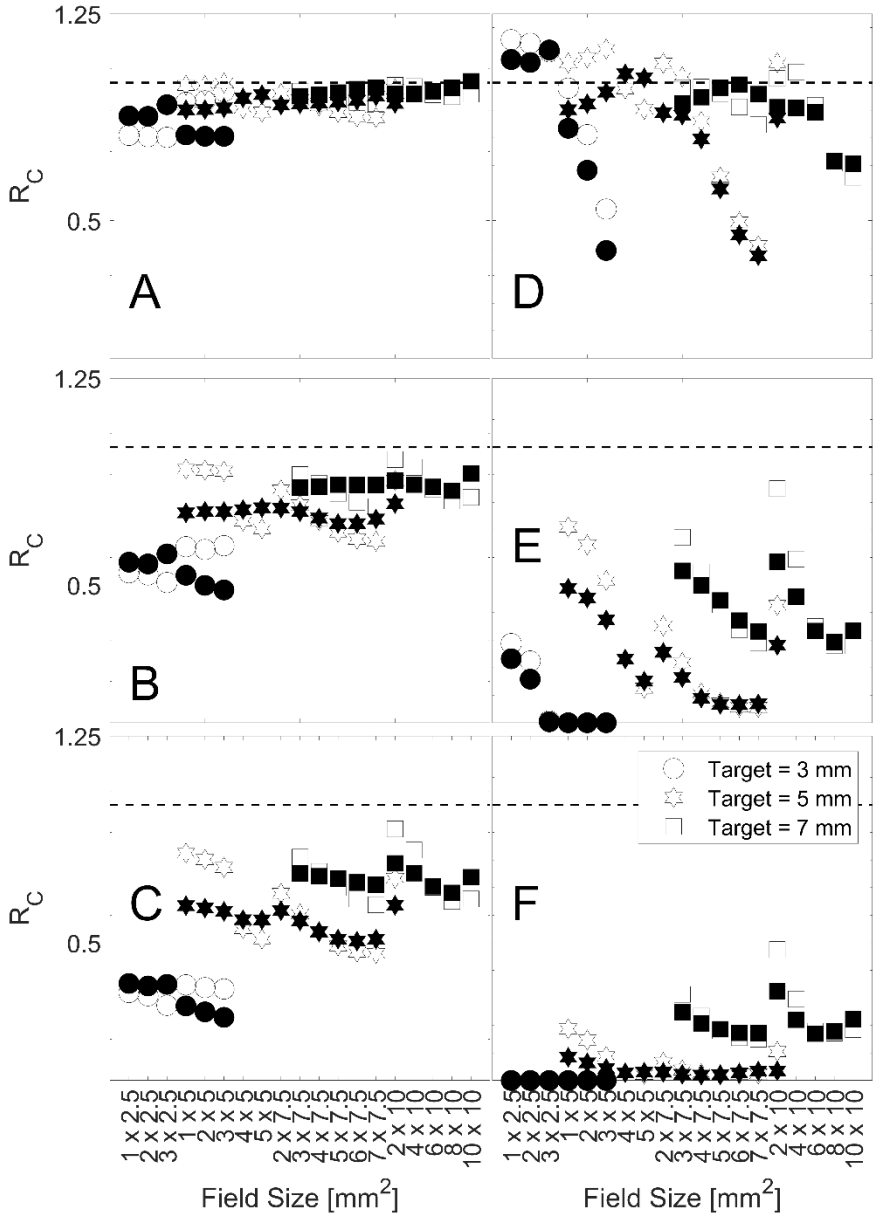

Figure 29: The ratio of the Paddick conformity index for deliveries with varying intrafraction motion. (A), (B), and (C) are plots for $L_{0.5\ mm}$, $L_{1.0\ mm}$, $L_{1.5\ mm}$, which represents linear motion up to 0.5, 1.0, and 1.5 mm in each dimension respectively. (D), (E), and (F) are plots for $S_{3/4}$, $S_{1/2}$, and $S_{1/4}$, which represents a linear motion of 2 mm in each dimension at ¾, ½, and ¼ of the way through treatment respectively. Open-face symbols represent the static collimator case and closed-face symbols represent the dynamic collimator case. The dashed line at unity represents the situation where a delivery with motion produces equal conformity to a delivery without motion.

Table 4: The average ratio of Paddick conformity index for the various cases of motion. The magnitudes and standard deviations are determined from averages across all apertures shown in Figure 29.

	Target Size (mm)		
Type of Motion	3	5	7
$L_{0.5\ mm}$	0.81 ± 0.07	0.93 ± 0.04	0.97 ± 0.02
$L_{1.0\ mm}$	0.49 ± 0.08	0.78 ± 0.09	0.89 ± 0.06
$L_{1.5\ mm}$	0.23 ± 0.07	0.61 ± 0.12	0.79 ± 0.10
$S_{3/4}$	0.38 ± 0.45	0.83 ± 0.26	0.92 ± 0.09
$S_{1/2}$	0.03 ± 0.08	0.30 ± 0.25	0.59 ± 0.20
$S_{1/4}$	0.00 ± 0.00	0.09 ± 0.09	0.38 ± 0.20

For any given TV, the choice of an aperture, and collimator orientation technique will vary dose hot-spots as well as the low – intermediate dose wash which influence the dosimetric conformity delivered to the target. This is visualized in Figure 30 where dosimetric profiles along three orthogonal axes through isocentre have been extracted for the treatment of a 5 mm target. The profiles are normalized to ensure that 99% of the TV is covered by the prescription dose. In this figure, it is shown that while square-like apertures (4 x 5 mm^2) produce a steeper dose-gradient outside of the TV when compared with rectangular-like aperture (3 x 7.5 mm^2), they deliver a larger dosimetric hotspot (~ 5.2% larger), which could pose a larger detriment to surrounding sensitive structures; and the steepness of the dose gradient could lead to a larger decrement in TV coverage when motion is present. The use of collimator rotation can be implemented to reduce the dosimetric hotspot (~ 8.4% as is depicted in the case of the 2 x 10 mm^2 aperture) reducing the dosimetric risk to surrounding tissues when motion is present. While this also leads to

a larger distribution of low – intermediate dose to surrounding tissues, this could minimize the decrements to conformity when motion is present for specific cases. For example, as is shown in Figure 29.A-C when treating a 3 mm sized target with a 1 x 2.5, 2 x 2.5, or 3 x 2.5 mm^2 field when linear motion is present, using a dynamic collimator produces a 12 ± 3% higher R_C. Seen across Figure 9.A-C is the trend of a higher R_c with more rectangular apertures, as well as some values of R_c greater than unity. This effect is due to the relative shrinking of the TV coverage in the case of motion when compared to the shrinking of prescription isodose volume in the case of motion. For example, when treating a 3 mm sized target with as 1 x 2.5 mm^2 field, the PIV_m is 63.4% of the PIV_{no}, whereas the TV_m is 73.2% of the TV_{no}, making the denominator (in the numerator of the equation in Section 4.4.5) smaller, and the resulting quotient greater than unity.

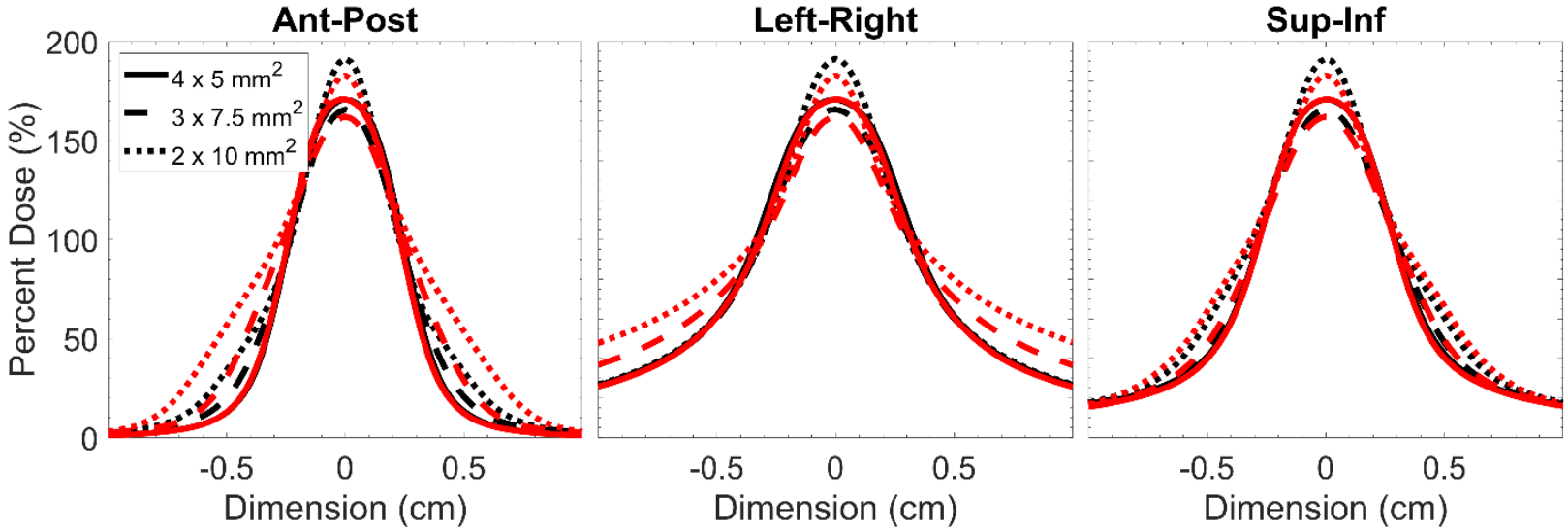

Figure 30: Dose profiles through the three orthogonal axis along isocentre for a delivery to a 5 mm sized target with a 4 x 5, 3 x 7.5, and 2 x 10 mm^2 field. Black lines represent the static collimator case and red lines represent the dynamic collimator case. Profiles were normalized to ensure that 99% of the target volume was covered by the prescription dose.

4.6 DISCUSSION

For the majority of the analysis considered in this work, many of the pairings of aperture size for a given TV would be clinically impractical. The purpose of performing the analysis was to demonstrate the benefits and compromises one must make when considering TV coverage, hot spots, and magnitude of dose received to abutting tissues, and dose-gradients. In the past decade, irradiation of lesions < 1 cc. using VMAT, or DCA therapy have appeared for brain metastases[171,172] and TN.[122] Popple *et al*. were the first to implement the use of a virtual cone with an arc-based delivery for treating small targets such as TN with arc-based and static port deliveries respectively.[118] That work determined that the TV coverage by the 50% isodose line was 0.054 – 0.087 cc for a virtual cone shaped by the two central leaves of the MLC and a 1.6 – 2.6 mm gap. The data in this investigation agrees well as TV coverage by the 50% isodose line is 0.051 – 0.093 cc for a virtual cone shaped by the two central leaves of the MLC and a 1 – 3mm gap. For the range of all apertures tested in this investigation, a TV coverage by the 50% isodose line is 0.022 – 1.359 cc.

It should be noted that when using an odd number of leaf pairs, the center of the treatment field is not located on the central axis and would require small couch motions to preserve target position relative to treatment aperture. Such motions have been demonstrated previously.[240] Implications of mechanical imperfections in motion are not considered but have been considered in a previous investigation.[240]

A short-coming of this investigation is the use of an 8.2 cm water sphere to represent a cranial phantom. This approximation was used to balance the computational

requirements (time and memory) for conducting simulations with sufficient resolution. To test if this approximation had any impact on the dosimetric contribution of scatter, a single simulation with a 2 x 5 mm^2 aperture was conducted with a cropped section of water sphere that measured 4 x 4 x 20 cm^3, with the longest dimension along beam-line, and a 0.4 mm isotropic voxel size (time = 27.4 hours). Using the same superposition methodology outlined above, the width of the dosimetric profiles defined by the 50 % isodose line is 0.30 mm larger along ant-post, 0.45 mm larger along sup-inf, and 0.35 mm larger along left-right when comparing the simulation of cranial phantom to the water sphere phantom.

Another limitation is the exploration of the dosimetric solution space when simulating intrafraction motion. There are an infinite number of choices that could be made when simulating motion traces during delivery. The varying degree of motions presented in this work: $\boldsymbol{L_{0.5mm}}$ to $\boldsymbol{L_{1.5\ mm}}$ as well as $\boldsymbol{S_{1/4}}$ to $\boldsymbol{S_{\frac{3}{4}}}$ should provide clinicians with a meaningful way to consider the impact of motion in the context of their own clinic's immobilization approaches. The motion traces used in this work were restricted to approaches utilized by other investigators to model the impact of motion on dose metrics,[169,171,248,249] and furthermore, to utilized average trends of motion that have been observed in the literature for cranial SRS.[29,137,162,163,165,166,171,247]

Neither of the collimation methods (static or dynamic) demonstrated a consistent dosimetric benefit; albeit, the 10% isodose line appeared to be most impacted by the dynamic collimator. The ranges for V_{70}, V_{50}, V_{30}, and V_{10} are -0.043 to 0.060, -0.033 to 0.077, -0.078 to 0.156 and -0.789 to 0.579 cc respectively. The dynamic collimator delivery led to a reduction in the high dose (V_{70}), and low dose (V_{10}) wash for the majority

of cases, with the largest reductions occurring when the target size is ~60 to ~80% of the longest field size dimension and the length to width ratio of the field is ~ 1.25 to ~ 1.40 for spherical targets.

In this work, the impact of motion in the context of the volume receiving the prescription dose was highly variable across different aperture sizes, target sizes, and different magnitudes of motions. For a linear drift of 1.5 mm in each dimension (2.60 mm 3D-shift vector), the ratio of the dose covering 95% of the volume in the case of motion to the case of no-motion ranged from 53.55 to 98.23 % of the no-motion prescription dose. Without motion, the dose covering 95 % of the volume is ≥ 100% of the prescription dose. Larger TVs ≥ 5 mm exhibited a difference of V_{95} between 14.56 – 100 % across all movement traces and smaller targets sometimes had 0% of their volume covered by the prescription dose due to dose-blurring from motion. The magnitude of these differences are largely in agreement with Roper *et al*. which saw $D_{95} < 60\%$, and $V_{95} < 40\%$ when considering 2^{o} rotations during the treatment of lesions far from isocentre when irradiating multiple metastases with a single isocentre; as rotations to points far off-axis would result in large perceived 3D-shifts with respect to isocentre (similar to some movement traces simulated in this work).[171]

As is shown in Figure 30, the use of a dynamic collimator could push intermediate doses into a larger volume. This idea in conjunction with the size of aperture chosen (which dictates the prescription dose criteria that covers the TV) leads to some values (shaded symbols) being higher in Figure 29 when compared with the static collimator (open symbols). While not all data is shown, the static collimator produces a higher R_c in 59.6,

50.0, 52.6% of cases for the 3, 5, and 7 mm target respectively; the clinical significance of cases where the dynamic collimator produces plans with an R_c closer to unity is unknown. Different applications of the dynamic collimator could be used for dose-sparing in specific scenarios where sensitive structures abut the TV and maximum dose tolerances have been reached.

4.7 CONCLUSIONS

In this work, we have demonstrated the dosimetric trade-offs between aperture size and target size when irradiating with virtual cones. Larger apertures (effective area) produce smaller hotspots (D_5) at the expense of delivering larger absolute doses to surrounding tissues. We have also shown the dosimetric impact of intrafraction motion consistent with previously published data derived from thermoplastic mask immobilization systems. For a given target size, the relative dosimetric penalties of intrafraction motion are smaller for larger aperture. In a representative example, the D_5 for a larger aperture (6 x 10 mm^2) in the 1^{st}, 2^{nd}, and 3^{rd} concentric shell was 39%, 24%, and 14% smaller respectively when compared with the delivery using the smaller aperture (2 x 5 mm^2). Rotating the collimator throughout delivery is beneficial in minimizing the volumes covered by the intermediate dose wash in the majority of cases (50 and 30% of the prescription dose), but the clinical significance of these findings are unknown. Apertures with a larger length to width ratio minimized the reduction in conformity when motion is present. The data from this work illustrates the growing urgency and necessity for sub-mm positioning when treating smaller targets.

CHAPTER 5. MANUSCRIPT 2: REGION-OF-INTEREST INTRA-ARC MV IMAGING TO FACILITATE SUB-MM POSITIONAL ACCURACY WITH MINIMAL IMAGING DOSE DURING TREATMENT DELIVERIES OF SMALL CRANIAL LESIONS

5.1. PROLOGUE

This manuscript explores one methodology for minimizing the dosimetric impact of motion by means of online positional corrections with BEV imaging. In this work, an optimal ROI aperture generation algorithm was developed to create for MV imaging apertures; the candidate apertures conform to anatomical sites which provide enough textural information (with respect to the image) for sub-mm repositioning in the presence of SRS magnitude motion. Additionally, using small ROI aperture enables for large reductions in the delivered imaging dose. This work provides clinicians with a technique to implement online positional verifications during treatment, allowing for the size of the imaging aperture, and frequency of imaging to be adjusted accordingly with respect to clinical objectives.

This work has been submitted to the Journal of Applied Clinical Medical Physics and has been accepted:

> "Church C, Parsons D, Syme A. *Region-of-interest intra-arc MV imaging to facilitate sub-mm positional accuracy with minimal imaging dose during treatment deliveries of small cranial lesions."*

5.2. ABSTRACT

Purpose: To automate the generation of region of interest apertures for use with MV imaging for online-positional corrections during cranial SRS.

Materials and Methods: Digitally reconstructed radiographs were created for a 3D-printed skull phantom at five-degree gantry angle increments for a three-arc beam arrangement. At each angle, 3000 random rectangular apertures were generated and 100 shifts on a grid were applied to the anatomy within the frame. For all shifts, the mutual information (MI) between the shifted and unshifted DRR was calculated to derive an average MI gradient. The top ten percent of apertures that minimized registration errors were overlayed, normalized, and discretely thresholded at the 50%, 60%, 70%, 80%, and 90% isoline level to generate imaging plans. Imaging was acquired with the skull while implementing simulated patient motion on a linac. Control point-specific couch motions were derived to align the skull to its planned positioning.

Results: Apertures with a range of repositioning errors less than 0.1 mm possessed a 42% larger average MI gradient when compared with apertures with a range greater than 1 mm. Dose calculations with MC exhibited an 84% reduction in the dose received by 50% of the skull with the 50% thresholded plan when compared to a constant 22 x 22 cm^2 imaging plan. For all different imaging plans (with and without motion) the calculated median 3D-errors with respect to the tracking of a metal-BB fiducial positioned at isocentre in the skull were sub-mm except for the 80% thresholded plan.

Conclusions: Sub-mm positional errors are achievable with couch motions derived from control point-specific ROI imaging. Smaller apertures that conform to an anatomical ROI can be utilized to minimize the imaging dose incurred at the expense of larger errors.

5.3. INTRODUCTION

Cranial SRS has been shown to achieve high tumour control rates (greater than 95%) in pituitary adenomas,[253] high obliteration rates (78%) of AVMs,[254] and lengthen the median survival of patients with 1-3 brain metastases while subsequently reducing neurocognitive decline.[255] This precision therapy delivers large doses in a single fraction (or a small number of fractions in the case of SRT) and uses techniques that promote rapid dose fall off of dose outside of the targets. In the case of certain functional disorders (e.g. TN), prescription doses can be as high as 90 Gy[245] and beam-on-times can be as long as 19.4 ± 0.6 mins with an average delivered MU of 19444 ± 611 at 1000 MU/min.[256] Trends in SRS treatment have moved away from invasive head frames toward non-invasive thermoplastic mask-based immobilization. Studies have shown that the combination of long treatment times and mask-based immobilization can lead to patient motions on the order of 2-3 mm.[137,144] The dosimetric consequences of intrafraction motion on small targets and the surrounding tissues have been previously reported,[240] and those findings suggest that additional methods, beyond frameless immobilization, could be beneficial for ensuring accurate treatment delivery.

Various considerations go into the choice of the size of margins placed around the gross tumour volume, one of which being the expected patient motion during therapy.

However, increasing numbers of centers have been reporting the use of no planning TV margins (49.1% of centers).[257] While techniques for patient-alignment vary across centers, the majority utilize MRI fusion with CT simulation for planning, and utilize CBCT or registration of DRRs with volumetric CTs on the day for verification of isocentre position with respect to the patients' coordinate frame.[148,258,259] Beyond high-precision set-up, intrafractional motion management strategies have made their way into various treatment modalities such as GammaKnife (Elekta AB, Crawley, United Kingdom),[137] which utilizes IR-based monitoring or optical surface monitoring, or CK (Accuray Inc., Sunnyvale, CA),[260,261] which monitors motion with periodic orthogonal kV imaging every 5 – 150 seconds (user defined). Several intrafraction motion monitoring systems for C-arm linear accelerators (linacs) are currently clinically available, some of which are: 1) the ExacTrac system (BrainLab AG, Munich, Germany) which can utilize an IR camera monitoring device for fiducial-tracking in conjunction with two floor-mounted kV x-ray systems to 3D-localize the patient by comparing images to plan-generated digitally reconstructed radiographs.[163] This system requires hardware external to the accelerator and can acquire one image per second.[262] 2) Optical imaging with lasers or speckled light-patterns such as the AlignRT system (Vision RT, London, UK) which relies on skin-monitoring and has several limitations: it can lead to false-positives and false negatives, it requires less restrictive immobilization masks which could lead to motion, and imaging could be occluded by the onboard imaging arms of the gantry.[135,263] For C-arm linacs that are not equipped with an imaging system like Exactrac, development of novel motion

minimization schemes would be beneficial. In this work, we explore the use of intra-arc imaging with the MV imaging beam to correct for motions detected in the BEV.

The imaging dose accrued with MV imaging[264] or CBCT[265] has been a concern with image-guided radiation therapy, in particular with pediatric cases. Several works have explored the use region-of-interest (ROI) CBCT[266,267] and MV-CT[268] and found possible dose reductions of 16-90% and 15-75% with ROI based CBCT and MV-CT respectively when compared with full-field imaging. While cupping artifacts were present, using smaller imaging apertures with the MV-imaging beam presented minimal losses to CNR when delineating bony anatomy.[268] We propose that BEV optimal imaging apertures can be used to achieve sub-mm intra-arc target localization by deriving necessary couch-shifts on a control point-specific basis with image registration. The frequency of imaging could be user-defined to balance tolerance for expected motion with imaging dose and treatment delivery efficiency. Herein we report a method for the generation and evaluation of apertures for ROI imaging and quantify the results of image registration tests as a function of aperture size. The technique is then used to demonstrate the feasibility of correcting for motions as a result of mechanical imperfections during gantry rotation, as well as intrafractional motion with the MV imaging beam in a clinical setting.

5.4. MATERIALS AND METHODS

5.4.1. Phantom Fabrication

The skull of an anonymized cranial SRS case at the Nova Scotia Health was contoured (with the exclusion of the mandible) with 3D Slicer (https://www.slicer.org/) as shown in Figure 31. The skull was 3D printed at 90% scale with a copper-doped PLA filament (3D Printing Canada, Hamilton, Canada) using a 0.3 mm layer height and at a print speed of 40 mm/s. The infill factor for the skull was chosen to be 100% as it maximized the Hounsfield units (HU) when scanned with a CT-scanner (396.53 ± 20.19). The purpose of this choice was to fall within the range of reported HU for real cranial bone which contains a composite of various bone types (cancellous, cortical) which produce HU within the range of 400 to 1500. To emulate brain tissue the skull was filled with gelatin. A 2 mm metal-BB was placed at the center of the skull after filling the skull halfway and letting the gelatin cure for three hours. The BB served as a tracking fiducial during imaging and was placed at isocentre. The rest of the skull was then filled and sealed, without filling the sinus-cavities with gelatin. The back of the skull was planed and leveled to ensure a consistent placement (pitch-independent) between the CT-couch and the couch on the linac.

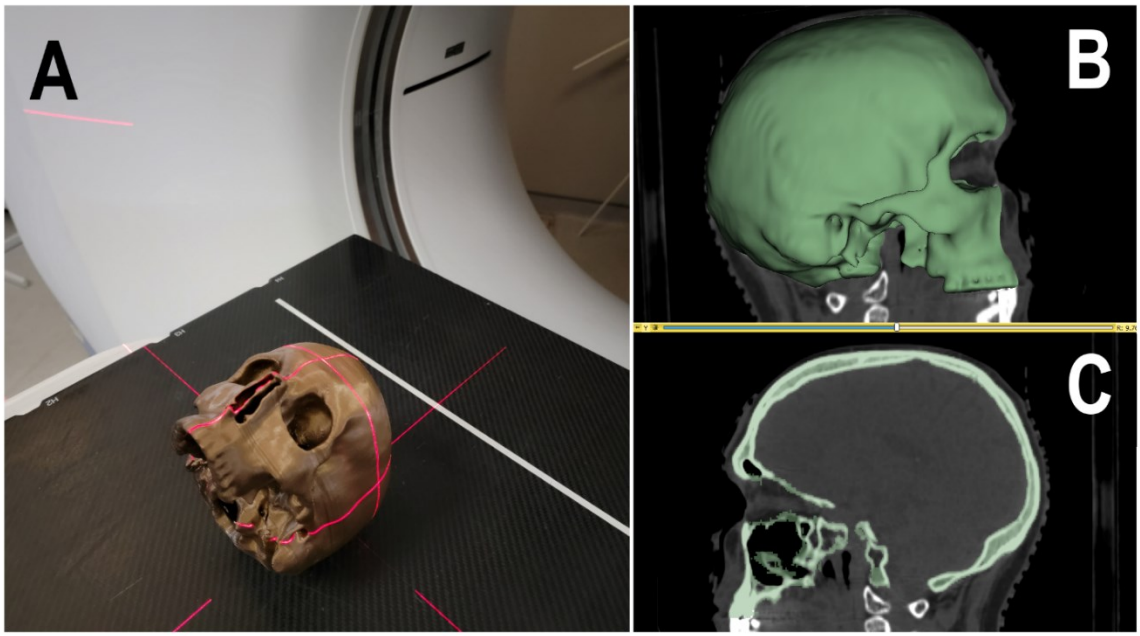

Figure 31: (A) The printed skull aligned on the CT-bed for imaging. (B) The 3D model of the skull embedded in a sagittal view of the skull. (C) A sagittal view of the skull with the contoured regions highlighted in green.

5.4.2. Treatment Workflow

A method for control point-specific patient position correction is shown in Figure 32. The generic workflow allows for an arbitrary number of gantry and couch angle combinations for imaging, defined as imaging points, distributed according to user preference. For the purposes of this evaluation, imaging points were evaluated at all points throughout a series of non-coplanar arc geometries as described below (to within a 5-degree gantry angle resolution).

To begin, a high-resolution CT scan (0.625 mm slice thickness) was acquired of the phantom and imported into the Eclipse TPS (version 15.3; Varian Medical Systems,

Inc. Palo Atlo, CA). A treatment plan consisting of 3 arcs was created for the purpose of defining the treatment and imaging geometry (in particular, the location of isocentre which is essential for the subsequent steps of the algorithm). The arc geometry in this study consisted of one full axial arc and two partial arcs with the couch rotated to + and – 45 degrees. For the imaging-arc with the couch angle at 0 degrees, the EPID was set to 50.0 cm in the vertical direction. When the couch was at ± 45 degrees, the EPID was extended to 80.0 cm in the vertical direction in order to avoid couch-EPID collisions. The gantry-couch angle combinations in this work allowed for imaging at every control-point. However, there are gantry-couch angle combinations that would preclude the possibility of BEV due to collisions of the EPID with the couch and/or patient. For example, with a vertex arc (gantry ranging from 180.0 degrees to 15 degrees in 5-degree increments, Varian IEC coordinates), nearly half of the imaging control points could be inaccessible (approximately from 250 degrees to 345 degrees Varian IEC coordinates) due collisions of the EPID with the couch or patient. The full specifications of the arcs are shown in Table 5. Control points, which are defined as any unique gantry and couch angle combination, were defined every 5 degrees of gantry rotation. Isocentre was located at the center of the metal-BB. The DICOM plan object and images were then exported for further use in MATLAB (R2020b, The Mathworks, Inc. Natick, MA).

Table 5: Arc geometry specifications in Eclipse coordinates.

Arc	Couch Angle (degrees)	Gantry Span (degrees)
One	0	180.1 - 179.9, CW
Two	45	179.9 – 5, CCW
Three	315	180 – 360, 0 – 5, CW

From this volumetric CT, MATLAB-generated DRRs were created for each control point using Siddon's Method.[222] Prior to DRR generation, the voxels within the volumetric CT in a 60 x 60 x 40 pixel neighbourhood around the centre of the BB were assigned a value of 36.1 HU; this corresponded to the average HU of the gelatin material within the skull (taken from a 20 x 20 x 20 voxel neighbourhood in slices that did not contain the BB). To facilitate efficient image acquisition, imaging plans were created for use in developer mode on a TrueBeam Stx platform (Varian Medical Systems Inc. Palo, Alto, CA). The plans consisted of the arcs described in Table 5 with imaging control points (where a high-resolution MV image was acquired) defined every five degrees of gantry rotation. Prior to delivery of the imaging plans, a CBCT was acquired to align the phantom to its planning CT with errors along each linear couch axis being less than 0.1 mm, and couch rotation (yaw) errors being less than 0.1 degree. This form of alignment will leave residual positional errors that result from the disagreement between the MV and kV isocentres, which are typically found to be less than one millimetre. In this study, image acquisition and analysis were decoupled as the analysis was performed in MATLAB (described below in section II.D). In a clinical setting, the workflow would be altered to permit image registration, and repositioning to occur in pseudo real time at a given control point.

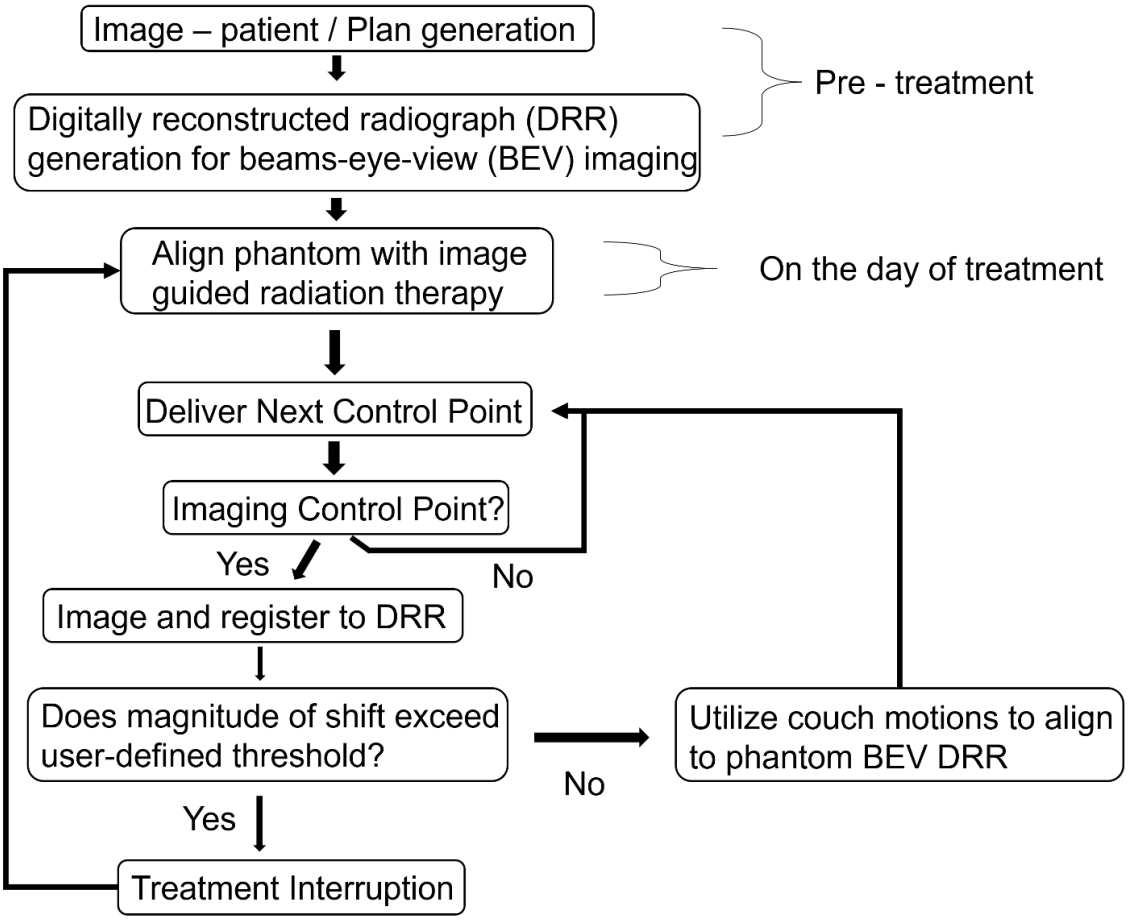

Figure 32: An example of a clinical workflow for control point-specific image repositioning.

5.4.3. Control Point-Specific Apertures

One objective of this work is to identify apertures that are capable of providing accurate registration information following motion, regardless of the direction of that motion. Such a set of apertures is required at all possible imaging points along the arcs. A second objective is to determine how small an aperture can be used such that accurate registration information is still generated while minimizing the dose delivered to acquire

that information. Apertures that conformed to an anatomical ROI were explored for use in control point-specific repositioning with image registration. To choose the location and size of the control-point-specific ROIs, an analysis of the repositioning capabilities of various apertures was assessed as follows. For each BEV, 3000 rectangular apertures shaped by the MLCs were generated with a randomly sampled central position and size ranging from 0.375 to 37.5 cm^2. The size and position of each aperture was used to create two cropped images; one of the images was shifted laterally and/or vertically with 100 simulated shifts on a grid (up to ±2 mm in steps of 0.04 mm in each direction perpendicular to the BEV at isocentre). For each shift, the shifted-image (shifted anatomy) was registered to the unshifted imaged (unshifted anatomy) with Mattes Mutual Information in MATLAB. For each BEV, the top 10% of apertures that minimized the mean and standard deviation of registration errors from the simulated shifts (on a grid) were selected for contribution to a composite image. Binary masks of these apertures were overlayed and summed (i.e. each time a voxel of the unshifted DRR was included in a binary mask, the value of that pixel was increased by 1) to create topographical maps which highlighted anatomy that was commonly included in the best-performing apertures; an example of one map is shown in Figure 33A as an overlay on top of the DRR with the BB present for illustrative purposes (it was removed for DRR image registration purposes as described previously). Imaging plans comprised of control point-specific apertures were created based on discrete threshold levels from the topographical maps shown in Figure 33B. Higher thresholds represented smaller apertures. The apertures were defined by the bounding rectangle for a given isovalue line and made as rectangles with the MLC and the jaws shown in Figure

33C. The impact of threshold-level on the mean registration error was assessed for known-shifts applied during an imaging arc.

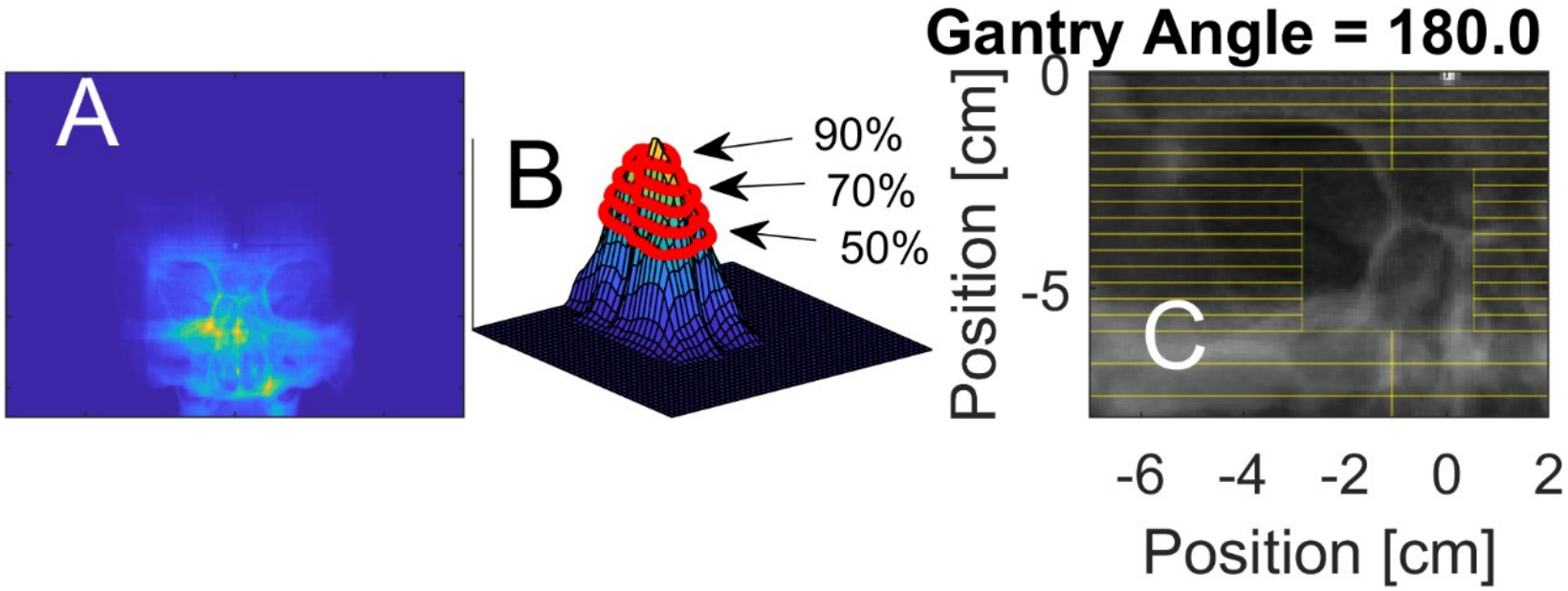

Figure 33: (A) Mask overlay of top 10% of apertures which minimized registration errors. (B) Topographical map created from sum of top 10% apertures which minimized registration, peak indicates most common pixels shared by apertures, and contours depict thresholds for aperture designs. (C) An aperture design derived from the 80% threshold level depicted in (B).

To assess the feasibility of the thresholded-imaging plans derived from the 3D-printed skull analysis for use with different clinical cases, an imaging plan (with the 60% thresholded aperture) was applied to DRRs generated for six anonymized, previously treated clinical SRS patients with skull volumes ranging from 2.5 x 10^3 to 3.5 x 10^3 cc. To scale the location and size of the ROI apertures, we calculated the cubed root of the relative volumetric scaling factor between the case in question and the 3D-printed skull for which the ROI apertures were derived; this factor was used to scale each dimension of the aperture (X/Y extent) as well as the vector position of the aperture with respect to isocentre (location of the metal-bb) for each BEV. For each case, the grid-shifting analysis described above for deriving the apertures was applied for each BEV to assess the mean registration error with a ±2.5 mm range.

In an effort to quantitatively characterize image information that yields sub-mm registration results, two characteristics of the anatomy seen within the ROIs (delineated by the apertures created in the analysis above and restricting the analysis to apertures greater or equal to 4 cm^2) were investigated. For the purposes of this analysis, we have separated apertures into two groups: "Good" apertures were those that produced a range of registration errors (defined by difference between the 95th percentile and 5th percentile errors) less than 0.1 mm, and a mean error less than ±0.1 mm across the entire shift grid. "Bad" apertures were defined as ones that possessed a range of errors greater than 1 mm.

First, the 2D-directional gradient of the image contained in each aperture was calculated. The angular directions of the vectors that comprised the gradient images were binned into a histogram with eight bins, each having a 45-degree directional span. The

contribution of each pixel was weighted by the magnitude of the gradient in that pixel. For the purpose of evaluating the characteristics of good versus bad imaging apertures, the polar histograms were parameterized by the variance of counts across the apertures and normalized by the sum of counts in the histogram.

Second, the MI between the anatomy contained within a given aperture and the same anatomy when it is shifted was calculated (using a grid-based shifting pattern as described earlier). This produced a 2D array of 121 MI values with the central element having the highest value (*i.e.* unshifted images have the highest possible MI score) and values decrease for all shifted positions. This information was condensed by calculating the mean difference between all pixels with respect to the central pixel.

The condensed information for both the gradient polar histograms and MI mean difference were calculated for 30 good and 30 bad apertures at gantry angles ranging from 0^{o} to 360^{o} in 45^{o} increments (*i.e.* a total of 480 apertures). Scatter plots of the parameterized polar plots against the parameterized MI data were generated to determine if the metric was predictive of aperture quality.

5.4.4. Motion Correction and Targeting Accuracy

Two forms of positional errors were explored in this investigation; namely: 1) mechanical imperfections of the dynamic motions of the linac (gantry rotation at different couch positions) during delivery. 2) Simulated intrafractional motion. In the following subsections, the methodology for detecting, and correcting for motions with the tracking

of a high-Z fiducial, as well as anatomical image registration is explained. In addition, the simulation of intrafractional motion, and the comparison of the performance of the two repositioning strategies is described.

5.4.4.1. Repositioning by Tracking High-Z Fiducial

Following the method described in Parsons *et al*.[269] a small aperture was created with the jaws (2.5 x 2.5 cm^2) for imaging. The center of the metal-BB was identified using a maximum convolution approach which maximized values within the BB and zeroed all objects that appeared larger than the physical size of the BB. The center of the BB was then compared with the center of the EPID as depicted in Figure 34. The deviation of the BB was used to derive the necessary couch motions to position the BB at the center of the EPID with:

$$\begin{bmatrix} \Delta Lat_{\theta,\varphi} \\ \Delta Lng_{\theta,\varphi} \\ \Delta Vrt_{\theta,\varphi} \end{bmatrix} = \begin{bmatrix} cos\varphi & -sin\varphi & 0 \\ sin\varphi & cos\varphi & 0 \\ 0 & 0 & 1 \end{bmatrix} \begin{bmatrix} (BB_x - EPID_x)cos\vartheta \\ (BB_y - EPID_y) \\ (BB_x - EPID_x)sin\vartheta \end{bmatrix} \quad \textbf{(42)}$$

Where $BB_{x/y}$ is the detected center of the BB and $EPID_{x/y}$ is the center of the EPID in the x and y direction for a given BEV, respectively. The angles θ and φ are the gantry and couch angle, respectively.

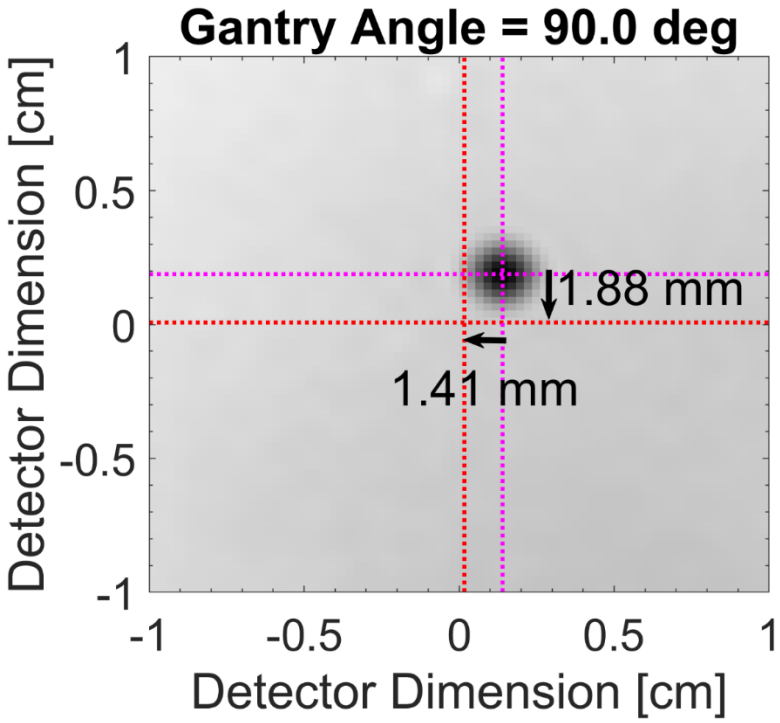

Figure 34: Example of the detection of the center of the BB (magenta line intersection) with respect to the center of the electronic portal imaging device (red line intersection). The detected shifts for this control point are shown for the case of a sudden 1.5 mm shift along each linear couch axis with the gantry at 90 degrees and the couch at 0 degrees.

5.4.4.2. Repositioning with Anatomical Image Registration

To perform anatomy-based registration, images were pre-processed with normalization and histogram equalization.[133] Following pre-processing, images were registered using the imregister function in MATLAB with Mattes MI using all pixels for registration, and an initial radius of 6.25×10^{-4}. The deviation of the EPID image from the DRR (shown with the bb present for illustrative purposes) as depicted in Figure 35 was used to calculate the necessary couch motions to align the phantom with respect to the BEV

as described in section 5.4.4.1 above. Two different forms of anatomical imaging were acquired: 1) Utilizing open-field anatomical imaging (shown in Figure 35A) with a 22 x 22 cm^2 field which will herein be referred to as ANA_{Open}. 2) Utilizing control point-specific apertures as depicted in Figure 35B, which will herein be referred to as ANA_{60} or ANA_{80} for the 60% and 80% thresholded apertures, respectively. With the ROI imaging, the EPID images were cropped to the physical size of the aperture prior to registration. None of the ROI apertures considered in the work imaged the BB embedded in the centre of the skull. The detected couch motions for repositioning with anatomical registration was compared to the same corrections derived with the tracking of the metal-BB; The tracking of the metal-BB was considered the gold standard for repositioning due to the high contrast presence for any BEV.

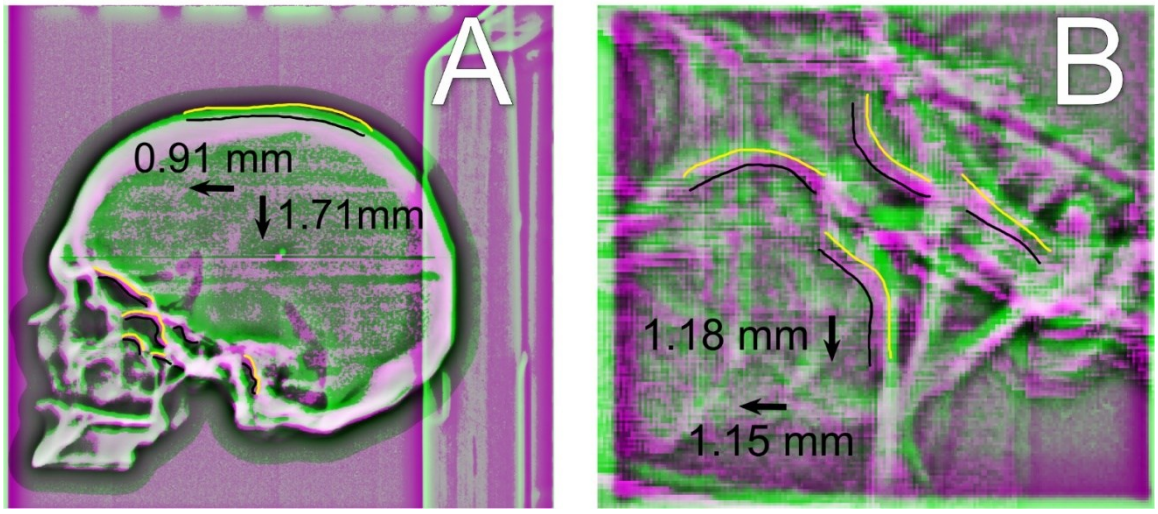

Figure 35: Example of anatomical registration between MV image with the electronic portal imaging device (green overlay) and a MATLAB generated DRR (magenta overlay). Yellow lines were drawn to highlight example edges of anatomical features in the EPID image while black lines depict the same example edges in the DRR. (A) Registration with an open field (22 x 22 cm^2). (B) Registration with an 80% thresholded aperture described in Figure 33. The detected shifts for this control point are shown for the case of a sudden 1.5 mm shift along each linear couch axis with the gantry at 90 degrees and the couch at 0 degrees.

5.4.4.3. Simulated Intrafractional Motion

In this study, intrafractional motion was simulated with simplistic motion traces to evaluate the repositioning capabilities of the registration algorithm when there were known deviations of the phantom. For one motion trace, the phantom was linearly moved 1.5 mm in each direction over the full treatment duration (*i.e.*, first control point had 0 mm of motion, last control point the couch was shifted 1.5 mm in each linear couch axis). The other motion trace emulated a sudden 1.5 mm shift in each linear couch axis that occurred halfway through the axial arc (the first arc delivered). For both cases (motion or no motion),

positioning errors were assessed by comparing the results of image registration (between DRR and EPID) to the tracking of a metal-BB with respect to the center the EPID. This ensured that any positioning errors that resulted from mechanical issues like EPID sag did not impact the comparison of the two registration techniques.

5.4.5. Imaging Dose Calculation

Dose distributions for each imaging arc with a given aperture design was calculated using EGSnrc. The treatment head of the TrueBeam STx platform was simulated using a previously-validated 2.5 MV photon beam generated in VirtuaLinac (Varian Medical Systems, Inc., Palo Alto, CA).[270] The phase space was located 73 cm above isocentre and was validated as accurate to better than 2% compared to measured depth dose and off-axis profiles. This served as the input for a BEAMnrc model containing the jaws,[271] HDMLC and mylar exit window. These three components were modeled using exact geometric and material specifications provided by Varian Medical Systems. This was used as an input to DOSXYZnrc.[231] The phantom was created with voxel sizes of 9.62 mm^3 from the CT of the ATOM (Model 701, Computerized Imaging Reference Systems, Inc. Norfolk, VA) head phantom. An ECUT = 0.512 MeV and a PCUT = 0.010 MeV was used with 10^{10} histories for each arc. An equal number of monitor units was delivered for each imaging control point using the definition of monitor units defined for Source-21 within DOSXYZnrc.

5.5. RESULTS

5.5.1. Characterization of High-Quality Imaging Apertures

A few examples of the outcomes from the aperture-searching algorithm described in section 5.4.3 are shown in Figure 36. Here, a topographical map, as depicted in Figure 33A-B, is shown as a colorwash over a DRR for a given BEV, with a bounding rectangle delineating a ROI for imaging with the 80% threshold line. The accompanying gantry and couch orientations for the depicted beams are shown as a rendering of the linac with the phantom included in the row below the colour wash. The colour wash depicted in these images highlight (as bright colours from the colour wash) anatomical features that were common to the top 10% of apertures which exhibited minimal registration errors. Qualitatively, these examples also depict regions that would be poor for imaging to minimize positional errors (identified as dark colours in the wash). Regions with poor registration capabilities tend to contain a lack of bony landmarks (such as the middle of the skull). Potentially counter intuitively, some regions of bony anatomy do not feature prominently in the highlighted apertures. This meant that those regions did not meet the criteria for "good" apertures described previously and suggests that those regions may estimate registration-derived shifts that are erroneous in a subset of motion cases (i.e., they could have excellent registration results, but only in a subset of patient motion directions).

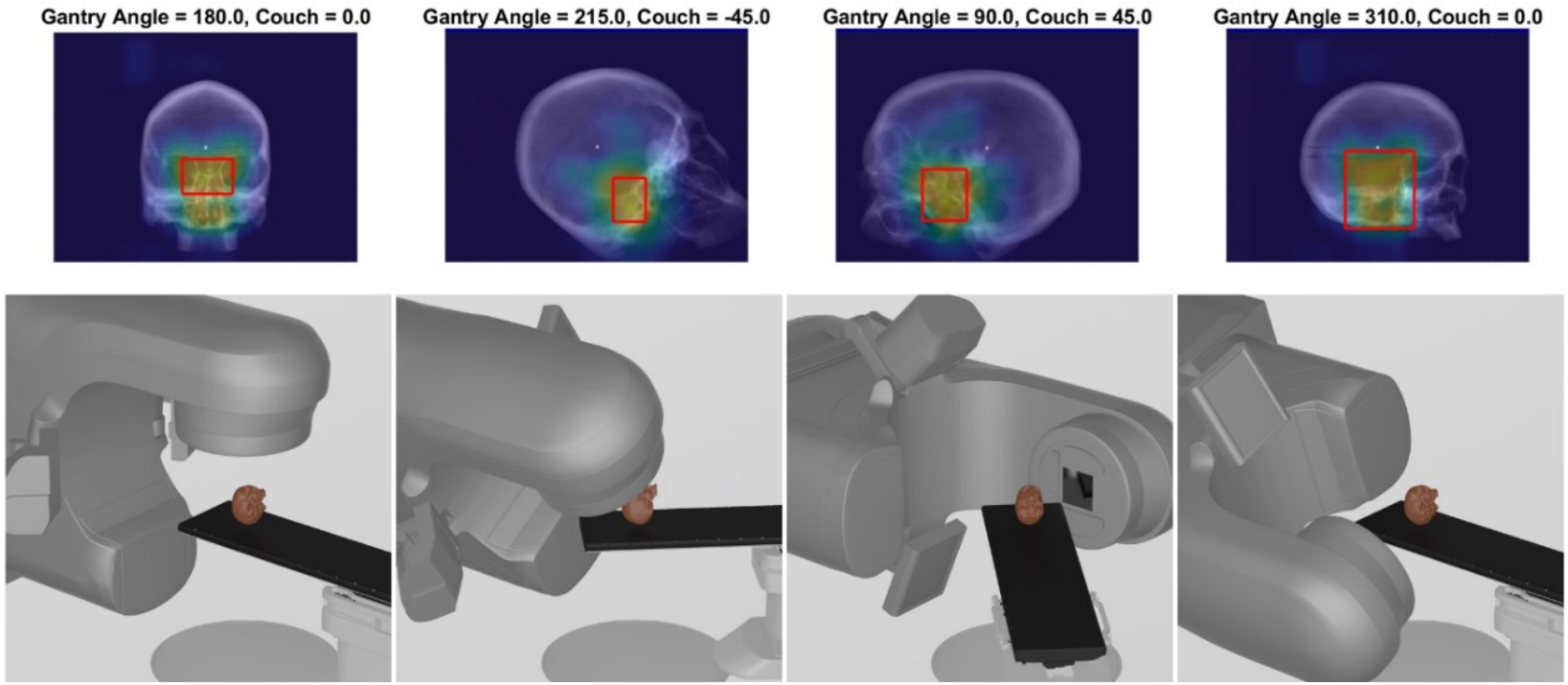

Figure 36: Examples of the top 10% of apertures which minimized registration errors for four different BEV depicted as a colour wash overlayed onto a DRR. Bright colours highlight the anatomical regions shared by the proportion of the top 10% of apertures. The red box articulates the 80% threshold level for creation of an imaging aperture for the respective BEV. The accompanying couch and gantry positions are depicted in the row below the BEV.

An example of a good and bad aperture for repositioning is demonstrated in Figure 37. Here the polar histogram for the good aperture is shown to contain a more uniform distribution of directional information whereas the bad aperture is heavily unidirectional. Additionally, the MI distribution for simulated shifts depicts a rapid drop off in all directions with the good aperture, whereas the bad aperture depicts a sharper drop off in some directions and not in others (implying repositioning capabilities would be strong in some directions and weaker in others); also the magnitude of the central pixel is lower with the bad aperture which implies a smaller quantity of high-entropy content. As described in section 5.4.3, the behaviour of these data across multiple apertures and BEVs was condensed and is depicted in Figure 38. Within this parameterized data, the average polar histogram of good apertures contains 112% more counts than bad apertures. This could be the result of apertures being larger and/or containing a relatively larger presence of high-contrast feature with strong directional gradients (e.g, bone bordering soft tissue). There is an evident clustering of data between the two aperture subsets. While the magnitude of variance of the polar histogram alone does not appear to be enough to distinguish between good and bad apertures, the average MI difference does as it is 40% larger for good apertures when compared with bad apertures. The mean and standard deviation of the compass plot variance is 0.11 ± 0.15 and 0.04 ± 0.02 for bad and good apertures, respectively. The variance metric in conjunction with the average MI difference could be used to identify apertures that have strong repositioning capabilities but only in a few directions.

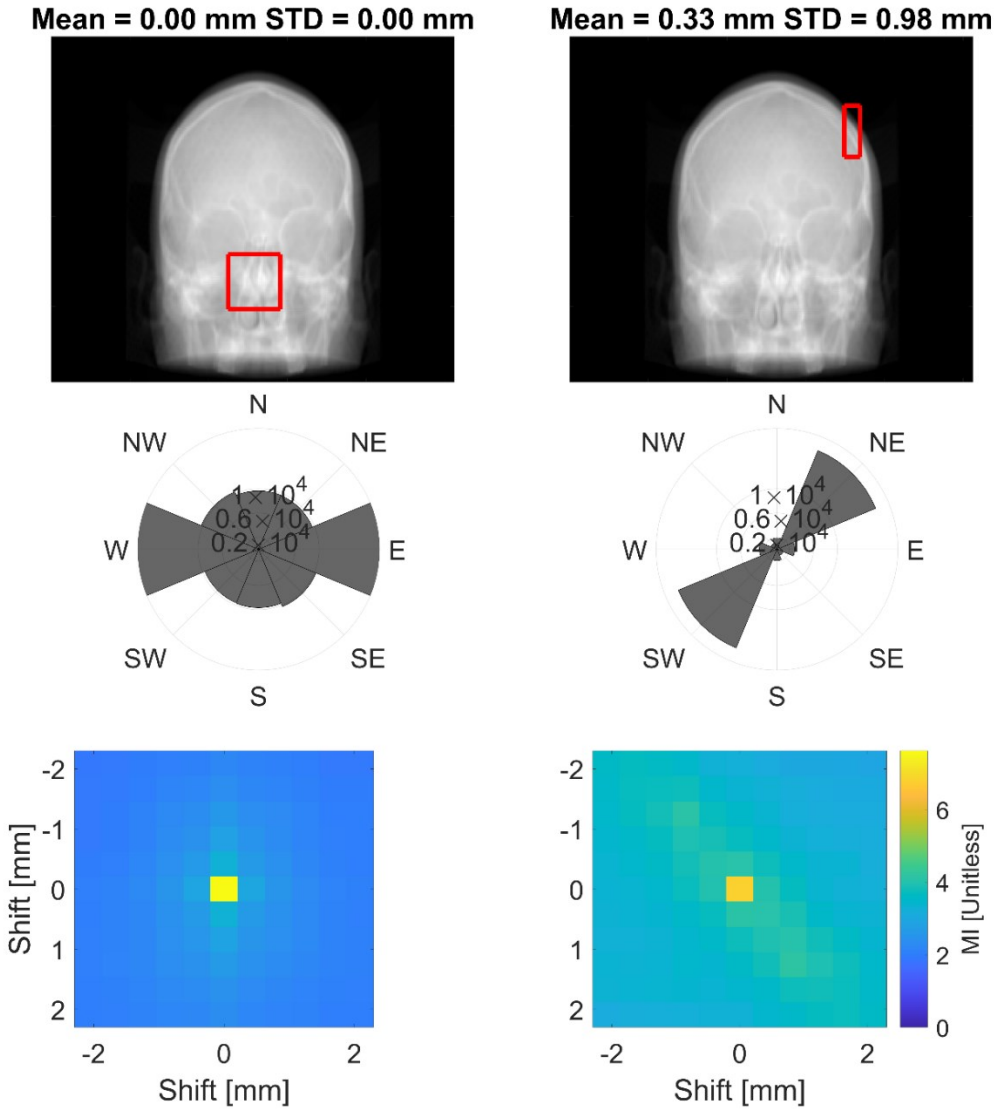

Figure 37: An example of directional and Mutual information-based characteristics for an aperture with low registration errors (left column) and an aperture with worse registration errors (right column). The second rows depicts a polar histogram where the counts are the pixel values of weighted-gradient image of the anatomy contained within the aperture (depicted by red rectangle in the top row). The bottom row depicts the mutual information between unshifted and shifted anatomy contained within the aperture for 2D-shifts with respect to the beams-eye-view.

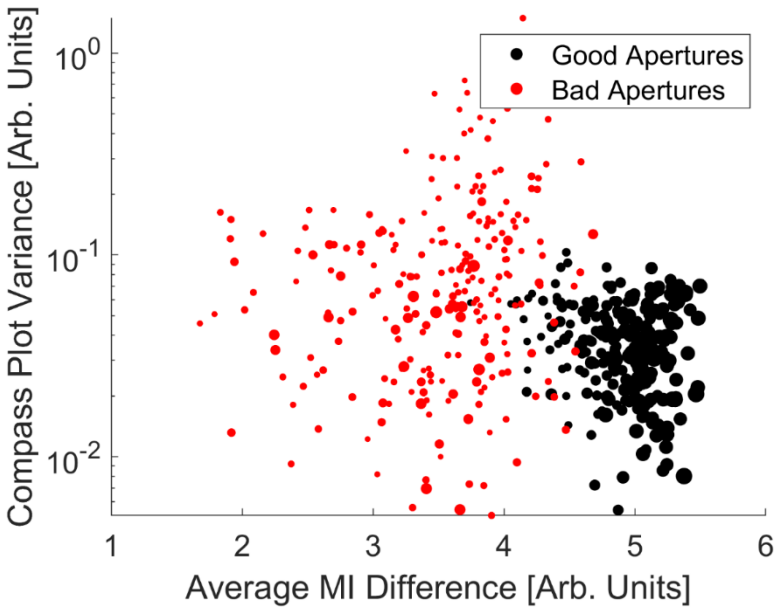

Figure 38: Variance of compass plot depicted in Figure 37 normalized by the total counts with respect to the average MI difference derived from the bottom row plots in Figure 37. Black circles represent good apertures with a range of registration errors less than 0.1mm and a mean registration error less than 0.1 mm and red circles represent bad apertures with a range of registration errors greater than 1 mm. The size of the markers are indicative of the size of the aperture. The smallest markers represent at 4 cm^2 field size, and the largest markers represent a 36 cm^2 field size.

5.5.2. Dose Reduction with ROI Apertures

Reducing of the size of the imaging aperture leads to a reduction in the imaging dose. There was an 83% reduction in the dose received by 50% of the volume (D_{50}) throughout the skull for an axial imaging arc with the 50% thresholded plan when compared to imaging plan with an open aperture (22 x 22 cm2). From the 50% to 90% thresholded imaging plan, the D_{50} throughout the skull was reduced by 87%. The normalized integral dose with decreasing field sizes (notated by threshold levels from the surface plot in Figure 33) decreased in a linear fashion from the 50% to 90% threshold.

Qualitatively these results are visualized with a dose wash calculated with MC simulations in Figure 39, where this a notable reduction in the magnitiude, and size of the imaging dose distribution. The imaging arc simulations with a 22 x 22 cm2 field had a less than 4%, and 3% voxel uncertainty for doses greater than or equal to 50% and 90% of the maximum dose, respectively.

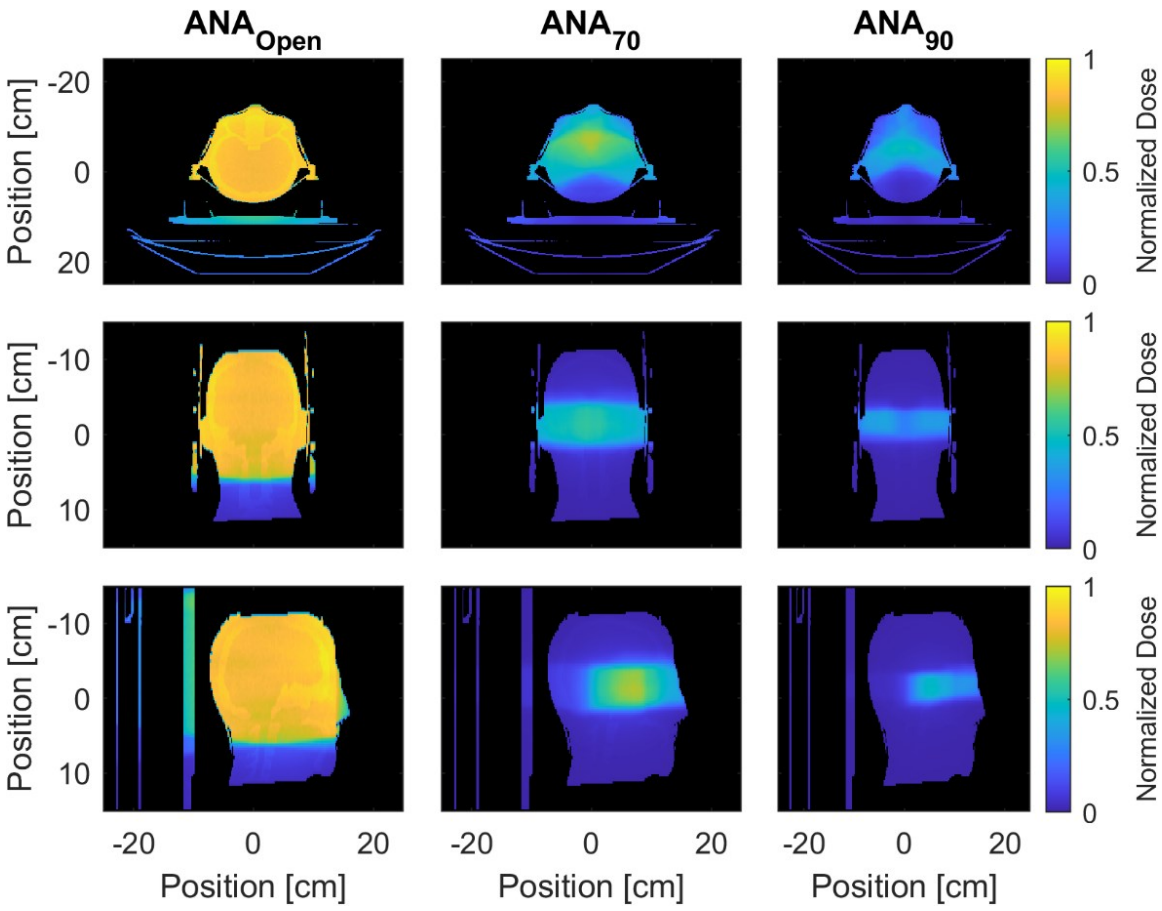

Figure 39: Dose washes for the central axial, coronal, and sagittal planes calculated with Monte Carlo for ANA_{Open} (22 x 22 cm^2 field size), ANA_{70} (70% thresholded aperture design), and ANA_{90} (90% thresholded aperture design); where ANA refers to imaging of cranial anatomy with the 2.5 MV imaging beam. Each dose wash was normalized to the max dose of the ANA_{Open} plan.

5.5.3. Registration Errors

Pre-Imaging alignment with a CBCT reported positional differences with the planning CT of less than 0.1 mm in any dimension as well as less than 0.1 degrees of couch rotation (yaw). The maximum detected offset of the BB from isocentre without simulated intrafractional motion is shown in Table 6. The errors represented in this table would be indicative of a single point for calculating the isocentric sphere comparably calculated with a WL test.

Table 6: Maximum detected offsets in the lateral, vertical, and longitudinal couch motions (in mm) of the metal-BB when the couch is positioned at idealized isocentre.

Couch Angle	- 45	0	45
Lateral [mm]	0.71	0.15	0.10
Vertical [mm]	0.18	0.23	0.18
Longitudinal [mm]	0.42	0.34	0.18

During simulated linear motion, the 2D positional errors (i.e. positional error in the BEV) with respect to BB-tracking were less than one millimetre in 100%, 89%, and 57% of imaging control points for open-field imaging (ANAopen), and thresholded imaging (ANA_{60} and ANA_{80}), respectively. During a simulated sudden persistent-motion, the 2D positional errors with respect to BB-tracking were less than one millimetre in 100%, 82%, and 42% of imaging control points for open-field imaging (ANAopen), and thresholded imaging (ANA_{60} and ANA_{80}), respectively. In Figure 40 the repositioning capabilities of imaging with progressively smaller apertures (from an open field with a 22 x 22 cm^2

aperture to the 80% thresholded plan derived from Figure 33) is presented as the difference from the detected shifts with metal-BB tracking. In Figure 40A the 3D repositioning errors based upon the detected couch shifts are shown. All median 3D-errors are sub-mm indicated by the center line in the box. The 2D repositioning errors with respect to the BEV are shown in Figure 40B. All median 2D-errors are sub-mm with the exception of the T8 imaging (equivalently ANA_{80} with an 80% thresholded plan but changed for display purposes) with a sudden shift for which a 1.16 mm discrepancy was observed.

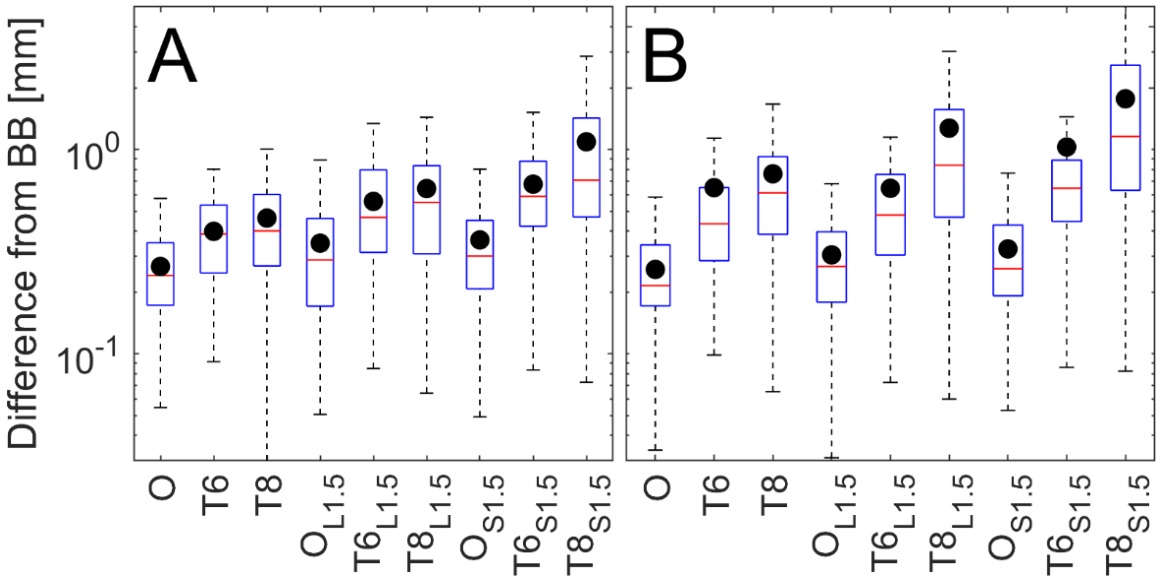

Figure 40: Registration errors for the various imaging acquisitions with respect to BB-tracking. (A) represents 3D-errors detected using image registration with respect to BB-tracking. (B) represents 2D-errors with respect to BB-tracking for each beams-eye-view. The mean value is depicted by the black circles overlayed on each box. O = open field imaging, T6 = thresholded imaging at the 60% isoline level, T8 = thresholded imaging at the 80% isoline level, L1.5 = linear shifting up to 1.5 mm while imaging, S1.5 = sudden shift of 1.5 mm while imaging.

The registration error detected for the grid-shifting analysis with the clinical cases using the 60% thresholded aperture imaging plan is shown in Figure 41. For the clinical cases, the 99th percentile of registration errors were less than 0.1 mm across all gantry angles and all simulated shifts on a grid. For patients 1-6, the volumetric scaling factor was determined to be 1.13, 1.18, 1.06, 1.15, 1.16, 1.06, respectively.

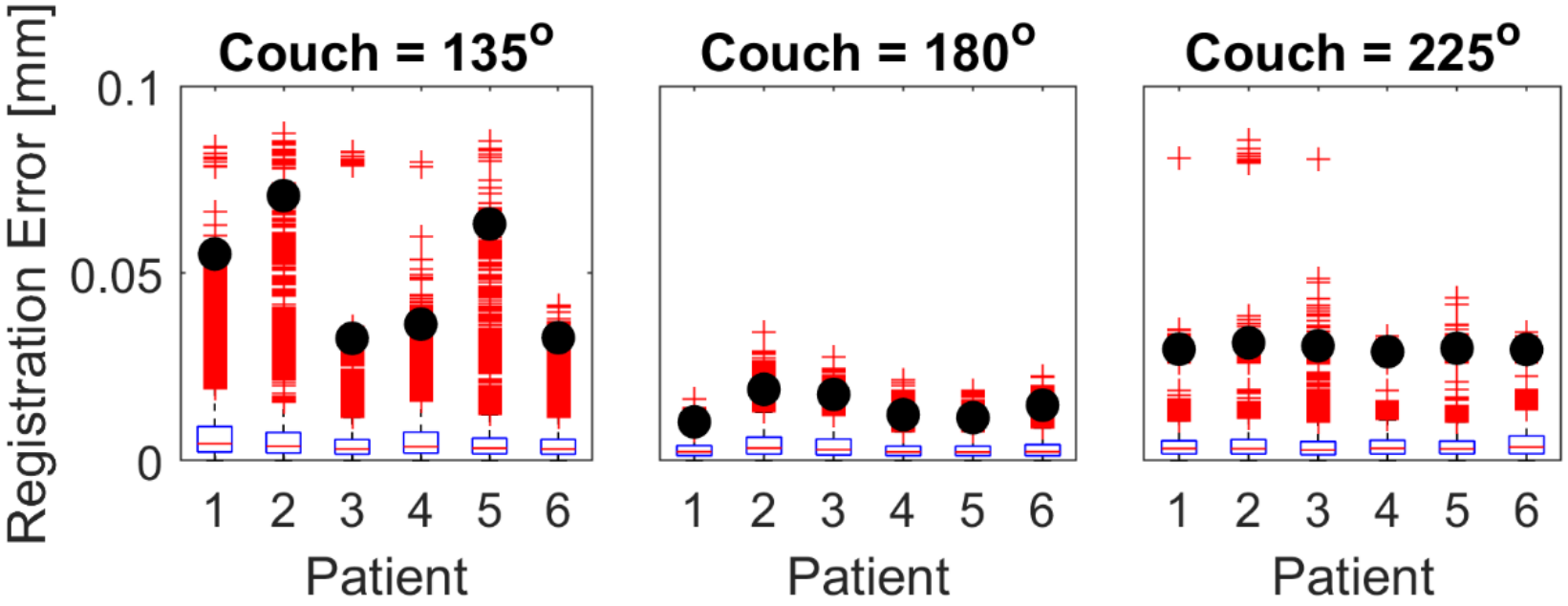

Figure 41: Registration errors detected across all gantry angles (179.9 – 355° for couch = 135°, 180.1 –5° for couch = 225° and 180.1– 175° for couch = 180°; IEC coordinates) and all simulated shifts on a +/- 2.5 mm grid with respect to the beams-eye-view for six clinical cases. Red plus signs indicate outliers which represent the top twenty-five percentile of registrations errors detected, and the black circles represent the 99th percentile registration error detected.

5.6. DISCUSSION

This study investigates the complex relationship that exists between imaging aperture size and location, patient dose and image registration accuracy. Larger aperture plans (ANA_{60}) were shown to maintain sub-mm registration errors while smaller apertures were not always able to do so (ANA_{80}). However, given the fact the imaging phantom utilized in this study represented the lower end of the HU range encountered in the skull, clinical images of a real skulls may provide improved contrast that could improve registration results, particularly for smaller ROI apertures. Several studies have identified the dose-reduction possibilities of volume-of-interest (VOI) kV-CBCT,[266] MV-CBCT. Robar *et al*. demonstrated a 39% reduction in dose when reducing the field size from 25 x 25 cm^2 to a 4 x 4 cm^2 withing a VOI when imaging with a 2.35 MV beam generated with a carbon target.[267,268] The findings of maximum dose reduction seen within this study were comparable, with a 34% dose reduction with a 2.5 MV beam when comparing a 22 x 22 cm^2 imaging plan with a 70% thresholded aperture plan with an average aperture size of 19.6 cm^2. Dose reduction when using a thresholded plan varies on a control-point-specific bases due to the varying size of the aperture for each respective BEV. Ding and Munro have shown that the D_{50} is ~0.8 cGy for a single 40 x 40 cm^2 image with the 2.5 MV Varian imaging beam (3.0 MU per image).[264] Extrapolating the average dose-reduction possibilities presented from the MC analysis in this work, using an ANA_{60} image would incur ~0.07 cGy D_{50} for the entire skull; and therefore ~10.10 cGy for a full imaging plan (images every 5 degrees, 72 control points for axial arc, 38 controls per non-coplanar arc). While this imaging dose is small compared to therapeutic dose in typical cranial SRS plans

which would be 1500-2400 cGy for brain metastases,[272] or 4778-8500 cGy for TN;[273] sensitive structures with strict dose tolerances may necessitate a reduction in imaging frequency. In a clinical setting this could be realized by imaging at a reduced frequency (*i.e.* every 20-degrees, or image every 500 MU, which would force more control points in sub-arcs with high dose delivery). An additional dose-reduction strategy could also include the reduction of monitor units delivered per image, though this would be accompanied by an increase in image noise. An investigation by Borsavage and colleagues found a 10-18% reduction in CNR between cortical bone and soft tissue when reducing the imaging dose from two to one cGy with a 2.5 MV beam.[128]

The use of a single planar 2D image for 3D-repositioning has the potential to incur positional errors along beamline due to the nature of the trigonometric approach for calculating couch positions from detected 2D shifts. It has been shown in several works that the majority of motions within a thermoplastic mask do not exceed 2.5 mm along any given dimension.[137,158,163,274,275] Considering extreme positional errors of 3 mm along beamline would only result in dose errors of approximately 0.60% based on inverse square changes. The main motivation for implementing the methodology proposed in this work is to minimize dosimetric errors that can occur in-plane for a given BEV. As shown in previous work in the context of treating with virtual cones, a 1.0 mm linear drift of a 4-mm-sized target along each direction can lead to an 11 % reduction of the volume receiving the prescription dose, and a 39% increase in the dose received by the healthy tissue immediately adjacent to the target.[240] A more complex 2D-3D registration could be utilized with MV/kV imaging as was proposed by Fu and Kuduvalli to better account for beam

direction position error.[276] When utilizing this method to image a head-and-neck phantom in 49 different simulated positions (within ± 20 mm and ± 5° along each orthogonal dimension), they found a mean 3D-registration error of 0.33 mm. While a WL test on a linac is usually implemented to validate a sub-mm isocentre volume,[9] the reported value is always smaller than the maximum deviation encountered in the analysis and it only represents a very small sampling of a very large parameter space (i.e. all possible couch/gantry combinations).

Rotational errors were not explicitly addressed in the methodology proposed in this work as separating translation and/or rotational components from single planar images is inherently difficult due to the coupling of rotational and translational information, except for limiting cases where rotations are orthogonal to the imaging plane (e.g, perceived yaw-rotations for an anterior-posterior MV image). Even with 2D-3D imaging, there exists a complex coupling of translations and rotations which was explored for 2D-3D MV imaging by Jans *et al*.[25] The methodology presented in this work may not be well-suited to accurately quantify complex rotational motions, however, it is well-suited for identifying discrepancies between BEV DRRs and intra-treatment images. As such, in addition to permitting the online correction of small positional errors, this methodology could also be utilized to detect positional discrepancies that exceed a user-defined threshold and trigger a treatment interruption to permit a more robust patient repositioning procedure. (e.g, CBCT or stereoscopic imaging).

A method such as the one outlined here has the potential to correct for positional errors that can go otherwise undetected during treatment delivery. However, for large

couch-angles imaging would be impossible due to collision of the gantry with the couch and/or patient. For example, when imaging a head and thoracic cavity phantom with the couch at 90 degrees, we found that imaging was possible for gantry angles from 180 to 200 degrees, and 340 to 15 degrees (Varian IEC coordinates). Safe operation of a linac necessitates the avoidance of a collision between the patient and the linac during the motion of its mechanical axes, and thus, these regions should be quantified. Northway *et al*. explored this concept by mapping patient-specific image sets to a library of body contours which were placed on the bed of a virtual linac model. With this model, collisions zones were mapped out for non-coplanar SBRT.[277] This approach could be extended to include a model of the imaging panel. Treatment plans could then be designed to avoid these regions, or at least inform the treatment team of the control points at which position verification imaging would not be possible. Implementing an imaging protocol as depicted in this investigation would benefit significantly from an efficiency point of view from a fast-switching target similar to the work explored by Berbeco *et al*.[278] and Yewondwossen *et al.*[279]

5.7. CONCLUSION

This investigation has demonstrated the capability of ROI control-point-specific MV imaging to detect and correct for intrafraction motion observed during cranial SRS therapies. The use of ROI MV-imaging has been shown to reduce the accrued imaging dose while balancing the proportion of visible anatomy needed to detect and correct for motions observed from a BEV. Although the method was based on a single skull, we have

demonstrated that the approach is generalizable. Compared to an open-field, aperture specific corrections can reduce imaging dose by up to 83% with a three-arc plan. For a 1.5 mm linear drift in phantom motion along each direction, 60% threshold design demonstrated a mean registration error of 0.56 ± 0. 33 mm. This is the first work that we are aware of to present a method for the construction of small, robust imaging apertures that balances the objectives of accurate intrafraction position detection and dose minimization.

CHAPTER 6. MANUSCRIPT 3: EVALUATION OF PLAN QUALITY AND TREATMENT EFFICIENCY IN VIRTUAL ISOCENTRE CRANIAL SRS TREATMENT PLANS

6.1 PROLOGUE

This manuscript establishes another methodology to minimize the dosimetric impact of motion established in Chapter 4. The ability to implement dynamic motions of the axes of a Varian TrueBeam™ linac during delivery in Developer mode have allowed for the exploration of trajectory radiotherapy,[229] a technique currently not implemented clinically. One such embodiment of trajectory radiotherapy is the movement of the treatment couch during delivery, in which the patient will be brought closer to the head of the linac, shortening the effective treatment distance. The impetus for such motions is the possible increase in treatment efficiency by means of reductions of monitor units via inverse square gains. This paper explores various aspects of trajectory radiotherapy when treating at a shortened, virtual isocentre. With clinical feasibility being a mandatory feature of the technique, the methodology takes previously delivered plans and converts them into a delivery at a shortened isocentre. Plan quality analysis is completed for a cohort of patients and a subset of these plans are delivered on a Varian TrueBeam™ STx linac to an anthropomorphic head phantom for dose verification and deliverability validation.

This work has been submitted to the Journal of Medical Physics and is currently under review:

"Church C, MacDonald R.L Parsons D, Syme A. *Evaluation of plan quality and treatment efficiency in virtual isocentre cranial SRS treatment plans*."

6.2 ABSTRACT

Introduction: Radiotherapy deliveries with dynamic couch motions that shorten the source-to-axis distance (SAD) relative to deliveries at a standard isocentre on a C-arm linac have the potential to increase treatment efficiency through the increase of the effective dose rate. In this investigation we convert clinically deliverable VMAT and DCA plans for cranial radiosurgery into virtual isocentre plans through implementation of couch trajectories that maintain the target at a shortened SAD throughout treatment.

Materials and Methods: A randomly sampled population of patients treated with cranial radiosurgery from within the last three years were separated into groups with one, two, and three lesions. All plans had a single isocentre (regardless of the number of targets), and a single prescription dose. Patient treatment plans were converted from their original delivery at a standard isocentre to a dynamic virtual isocentre in MATLAB (R2020b, The Mathworks, Inc. Natick, MA). The virtual isocentre plan featured a variable isocentre position based upon the closest achievable source-to-target distance (referred to herein as a virtual source-to-axis distance - vSAD) which avoided collision zones on a TrueBeam STx platform (Varian Medical Systems, Inc., Palo Alto, CA, USA). Apertures were magnified according to the vSAD and monitor units at a given control point were scaled based upon the inverse square law. Doses were calculated for the plans with a virtual

isocentre in the Eclipse (v13.6.23) treatment planning system (TPS) and were compared with the clinical plans. Plan metrics (MU, Paddick conformity index, gradient index, and the volume receiving 12 Gy or more), normal brain dose-volume differences, as well as maximum doses received by OARs were assessed. The values were compared between standard and virtual isocentre plans with Wilcoxon Sign Ranked Tests to determine significance. A subset of the plans were mapped to the MAX-HD anthropomorphic phantom (Standard Imaging, Middleton, WI, USA) which contained an insert housing EBT3 GafChromic™ film and a PTW 31010 microion chamber for dose verification on a linac.

Results: Delivering plans at a virtual isocentre resulted in an average reduction of 20.9% ($p = 3 \times 10^{-6}$) and 20.6% ($p = 3.0 \times 10^{-6}$) of MUs across all VMAT and all DCA plans, respectively. There was no significant change in OAR max doses received by plans delivered at a virtual isocentre. The low dose wash volume (dose level of 1.0 – 2.0 Gy or 5 – 11 % of the prescription dose) was increased (by approximately 20 cc) for plans with three lesions. Alternatively, this was equivalent to a 2.7 – 3.8% volumetric increase in normal tissue receiving the respective dose level when comparing the plan with a virtual isocentre to a plan with a standard isocentre. Gamma pass rates were 96.40% ± 2.90% and 95.07% ± 3.10% for deliveries at standard and virtual isocentre, respectively. Absolute point dose agreements were within -0.36% ± 3.45% and -0.55% ± 3.39% for deliveries at a standard and virtual isocentre, respectively. Potential time savings per arc were found to have linear relationship with the monitor units delivered per arc (savings of 0.009 s/MU with an $r^2 = 0.866$ when fit to plans with a single lesion).

Conclusions: Converting clinical plans at standard isocentre to a virtual isocentre design did not show any losses to plan quality while simultaneously improving treatment efficiency through MU reductions.

6.3 INTRODUCTION

When treating intracranial lesions with SRS, care is given to ensure proper patient positioning to maintain fidelity between planned and delivered doses. It has been shown that the magnitude of translational and rotational errors can reach 3 mm and 2 degrees, respectively, during SRS therapy with a thermoplastic immobilization system.[29,137,144,158,162,163,167,275] While intra-arc errors are much smaller (mean of 1 mm), it has been shown that larger positional errors can be seen with increasing treatment times.[137] In general, treatment times increase with increased prescription dose, use of heavily modulated treatment beams and, in the case of multiple metastases, treating single (or a small number of) lesions at a time.[116,172,280-282] Use of single isocentre treatments for multiple targets has been shown to significantly improve treatment efficiency; in a study by Nath *et al*., where 26 patients with a median of five lesions were treated with a single-isocentre using a Varian Trilogy Linac (dose rate of 1000 MU per minute), the median beam on times were 21.0 minutes (maximum time of 38.9 minutes).[116] Similar efficiencies were observed when treating with a Varian 21EX at 600 MU/min by Hardcastle *et al*., where median beam-on time was 15.0 minutes per isocentre, regardless of the number of lesions.[283] A trade off with this efficiency gain is the magnification of positioning error that

results from patient rotations.[171] This further suggests that maximizing treatment efficiency is an important objective of cranial SRS.

The requirement for efficient, highly conformal treatments has been recognized by the manufacturers of medical linear accelerators. Advancements include the introduction of FFF treatment beams to increase treatment dose rates, and reduction in MLC leaf widths to improve beam shaping. Additional drivers of efficiency arise from treatment planning. Algorithmic advancements in DCA treatments (e.g. MBSRS; Brainlab AG, Munich, Germany) leverage the MU reductions that result from the reduction of aperture modulation.[284] Others have modified the DCA method to permit binary collimation of targets to facilitate the concurrent treatment of targets with variable prescriptions doses.[285]

The concept of dynamic radiotherapy was developed in the 1980s.[286,287] Podgorsak *et al.* first studied the properties of this treatment type in 10 patient plans where dynamic rotation of the couch and gantry were delivered.[287] Dosimetric validation at the time was limited by experimental comparison with empirical calculations using several correction factors (for transmission through the frame and disagreement of doses measured between deliveries with or without dynamic rotation). Several modern studies have explored dosimetric and positional accuracy while implementing couch and gantry rotations during delivery. Rodrigues *et al*. found dose agreement with calculated doses to be within ±2% when treating targets with dynamic motions of the couch and gantry with electron arc therapy.[288] Similarly, Wilson *et al*. found agreement with dosimetric error of 1.1 ± 0.6% for delivered dose with an ion chamber and gamma pass rates of 96% greater evaluated with 2%/2mm.[289] Quality control procedures were devised by Yu *et al.* to assess positional

and dosimetric accuracy when dynamically moving the axes of a linac (MLC, couch rotation, couch translation, MLC movement) and found the translation accuracy of the couch to be 0.01 cm, rotational accuracy of the couch to be 0.3°, and dosimetric deviations to be less than 3%.[290] A Winston Lutz (WL) test assesses comparable information for standard isocentric deliveries; this suggests a more robust version of the WL test could be used for quality assurance testing, similar to the embodiment of the WL test for trajectory radiotherapy at shortened virtual isocentre demonstrated by Parsons *et al*.[269]

Recent work in the area of 4π radiotherapy has demonstrated the potential benefits of dynamic trajectories in radiotherapy (treatment deliveries in which the couch, gantry and collimator engage in continuous motion while the beam is on). The benefits include both a reduction in normal tissue doses as well as increases in monitor unit efficiency.[291-295] In one clinical trial with 4π-radiotherapy, treatment-time tolerability for N = 11 cases was found to be tolerable (8.625 ± 2.64 out of 10) and was found to not cause nausea.[290] To date, most of this research has focused on treatments delivered at the nominal isocentre of the treatment unit (i.e. conventional SAD treatments), however, the same capabilities that permit intra-treatment rotations of the couch also permit dynamic translations of the couch for the purpose of reducing the source-to-target distance. In this work we define the concept of a virtual isocentre. Whereas in conventional radiotherapy the term isocentre refers to a fixed point in space around which all mechanical axes rotate, herein, a virtual isocentre refers to a fixed point in the patient's anatomy (often the centre of mass of the target) through which the central axis of the radiation field passes, regardless of the position of any mechanical axis of the linear accelerator. In the context of the current work, the

difference between a conventional and virtual isocentre is driven by the use of a continuously varying source to target distance, herein referred to as a virtual source to axis distance, or vSAD. The vSAD technique offers a reduction in projected leaf width at virtual isocentre (proportional to the reduction in vSAD compared to the nominal SAD) and an inverse square-driven increase in dose rate at the target (which translates into a reduction in monitor units). Additionally, reducing the necessary monitor units to deliver a prescription dose has the potential benefit of reducing peripheral dose in patients owed to scatter as these have been shown to be 2 to 15 times higher in modulated plans which require a large number of monitor units (2 to 5 times the number of monitor units when compared with conformal treatment plans).[296]

An investigation by Mullins *et al*. explored the impact of using a vSAD treatment (with a fixed vSAD of 80 cm) on dose and plan quality metrics using a published treatment trajectory involving concurrent couch and gantry rotation.[287,289] They found a similar plan quality for vSAD deliveries when comparing isodoses, DVH as well as plan quality metrics. Additionally, they found a significant reduction in MUs ($p \leq 0.05$) for vSAD deliveries. In that work the authors required a fixed vSAD of 80 cm despite the fact that some control points of their trajectory could not achieve that vSAD due to collisions between the gantry and the patient or couch. The selected trajectory does not sample the 4π space as widely as some other SRS arc templates.[297] Furthermore, the study was restricted to single targets.

The current work introduces a variation on the vSAD concept by translating pre-existing clinical SRS plans to a shortened vSAD design. At each control point the vSAD

was chosen to bring the target as close to the accelerator exit window as possible without risking collision. Both VMAT and DCA plans were evaluated. Plans with up to three targets treated with a single isocentre were included in the study and a subset of the VMAT plans were delivered on a linac for dose verification. Our hypothesis was that treatment plans would be non-inferior to standard SAD plans with respect to dose metrics while producing a significant reduction in monitor units required to deliver the treatment.

6.4 MATERIALS AND METHODS

In this study VMAT and DCA plans were converted from a delivery at a standard SAD to a delivery at a dynamic vSAD. Fitting the complex apertures created with VMAT plans at virtual isocentre was limited by the geometric constraints of the projected leaf width. In particular, the inability to perfectly account for aperture magnification in the direction perpendicular to leaf travel placed a fundamental limitation on the accuracy with which the standard SAD apertures could be reproduced in the vSAD configuration. Therefore, plans with conformal apertures served as a control for assessing the fitting of apertures at a virtual isocentre as they were not subject to the same limitations for fitting.

6.4.1 Patient Selection

Twenty-eight previously treated cranial SRS patients were included in this study. Treatments were mono-isocentric and the number of targets ranged from 1 – 3. For this study, all patients received single fraction treatments, and in each plan, all targets received

the same prescription dose. Details of the patient cohort are presented in Table 7. The TPS used for plan creation was Eclipse (v13.6.23) with the Progressive Resolution Optimizer (v13.6.23) used for VMAT plan generation. Doses were calculated with the Analytic Anisotropic Algorithm (AAA; v13.6.23) and Acuros XB Advanced Dose Calculation algorithm (AXB; v15.6) with a 6X-FFF beam on a Varian TrueBeam STx platform (Varian Medical Systems Inc. Palo, Alto, CA) with an HDMLC120. Doses were calculated with a dose grid resolution size of 0.15 cm.

Table 7: Description of patient cohort used for retrospective planning.

Number of Mets	Number of Patients	Number of Arcs	D_{Rx} (cGy)	PTV Size [cc]
1	13	3 - 4	1800 - 2000	0.73 – 14.69
2	11	3 - 4	1800 - 2000	0.39 – 5.79
3	4	3 - 4	1800 - 2000	0.12– 5.98

6.4.2. Conventional SAD Planning

Patients described in section II.A were treated with VMAT plans using an arc template based on a previously-published study.[297] In some patients, one of the oblique arcs was dropped if treating a lateralized lesion. In a few cases, deviations from the couch angles prescribed in the published template were included to help avoid critical structures

in the brain. A full description of the plan geometries and characteristics is presented in the supplemental data. All VMAT plans were created by a certified Medical Physicist.

DCA plans were created by utilizing the same arc geometry (couch angles and gantry span) as the VMAT plans. Plan-specific collimator angles were chosen for patients with multiple lesions to avoid MLC-bridging between the conformal apertures created for individual targets. MLC fitting was performed with variable MLC margins (asymmetric margins and negative margins) to minimize discrepancies between the DVH of plans with multiple targets (e.g, over-coverage of one or more targets). Additionally, beam weightings were manually adjusted to reduce excessive hotspots. Across all clinical VMAT plans, no lesions had a volumetric coverage of less than 98.0% by the prescription dose. Therefore, all DCA and virtual plans were normalized to maintain a coverage constraint of 98.0% by the prescription dose.

6.4.3 Virtual Isocentre Plan Conversion

The anonymized treatment plans and structure sets were exported as a DICOM files and imported in MATLAB (R2020b, The Mathworks, Inc. Natick, MA). The control point-specific information (isocentre, gantry and couch angle) was used to convert the arc structure with N control points into N-1 individual static fields as depicted in Figure 42. The gantry angle of a given static field was taken as the mean of the two adjacent VMAT control points. Similarly, the MLC and jaw positions were linearly interpolated between the adjacent control points. Additionally, the MUs that would be continuously delivered as

the gantry rotates from one control point to the subsequent control point were delivered at the linearly interpolated control point.

The patient geometry from the original plan with a conventional SAD of 100 cm was converted to a geometry with a variable vSAD. For each control point (with a unique couch and gantry angle), the initial isocentre was shifted along the vector of the central axis to a user-defined SAD isocentre using a distance-of-closest-approach (DOCA) technique. The SAD for a given couch-gantry geometry was determined from a look-up-table which contained the DOCA for couch-gantry pairings in couch angle increments of 45^{o}, and gantry-angle increments of 5^{o}; these values were individually tested on a TrueBeam STx platform, incrementally decreasing the SAD for a given couch-gantry pairing until the collision-detection system was flagged, and then adding a safety buffer of two centimetres. The control point-specific SAD choices for the patient depicted in Figure 42 are shown in Figure 43 where the smallest SAD was limited to 80 cm (at some control-points, an SAD of 73 cm was possible) due to a beam calculation restriction in Eclipse that required a minimum source-to-surface distance (SSD) of approximately 57 cm. MUs were calculated at each control point based upon inverse-square scaling.

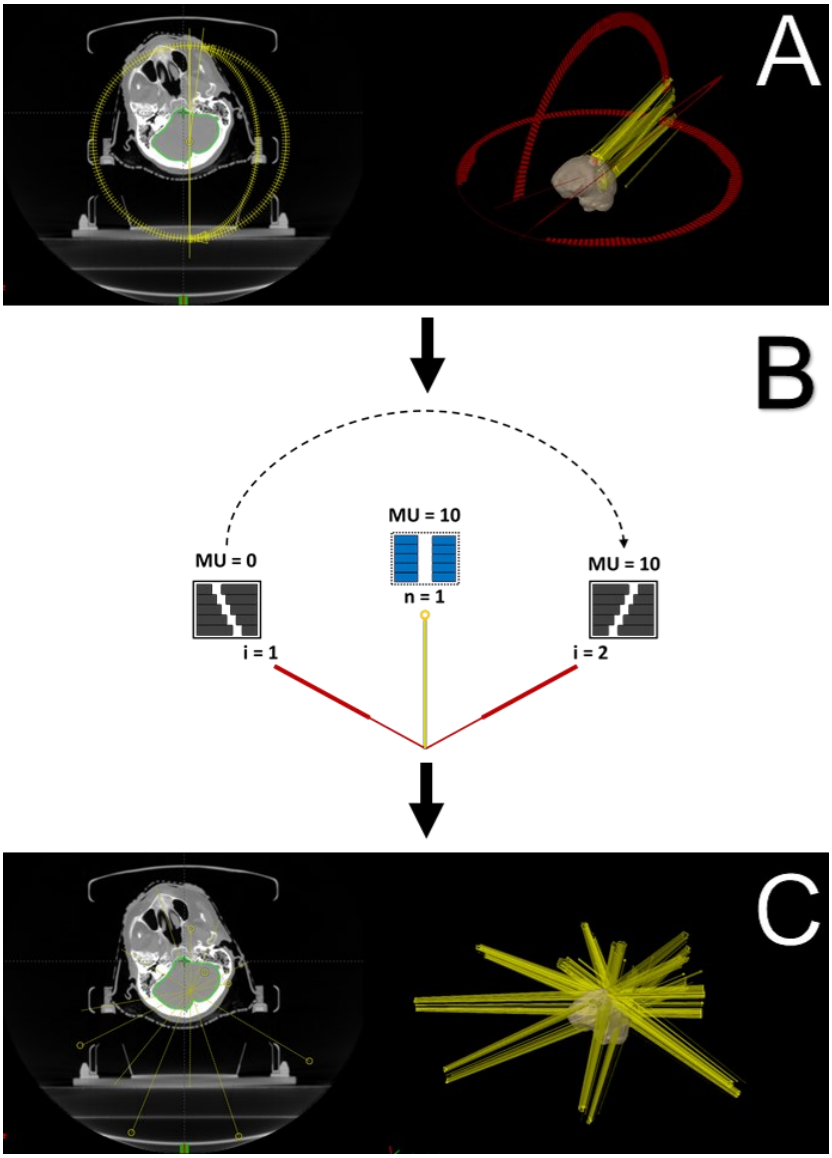

Figure 42: In (A), an axial view of a patient's CT along with a 3D rendering of the VMAT treatment arcs with the patients' structure set in the Eclipse treatment planning system (v13.6.23) is shown. (B) Is a demonstration of interpolating an arc geometry (red lines) with N control points into a static field (yellow line) between adjacent control points. MLC interpolation for static fields (blue MLCs) is achieved by averaging the leaf position across adjacent control points in the arc structure (grey MLCs). Similarly, monitor units that were delivered across adjacent control points during gantry rotation in the arc structure were forced to be all delivered at singular control points in the static field structure. A rendering of same VMAT plan converted to a series of static fields with a variable isocentre (depicted by the changing positions of the yellow circle in the axial view) for delivery at a distance of closest approach is shown in (C). Only a few control points are displayed for clarity purposes.

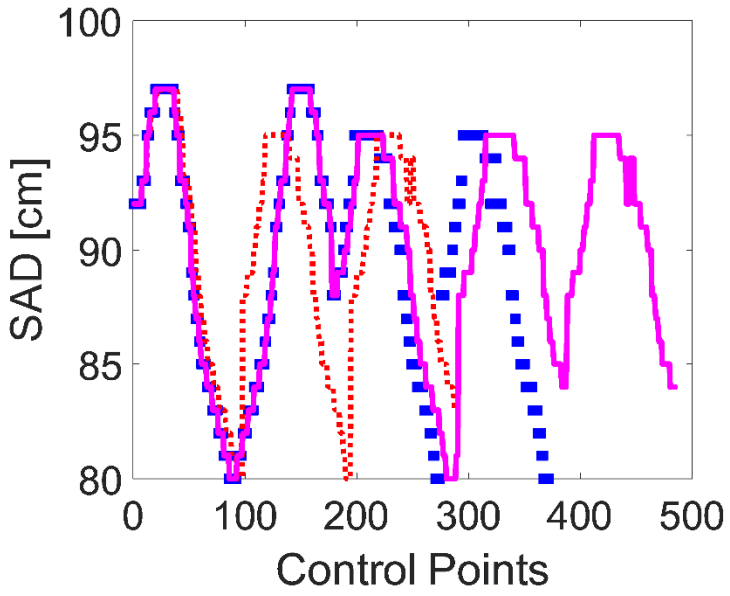

Figure 43: The control point-specific source-to-axis-distance for the patient depicted in Figure 42B (blue-squares) as well as two other patients in the study.

As mentioned above, the MLC/jaw positions were interpolated for each control point (in the virtual isocentre plan) at the midpoint between adjacent control points of the original plan. To project the aperture created by the MLCs at a standard SAD to a vSAD, a binary mask of the aperture (based upon physical MLC positions) was created and then magnified (according to the specific vSAD). The middle of the MLCs was then fit to the magnified mask based upon the physical size of the leaves at the virtual isocentre. The fitting of the aperture in Figure 44A at a virtual isocentre is shown in Figure 44B where yellow markers indicated differences in fitting outcomes due to the discretization of leaf widths owed to geometric minification.

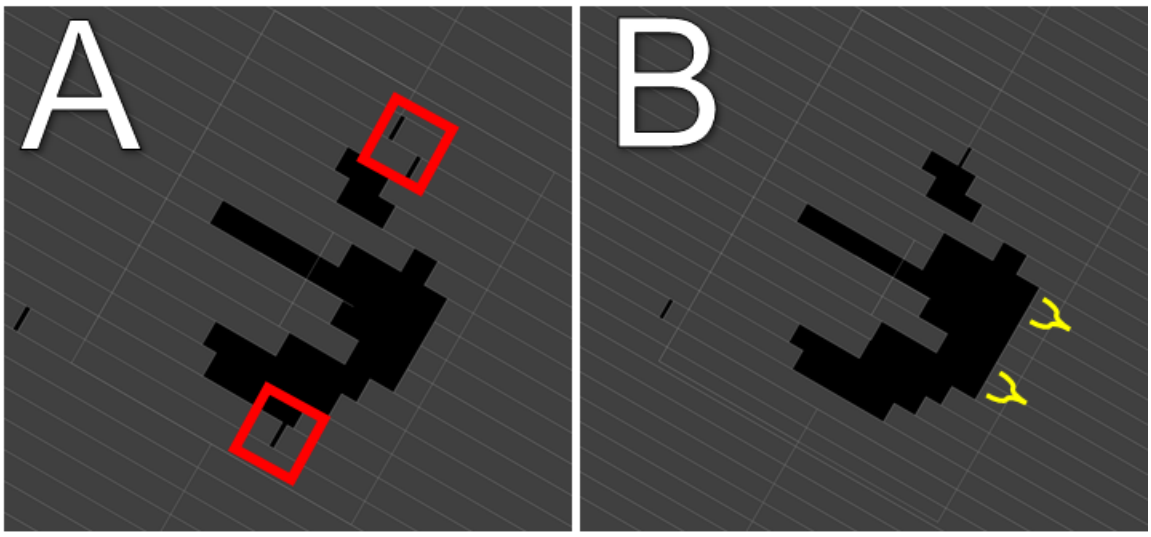

Figure 44: (A) MLC aperture at a standard isocentre where red squares highlight beamlets which are effectively abutting (< 0.2 mm gap) and were closed for fitting the MLCs at a virtual isocentre. (B) Depicts the MLCs aperture created by fitting the MLC bank in (A) at a virtual isocentre where yellow lines highlight differences in fitting as a result of discretization of leaf widths at a virtual isocentre.

6.4.4 Dose Analysis

Virtual isocentre plans were imported back into Eclipse and dose was calculated with the same dose grid resolution as the original plan (0.15 cm). Dose was calculated with preset values (inverse square-scaled MUs described in Section 6.4.3). Following calculation, plans were normalized such that 98% of the PTV was covered by the prescription dose. When multiple targets were being treated, the normalization ensured that 98% of the coldest target was covered by the prescription dose.

Plan quality metrics in this analysis included conformity and dose fall-off. For each PTV, the $CI_{Paddick}$[252] was calculated according to equation ((43):

$$CI_{Paddick} = \frac{TV_{PV}^2}{TV * PV} \quad \textbf{(43)}$$

Where TV_{PV} is the volume of the target covered by the prescription dose, TV is the target volume, and PV is the prescription isodose volume. Perfect coverage of the PTV by the prescription dose would result in a conformity index of unity, whereas over-coverage or under-coverage would take on values less than one. Additionally, a dose gradient metric[252] was calculated according to equation (41). When dose bridging between targets at the 50% isodose level was present for plans with multiple targets this metric was not calculated.

DVHs were calculated in Eclipse for all PTVs as well as OARs: lenses, eyes, optic nerves, optic chiasm, hippocampi, brain stem, and normal brain (brain – PTVs). These DVHs were exported from Eclipse and imported in MATLAB for analysis. For each OAR and PTV, the D_{max} was calculated from the DVH and defined as the minimum dose received by the hottest 0.1 cc of the volume. For normal brain tissue, the V_{12Gy} was quantified.

6.4.4.1 Statistical Analysis

Plan comparison analysis was grouped by treatment type (VMAT at standard SAD to VMAT at vSAD; or DCA at standard SAD to DCA at vSAD) and by target number (1, 2 or 3 targets). For each subset of plans, the plan quality metrics (MUs, V_{12Gy}, CI, GI) as well as the OAR dose metric (D_{max}) were compared with a Wilcoxon sign-ranked test. A

threshold for statistical significance was set at $p < 0.0036$ (0.05 / 14) based on a Bonferroni correction to account for multiple hypothesis testing (n = 14).

6.4.5 Fitting at a Virtual Isocentre

The choice to use a DOCA for the vSAD in the studied plans was driven primarily by the prospect of efficiency gains through significant reductions in MUs. However, the optimal vSAD with respect to MLC-target conformity may involve a more nuanced consideration of the magnified target projection and the relationship between target boundary and leaf boundaries in the direction perpendicular to leaf-travel. This complex relationship is illustrated in Figure 45 where a target has been conformally fit by the centre of the MLC leaves at three different vSADs. In Figure 45A, the projected size of the target at some vSAD intersects with the centre of the MLC leaves, causing two pairs of leaves to open leading to an increase in the normal tissue being exposed in the region of these leaf pairs. In Figure 45B, at a larger vSAD (the projected target size would appear smaller), the boundary of the target does not intersect with the centre of the MLC leaves causing the same leaf pairs to stay closed and occlude the target. To study this behaviour, we compared the fitting of a synthetic spherical target ranging from a 0.2 to 2.0 cm radius in MATLAB at a virtual isocentre ranging from 80 to 100 cm SAD. The targets were conformally fitted with the MLCs based upon the intersection of the centre of the leaves with the perimeter of the target with two different procedures: 1) The physical size of the target was magnified for a given vSAD and fit with the physical size of the MLC leaves based upon their

geometric minification at the vSAD. 2) The MLC leaves were used to fit to the target at 100 cm, and the mask for the aperture created by this fitting was then projected to a virtual isocentre (based upon geometric magnification) and the magnified mask was then fit by the physical size of the MLC leaves at the respective vSAD based on geometric minification. The second procedure is akin to what was implemented for the fitting of the aperture utilized in the patient study. For the VMAT cases this approach was followed because the aperture at each control point was determined through inverse optimization and matching this aperture as closely as possible was the objective. Either approach could have been implemented for the DCA plans, but for consistency we used method 2. For both procedures, geometric coverage metrics in the form of: 1) the normal tissue area present in the projection of the aperture was quantified and compared to the normal tissue present at 100 cm SAD. 2) The occlusion of the target by the MLC leaf corners was quantified and compared with the target occlusion by the fitting of the target at 100 cm SAD.

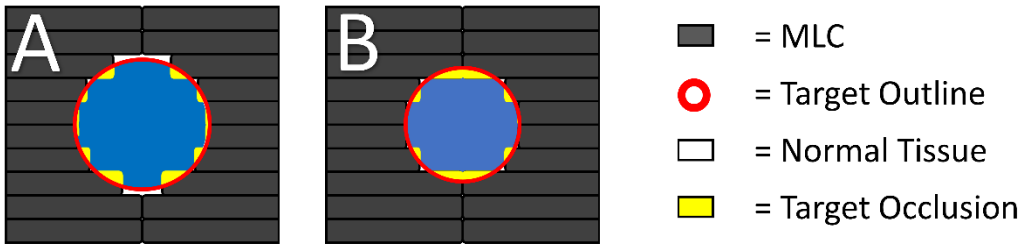

Figure 45: Demonstration of coverage when fitting the MLCs to a fixed physical target size. In (A), the target is located at a shorter vSAD than in (B) making the projection of the target (relative to the MLC) appear larger. White space depicts normal tissue that is not being shielded by the collimation aperture and yellow space depicts the projection of the target being occluded by the aperture.

6.4.6 Deliverability

To verify deliverability at a virtual isocentre, a subset of patients from this study (one met, n = 6, two mets, n = 2) were selected and their VMAT plans were mapped to an SRS anthropomorphic head phantom. The plans were converted from a DICOM structure to XML structure for delivery on a Varian STx linac in Developer Mode. For each patient, the original plan at a standard SAD was also delivered. To setup the phantom, a pre-treatment CBCT was used to align the head phantom. The phantom was aligned with couch translations and rotations (yaw) derived from image registration at the console. For cases with multiple lesions, the couch was translated at the beginning of treatment such that high dose region of one lesion fell on the measurement apparatus.

6.4.6.1 Dose Validation

For the subset of the patients mentioned above in Section 6.4.6, dose distributions were measured with EBT3 GafChromic™ film. MUs in the plans were reduced by half to avoid film saturation. After delivery, films were sealed in a dark envelope for twelve hours prior to scanning. Films were scanned with the EPSON EXPRESSION 10,000 XL using a 48-bit colour depth at 72 dpi. Five pre-scans were performed to heat up the bulb in the scanner and then films were scanned at the same spatial location on the scanner bed with an alignment template. Films scans were converted to dose distributions with the triple-channel film dosimetry outlined by Mayer *et al*.[236] and filtered using a median filter in a 5

x 5 pixel neighbourhood. Film doses were registered to the film-plane in the calculated dose distribution using Mattes Mutual Information in MATLAB. A 2D-3D gamma analysis[238] was calculated between the film dose and the calculated dose using dose difference and distance to agreement criteria of 5% and 1 mm respectively. Gamma values were suppressed for doses less than 10% of the maximum dose measured.

Absolute dose verification was measured with a PTW Semiflex Ionization Chamber 31010 (PTW, Freidburg, Germany). Measurements were cross-calibrated at 5 x 5 cm^2 using a Exradin A12 ion chamber (Standard Imaging, Middleton, WI, USA). All measurements were converted to doses with correction factors outlined in TRS-483.[208] Polarity (P_{pol}) and Recombination (P_{ion}) correction factors outlined in TG-51[173] were measured for dose rates of 600 MU/min and 1400 MU/min for field sizes ranging from 2 x 2 cm^2 to 5 x 5 cm^2 at SADs of 100 cm, 90 cm, and 80 cm. An additional correction factor was applied specifically for the PTW Semiflex 31010 described in TRS-483 for small field dosimetry.[208] To determine the appropriate correction factors for each plan, the effective field size was calculated for each control point similar to Wolfs *et al.*[298]:

$$EFS = \frac{2 * L * W}{L + W} \quad \textbf{(44)}$$

where L is the length of the field, determined from the participating leaves in the field, and W is the average width of the beamlet shaped by the MLC openings. Additionally, the dose rate was calculated between all adjacent control points in the plan. The median field size and dose rate was used to interpolate the appropriate plan-specific correction factors for conversion of measured charge with the ion chamber to dose.

6.4.6.2 XML Deliverability Analysis

For each plan, delivery timings between adjacent control points were calculated using velocity limits for XML deliveries in Varian Developer Mode. The velocity limits for the movable axes considered in this calculation are shown in Table 1. Timings were calculated for the original plans at a standard SAD and for plans at a vSAD. The time-limiting axis, including each MLC leaf, was calculated for each control point. The time accrued between arcs was discounted as this would be shared between a delivery at a standard and virtual isocentre. All cases in the planning study were added for this analysis as well as a mock-case for treating TN using the same arc geometry described in Thomas *et al.*[299] A total of ten arcs were delivered for the TN case, two axial, and eight non-coplanar, with 5000 MUs being delivered for each axial arc, and 2500 MUs for all non-coplanar arcs with equal weighting delivered at each control point. A secondary analysis of the data was also performed in which the MLC leaves in the vSAD plans were not considered as potential rate limiting components. This was performed for two reasons. First, the MLC leaf positions for the vSAD plans were not optimized for this delivery technique, and second, in the standard SAD plans optimized within the planning system, the MLCs were never the rate limiting component (likely due to leaf position optimization).

6.5 RESULTS

6.5.3 Plan Metric Comparisons

For all patients outlined in Table 7, OAR max doses and plan quality metrics were calculated at a standard SAD and vSAD for two planning techniques (VMAT and DCA). The means and standard deviations of these metrics across each patient population (separated by the number of lesions in the patient) are shown in Figure 46. Figure 46A shows the reduction of monitor units when treating at virtual isocentre (indicated by VMATV and DCAV) for the two different planning techniques (VMAT and DCA). When pooling the data (all patients regardless of number of lesions), plans delivered at a virtual isocentre resulted in an average reduction of 20.9% ($p = 3 \times 10^{-6}$) and 20.6% ($p = 3 \times 10^{-6}$) in the number of MUs across all VMAT and all DCA plans, respectively. Analyzing the data on a per lesion basis showed that there was an average reduction of 21.0% ($p = 0.0002$), 20.0% ($p = 0.001$) and 21.0% ($p = 0.13$) of MUs between VMAT plans at a standard isocentre and VMAT plans at a virtual isocentre with one, two, and three lesions, respectively. There was an average reduction of 21.4% ($p = 0.0002$), 20.3% ($p = 0.001$) and 20.9% ($p = 0.125$) of MUs between DCA plans at a standard isocentre and DCA plans at a virtual isocentre with one, two and three lesions, respectively. When considering the adjusted significance threshold for multiple comparisons, only MU differences for plans with one to two lesions were statistically significant for both VMAT and DCA plan comparisons, however the trend is robust and the lack of statistical significance in other groups can be attributed to the small sample sizes.

In Figure 46B the volume receiving 12 Gy or more is shown for the different plans. There were no statistically significant differences between any of the plan comparisons (plan type or number of lesions). The Paddick conformity index is depicted in Figure 46C where there were no significant differences between plan comparisons (plan type or number of lesions) except for the comparison between the DCA plans at a virtual isocentre and those at standard isocentre with two lesions (difference in CI equal to 0.03 with $p = 0.0025$). The Gradient index is shown in Figure 46D where the was no significant difference found between any of the plan comparisons (plan type or number of lesions).

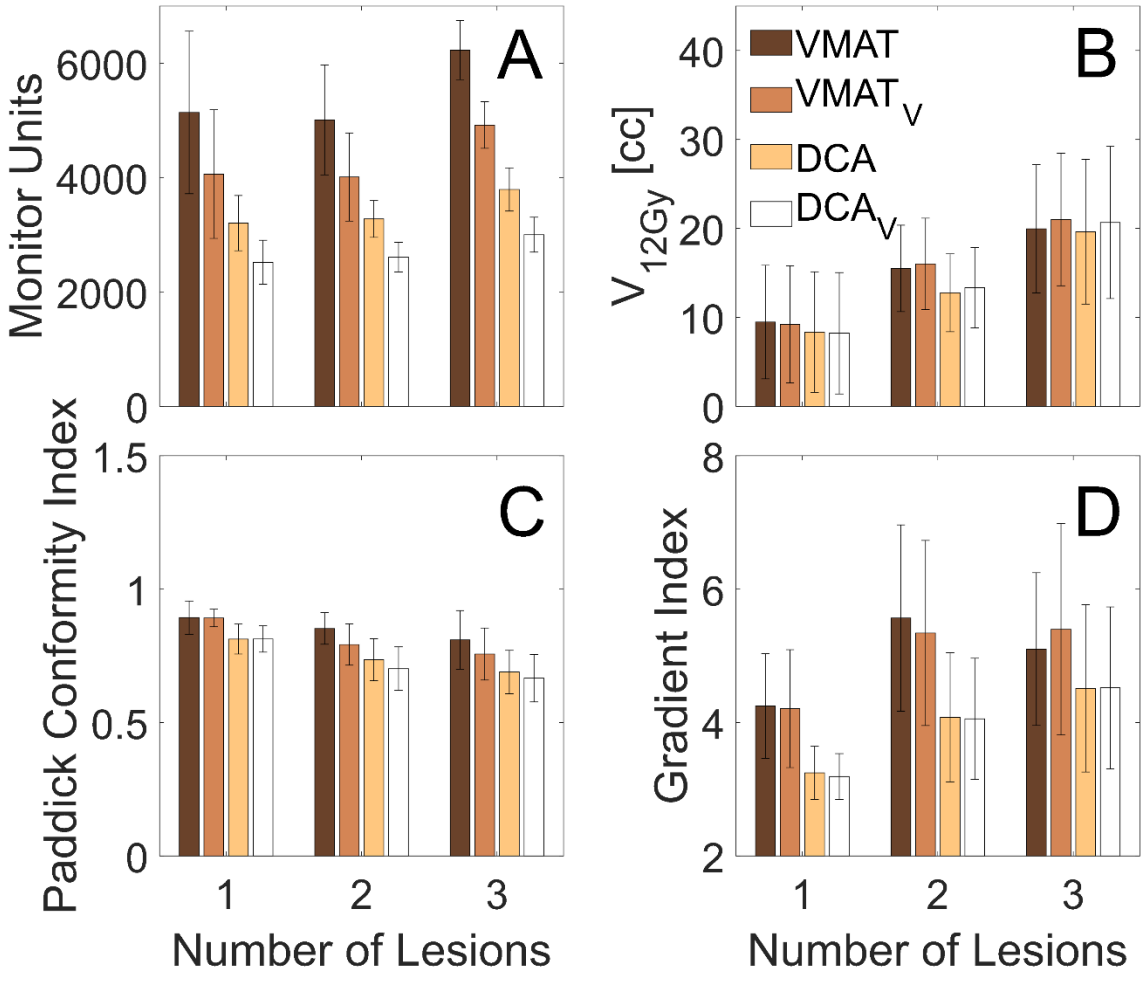

Figure 46: Mean and standard deviation of plan metrics calculated for each patient subset (one, two, three lesions) with each planning technique (VMAT or DCA) at a standard SAD and at a vSAD (e.g, VMAT$_V$, DCA$_V$). (A) Shows the total monitor units of the planning technique. (B) The volume receiving 12 Gy or more in normal brain (brain – PTV). (C) Paddick conformity index and (D) is the gradient index which have been averaged over all PTVs for plans with multiple lesions.

6.5.4 OAR Dose Differences

The mean and standard deviation of max doses received by OARs (quantified by the dose received by 0.1 cc) in the virtual plans is shown in Figure 47A The mean and

standard deviation in OAR max dose differences of the plans with a virtual isocentre with respect to a standard isocentre is shown in Figure 47B. Here a negative value indicates a smaller dose received by the OAR in the virtual plan. There was a statistically significant difference in the dose received by the right optic nerve (2.08 cGy less with vSAD, $p = 0.002$) when comparing VMAT plans with a single lesion and the dose received by the brainstem (4.52 cGy less with vSAD, $p = 0.002$) when comparing DCA plans with three lesions, though the clinical significance of such a difference is likely negligible. In general, cases with three lesions exhibited the largest differences in OAR max dose, though the clinical significance of those changes is again likely minimal.

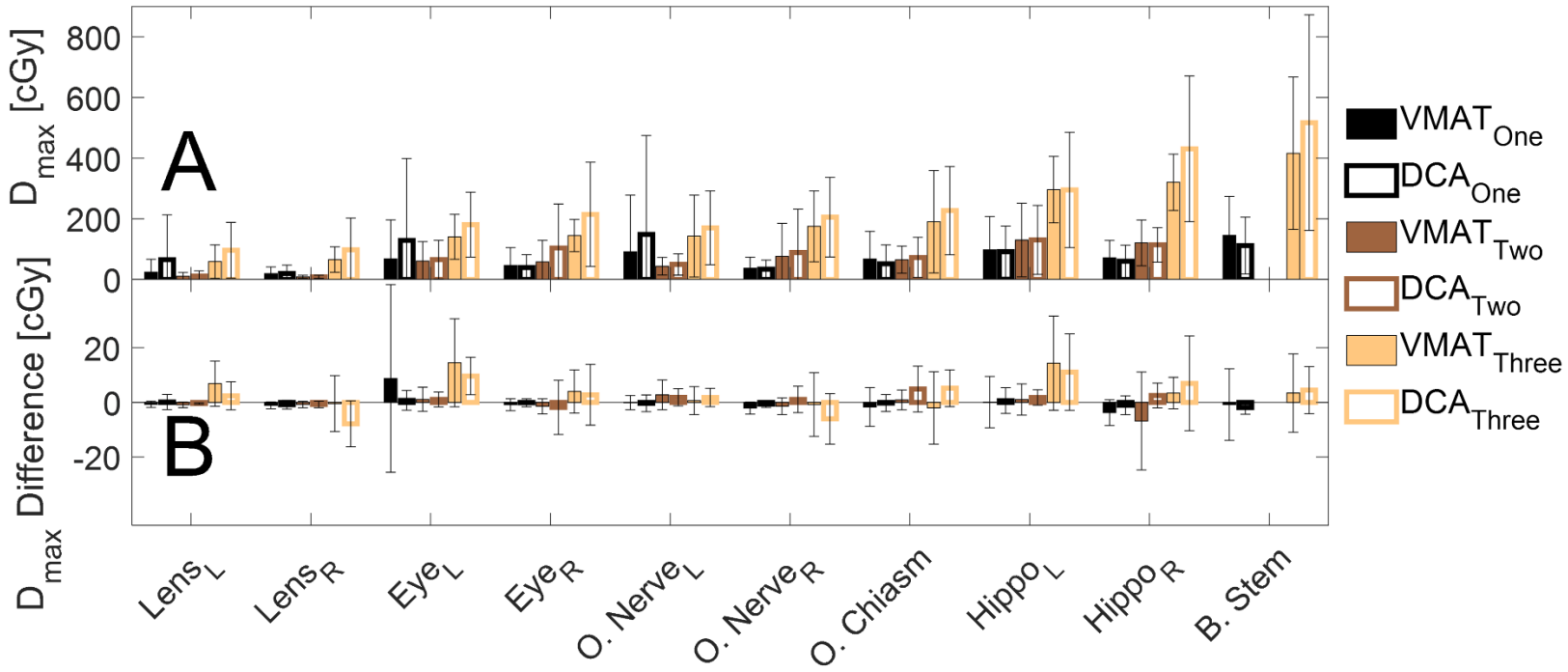

Figure 47: (A) The average and standard deviation of the maximum dose (quantified as the dose received by 0.1 cubic centimetres of the volume) received by the organs at risk (OAR) for each patient subset (one, two, three lesions) for each planning technique (VMAT or DCA) at a virtual isocentre (e.g, VMAT$_V$). (B) depicts the average and standard deviation of the maximum dose difference for OARs between the plans with a virtual isocentre and plans with standard isocentre. Positive values indicate that a larger dose was delivered by the plan with a virtual isocentre. All plans had a prescription dose in a range of 18 to 20 Gy for each target.

The DVH subtraction between virtual and standard plans for normal brain (brain subtracting PTVs) is shown in Figure 48. For context, the data points at a dose of 12 Gy are derived from the data shown in Figure 46B. When comparing plans with a single lesion, volume differences are minimal across all dose levels, but they are most pronounced at dose levels below 2.0 Gy, with a slight reduction in volume realized with the virtual isocentre plans (for both VMAT (Figure 48A) and DCA (Figure 48B)). For plans with two lesions, VMAT plans with a virtual isocentre resulted in an approximate 6.5 cubic cm (cc) increase in the volume of normal brain receiving 1.25 Gy or more, and DCA plans exhibit an approximate 10.2 cc increase in the volume of normal brain receiving 1.25 Gy or more as seen by the peak in the volume difference data. For plans with three lesions, VMAT plans at virtual isocentre exhibit an approximate 19.2 cc increase in the volume of normal brain receiving 2.16 Gy or more, and DCA plans exhibit an approximate 19.9 cc increase in the volume of normal brain receiving 1.06 Gy or more as seen by the peak in the volume difference data. The relative increase in the low dose washes for the patients with three lesions is shown as the volumetric percent difference in Figure 48C for VMAT plans and Figure 48D for DCA plans. For the same dose levels where there is a peak in the volume difference curves (2.16 Gy for VMAT and 1.06 Gy for DCA) the average volumetric percent difference is 3.8% and 2.7% for the VMAT and DCA plan comparisons, respectively.

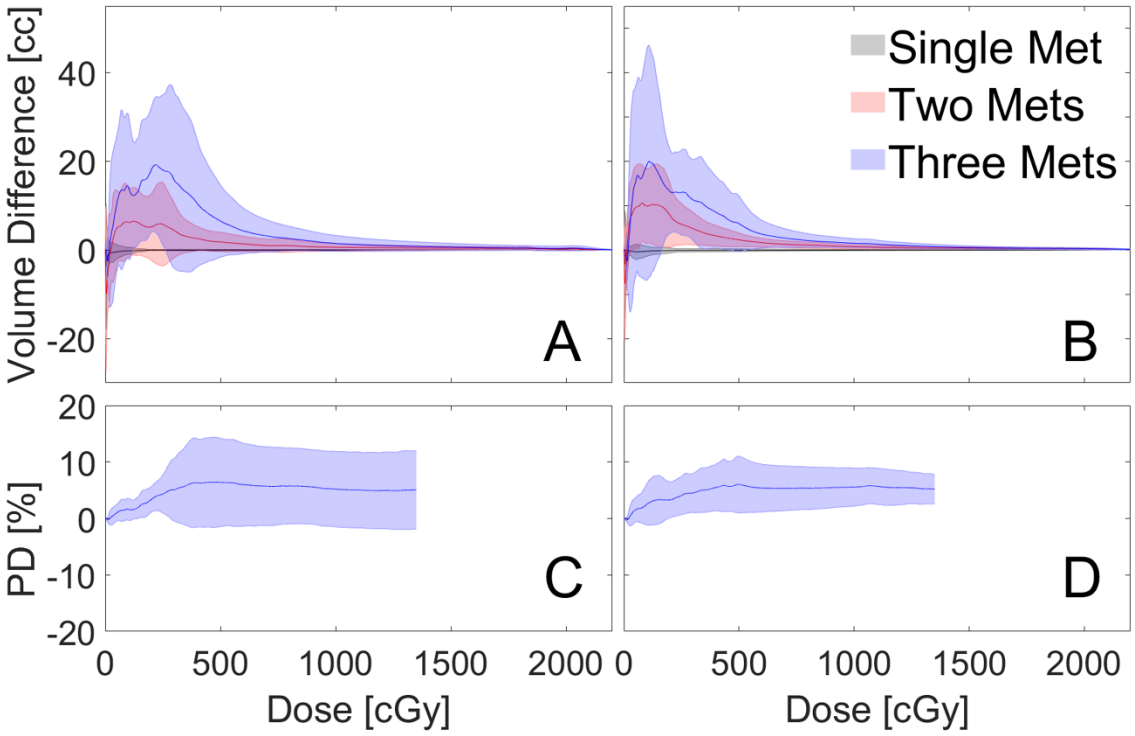

Figure 48: A subtraction of the normal brain DVH of the virtual isocentre plan (e.g., VMAT$_V$) from the DVH of the standard plan for each patient subset (one, two, three lesions). The mean is depicted by the lines and the envelope depicts the standard deviation across all patients in the set. (A) Depicts the DVH subtraction for the VMAT plans and (B) shows the DVH subtraction for the DCA plans. (C) Shows the volumetric percent difference (PD) between the VMAT plans with three lesions and (D) shows the PD for the DCA plans with three lesions. The analysis for (C) and (D) was restricted to the 13.5 Gy dose levels as volumes for larger doses are small (< 1 cc) and were not considered to be of clinical relevance.

6.5.5 Aperture at Virtual Isocentre

An assessment of MLC fitting to a synthetic spherical target at a virtual isocentre is shown in Figure 49 where geometric coverage indices (normal tissue exposed, and target occlusion) were quantitatively determined by the illustration depicted in Figure 45. In Figure 49A and Figure 49C MLC leaf fitting is performed on a spherical target which has

been magnified according to the vSAD. In Figure 49B and Figure 49D, fitting is performed on an aperture mask created by fitting the MLCs to a target at 100 cm and magnifying the aperture via geometric scaling at the vSAD. The values in each figure represent the difference in area (either exposed normal tissue or occluded target) between apertures at vSAD and apertures at standard SAD. Values less than ±0.004 cm^2 different are represented as black tiles. Values greater than zero depict more normal tissue area exposure for A) and B) and more target occlusion for C) and D) in the vSAD apertures compared to the standard SAD apertures. When fitting to a magnified target in Figure 49A, the maximum difference in area of normal tissue exposed in the aperture projection is 0.11 cm^2; while fitting the MLCs to a magnified aperture cm in Figure 49B exhibited a maximum area of normal tissues exposed in the aperture projection of 0.38 cm^2. The occlusion of the target by fitting to the geometrically magnified target is shown in Figure 49C and exhibits a maximum target occlusion of 0.13 cm^2; whereas the fitting to magnified aperture in Figure 49 exhibits a maximum occlusion of 0.36 cm^2. Qualitatively, the fitting of the geometrically magnified target appeared to exhibit an oscillatory trend of normal tissue area exposed and target occlusion with respect to varying SAD; the period of these oscillations appears to be larger for smaller targets and the amplitudes appear to be larger for larger targets.

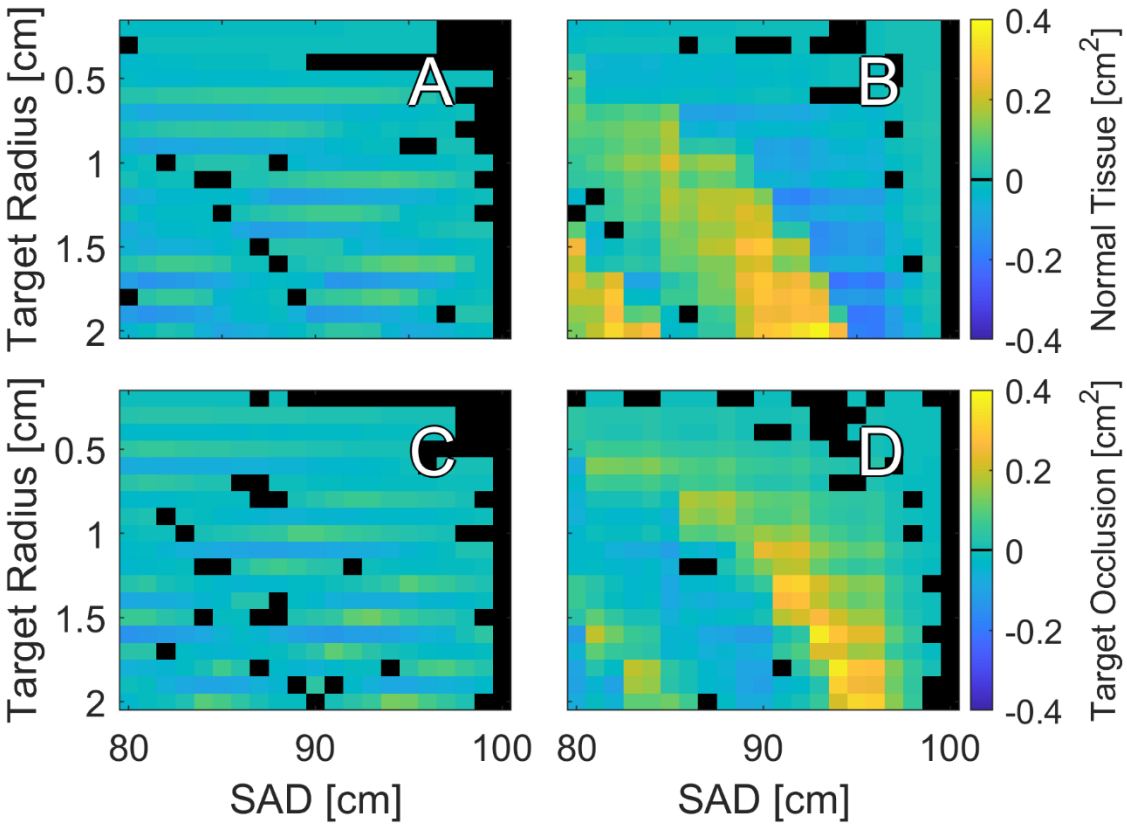

Figure 49: Geometric coverage metrics represented by difference in area between apertures at various shortened source to axis distances (SAD) and apertures at a standard SAD (100 cm). (A) and (B) shown the normal tissue exposed in the projection of the aperture at the target site. (C) and (D) shown the area of the target occluded by the MLC at the target site. (A) and (C) are a result of fitting a target that has been projected to a virtual isocentre by geometric magnification. (B) and (D) are a result of fitting the mask of an aperture fitted to a target at 100 cm SAD has been projected to a virtual isocentre and refit with the projected MLC leaf width at that isocentre. Black tiles represent values that are less than ± 0.004 cm^2 different from fitting at a standard SAD of 100 cm.

6.5.6 Dose Verification

Results in this section and section 6.5.7. focus on the VMAT treatment deliveries because we believe these are more representative of challenging deliveries from a mechanical point of view compared to DCA deliveries. The pass rates determined from a

2D-3D gamma analysis for the plans delivered on the linac is shown in Figure 50. Across the subset of patient plans which were delivered, the transformations to register the film dose to the dose plane in the Eclipse dose distribution was: -0.37 mm ± 0.64 mm in the LR-direction, -2.42 mm ± 1.47 mm in the SI-direction, and -0.01° ± 0.01° about the AP axis. Across these patients, the gamma pass rates were 96.40% ± 2.90% and 95.07% ± 3.10% for deliveries at standard and virtual isocentre, respectively. The average dose difference between measured and calculated doses with the ion chamber were -0.36% ± 3.45% and -0.55% ± 3.39% for deliveries at a standard and virtual isocentre, respectively. Average polarity correction factors were found to be 0.07% ± 0.15% and 0.09 ± 0.09% across all field sizes at dose rates of 600 MU/min and 1400 MU/min, respectively. Average ion recombination correction factors were found to be 0.43% ± 0.10% and 0.41% ± 0.08% across all field sizes at dose rates of 600 MU/min and 1400 MU/min, respectively. The calculated dosimetric hetereogeneity within the ion chamber volume, as determined by the difference between the maximum and minimum dose in the volume, was found to be 6.54% ± 2.08% and 7.35% ± 2.53% of the prescription dose for standard and virtual isocentre plans, respectively.

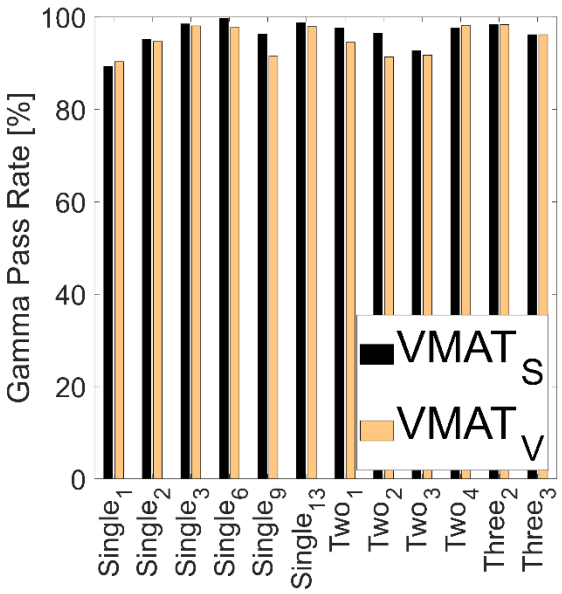

Figure 50: Gamma pass rates when determined from a 2D-3D analysis between dose measured with EBT3 GafChromic™ Film and dose calculated in Eclipse. Pixels which possessed less than 10% of the prescription dose were suppressed in the analysis. $VMAT_S$ represents plans delivered at a standard isocentre and $VMAT_V$ represents plans delivered at virtual isocentre.

6.5.7 Delivery Time Analysis

The time-limiting components for a virtual isocentre delivery are shown in Figure 51. For each patient, the fraction of control points limited by each component is shown and the potential time reductions are represented as a percent difference between the beam on time of the standard isocentre plan and the virtual isocentre plan. The analysis is performed twice for each patient: once based on simple (non-optimized) leaf fitting to each aperture without scheduling optimized MLC motions; and once with the assumption that properly optimized MLC leaf motions will eliminate control points in which MLC leaf motions are the rate limiting component. Justification for this assumption is the fact that the MLC leaf motions were not the rate limiting component for a single control point in any of the

standard SAD plans in which MLC motions were optimized. For the plans that had avoidance sectors for portions of the delivery, the time owed to the avoidance sector was excluded from the calculation of total delivery time. In the case of non-optimized MLC motions, for five out of eleven of the two lesion cases, and all three lesion cases, time savings were not realized with a virtual isocentre delivery. For these plans (Tw_1, Tw_2, Tw_3, Tw_4, Tw_7, Tw_9, Tw_{11}, Th_1, Th_2, Th_3, Th_4), there is a larger relative proportion of the delivery time being limited by aperture modulation. In many of the control points in which the time-limiting axis was the MLC, the magnification of the aperture required for the shortened vSAD necessitated the inclusion of a leaf pair that was not included in the standard SAD plan. Consequently, the affected leaf pair was either parked under the jaws prior to the control point in question or at least far removed from the treated area. As a result, the affected leaf pair had an abnormally large distance to travel, thus causing it to be the rate limiting component. Without leaf-sequencing optimization, the average time savings (for beam-on time) for cases with one, two and three lesions were 15.04%, -10.69% and -36.26%, respectively (negative numbers indicate longer beam-on times). Comparatively, with leaf-sequencing optimization, the average time savings for cases with one, two and three were 17.23%, 15.32% and 18.59%, respectively. The largest time savings of 19.81% (approximately 4:14 minutes) were realized with the TN case where 99.95% of the delivery time was dose rate limited.

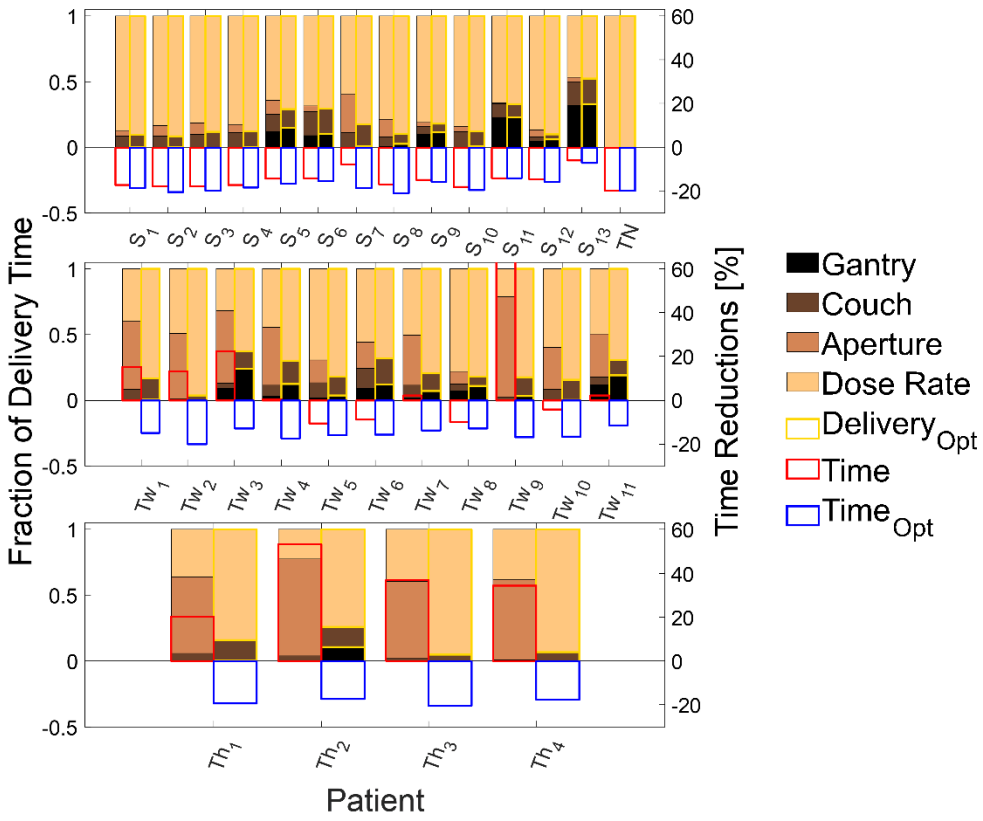

Figure 51: (Left – axis) Demonstrates the fraction of delivery time limited by the axes indicated in the legend for a virtual isocentre delivery. (Right-axis) Shows the potential time reductions for a virtual isocentre delivery expressed as a percent difference with respect to the standard isocentric delivery. 'S' indicates a plan with one lesion, 'Tw' indicates a plan with two lesions, 'Th' indicates a plan with three lesions with the subscript indicating patient number. TN represents a mock-plan for treating trigeminal neuralgia where 30000 MUs were delivered over 2 axial arcs and 8 non-coplanar arcs. The second bar in each grouping with a gold outline indicates the fraction of delivery time by each axis where leaf-sequencing optimizations were assumed. Similarly, the potential time savings with the optimization of leaf-sequence is indicated by the bar with a blue outline.

The calculated time savings per arc for a virtual isocentre delivery is shown in Figure 52. In this figure, the arcs for cases with a single lesion (including the TN case and excluding cases with avoidance sectors) were fit with linear regression. The fit was found to have a slope of 0.009s/MU with an $r^2 = 0.866$. In this figure, colour indicates the number of lesions in a plan (or the TN case). Time savings were seen in every arc for the single lesion cases except for two arcs ($Single_{11}$ – Arc 1, $Single_{13}$ – Arc 1), every arc in the two lesion cases except for two arcs (Two_7 – Arc1, Two_{11} – Arc 1), and all three lesion cases.

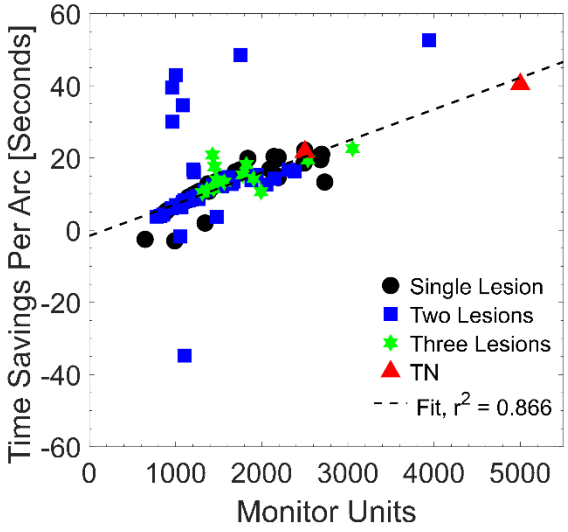

Figure 52: Time savings when delivering at a virtual isocentre in comparison to standard isocentric deliveries for individual arcs. Maximal time savings are depicted by incorporating additional time savings through optimized leaf-sequencing during delivery. The single lesions cases including TN were fit with linear regression.

6.6 DISCUSSION

A significant reduction in MU was found when delivering at virtual isocentre across all patients with an average reduction of 1000 to 1300 MU and 670 to 790 MU between

VMAT plans and DCA plans respectively. When significance was assessed for cases sorted by number of lesions, significance was not found for plans with three lesions. This was due to the small number of cases assessed with multiple lesions (N = 4 for three lesions) paired with the adjustment to the significance threshold for multiple paired comparisons with a Bonferroni correction. Regardless, there was still a trend of MU reductions across all patients (20.9% for VMAT plans and 20.6% for DCA plans) when delivering at a virtual isocentre. The MU reductions found in this investigation with the control point-specific vSAD could be seen as indicative of a theoretical limit on the maximum possible time reductions available during delivery. In this work we found that time savings up to 19.87% were achievable when the dose-rate was time limiting axis for 99.95% of the treatment time in a TN case. For TN cases, prescription doses can be escalated higher than those analyzed in this study, suggesting that savings in beam time could be even higher in absolute terms.[40-43] During radiosurgery, procedures in which doses range from 15 to 24 Gy, dose-rate modulation during delivery can occur causing one of the other axes to become a time limiting component (gantry rotation, couch translation, aperture modulation) and could limit the time-saving potential of a virtual isocentre delivery. This limitation was observed in the single lesion cases (1 through 6) analyzed in this study where time savings were on average 15.03% ± 3.95%. In the other cases analyzed with multiple lesions, where MLC travel was the largest time-limiting component during delivery, time savings were not observed when delivering at a virtual isocentre. While it is possible that the virtual isocentre approach does not universally confer time savings, it is possible that the observed increases in treatment time in this study could be, at least partially, attributable

to the non-optimized leaf motion sequencing used. When magnifying an aperture to move from standard isocentre to virtual isocentre, it was found that in the five cases mentioned in Section 6.5.7, an additional 104 ± 68 s of beam on time was attributed to the recruitment of MLC leaf pairs into the field that were not involved in the standard isocentric aperture; this was determined by calculating the difference between the current MLC travel time and the time of the next time-limiting axis. This calculation was performed to provide a fair comparison with standard isocentric plans where leaf sequence optimization had been performed; in these plans MLC motion was never the rate limiting step and it would not be unreasonable to assume that could still be the case for vSAD treatments. Leaf-sequence optimization could be used to improve the efficiency of these plans and should be investigated further as reducing treatment times is useful for reducing the possibility and magnitude of intrafractional motion.[137,144,165,274,285] Reducing intrafractional motion errors is crucial for minimizing losses in target dose coverage, as well as dose spread into target-adjacent normal tissue.[169,171,240,249]

An implementation of a vSAD delivery is not restricted to fixed arc templates; it could be used for static gantry IMRT as well as dynamic trajectory radiotherapy where all axes (couch, gantry, collimator) move in synchrony during treatment. Alternatively, utilizing a virtual isocentric therapy with an extended SAD could maximize collision zone avoidance in the 4π delivery space for dynamic radiotherapy. Additionally, extended SAD therapies have the potential of treating larger lesions through geometric minification. However, dosimetric benefits for 4π deliveries with an extended SAD would have to be balanced with MU increases (similarly increased treatment times) and coarser aperture

resolutions. While vSAD therapies are possible with dynamic couch trajectories, the positional accuracy during non-standard SAD therapies should not be assumed. In an investigation by Parsons *et al*. found that dynamic couch trajectories with idealistic circular trajectories resulted in a maximum positional error of 2.1 mm for a 77cm constant SAD.[269] Errors of this magnitude have been shown to result in clinically relevant dosimetric losses when treating cranial lesions.[169,171,240] These findings suggest the need for patient-specific QA for couch-trajectory therapies to minimize positional errors.

In the investigation by Mullins *et al.*, an inverse optimization framework was built for VMAT plan creation. Plans created in that work demonstrated no loss in plan quality compared to plans at a standard isocentre.[300] Our work did not feature an optimization framework for VMAT at a vSAD, but we nonetheless found that plan quality was similarly unaffected when optimized apertures from a standard SAD VMAT plan were magnified and projected to the vSAD. The maximum doses received by the OARs did not significantly differ from the original plan. All doses were considered clinically acceptable and any violations of these criteria with the virtual isocentre plans were also present in the original plans (e.g, patient #2 with three lesions had 10 cc of normal brain tissue receiving 16.8 Gy at a standard SAD and 17.0 Gy at a vSAD, where our clinical objective is to keep this metric below 12.0 Gy). Reduced SAD treatment fields will exhibit a greater degree of beam divergence compared to their conventional SAD counterparts. This results in a reduced volume of normal tissue exposure proximal to the target and an increased volume distal to the target. In the current study, the consequences of this variation in beam geometry were not significant in any of the evaluated dose metrics. As the number of

targets increased, however, there was a trend toward increased low dose wash (1 – 2 Gy) with the vSAD approach. The clinical consequences of this dose enhancement may not be significant for a given treatment but may merit further consideration when considered in the context of retreatments.

Projecting the aperture to a virtual isocentre and fitting to the projection is a simple task in the direction of leaf travel but is inherently limited in the direction perpendicular to leaf travel due to the discretization of leaf boundaries (defined by the projected leaf width). Fitting to the projected aperture produced an average Dice similarity coefficient across all control points and all patients (when comparing to the apertures in the original plan for VMAT) of 93.0% for patients with a single lesion, 92.2% for patients with two lesions and 90.7% for patients with three lesions. Despite these differences, this simplistic approach of magnifying apertures from a standard SAD still produced clinically acceptable treatment plans. Apertures created at a virtual isocentre for DCA exhibited a higher fidelity with standard isocentric plans as they did not possess the same challenge of fitting to complex apertures shapes leading to erroneous openings. Instead, the discretization of the leaves perpendicular motion is the limiting factor for optimally fitting to a target. This work presented geometric coverage metrics in the form of normal tissue exposure and target occlusion which could be used to inform the ideal vSAD (minimizing normal tissue exposure for example).

Two important risk factors for trajectory radiotherapy include patient safety (*i.e,* collisions) and the patient's ability to tolerate motion. Few publications address these issues in the literature. Northway *et al*. formulated a technique for mapping out couch-gantry, and

couch-patient collision zones using a convex hull of the patient's body contour.[277] this technique could be applied to assessing collisions with trajectory radiotherapy with a shortened virtual isocentre. Lyu *et al*. implemented monotonically increasing couch angles with trajectory radiotherapy to minimize inertial forces being exerted on the patient during delivery.[301] In this work we were unable to assess the accelerations produced by translational couch trajectories as this information is not accessible in the Varian TrueBeam Developer mode at this time.[289] To evaluate several aspects of trajectory radiotherapy (safety, feasibility, dosimetric benefit, patient tolerance) a phase I trial was conducted with static gantry IMRT where dynamic motions of the couch (rotation and translation) were implemented between ports;[302] Intrafractional motion was determined to be less than 1.0 mm using kV-kV registration (three to four images every three to four couch kicks) and patient tolerability was high 8.625 ± 2.64 (10 being perfectly tolerable) for the 11 patients tested.

6.7 CONCLUSION

This work has demonstrated that cranial SRS treatments delivered with a vSAD technique require significantly fewer monitor units, have improved treatment efficiency (approximately 0.009 s/MU, r2 = 0.866) and are dosimetrically equivalent to conventional SAD plans. These conclusions held for all studied cases which included both VMAT and DCA plans and plans involving one, two or three targets. While beam divergence increases low dose distal to the target for vSAD plans, this work has shown that this negligibly affects the dose received by normal brain for cases with one and two lesions. For plans with three

lesions, there is an evident increase in the low-dose (approximately 2.0 Gy) which could be undesirable for cases which necessitate retreatment. Fitting targets conformally at a virtual isocentre is subject to the discretization of the MLC leaf width perpendicular to leaf motion; this work has shown that target-size specific SAD choices can be made to minimize normal tissue exposure while maximizing potential control point-specific MU reductions.

CHAPTER 7. CONCLUSION

7.1. SUMMARY

The purpose of this thesis was to establish viable strategies for improving the efficiency, and fidelity of cranial SRS therapies. Irrespective of treatment vendor with C-arm linacs and/or delivery technique (*e.g,* DCA or VMAT), intrafractional motions up to a few millimetres will be a reality of therapies that utilize thermoplastic immobilization systems. Treatment margins are commonly added to offset any potential dosimetric detriments owed to motion (internal tumour volume), and/or setup errors (which are encompassed within the PTV). However, complex treatment scenarios do exist where the proximity of lesions to critical structures (*e.g*, brain stem, optic nerve) necessitate that the dose falls off precipitously towards the OAR, thus internal tumor volume margins likely will not adequately encapsulate motion. The first manuscript (Chapter 4) explored the dosimetric impact of simulated SRS-magnitude motions in the context of treating small targets ($\leq$ 1.0 cm diameter) with small apertures ($\leq$ 1.0 x 1.0 cm^2). The second manuscript (Chapter 5) introduced an online positional correction methodology with ROI MV-imaging to detect and correct for SRS magnitude motions. This technique established a way to generate ROI aperture templates (for a given couch-gantry angle combination) which can be deployed with variable size and/or frequency to achieve a certain degree of positional accuracy while minimizing imaging dose. In the third manuscript (Chapter 6) a strategy to minimize the magnitude and/or frequency of intrafractional motion was introduced by

means of improved treatment efficiency. Treatment efficiencies were realized by implementing couch trajectories with shortened source-to-target distances, increasing the effective dose rate through inverse square gains. These techniques, when used independently or in synchrony, have the potential to improve the fidelity between planned and delivered treatments by minimization of the dosimetric detriments owed to motion.

The first manuscript explored the dosimetric characteristics of a new treatment technique, referred to as a virtual cone, which was introduced by Popple *et al.*[118] In the original work by Popple *et al*.,[118] the concept of a virtual cone was defined as a combination of arc geometries (couch, collimator, gantry, static aperture size) to produce a dose distribution comparable to that of a 4 millimetre stereotactic cone. The first manuscript was therefore an extension of the technique established by Popple *et al*.,[118] where a virtual cone was simulated with different sized apertures as well as with a dynamically rotating aperture. These two-treatment paradigms were investigated for varying target sizes (1 to 10 mm diameter) and in the presence of simulated intrafractional motion. Treating with a virtual cone creates a clinically complex scenario where suitable pairings of aperture/target sizes would be dictated by isodose prescription criteria and proximity of the target to sensitive clinical structures. An additional layer of complexity was added when implementing a virtual cone with a dynamically rotating collimator as maximum doses (in target and surrounding normal tissue) were generally reduced at the expense of larger low dose washes to the surrounding tissues due to the spreading of the low dose wash. The dosimetric impact of motion followed expected trends, where larger degrees of motion, and higher frequency of motion (represented as a persistent shift at different time points)

caused larger detriments (reduced conformity and larger geographic misses in surrounding tissues). Preserving plan quality in the presence of motion would require a nuanced approach, balancing the multivariate solution space where even in some instances, the use of the dynamic virtual cone was more robust against the dosimetric impact of motion.

The second manuscript introduced an online positional correction technique with ROI MV-imaging and treatment couch motions. The methodology used ROI apertures that conform to anatomical sites with enough textural information to be used for image registration to achieve sub-mm positional accuracy. Common to all high-quality apertures is a larger degree of MI fall-off (in the presence of motion) and a uniform distribution of textural information. The last point was a crucial element for the robustness of a singular ROI aperture for imaging in the presence of varying directionality of motion. The feasibility of ROI imaging plans with two candidate aperture sizes (smaller and larger) were explored by imaging a head phantom on a Varian TrueBeam™ STx linac for two types of simulated motions. In this clinical scenario, realistic imaging challenges such as a reduction in contrast, can pose a challenge for registration accuracy. While the larger aperture imaging plan was more robust for motion detection, it also intuitively came at the price of a larger accrued imaging dose. Implementation of this technique relies on the utilization of the 2.5 MV imaging beam for improved image contrast, which at this time, poses a significant treatment interruption for target switching; albeit, implementation of fast target-switching systems is an area of ongoing research.[278,279] Most likely, integration of this technique would require a reduced imaging-frequency (compared with what was investigated in this study) and would likely only be used when certain proportions of a

treatment arc risks dosing laterally proximal sensitive structures with respect to the BEV. Use of detector with a higher detective quantum efficiency as demonstrated by Myronakis *et al*.,[303] could be utilized to enable high image-sampling with comparable, or less accrued imaging dose.

The third manuscript demonstrated an alternative methodology for motion management by means of improved treatment efficiency. Higher efficiency treatments were achieved by implementing treatment couch trajectories during delivery, where the treatment distance was reduced as much as possible while avoiding collisions. The impetus for treating at shortened SAD is the reduction in necessary monitor units through increases of effective dose rate via inverse square gains. Another possible benefit for delivering at a shortened SAD is the minification of the projected MLC leaf width at the site of the target. In this work, previously treated VMAT plans with 1-3 lesions (and DCA plans generated with the same arc structure) using a single, static isocentre, were converted into a plan with a dynamic, virtual isocentre, with a criterion for delivering at distance of closest approach (for a given couch-gantry geometry). Plan quality metrics between standard, and virtual isocentre plans. A dose verification for a subset of the plans was conducted by mapping the plans to an anthropomorphic head phantom with an insert that house radiochromic film and an ion chamber. Dose distributions evaluated using a gamma analysis with a 5%/1mm criteria were found to clinically feasible (pass rates: $\geq$ 95.0%) and absolute dose measurements were found to agree within 0.72% $\pm$ 2.86%. A statistically significant reduction of up to 21.0% of MUs was observed for virtual isocentre deliveries without any statistically significant reduction in other plan quality metrics (CI, GI, V_{12Gy}). A large

degree of low dose wash (approximately V_{2Gy}) was observed when treating cases with three lesions at virtual isocentre, albeit these differences are not likely clinically significant as they only represent a 3.0 – 5.0% volumetric increase compared with standard isocentric plans. While dosimetric benefits were not realized by minification of MLC leaf widths, treatment efficiencies up to 15.0% were seen with single lesion cases. Time savings were not achieved for cases with avoidance sectors, and for cases with high degrees of MLC modulation. For the latter, the majority of treatment inefficiencies were owed to unoptimized leaf-sequencing, leading to singular leaf pairs being recruited in adjacent control points to move large distances. Time savings for cases with multiple lesions could be realized if leaf sequencing optimization strategies had been implemented.[83,86,304]

7.2. FUTURE WORK

The topics investigated in this thesis have introduced strategies to minimize the impact of motion during therapy by means of utilization of onboard imaging, and trajectories of one of the dynamic axes available on a C-arm linac. The implementation of the techniques demonstrated in this work is only one such embodiment of their utility in the delivery of efficient, and precise radiation therapy.

7.2.1. Trajectory Radiotherapy Quality Assurance

A mandatory requirement for treating with SRS as set out by AAPM Task Group 142[14] is the coincidence of mechanical and radiation isocentre to be $\leq \pm 1.0$ mm. While various testing regimens, as mentioned in Section 1.4, assess this coincidence for the

motions of a linac at 100 cm SAD, the same information should not be assumed to hold true when implementing trajectory radiotherapy. In the work demonstrated in Chapter 6, idealized couch motions were derived from 3D path-tracing of beamlines defined at arbitrary geometries. Implementation of these motions on the treatment unit is reliant on the various electro-mechanical components of couch-stand driving the couch top to requested positions accurately, and reliably. For non-coplanar, standard isocentric trajectory radiotherapy, quality assurance protocols have been postulated by Yu *et al.*[290] and further refined by Byron *et al*.[305]

There are not currently any protocols for assessing the coincidence of mechanical and radiation isocentre when implementing translational couch trajectories as demonstrated in Chapter 6. In Figure 53, a possible quality assurance protocol for implementing corrections to idealized couch trajectories is demonstrated, where corrections are derived using equation (42) with images similar to those presented in Chapter 5. This data was collected by taking a series of images with the 2.5 MV imaging beam using a custom-made XML script in Developer mode. The imaging phantom was a simple solid-water phantom (30 x 30 x 10 cm^3) with a metal-bb embedded in the centre place on the end of the treatment couch. The test was repeated with a weight-loaded couch using an anthropomorphic body phantom with additional slabs of solid water that in combination weighed a total of 150 lbs. Weight-loading was assessed as work by Towns *et al*. had demonstrated that couch flexion of up to 4.0 mm was observed; albeit with heavier patients.[306]

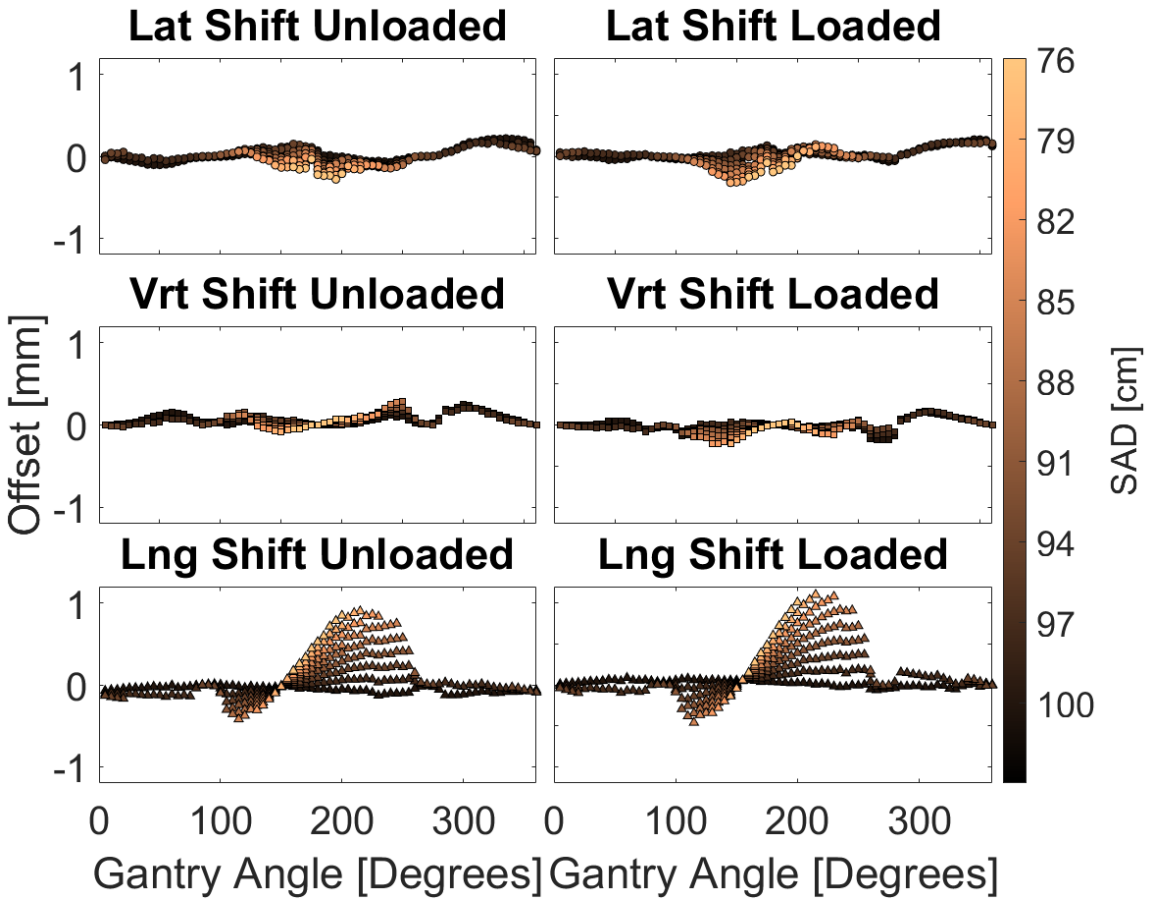

Figure 53: For varying couch and gantry angles at varying source-to-axis-distances, images were acquired on a Varian TrueBeam™ STx to derive positional corrections to maintain fidelity between radiation and mechanical isocentre. 3D-Positional corrections for an axial arc (couch = 0^{o}) were derived using equation (42), from images similar to those represented in Figure 34 for an unloaded treatment couch, and a loaded treatment couch (with 150lb anthropomorphic body phantom).

Corrections to couch trajectories when collecting data for Chapter 6 as outlined in Section 6.4.6 were not implemented, and even so, dosimetric measurements were not significantly different from measurements implemented at a standard isocentre. This result is likely due to the fact that the target sizes explored in Chapter 6 were sufficiently large that any positional errors while implementing couch trajectories had minimal dosimetric

effects. For smaller targets, such nerve ablation therapies, the motions could have serious dosimetric effects. An investigation by Parsons *et al.* explored the dosimetric impact of delivering shortened SAD therapies with ultra-small apertures (single leaf-pair with a 1.0 mm opening) with and without positional corrections of idealized couch trajectories; they found corrections to couch motions could reduce the width of the dose profile by up to 1.2 mm at 30% of D_{max}.[269] The data presented in Figure 53 is a generalized embodiment of the EPID-based WL test for virtual isocentre therapies as introduced by Parsons *et al.*,[269] and could easily be integrated into pre-treatment SRS quality assurance protocols. A logical next step for the integration of translational couch trajectory radiotherapy in the clinic, would be to establish robust quality assurance procedures.

7.2.2. Virtual Isocentre Delivery Optimization

Unlocking the use of the dynamic axes of a linac during delivery has been shown by several investigators to confer a quantifiable dosimetric benefit for conformity, and for normal tissue dose sparing.[289,291,293-295,307-309] Similar to the investigation by Mullins *et al.*,[300] trajectory radiotherapy at shortened virtual isocentre, as demonstrated in Chapter 6, did not yield any dosimetric benefit with respect to improved conformity (as a result of finer resolution of the MLC due to geometric minification at a shortened SAD). These results are in contrast with findings by Bratengeier *et al*.[310,311] where normal tissue sparing proximal to a spherical target was reduced for isodose volumes between 40% to 90% when delivering at a constant 70 cm SAD. The authors posit that the reduction of penumbral width observed with shortened virtual isocentre therapies would serve a higher utility for

improving plan quality.[310] While these results are promising, they are not generalizable for all treatment vendors (their study was conducted with an Agility™ MLC model (Elekta AB, Stockholm, Sweden)), as penumbral width is dictated by focal spot size, leaf shape/transmission, and SAD.[312] Further characterization of the penumbral dose with the Varian TrueBeam™ MLC would be needed to assess any realizable dosimetric benefits for treating at virtual isocentre.

The main benefit for treating at a shortened virtual is the efficiencies created by means of increased dose-rate. Time savings were seen when converting several previously delivered plans to a delivery at a virtual isocentre. But, in some cases (with avoidance sectors or treating multiple lesions simultaneously), delivery at a virtual isocentre lengthened the time of treatment, and the majority of these instances were owed to unoptimized leaf-sequencing. Optimized fluence patterns in the original plan (at a standard 100cm SAD) were geometrically projected to a virtual isocentre and refit with geometrically minified leaf widths. In many instances, this fitting procedure resulted in erroneous fittings due to the discretization of the MLC leaf widths, necessitating forced closures on a control point-specific basis. This process led to scenarios where adjacent control points would recruit shielded leaves (placed underneath the jaws) resulting in lengthy MLC travel times. In a clinical implementation of virtual isocentre delivery optimization, a two-step optimization,[81] or simultaneous optimization[83,86,300,313] of leaf trajectories would be implemented. For the cases with multiple lesions, a larger viable deliverability solution space could be developed by allowing the collimator to rotate dynamically throughout delivery; An analogous investigation by MacDonald *et al*.[307] could

be adapted to develop optimization techniques for treating multiple lesions at virtual isocentre.

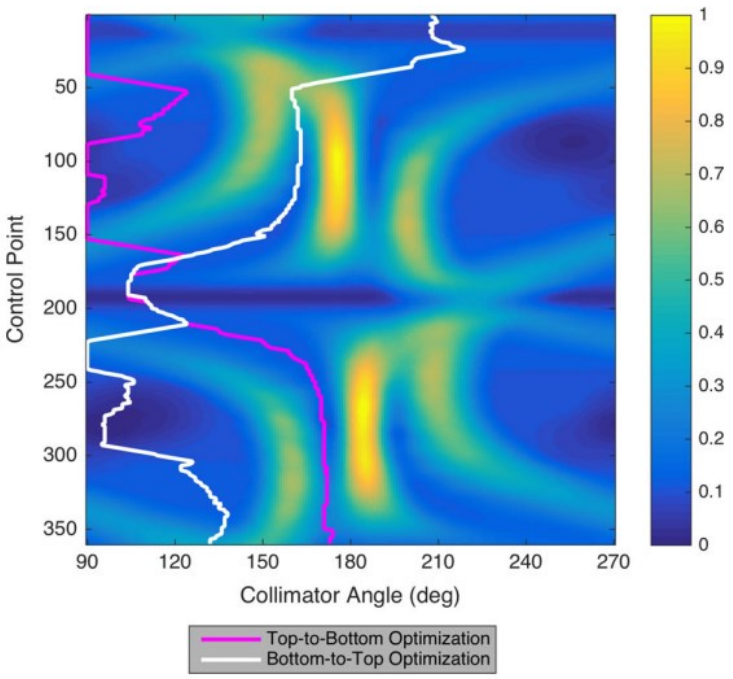

Figure 54: A demonstration of idealized collimator trajectories to minimize normal tissue exposure (indicated by colour bar with arbitrary units) for a three coplanar arc arrangement; figure from MacDonald *et al.*[307]

7.2.3. Clinical Utility

The integration of the virtual cone technique as demonstrated in Chapter 4 is ultimately left to the discretion of the oncology staff within a clinic. The technique has been shown to deliver comparable doses to stereotactic cones,[118,119] has been integrated into a clinical environment,[299] and has the advantage of not requiring externally mounted hardware. The latter allows for the virtual cone technique to be delivered at a shortened virtual isocentre with the time savings posited in Chapter 6; where time savings were on

the order of 4 to 5 minutes for therapies where a virtual cone would be used (*e.g,* TN with MUs > 25000).

Implementation of trajectory radiotherapy at a shortened virtual isocentre introduces a new degree-of-freedom by which plans can be optimized for treatment efficiency. From a practical perspective, delivery at a shortened isocentre is only useful when the increase in dose-rate between adjacent control points does not cause any of the mechanical motions of the linac (couch motions, gantry rotation, MLC travel) to become the time limiting axis. Anecdotal observation suggests that the collisional zones between the couch and gantry while the gantry rotates from a posterior-anterior delivery up to anterior-posterior (approximately 180.0E – 60^{o} or 180^{o} to 300^{o}, Varian IEC coordinates) do not allow for a substantial reduction in treatment distances, and thus, do not confer a substantial advantage for implementing couch trajectories for the purposes of leveraging increases in dose-rate. This leaves a theoretical 120^{o} cone of delivery as depicted in Figure 55 where appreciable times savings could be achieved. This problem is juxtaposed with the location of the lesion, *i.e*, treatment plans for lesions in the anterior cranial fossa would likely benefit the most from shortened virtual isocentre deliveries as these plans would likely request large magnitudes of MUs in the 120^{o} cone due to the proximity of the target to the source. Exploration of shortened virtual isocentre deliveries for various classes of lesions would be useful to establish criteria for assessing its utility.

Trajectory radiotherapy presented in this work is only one such embodiment of the technique. Many investigators have demonstrated dynamic couch, gantry, and collimator rotation. The largest limiting factor for deliverability in the 4π space is collisions between

the components of the linac and/or patient. Translations of the couch using the methodologies presented in Chapter 6 could be analogously implemented with the intent to extend the deliverability of the 4π space by treating at an extended virtual isocentre. The dosimetric benefits of such an implementation would necessitate a further investigation as the divergence of the beam, and the coarseness of the projected MLC width could pose other unforeseen issues.

Figure 55: A pictorial representation of possible treatment efficiencies by means of shortened virtual isocentre delivery, where a red colour indicates the highest possible dose-rate.

7.3. CONCLUSIONS

Radiosurgery is a therapeutic technique that delivers large doses in a single fraction. SRS necessitates stringent tolerances on mechanical and radiation precision to ensure adequate therapeutic outcomes and normal tissue sparing. Intrafractional patient motion is an unavoidable reality of radiation therapy, even when utilizing immobilization systems. The advent of frameless immobilization systems such as a thermoplastic mask have drastically improved several aspects of the clinical experience for SRS or SRT; however, these improvements come at the cost of increased magnitudes, and frequencies of motion during therapy. This research demonstrated that SRS-magnitude motions can have clinically significant detriments to therapeutic coverages, as well as normal tissue sparing, which is exacerbated when treating small lesions ($\leq$ 1.0 cm in diameter). To minimize the impact of these motions, two methodologies were presented: 1) Online positional corrections derived from MV ROI-imaging using couch translations. 2) Increased treatment efficiency through increases of the effective-dose rate by delivering at a shortened virtual isocentre. The implementation of these two techniques could be applied independently or in synchrony to maximize the fidelity between planned and delivered doses. One example would be the implementation of these techniques for improving the delivery quality of virtual cone treatments as presented in Chapter 4, where intrafractional motion was simulated.

The methodologies developed in this thesis are proof-of-concept techniques which could be easily translated into a clinical setting. Both techniques achieved improvements in treatment accuracy by utilizing the various facets of a linac's operation (imaging,

mechanical motions). Without any need for additional hardware or software for implementation, these techniques are accessible to a large assortment of clinics with minimal financial burden.

REFERENCES

1. Koehler A, Preston W. Protons in radiation therapy: comparative dose distributions for protons, photons, and electrons. *Radiology.* 1972;104(1):191-195.
2. Hall EJ, Giaccia, Amato J. *Radiobiology for the Radiologist.* Vol 6: Philadelphia; 2006.
3. Bray F, Laversanne M, Weiderpass E, Soerjomataram I. The ever-increasing importance of cancer as a leading cause of premature death worldwide. *Cancer.* 2021;127(16):3029-3030.
4. Sung H, Ferlay J, Siegel RL, et al. Global cancer statistics 2020: GLOBOCAN estimates of incidence and mortality worldwide for 36 cancers in 185 countries. *CA: Cancer J Clin.* 2021;71(3):209-249.
5. Miller KD, Nogueira L, Mariotto AB, et al. Cancer treatment and survivorship statistics, 2019. *CA: Cancer J Clin.* 2019;69(5):363-385.
6. Leksell L. Stereotactic radiosurgery. *J Neurol Neurosurg Psychiatry.* 1983;46(9):797-803.
7. Leksell L. The stereotactic method and radiosurgery of the brain. *Acta chir scand.* 1951;102:316-319.
8. Leksell L, Herner T, Liden K. Stereotaxic radiosurgery of the brain. *Kungl Fysiografiska Sällsk Lund Förh.* 1955;25(17):1-10.
9. Schell MC, Bova FJ, Larson DA, et al. Stereotactic Radiosurgery: Report of Task Group 42 Radiation Therapy Committee. *AAPM.* 1995.
10. Adler Jr JR, Colombo F, Heilbrun MP, Winston K. Toward an expanded view of radiosurgery. *Neurosurg.* 2004;55(6):1374-1376.
11. Papiez L, Timmerman R. Hypofractionation in radiation therapy and its impact. *Med Phys.* 2008;35(1):112-118.
12. Marks LB. Extrapolating hypofractionated radiation schemes from radiosurgery data: regarding Hall et al. *Int J Radiat Oncol Biol Phys.* 1995;32(1):274-276.
13. Niranjan A, Flickinger JC. Radiobiology, principle and technique of radiosurgery. *Prog Neurol Surg.* 2008;21:32-42.
14. Klein EE, Hanley J, Bayouth J, et al. Task Group 142 report: quality assurance of medical accelerators. *Med Phys.* 2009;36(9):4197 - 4212.
15. Leskell L. A Stereotaxic Apparatus For Intracerebral Surgery. *Acta Chir Scand.* 1949;99:229 - 233.
16. Leskell L. Stereotaxic Radiosurgery In Trigeminal Neuralgia. *Acta Chir Scand.* 1971;137:173 - 184.
17. Johns H, Bates L, Watson T, et al. 1000 Curie cobalt units for radiation therapy. II. Depth dose data and diaphragm design for the Saskatchewan 1000 curie cobalt unit. *Br J Radiol.* 1952;25(294):302 - 308.
18. Mendel JT, Schroeder S, Plitt A, et al. Expanded Radiosurgery Capabilities Utilizing Gamma Knife Icon™. *Cureus.* 2021;13(3).

19. Bull J. The history of computed tomography. In: *Computerized tomography.* Springer; 1980:3-6.
20. Tsien CI, Drzymala RE, Rich K. Imaging Advances in Stereotactc Radiosurgery. *Mo Med.* 2015;112(5):373.
21. Mugler III JP, Brookeman JR. Three-dimensional magnetization-prepared rapid gradient-echo imaging (3D MP RAGE). *Magn Reson Imaging.* 1990;15(1):152-157.
22. Danieli L, Riccitelli G, Distefano D, et al. Brain tumor-enhancement visualization and morphometric assessment: a comparison of MPRAGE, SPACE, and VIBE MRI techniques. *Am J Neuroradiol.* 2019;40(7):1140-1148.
23. Anzalone N, Essig M, Lee S-K, et al. Optimizing contrast-enhanced magnetic resonance imaging characterization of brain metastases: relevance to stereotactic radiosurgery. *Neurosurg.* 2013;72(5):691-701.
24. Balériaux D, Colosimo C, Ruscalleda J, et al. Magnetic resonance imaging of metastatic disease to the brain with gadobenate dimeglumine. *Neuroradiology.* 2002;44(3):191-203.
25. Yuh W, Tali ET, Nguyen HD, Simonson TM, Mayr NA, Fisher DJ. The effect of contrast dose, imaging time, and lesion size in the MR detection of intracerebral metastasis. *Am J Neuroradiol.* 1995;16(2):373-380.
26. Krautmacher C, Willinek WA, Tschampa HJ, et al. Brain tumors: full-and half-dose contrast-enhanced MR imaging at 3.0 T compared with 1.5 T—initial experience. *Radiology.* 2005;237(3):1014-1019.
27. Paulson ES, Crijns SP, Keller BM, et al. Consensus opinion on MRI simulation for external beam radiation treatment planning. *Radiother Oncol.* 2016;121(2):187-192.
28. Nagtegaal SH, van Lier AL, den Boer AA, et al. Does an immobilization mask have added value during planning magnetic resonance imaging for stereotactic radiotherapy of brain tumours? *Phys Imaging Radiat Oncol.* 2020;13:7-13.
29. Tryggestad E, Christian M, Ford E, et al. Inter-and intrafraction patient positioning uncertainties for intracranial radiotherapy: a study of four frameless, thermoplastic mask-based immobilization strategies using daily cone-beam CT. *Intl J Radiat Oncol Biol Phys.* 2011;80(1):281-290.
30. Seravalli E, Van Haaren P, Van Der Toorn P, Hurkmans C. A comprehensive evaluation of treatment accuracy, including end-to-end tests and clinical data, applied to intracranial stereotactic radiotherapy. *Radiother Oncol.* 2015;116(1):131-138.
31. Torfeh T, Hammoud R, Perkins G, et al. Characterization of 3D geometric distortion of magnetic resonance imaging scanners commissioned for radiation therapy planning. *Magn Reson Imaging.* 2016;34(5):645-653.
32. Fransson A, Andreo P, Pötter R. Aspects of MR image distortions in radiotherapy treatment planning. *Strahlenther Onkol.* 2001;177(2):59-73.
33. Stanescu T, Wachowicz K, Jaffray D. Characterization of tissue magnetic susceptibility-induced distortions for MRIgRT. *J Appl Clin Med Phys.* 2012;39(12):7185-7193.

34. Putz F, Mengling V, Perrin R, et al. Magnetic resonance imaging for brain stereotactic radiotherapy. *Strahlenther Onkol.* 2020;196(5):444-456.
35. Kleihues P, Louis DN, Scheithauer BW, et al. The WHO classification of tumors of the nervous system. *J Neuropathol Exp Neurol.* 2002;61(3):215-225.
36. Rohringer M, Sutherland GR, Louw DF, Sima AA. Incidence and clinicopathological features of meningioma. *J Neurosurg.* 1989;71(5):665-672.
37. Solero C, Giombini S, Morello G. Suprasellar and olfactory meningiomas. Report on a series of 153 personal cases. *Acta neurochirurgica.* 1983;67(3):181-194.
38. Flickinger JC, Kondziolka D, Maitz AH, Lunsford LD. Gamma knife radiosurgery of imaging-diagnosed intracranial meningioma. *Int J Radiat Oncol Biol Phys.* 2003;56(3):801-806.
39. Buss EJ, Wang TJ, Sisti MB. Stereotactic radiosurgery for management of vestibular schwannoma: a short review. *Neurosurg Rev.* 2021;44(2):901-904.
40. Tsao MN, Sahgal A, Xu W, et al. Stereotactic radiosurgery for vestibular schwannoma: International Stereotactic Radiosurgery Society (ISRS) practice guideline. *J Radiosurg SBRT.* 2017;5(1):5.
41. Timmer FC, Hanssens PE, van Haren AE, et al. Follow-up after gamma knife radiosurgery for vestibular schwannomas: Volumetric and axial control rates. *Laryngoscope.* 2011;121(7):1359-1366.
42. Kondziolka D, Lunsford LD, McLaughlin MR, Flickinger JC. Long-term outcomes after radiosurgery for acoustic neuromas. *N Engl J Med.* 1998;339(20):1426-1433.
43. Chung W-Y, Liu K-D, Shiau C-Y, et al. Gamma knife surgery for vestibular schwannoma: 10-year experience of 195 cases. *J Neurosurg.* 2005;102(Special_Supplement):87-97.
44. Moftakhar P, Hauptman JS, Malkasian D, Martin NA. Cerebral arteriovenous malformations. Part 1: cellular and molecular biology. *Neurosurg Focus.* 2009;26(5):E10.
45. Flickinger JC, Kondziolka D, Maitz AH, Lunsford LD. An analysis of the dose–response for arteriovenous malformation radiosurgery and other factors affecting obliteration. *Radiother Oncol.* 2002;63(3):347-354.
46. Ilyas A, Ding D, Hixson HR, Xu Z, Starke RM, Sheehan JP. Volume-staged stereotactic radiosurgery for large intracranial arteriovenous malformations. *J Clin Neuro.* 2017;43:202-207.
47. Seymour ZA, Sneed PK, Gupta N, et al. Volume-staged radiosurgery for large arteriovenous malformations: an evolving paradigm. *J Neurosurg.* 2016;124(1):163-174.
48. Pollock BE, Link MJ, Stafford SL, Lanzino G, Garces YI, Foote RL. Volume-staged stereotactic radiosurgery for intracranial arteriovenous malformations: outcomes based on an 18-year experience. *Neurosurg.* 2017;80(4):543-550.
49. Laws Jr ER, Vance ML. Radiosurgery for pituitary tumors and craniopharyngiomas. *Neurosurg Clin N Am.* 1999;10(2):327-336.
50. Sallabanda K, Usychkin S, Puebla F, et al. Stereotactic radiosurgery in pituitary adenomas: long-term single institution experience and role of the hypothalamic-pituitary axis. *J Radiosurg SBRT.* 2011;1(3):213.

51. Minniti G, Clarke E, Scaringi C, Enrici RM. Stereotactic radiotherapy and radiosurgery for non-functioning and secreting pituitary adenomas. *Rep Pract Oncol Radiother.* 2016;21(4):370-378.
52. Tuleasca C, Régis J, Sahgal A, et al. Stereotactic radiosurgery for trigeminal neuralgia: a systematic review: International Stereotactic Radiosurgery Society Practice Guidelines. *J Neurosurg.* 2018;130(3):733-757.
53. Elaimy AL, Mackay AR, Lamoreaux WT, et al. Clinical outcomes of gamma knife radiosurgery in the salvage treatment of patients with recurrent high-grade glioma. *World Neurosurg.* 2013;80(6):872-878.
54. Chuang CF, Chan AA, Larson D, et al. Potential value of MR spectroscopic imaging for the radiosurgical management of patients with recurrent high-grade gliomas. *Technol Cancer Res Treat.* 2007;6(5):375-382.
55. Patchell RA. The management of brain metastases. *Cancer Treat Rev.* 2003;29(6):533-540.
56. Suh JH. Stereotactic radiosurgery for the management of brain metastases. *N Engl J Med.* 2010;362(12):1119-1127.
57. Shaw E, Scott C, Souhami L, et al. Single dose radiosurgical treatment of recurrent previously irradiated primary brain tumors and brain metastases: final report of RTOG protocol 90-05. *Int J Radiat Oncol Biol Phys.* 2000;47(2):291-298.
58. Shehata MK, Young B, Reid B, et al. Stereotatic radiosurgery of 468 brain metastases≤ 2 cm: implications for SRS dose and whole brain radiation therapy. *Int J Radiat Oncol Biol Phys.* 2004;59(1):87-93.
59. Kocher M, Wittig A, Piroth MD, et al. Stereotactic radiosurgery for treatment of brain metastases. *Strahlenther Onkol.* 2014;190(6):521-532.
60. Sahgal A, Barani IJ, Novotny Jr J, et al. Prescription dose guideline based on physical criterion for multiple metastatic brain tumors treated with stereotactic radiosurgery. *Int J Radiat Oncol Biol Phys.* 2010;78(2):605-608.
61. Hartmann GH, Lutz W, Arndt J, et al. *Quality assurance program on stereotactic radiosurgery: report from a quality assurance task group.* 1st ed: Springer; 1995.
62. Lutz W, Winston KR, Maleki N. A system for stereotactic radiosurgery with a linear accelerator. *Int J Radiat Oncol Biol Phys.* 1988;14(2):373-381.
63. Low DA, Li Z, Drzymala RE. Minimization of target positioning error in accelerator-based radiosurgery. *Med Phys.* 1995;22(4):443-448.
64. Grimm J, Grimm SYL, Das IJ, et al. A quality assurance method with submillimeter accuracy for stereotactic linear accelerators. *J Appl Clin Med Phys.* 2011;12(1):182-198.
65. Winkler P, Bergmann H, Stuecklschweiger G, Guss H. Introducing a system for automated control of rotation axes, collimator and laser adjustment for a medical linear accelerator. *Phys Med Biol.* 2003;48(9):1123.
66. Betti O, Derechinsky V. Hyperselective encephalic irradiation with linear accelerator. In: *Adv Stereotact Funct Neurosurg.* Springer; 1984:385-390.
67. Das IJ, Dowries MB, Corn BW, Curran WJ, Werner-Wasik M, Andrews DW. Characteristics of a dedicated linear accelerator-based stereotactic radiosurgery-radiotherapy unit. *Radiother Oncol.* 1996;38(1):61-68.

68. Goldbaum DS, Hurley JD, Hamilton RJ. A simple knowledge-based tool for stereotactic radiosurgery pre-planning. *J Appl Clin Med Phys.* 2019;20(12):97-108.
69. Adler Jr JR, Chang SD, Murphy MJ, Doty J, Geis P, Hancock SL. The Cyberknife: a frameless robotic system for radiosurgery. *Stereotact Funct Neurosurg.* 1997;69(1-4):124-128.
70. Biasi G, Petasecca M, Guatelli S, et al. CyberKnife® fixed cone and Iris™ defined small radiation fields: Assessment with a high-resolution solid-state detector array. *J Appl Clin Med Phys.* 2018;19(5):547-557.
71. Arnfield MR, Siebers JV, Kim JO, Wu Q, Keall PJ, Mohan R. A method for determining multileaf collimator transmission and scatter for dynamic intensity modulated radiotherapy. *Med Phys.* 2000;27(10):2231-2241.
72. Cosgrove VP, Jahn U, Pfaender M, Bauer S, Budach V, Wurm RE. Commissioning of a micro multi-leaf collimator and planning system for stereotactic radiosurgery. *Radiother Oncol.* 1999;50(3):325-335.
73. Sharma DS, Dongre PM, Mhatre V, Heigrujam M. Physical and dosimetric characteristic of high-definition multileaf collimator (HDMLC) for SRS and IMRT. *J Appl Clin Med Phys.* 2011;12(3):142-160.
74. Bahr G, Kereiakes JG, Horwitz H, Finney R, Galvin J, Goode K. The method of linear programming applied to radiation treatment planning. *Radiology.* 1968;91(4):686-693.
75. Hope C, Orr J. Computer optimization of 4 MeV treatment planning. *Phys Med Biol.* 1965;10(3):365.
76. Borghero YO, Salehpour M, McNeese MD, et al. Multileaf field-in-field forward-planned intensity-modulated dose compensation for whole-breast irradiation is associated with reduced contralateral breast dose: a phantom model comparison. *Radiother Oncol.* 2007;82(3):324-328.
77. Bortfeld T. IMRT: a review and preview. *Phys Med Biol.* 2006;51(13):R363.
78. Bortfeld T, Bürkelbach J, Boesecke R, Schlegel W. Methods of image reconstruction from projections applied to conformation radiotherapy. *Phys Med Biol.* 1990;35(10):1423.
79. Brahme A, Roos J-E, Lax I. Solution of an integral equation encountered in rotation therapy. *Phys Med Biol.* 1982;27(10):1221.
80. Brahme A. Optimization of stationary and moving beam radiation therapy techniques. *Radiother Oncol.* 1988;12(2):129-140.
81. Xia P, Verhey LJ. Multileaf collimator leaf sequencing algorithm for intensity modulated beams with multiple static segments. *Med Phys.* 1998;25(8):1424-1434.
82. Ling CC, Burman C, Chui CS, et al. Conformal radiation treatment of prostate cancer using inversely-planned intensity-modulated photon beams produced with dynamic multileaf collimation. *Int J Radiat Oncol Biol Phys.* 1996;35(4):721-730.
83. Shepard DM, Earl MA, Li XA, Naqvi S, Yu C. Direct aperture optimization: a turnkey solution for step-and-shoot IMRT. *Med Phys.* 2002;29(6):1007-1018.
84. Jones S, Williams M. Clinical evaluation of direct aperture optimization when applied to head-and-neck IMRT. *Medical Dosimetry.* 2008;33(1):86-92.

85. Otto K. Volumetric modulated arc therapy: IMRT in a single gantry arc. *Medical physics.* 2008;35(1):310-317.
86. Otto K. Volumetric modulated arc therapy: IMRT in a single gantry arc. *Med Phys.* 2008;35(1):310-317.
87. Hofmaier J, Bodensohn R, Garny S, et al. Single isocenter stereotactic radiosurgery for patients with multiple brain metastases: dosimetric comparison of VMAT and a dedicated DCAT planning tool. *Radiation Oncology.* 2019;14(1):1-8.
88. Velten C, Kabarriti R, Garg M, Tomé WA. Single isocenter treatment planning techniques for stereotactic radiosurgery of multiple cranial metastases. *Phys Imaging Radiat Oncol.* 2021;17:47-52.
89. Huang Y, Chin K, Robbins JR, et al. Radiosurgery of multiple brain metastases with single-isocenter dynamic conformal arcs (SIDCA). *Radiother Oncol.* 2014;112(1):128-132.
90. Gevaert T, Steenbeke F, Pellegri L, et al. Evaluation of a dedicated brain metastases treatment planning optimization for radiosurgery: a new treatment paradigm? *Radiat Oncol J.* 2016;11(1):1-7.
91. Pokhrel D, Palmiero AN, Bernard ME, St Clair W. Dynamic conformal arcs-based single-isocenter VMAT planning technique for radiosurgery of multiple brain metastases. *Med Dosim.* 2021;46(2):195-200.
92. Molinier J, Kerr C, Simeon S, et al. Comparison of volumetric-modulated arc therapy and dynamic conformal arc treatment planning for cranial stereotactic radiosurgery. *J Appl Clin Med Phys.* 2016;17(1):92-101.
93. Ding C, Saw CB, Timmerman RD. Cyberknife stereotactic radiosurgery and radiation therapy treatment planning system. *Med Dosim.* 2018;43(2):129-140.
94. Shepard DM, Ferris MC, Ove R, Ma L. Inverse treatment planning for Gamma Knife radiosurgery. *Med Phys.* 2000;27(12):2748-2756.
95. Thomas EM, Popple RA, Wu X, et al. Comparison of plan quality and delivery time between volumetric arc therapy (RapidArc) and Gamma Knife radiosurgery for multiple cranial metastases. *Neurosurg.* 2014;75(4):409-418.
96. Han EY, Wang H, Luo D, Li J, Wang X. Dosimetric comparison of fractionated radiosurgery plans using frameless Gamma Knife ICON and CyberKnife systems with linear accelerator–based radiosurgery plans for multiple large brain metastases. *J Neurosurg.* 2019;132(5):1473-1479.
97. Potrebko PS, Keller A, All S, et al. GammaKnife versus VMAT radiosurgery plan quality for many brain metastases. *J Appl Clin Med Phys.* 2018;19(6):159-165.
98. Liu H, Andrews DW, Evans JJ, et al. Plan quality and treatment efficiency for radiosurgery to multiple brain metastases: non-coplanar RapidArc vs. Gamma Knife. *Front Oncol.* 2016;6:26.
99. Posner J. Management of brain metastases. *Rev Neurol.* 1992;148(6-7):477-487.
100. Serizawa T, Iuchi T, Ono J, et al. Gamma knife treatment for multiple metastatic brain tumors compared with whole-brain radiation therapy. *J Neurosurg.* 2000;93(supplement_3):32-36.
101. Wen PY, Loeffler JS. Brain metastases. *Current Treat Options Oncol.* 2000;1(5):447-457.

102. Kondziolka D, Patel A, Lunsford LD, Kassam A, Flickinger JC. Stereotactic radiosurgery plus whole brain radiotherapy versus radiotherapy alone for patients with multiple brain metastases. *Int J Radiat Oncol Biol Phys.* 1999;45(2):427-434.
103. Cairncross JG, Kim JH, Posner JB. Radation therapy for brain metastases. *Ann Neurol.* 1980;7(6):529-541.
104. Cairncross JG, Salmon J, Kim JH, Posner JB. Acute parotitis and hyperamylasemia following whole-brain radiation therapy. *Ann Neurol.* 1980;7(4):385-387.
105. Andrews DW, Scott CB, Sperduto PW, et al. Whole brain radiation therapy with or without stereotactic radiosurgery boost for patients with one to three brain metastases: phase III results of the RTOG 9508 randomised trial. *Lancet.* 2004;363(9422):1665-1672.
106. Yamamoto M, Kawabe T, Sato Y, et al. Stereotactic radiosurgery for patients with multiple brain metastases: a case-matched study comparing treatment results for patients with 2–9 versus 10 or more tumors. *J Neurosurg.* 2014;121(Suppl_2):16-25.
107. Dropcho EJ. Neurotoxicity of radiation therapy. *Neurol Clin.* 2010;28(1):217-234.
108. Tallet AV, Azria D, Barlesi F, et al. Neurocognitive function impairment after whole brain radiotherapy for brain metastases: actual assessment. *Radiat Oncol J.* 2012;7(1):1-8.
109. Nguyen TK, Sahgal A, Detsky J, et al. Single-fraction stereotactic radiosurgery versus hippocampal-avoidance whole brain radiation therapy for patients with 10 to 30 brain metastases: a dosimetric analysis. *Int J Radiat Oncol Biol Phys.* 2019;105(2):394-399.
110. Hofmaier J, Bodensohn R, Garny S, et al. Single isocenter stereotactic radiosurgery for patients with multiple brain metastases: dosimetric comparison of VMAT and a dedicated DCAT planning tool. *Radiat Oncol J.* 2019;14(1):1-8.
111. Kuntz L, Matthis R, Wegner N, Lutz S. Dosimetric comparison of mono-isocentric and multi-isocentric plans for oligobrain metastases: A single institutional experience. *Cancer Radiother.* 2020;24(1):53-59.
112. Taylor M, Williams J, Gleason Jr JF. Effects of multileaf collimator design and function when using an optimized dynamic conformal arc approach for stereotactic radiosurgery treatment of multiple brain metastases with a single isocenter: a planning study. *Cureus.* 2020;12(8).
113. Agazaryan N, Tenn S, Lee C, et al. Simultaneous radiosurgery for multiple brain metastases: technical overview of the UCLA experience. *Radiat Oncol J.* 2021;16(1):1-9.
114. Meeks SL, Mercado CE, Popple RA, et al. Practical Considerations for Single Isocenter LINAC Radiosurgery of Multiple Brain Metastases. *Pract Radiat Oncol.* 2021.
115. Liu H, Thomas EM, Li J, et al. Interinstitutional plan quality assessment of 2 linac-based, single-isocenter, multiple metastasis radiosurgery techniques. *Adv Radiat Oncol.* 2020;5(5):1051-1060.

116. Nath SK, Lawson JD, Simpson DR, et al. Single-isocenter frameless intensity-modulated stereotactic radiosurgery for simultaneous treatment of multiple brain metastases: clinical experience. *Int J Radiat Oncol Biol Phys.* 2010;78(1):91-97.
117. Clark GM, Popple RA, Young PE, Fiveash JB. Feasibility of single-isocenter volumetric modulated arc radiosurgery for treatment of multiple brain metastases. *Int J Radiat Oncol Biol Phys.* 2010;76(1):296-302.
118. Popple RA, Wu X, Brezovich IA, et al. The virtual cone: A novel technique to generate spherical dose distributions using a multileaf collimator and standardized control-point sequence for small target radiation surgery. *Adv Radiat Oncol.* 2018;3(3):421-430.
119. Thomas E, Middlebrooks E, Popple R, et al. Pilot trial of frameless virtual cone stereotactic radiosurgical thalamotomy and advanced functional connectivity parcellation of the thalamus for intractable tremor. *Int J Radiat Oncol Biol Phys.* 2018;102(3):e478-e479.
120. Fontanella A, Wild A, Lim S, et al. A dosimetric analysis of dorsal nerve root ablation therapy using a virtual cone technique. *Int J Radiat Oncol Biol Phys.* 2018;102(3):e510.
121. Brown TA, Ayers RG, Popple RA. Commissioning a multileaf collimator virtual cone for the stereotactic radiosurgery of trigeminal neuralgia. *Journal of Applied Clinical Medical Physics.* 2022.e13562.
122. Stevens MTR, Lobb EC, Yenice KM. Validation of MLC-based linac radiosurgery for trigeminal neuralgia. *J Appl Clin Med Phys.* 2018;19(4):214-221.
123. Dong L, Boyer AL. An image correlation procedure for digitally reconstructed radiographs and electronic portal images. *Int J Radiat Oncol Biol Phys.* 1995;33(5):1053-1060.
124. Gonzales RC, Woods RE. Digital Image Processing Reading. *MA: Addison-Wesley.* 1987.
125. Song KH, Snyder KC, Kim J, et al. Characterization and evaluation of 2.5 MV electronic portal imaging for accurate localization of intra-and extracranial stereotactic radiosurgery. *J Appl Clin Med Phys.* 2016;17(4):268-284.
126. Ding GX, Munro P. Characteristics of 2.5 MV beam and imaging dose to patients. *Radiother Oncol.* 2017;125(3):541-547.
127. Ding G, Munro P. The Imaging Dose to Patients From a 2.5 MV Imaging Beam. *Int J Radiat Oncol Biol Phys.* 2017;99(2):E654.
128. M.Borsavage J, Cherpak A, Robar JL. Investigation of planar image quality for a novel 2.5 MV diamond target beam from a radiotherapy linear accelerator. *Radiat Oncol J.* 2020;16:103-108.
129. Parsons D, Robar JL, Sawkey D. A Monte Carlo investigation of low-Z target image quality generated in a linear accelerator using Varianˈs VirtuaLinac a. *Med Phys.* 2014;41(2):021719.
130. Fu D, Kuduvalli G. A fast, accurate, and automatic 2D–3D image registration for image-guided cranial radiosurgery. *Med Phys.* 2008;35(5):2180-2194.

131. Li W-z, Liang Z-w, Cao Y, et al. Estimating intrafraction tumor motion during fiducial-based liver stereotactic radiotherapy via an iterative closest point (ICP) algorithm. *Radiat Oncol J.* 2019;14(1):1-8.
132. Darvish-Molla S, Spurway A, Sattarivand M. Comprehensive characterization of ExacTrac stereoscopic image guidance system using Monte Carlo and Spektr simulations. *Phys Med Biol.* 2020;65(24):245029.
133. Jans HS, Syme AM, Rathee S, Fallone BG. 3D interfractional patient position verification using 2D-3D registration of orthogonal images. *Med Phys.* 2006;33(5):1420 - 1439.
134. Stroian G, Falco T, Seuntjens J. Elimination of ghost markers during dual sensor-based infrared tracking of multiple individual reflective markers. *Med Phys.* 2004;31(7):2008-2019.
135. Li G, Ballangrud Å, Kuo LC, et al. Motion monitoring for cranial frameless stereotactic radiosurgery using video-based three-dimensional optical surface imaging. *Med Phys.* 2011;38(7):3981-3994.
136. Elekta Instrument A. High definition motion management-enabling stereotactic Gamma Knife® radiosurgery with non-rigid patient fixations (White Paper); 2015. In.: Art.
137. MacDonald RL, Lee Y, Schasfoort J, Soliman H, Sahgal A, Ruschin M. Real-Time Infrared Motion Tracking Analysis for Patients Treated With Gated Frameless Image Guided Stereotactic Radiosurgery. *Int J Radiat Oncol Biol Phys.* 2020;106(2):413 - 421.
138. Wright G, Schasfoort J, Harrold N, Hatfield P, Bownes P. Intra-fraction motion gating during frameless Gamma Knife® Icon™ therapy: the relationship between cone beam CT assessed intracranial anatomy displacement and infrared-tracked nose marker displacement. *J Radiosurg SBRT.* 2019;6(1):67.
139. Beddar AS, Kainz K, Briere TM, et al. Correlation between internal fiducial tumor motion and external marker motion for liver tumors imaged with 4D-CT. *Int J Radiat Oncol Biol Phys.* 2007;67(2):630-638.
140. Lightstone A, Benedict SH, Bova FJ, Solberg TD, Stern RL. Intracranial stereotactic positioning systems: Report of the american association of physicists in medicine radiation therapy committee task group no. 68. *Med Phys.* 2005;32(7Part1):2380-2398.
141. Lunsford LD, Leksell D. The LEKSELL system. In: *Modern stereotactic neurosurgery.* Springer; 1988:27-46.
142. Hadley MN, Shetter AG, Amos MR. Use of the Brown-Roberts-Wells stereotactic frame for functional neurosurgery. *Stereotact Funct Neurosurg.* 1985;48(1-6):61-68.
143. Couldwell WT, Apuzzo ML. Initial experience related to the use of the Cosman-Roberts-Wells stereotactic instrument. *J Neurosurg.* 1990;72(1):145-148.
144. Ramakrishna N, Rosca F, Friesen S, Tezcanli E, Zygmanszki P, Hacker F. A clinical comparison of patient setup and intra-fraction motion using frame-based radiosurgery versus a frameless image-guided radiosurgery system for intracranial lesions. *Radiother Oncol.* 2010;95(1):109 - 115.

145. Gill S, Thomas D, Warrington A, Brada M. Relocatable frame for stereotactic external beam radiotherapy. *Int J Radiat Oncol Biol Phys.* 1991;20(3):599-603.
146. Kassaee A, Das IJ, Tochner Z, Rosenthal DI. Modification of Gill-Thomas-Cosman frame for extracranial head-and-neck stereotactic radiotherapy. *Int J Radiat Oncol Biol Phys.* 2003;57(4):1192-1195.
147. Pham NLL, Reddy PV, Murphy JD, et al. Frameless, real-time, surface imaging-guided radiosurgery: update on clinical outcomes for brain metastases. *Transl Cancer Res.* 2014;3(4):351-357.
148. Minniti G, Scaringi C, Clarke E, Valeriani M, Osti M, Enrici RM. Frameless linac-based stereotactic radiosurgery (SRS) for brain metastases: analysis of patient repositioning using a mask fixation system and clinical outcomes. *Radiat Oncol J.* 2011;6:158.
149. Hanna SA, Mancini A, Dal Col AH, Asso RN, Neves-Junior WFP. Frameless image-guided radiosurgery for multiple brain metastasis using VMAT: a review and an institutional experience. *Frontiers in oncology.* 2019.703.
150. Gevaert T, Verellen D, Engels B, et al. Clinical evaluation of a robotic 6-degree of freedom treatment couch for frameless radiosurgery. *Int J Radiat Oncol Biol Phys.* 2012;83(1):467-474.
151. Pavlica M, Dawley T, Goenka A, Schulder M. Frame-based and mask-based stereotactic radiosurgery: The patient experience, compared. *Stereotact Funct Neurosurg.* 2021;99(3):241-249.
152. Sedrak M, Alaminos-Bouza AL, Srivastava S. Coordinate systems for navigating stereotactic space: how not to get lost. *Cureus.* 2020;12(6).
153. Ali I, Tubbs J, Hibbitts K, et al. Evaluation of the setup accuracy of a stereotactic radiotherapy head immobilization mask system using kV on-board imaging. *J Appl Clin Med Phys.* 2010;11(3):26-37.
154. Keeling V, Hossain S, Jin H, Algan O, Ahmad S, Ali I. Quantitative evaluation of patient setup uncertainty of stereotactic radiotherapy with the frameless 6D ExacTrac system using statistical modeling. *J Appl Clin Med Phys.* 2016;17(3):111-127.
155. Sedrak M, Bruna A, Alaminos-Bouza AL, Brown RA. Novel geometries for stereotactic localizers. *Cureus.* 2021;13(6).
156. Verbakel WF, Lagerwaard FJ, Verduin AJ, Heukelom S, Slotman BJ, Cuijpers JP. The accuracy of frameless stereotactic intracranial radiosurgery. *Radiother Oncol.* 2010;97(3):390-394.
157. Tideman Arp D, Carl J. exactrac x-ray and beam isocenters—What's the difference? *Med Phys.* 2012;39(3):1418-1423.
158. Babic S, Lee Y, Ruschin M, et al. To frame or not to frame? Cone-beam CT-based analysis of head immobilization devices specific to linac-based stereotactic radiosurgery and radiotherapy. *J Appl Clin Med Phys.* 2018;19(2).
159. Jursinic P. Comparison of head immobilization with a metal frame and two different models of face masks. *J Cancer Cure.* 2018;1(1):36-40.

160. Li W, Cashell A, Lee I, et al. Patient perspectives on frame versus mask immobilization for gamma knife stereotactic radiosurgery. *Journal of Medical Imaging and Radiation Sciences.* 2020;51(4):567-573.
161. Dekker J, Rozema T, Böing-Messing F, Garcia M, Washington D, de Kruijf W. Whole-brain radiation therapy without a thermoplastic mask. *Phys Imaging Radiat Oncol.* 2019;11:27-29.
162. Gevaert T, Verellen D, Engels B, et al. Clinical evaluation of a robotic 6-degree of freedom treatment couch for frameless radiosurgery. *Int J Radiat Oncol Biol Phys.* 2012;83(1):467-474.
163. Lewis BC, Snyder WJ, Kim S, Kim T. Monitoring frequency of intra-fraction patient motion using the ExacTrac system for LINAC-based SRS treatments. *J Appl Clin Med Phys.* 2018;19(3):58 - 63.
164. Carminucci A, Nie K, Weiner J, Hargreaves E, Danish SF. Assessment of motion error for frame-based and noninvasive mask-based fixation using the Leksell Gamma Knife Icon radiosurgery system. *J Neurosurg.* 2018;129(Suppl1):133-139.
165. Mangesius J, Seppi T, Weigel R, et al. Intrafractional 6D head movement increases with time of mask fixation during stereotactic intracranial RT-sessions. *Radiat Oncol J.* 2019;14(1):231.
166. Bichay TJ, Mayville A. The continuous assessment of cranial motion in thermoplastic masks during cyberknife radiosurgery for trigeminal neuralgia. *Cureus.* 2016;8(5).
167. Hoogeman MS, Nuyttens JJ, Levendag PC, Heijmen BJ. Time dependence of intrafraction patient motion assessed by repeat stereoscopic imaging. *Int J Radiat Oncol Biol Phys.* 2008;70(2):609-618.
168. Murphy MJ, Chang SD, Gibbs IC, et al. Patterns of patient movement during frameless image-guided radiosurgery. *Int J Radiat Oncol Biol Phys.* 2003;55(5):1400-1408.
169. Guckenberger M, Roesch J, Baier K, Sweeney RA, Flentje M. Dosimetric consequences of translational and rotational errors in frame-less image-guided radiosurgery. *Radiat Oncol J.* 2012;7(1):1-8.
170. Wang H, Shiu A, Wang C, et al. Dosimetric effect of translational and rotational errors for patients undergoing image-guided stereotactic body radiotherapy for spinal metastases. *Int J Radiat Oncol Biol Phys.* 2008;71(4):1261-1271.
171. Roper J, Chanyavanich V, Betzel G, Switchenko J, Dhabaan A. Single-Isocenter Multiple-Target Stereotactic Radiosurgery: Risk of Compromised Coverage. *Int J Radiat Oncol Biol Phys.* 2015;93(3):540 - 546.
172. Minniti G, Capone L, Alongi F, et al. Initial Experience With Single-Isocenter Radiosurgery to Target Multiple Brain Metastases Using an Automated Treatment Planning Software: Clinical Outcomes and Optimal Target Volume Margins Strategy. *Adv Radiat Oncol.* 2020;5(5):856 - 864.
173. Almond PR, Biggs PJ, Coursey BM, et al. AAPM's TG-51 protocol for clinical reference dosimetry of high-energy photon and electron beams. *Med Phys.* 1999;26(9):1847-1870.

174. Karzmark C, Morton RJ, Corporation MPP. *A primer on theory and operation of linear accelerators in radiation therapy.* Medical Physics Publishing Corporation; 1989.
175. Wangler TP. *RF Linear accelerators.* John Wiley & Sons; 2008.
176. CJ K, RJ M. *A Primer on Theory and Operation of Linear Accelerators in Radiation Therapy.* 2 ed: Medical Physics Pub Corp; 1997.
177. Mayles P, Nahum A, Rosenwald J-C. *Handbook of radiotherapy physics: theory and practice.* CRC Press; 2007.
178. Cronin J. Modern dispenser cathodes. *IEE Proceedings I-Solid-State and Electron Devices.* 1981;128(1):19-32.
179. Podgorsak EB. Review of radiation oncology physics: a handbook for teachers and students. *Vienna, Austria: IAE Agency.* 2003.13.
180. Attix FH. *Introduction to radiological physics and radiation dosimetry.* John Wiley & Sons; 2008.
181. Tissue Substitutes in Radiation Dosimetry and Measurement, Report 44 of the International Commission on Radiation Units and Measurements. In. Bethesda, MD: ICRU; 1989.
182. Evans RD, Evans R. The atomic nucleus. 1955.
183. Bethe HA, Ashkin J. Experimental nuclear physics. *Wiley, New York.* 1953.
184. Møller C. über den Stoss zweier Teilchen unter Berücksichtigung der Retardation der Kräfte. *Zeitschrift für Physik.* 1931;70(11):786-795.
185. Podgoršak EB. *Radiation physics for medical physicists.* Vol 1: Springer; 2006.
186. Landau LD, Rumer G. The cascade theory of electronic showers. *Proceedings of the Royal Society of London Series A Mathematical and Physical Sciences.* 1938;166(925):213-228.
187. Mainegra-Hing E, Rogers D, Tessier F, Walters B. The EGSnrc code system: monte carlo simulation of electron and photon transport. *NRCC Report PIRS-701.* 2020.
188. Nelson WR, Hirayama H, Rogers DW. *EGS4 code system.* Stanford Linear Accelerator Center, Menlo Park, CA (USA);1985.
189. Kawrakow I, Mainegra-Hing E, Rogers D, Tessier F, Walters B. The EGSnrc code system: Monte Carlo simulation of electron and photon transport, NRCC Report PIRS-701. *Ottawa (ON): National Research Council of Canada.* 2006.
190. Perkins S, Cullen D, Chen M, Hubbell J, Rathkopf J, Scofield J. Lawrence Livermore National Laboratory Report UCRL-50400. In.: October; 1991.
191. Berger MJ. Monte Carlo calculation of the penetration and diffusion of fast charged particles. *Meth Comp Phys.* 1963;135.
192. Berger MJ, Seltzer SM. Stopping powers and ranges of electrons and positrons. 1982.
193. Bielajew AF, Rogers DW. Electron step-size artefacts and PRESTA. In: *Monte Carlo transport of electrons and photons.* Springer; 1988:115-137.
194. Koch HW, Motz J. Bremsstrahlung cross-section formulas and related data. *Rev Mod Phys.* 1959;31(4):920.
195. Sievinen J, Ulmer W, Kaissl W. AAA Photon Dose Calculation Model in Eclipse™. *Varian Medical Systems.*

196. Ulmer W, Harder D. Applications of a triple Gaussian pencil beam model for photon beam treatment planning. *Med Phys.* 1996;6(2):68-74.
197. Ulmer W, Harder D. A triple Gaussian pencil beam model for photon beam treatment planning. *Med Phys.* 1995;5(1):25-30.
198. Wareing TA, Morel JE, McGhee JM. Coupled electron-photon transport methods on 3-D unstructured grids. *Trans Am Nucl Soc.* 2000;83:240-242.
199. Wareing TA, McGhee JM, Morel JE, Pautz SD. Discontinuous finite element SN methods on three-dimensional unstructured grids. *Nucl Sci Engr.* 2001;138(3):256-268.
200. Failla GA, Wareing T. Acuros XB advanced dose calculationm for the Eclipse treatment planning system. *Varian Medical Systems.*
201. Muir B, Rogers D. Monte Carlo calculations of, the beam quality conversion factor. *Med Phys.* 2010;37(11):5939-5950.
202. Kawrakow I. *egspp: The EGSnrc C++class library.* Ottawa, Canada: National Research Council of Canada;2005.
203. McEwen M, DeWerd L, Ibbott G, et al. Addendum to the AAPM's TG-51 protocol for clinical reference dosimetry of high-energy photon beams. *Med Phys.* 2014;41(4):041501.
204. Weinhous MS, Meli JA. Determining Pion, the correction factor for recombination losses in an ionization chamber. *Med Phys.* 1984;11(6):846-849.
205. Gross B. Compton current and polarization in gamma-irradiated dielectrics. *J Appl Phys.* 1965;36(5):1635-1641.
206. Pruitt JS, Loevinger R. The photon-fluence scaling theorem for Compton-scattered radiation. *Med Phys.* 1982;9(2):176-179.
207. Boag J. Distortion of the electric field in an ionization chamber due to a difference in potential between guard ring and collector. *Phys Med Biol.* 1964;9(1):25.
208. Palmans H, Andreo P, Huq MS, Seuntjens J, Christaki KE, Meghzifene A. Dosimetry of small static fields used in external photon beam radiotherapy: Summary of TRS-483, the IAEA–AAPM international Code of Practice for reference and relative dose determination. *Med Phys.* 2018;45(11):e1123-e1145.
209. López-Sánchez M, Pérez-Fernández M, Fandiño JM, et al. An EGS Monte Carlo model for Varian TrueBEAM treatment units: Commissioning and experimental validation of source parameters. *Phys Med.* 2019;64:81-88.
210. Devic S. Radiochromic film dosimetry: past, present, and future. *Phys Med.* 2011;27(3):122-134.
211. Sutherland J, Rogers D. Monte Carlo calculated absorbed-dose energy dependence of EBT and EBT2 film. *Med Phys.* 2010;37(3):1110-1116.
212. Sharma M, Singh R, Dutt S, Tomar P, Trivedi G, Robert N. Effect of absorbed dose on post-irradiation coloration and interpretation of polymerization reaction in the Gafchromic EBT3 film. *Radiat Phys Chem.* 2021;187:109569.
213. Gill S, Hill R. A study on the use of Gafchromic™ EBT3 film for output factor measurements in kilovoltage X-ray beams. *Australas Phys Eng Sci Med.* 2013;36(4):465-471.

214. Alnawaf H, Butson MJ, Cheung T, Peter K. Scanning orientation and polarization effects for XRQA radiochromic film. *Phys Med.* 2010;26(4):216-219.
215. Cheung T, Butson MJ, Peter K. Post-irradiation colouration of Gafchromic EBT radiochromic film. *Phys Med Biol.* 2005;50(20):N281.
216. Devic S, Seuntjens J, Hegyi G, et al. Dosimetric properties of improved GafChromic films for seven different digitizers. *Med Phys.* 2004;31(9):2392-2401.
217. Gräfe JL, Owen J, Eduardo Villarreal-Barajas J, Khan RF. Characterization of a 2.5 MV inline portal imaging beam. *J Appl Clin Med Phys.* 2016;17(5):222-234.
218. Parsons D. *The Production and Detection of Optimized Low-Z Linear Accelerator Target Beams For Image Guidance in Radiotherapy*: Department of Physics and Atmospheric Science, Dalhousie University; 2012.
219. Gete E, Duzenli C, Milette MP, et al. A Monte Carlo approach to validation of FFF VMAT treatment plans for the TrueBeam linac. *Med Phys.* 2013;40(2):021707.
220. Sukumar P, Padmanaban S, Jeevanandam P, Kumar SS, Nagarajan V. A study on dosimetric properties of electronic portal imaging device and its use as a quality assurance tool in Volumetric Modulated Arc Therapy. *Rep Pract Oncol Radiother.* 2011;16(6):248-255.
221. Song K, Kim J, Wen N, et al. SU-E-J-147: Quantitative Analysis of 2.5 MV Portal Imaging Performance Compared to KV and 6MV Portal Imaging On the Novel Edge LINAC. *Med Phys.* 2014;41(6Part8):190-190.
222. Siddon RL. Fast calculation of the exact radiological path for a three-dimensional CT array. *Med Phys.* 1985;12(2):252 - 255.
223. Viola P, Wells III WM. Alignment by maximization of mutual information. *Int J Comput Vis.* 1997;24(2):137-154.
224. Lemieux L, Jagoe R, Fish D, Kitchen N, Thomas D. A patient-to-computed-tomography image registration method based on digitally reconstructed radiographs. *Med Phys.* 1994;21(11):1749-1760.
225. Shannon CE. A mathematical theory of communication. *Bell Syst Tech J.* 1948;27(3):379-423.
226. Hill DL, Batchelor PG, Holden M, Hawkes DJ. Medical image registration. *Phys Med Biol.* 2001;46(3):R1.
227. Zylka W, Wischmann H-A. On geometric distortions in CT images. Paper presented at: Proceedings of 18th Annual International Conference of the IEEE Engineering in Medicine and Biology Society1996.
228. Liu RR, Rudin S, Bednarek DR. Super-global distortion correction for a rotational C-arm x-ray image intensifier. *Med Phys.* 1999;26(9):1802-1810.
229. Systems VM. TrueBeam™ Developer Mode. In.
230. Rogers D, Faddegon B, Ding G, Ma CM, We J, Mackie T. BEAM: a Monte Carlo code to simulate radiotherapy treatment units. *Med Phys.* 1995;22(5):503-524.
231. Walters B, Kawrakow I, Rogers D. *DOSXYZnrc users manual.* Ottawa, Canada2018.
232. Constantin M, Perl J, LoSasso T, et al. Modeling the TrueBeam linac using a CAD to Geant4 geometry implementation: dose and IAEA-compliant phase space calculations. *Med Phys.* 2011;38(7):4018-4024.

233. Zhan L, Jiang R, Osei EK. Beam coordinate transformations from DICOM to DOSXYZnrc. *Phys Med Biol.* 2012;57(24):N513.
234. Lobo J, Popescu IA. Two new DOSXYZnrc sources for 4D Monte Carlo simulations of continuously variable beam configurations, with applications to RapidArc, VMAT, TomoTherapy and CyberKnife. *Phys Med Biol.* 2010;55(16):4431.
235. De Boor C, De Boor C. *A practical guide to splines.* Vol 27: springer-verlag New York; 1978.
236. Mayer RR, Ma F, Chen Y, et al. Enhanced dosimetry procedures and assessment for EBT2 radiochromic film. *Med Phys.* 2012;39(4):2147-2155.
237. Palmer AL, Bradley D, Nisbet A. Evaluation and implementation of triple-channel radiochromic film dosimetry in brachytherapy. *J Appl Clin Med Phys.* 2014;15(4):280-296.
238. Low DA, Harms WB, Mutic S, Purdy JA. A technique for the quantitative evaluation of dose distributions. *Med Phys.* 1998;25(5):656-661.
239. Styner M, Brechbuhler C, Szckely G, Gerig G. Parametric estimate of intensity inhomogeneities applied to MRI. *IEEE Trans Med Imag.* 2000;19(3):153-165.
240. Church C, Parsons D, Syme A. Investigating the impacts of intrafraction motion on dosimetric outcomes when treating small targets with virtual cones. *J Appl Clin Med Phys.* 2021;22(8):60 - 71.
241. Ma C-MC. Physics and Dosimetric Principles of SRS and SBRT. *Mathews J Cancer Sci.* 2019;4(2):1-16.
242. Hsu S-M, Lai Y-C, Jeng C-C, Tseng C-Y. Dosimetric comparison of different treatment modalities for stereotactic radiotherapy. *Radiat Oncol J.* 2017;12(1):1-11.
243. Ballangrud Å, Kuo LC, Happersett L, et al. Institutional experience with SRS VMAT planning for multiple cranial metastases. *J Appl Clin Med Phys.* 2018;19(2):176-183.
244. Benedict SH, Yenice KM, Followill D, et al. Stereotactic body radiation therapy: the report of AAPM Task Group 101. *Med Phys.* 2010;37(8):4078-4101.
245. Rashid A, Pintea B, Kinfe TM, Surber G, Hamm K, Boström JP. LINAC stereotactic radiosurgery for trigeminal neuralgia –retrospective two-institutional examination of treatment outcomes. *Radiat Oncol J.* 2018;13(1):153.
246. Lutz W, Winston KR, Maleki N. A system for stereotactic radiosurgery with a linear accelerator. *International Journal of Radiation Oncology* Biology* Physics.* 1988;14(2):373-381.
247. Belcher AH, Liu X, Chmura S, Yenice K, Wiersma RD. Towards frameless maskless SRS through real-time 6DoF robotic motion compensation. *Phys Med Biol.* 2017;62(23):9054.
248. Kim S, Jin H, Yang H, Amdur RJ. A study on target positioning error and its impact on dose variation in image-guided stereotactic body radiotherapy for the spine. *Int J Radiat Oncol Biol Phys.* 2009;73(5):1574-1579.
249. Ong CL, Dahele M, Cuijpers JP, Senan S, Slotman BJ, Verbakel WF. Dosimetric impact of intrafraction motion during RapidArc stereotactic vertebral radiation

therapy using flattened and flattening filter-free beams. *Int J Radiat Oncol Biol Phys.* 2013;86(3):420-425.
250. Lang E, Naraghi R, Tanrikulu L, et al. Neurovascular relationship at the trigeminal root entry zone in persistent idiopathic facial pain: findings from MRI 3D visualisation. *J Neurol Neurosurg Psychiatry.* 2005;76(11):1506-1509.
251. Garnier N, Amblard R, Villeneuve R, et al. Detectors assessment for stereotactic radiosurgery with cones. *J Appl Clin Med Phys.* 2018;19(6):88-98.
252. Paddick I, Lippitz B. A simple dose gradient measurement tool to complement the conformity index. *J Neurosurg.* 2006;105:194 - 205.
253. Sheehan JP, Starke RM, Mathieu D, et al. Gamma Knife radiosurgery for the management of nonfunctioning pituitary adenomas: a multicenter study. *J Neurosurg.* 2013;119(2):446 - 456.
254. Yen C-P, Schlesinger D, Sheehan JP. Natural history of cerebral arteriovenous malformations and the risk of hemorrhage after radiosurgery. *Prog Neurol Surg.* 2013;27:5 - 21.
255. Mainwaring W, Bowers J, Pham N, et al. Stereotactic Radiosurgery Versus Whole Brain Radiation Therapy: A Propensity Score Analysis and Predictors of Care for Patients With Brain Metastases From Breast Cancer. *Clin Breast Cancer.* 2019;19(2):e343 - e351.
256. Pokhrel D, Sood S, McClinton C, et al. Linac-based stereotactic radiosurgery (SRS) in the treatment of refractory trigeminal neuralgia: Detailed description of SRS procedure and reported clinical outcomes. *J Appl Clin Med Phys.* 2017;18(2):136 - 143.
257. Blomain ES, Kim H, Garg S, et al. Stereotactic radiosurgery practice patterns for brain metastases in the United States: a national survey. *Int J Radiat Oncol Biol Phys.* 2018;7(3):241-246.
258. Pham N-LL, Reddy PV, Murphy JD, et al. Frameless, real-time, surface imaging-guided radiosurgery: update on clinical outcomes for brain metastases. *Transl Cancer Res.* 2014;3(4):351 - 357.
259. Hanna SA, Mancini A, Col AHD, Asso RN, Neves-Junior WFP. Frameless Image-Guided Radiosurgery for Multiple Brain Metastasis Using VMAT: A Review and an Institutional Experience. *Front Oncol.* 2019;9:703.
260. Jr JRA, Chang SD, Murphy MJ, Doty J, Geis P, Hancock SL. The Cyberknife: a frameless robotic system for radiosurgery. *Stereotact Funct Neurosurg.* 1997;69:124 - 128.
261. Kilby W, Dooley JR, Kuduvalli G, Sayeh S, Jr CRM. The CyberKnife® Robotic Radiosurgery System in 2010. *Technol Cancer Res Treat.* 2010;9(5):433 - 452.
262. Stevens MTR, Parsons DD, Robar JL. Continuous monitoring of prostate position using stereoscopic and monoscopic kV image guidance. *Med Phys.* 2016;43(5):2558-2568.
263. Manger RP, Paxton AB, Pawlicki T, Kim GY. Failure mode and effects analysis and fault tree analysis of surface image guided cranial radiosurgery. *Med Phys.* 2015;42(5):2449-2461.

264. Ding GX, Munro P. Characteristics of 2.5 MV beam and imaging dose to patients. *Radiother Oncol.* 2017;125:541 - 547.
265. Olch AJ, Alaei P. How low can you go? A CBCT dose reduction study. *Radiat Oncol J.* 2021;22(2):85 - 89.
266. Parsons D, Robar JL. An investigation of kV CBCT image quality and dose reduction for volume-of-interest imaging using dynamic collimation. *Med Phys.* 2015;42(9):5258 - 5269.
267. Lai C-J, Chen L, Zhang H, et al. Reduction in x-ray scatter and radiation dose for volume-of-interest (VOI) cone-beam breast CT--a phantom study. *Phys Med Biol.* 2009;54(21):6691 - 6709.
268. Robar JL, Parsons D, Berman A, MacDonald A. Volume-of-interest cone-beam CT using a 2.35 MV beam generated with a carbon target. *Med Phys.* 2012;39(7):4209 - 4218.
269. Parsons D, Church C, Syme A. Toward a pre-clinical irradiator using clinical infrastructure. *Phys Med.* 2019;58:21 - 31.
270. Parsons D, Robar JL, Sawkey D. A Monte Carlo investigation of low-Z target image quality generated in a linear accelerator using Varian's VirtuaLinac. *Medical physics.* 2014;41(2).
271. Rogers DW, Faddegon BA, Ding GX, Ma CM, We J, Mackie TR. BEAM: a Monte Carlo code to simulate radiotherapy treatment units [published online ahead of print 1995/05/01]. *Med Phys.* 1995;22(5):503-524.
272. Ma C-MC. Physics and Dosimetric Principles of SRS and SBRT. *J Cancer Sci.* 2019;4(2):22.
273. Singh R, Davis J, Sharma S. Stereotactic Radiosurgery for Trigeminal Neuralgia: A Retrospective Multi-Institutional Examination of Treatment Outcomes. *Cureus.* 2016;8(4):e554.
274. Hoogeman MS, Nuyttens JJ, Levendag PC, Heijmen BJM. Time dependence of intrafraction patient motion assessed by repeat stereoscopic imaging. *Int J Radiat Oncol Biol Phys.* 2008;70(2):609 - 618.
275. Barnes M, Yeo A, Thompson K, Phillips C, Kron T, Hardcastle N. A retrospective analysis of setup and intrafraction positional variation in stereotactic radiotherapy treatments. *J Appl Clin Med Phys.* 2020;21(12):109-119.
276. Fu D, Kuduvalli G. A fast, accurate, and automatic 2D-3D image registration for image-guided cranial radiosurgery. *Med Phys.* 2008;35(5):2180 - 2194.
277. Northway C, Lincoln JD, Little B, Syme A, Thomas CG. Patient-Specific Collision Zones for 4π Trajectory Optimized Radiation Therapy. *Med Phys.* 2022.
278. Berbeco RI, Detappe A, Tsiamas P, Parsons D, Yewondwossen M, Robar J. Low Z target switching to increase tumor endothelial cell dose enhancement during gold nanoparticle-aided radiation therapy. *Med Phys.* 2016;43(1):436-442.
279. Yewondwossen M, Robar J, Parsons D. WE-DE-BRA-08: A Linear Accelerator Target Allowing Rapid Switching Between Treatment and High-Contrast Imaging Modes. *Med Phys.* 2016;43(6Part40):3814-3814.

280. Tsao M, Xu W, Sahgal A. A meta-analysis evaluating stereotactic radiosurgery, whole-brain radiotherapy, or both for patients presenting with a limited number of brain metastases. *Cancer.* 2012;118(9):2486-2493.
281. Palmer JD, Sebastian NT, Chu J, et al. Single-Isocenter Multitarget Stereotactic Radiosurgery Is Safe and Effective in the Treatment of Multiple Brain Metastases [published online ahead of print 2020/02/14]. *Adv Radiat Oncol.* 2020;5(1):70-76.
282. Lau SK, Zakeri K, Zhao X, et al. Single-isocenter frameless volumetric modulated arc radiosurgery for multiple intracranial metastases. *Neurosurg.* 2015;77(2):233-240.
283. Hardcastle N, Tome WA. On a single isocenter volumetric modulated arc therapy SRS planning technique for multiple brain metastases. *J Radiosurg SBRT.* 2012;2(1):1.
284. Wang J, Jin X, Peng J, Xie J, Chen J, Hu W. Are simple IMRT beams more robust against MLC error? Exploring the impact of MLC errors on planar quality assurance and plan quality for different complexity beams. *J Appl Clin Med Phys.* 2016;17(3):147-157.
285. MacDonald RL, Thomas CG, Ward L, Syme A. Intra-arc binary collimation algorithm for the optimization of stereotactic radiotherapy treatment of multiple metastases with multiple prescriptions. *Med Phys.* 2018;45(12):5597-5607.
286. Davey P, Schwartz M, O'Brien P, Gillies B. Dynamic Radiosurgery at the Toronto-Bayview Regional Cancer Centre, 1988-2007. *Can J Neurol Sci.* 2012;39(3):299-303.
287. Podgorsak EB, Olivier A, Pla M, Lefebvre P-Y, Hazel J. Dynamic stereotactic radiosurgery. *Int J Radiat Oncol Biol Phys.* 1988;14(1):115-126.
288. Rodrigues A, Yin F-F, Wu Q. Dynamic electron arc radiotherapy (DEAR): a feasibility study. *Phys Med Biol.* 2013;59(2):327.
289. Wilson B, Otto K, Gete E. A simple and robust trajectory-based stereotactic radiosurgery treatment. *Med Phys.* 2017;44(1):240-248.
290. Yu VY, Fahimian BP, Xing L, Hristov DH. Quality control procedures for dynamic treatment delivery techniques involving couch motion. *Med Phys.* 2014;41(8Part1):081712.
291. Wild E, Bangert M, Nill S, Oelfke U. Noncoplanar VMAT for nasopharyngeal tumors: plan quality versus treatment time. *Med Phys.* 2015;42(5):2157-2168.
292. Smyth G, Evans PM, Bamber JC, et al. Non-coplanar trajectories to improve organ at risk sparing in volumetric modulated arc therapy for primary brain tumors. *Radiother Oncol.* 2016;121(1):124-131.
293. QM Reis C, Little B, Lee MacDonald R, Syme A, Thomas CG, Robar JL. SBRT of ventricular tachycardia using 4pi optimized trajectories. *J Appl Clin Med Phys.* 2021.
294. Lee MacDonald R, Thomas CG. Dynamic trajectory-based couch motion for improvement of radiation therapy trajectories in cranial SRT. *Med Phys.* 2015;42(5):2317-2325.
295. Fix MK, Frei D, Volken W, et al. Part 1: optimization and evaluation of dynamic trajectory radiotherapy. *Med Phys.* 2018;45(9):4201-4212.

296. Sharma SD, Upreti RR, Deshpande DD. Use of peripheral dose data from uniform dynamic multileaf collimation fields to estimate out-of-field organ dose in patients treated employing sliding window intensity-modulated radiotherapy. *Phys Med Biol.* 2006;51(11):2987.
297. Clark GM, Popple RA, Prendergast BM, et al. Plan quality and treatment planning technique for single isocenter cranial radiosurgery with volumetric modulated arc therapy. *Pract Radiat Oncol.* 2012;2(4):306-313.
298. Wolfs CJ, Swinnen AC, Nijsten SM, Verhaegen F. Should dose from small fields be limited for dose verification procedures?: uncertainty versus small field dose in VMAT treatments. *Phys Med Biol.* 2018;63(20):20NT01.
299. Brown TA, Ayers RG, Popple RA. Commissioning a multileaf collimator virtual cone for the stereotactic radiosurgery of trigeminal neuralgia. *J Appl Clin Med Phys.* 2022.e13562.
300. Mullins J, Renaud MA, Heng V, Ruo R, DeBlois F, Seuntjens J. Trajectory-based VMAT for cranial targets with delivery at shortened SAD. *Med Phys.* 2020;47(7):3103-3112.
301. Lyu Q, Victoria YY, Ruan D, Neph R, O'Connor D, Sheng K. A novel optimization framework for VMAT with dynamic gantry couch rotation. *Phys Med Biol.* 2018;63(12):125013.
302. Victoria YY, Landers A, Woods K, et al. A prospective 4π radiation therapy clinical study in recurrent high-grade glioma patients. *Int J Radiat Oncol Biol Phys.* 2018;101(1):144-151.
303. Myronakis M, Huber P, Lehmann M, et al. Low-dose megavoltage cone-beam computed tomography using a novel multi-layer imager (MLI). *Med Phys.* 2020;47(4):1827-1835.
304. Romeijn HE, Ahuja RK, Dempsey JF, Kumar A. A column generation approach to radiation therapy treatment planning using aperture modulation. *SIAM J Opt.* 2005;15(3):838-862.
305. Wilson B, Gete E. Machine-specific quality assurance procedure for stereotactic treatments with dynamic couch rotations. *Med Phys.* 2017;44(12):6529-6537.
306. Towns P, Free B, Cernica G, Podgorsak MB. Practical issues in treating heavy patients on a LINAC treatment couch. *J Appl Clin Med Phys.* 2005;6(1):135-142.
307. MacDonald RL, Thomas CG, Syme A. Dynamic collimator trajectory algorithm for multiple metastases dynamic conformal arc treatment planning. *Medical physics.* 2018;45(1):5-17.
308. Langhans M, Unkelbach J, Bortfeld T, Craft D. Optimizing highly noncoplanar VMAT trajectories: the NoVo method. *Phys Med Biol.* 2018;63(2):025023.
309. Papp D, Bortfeld T, Unkelbach J. A modular approach to intensity-modulated arc therapy optimization with noncoplanar trajectories. *Phys Med Biol.* 2015;60(13):5179.
310. Bratengeier K, Holubyev K, Wegener S. Steeper dose gradients resulting from reduced source to target distance—a planning system independent study. *J Appl Clin Med Phys.* 2019;20(1):89-100.

311. Bratengeier K, Herzog B, Wegener S, Holubyev K. Finer leaf resolution and steeper beam edges using a virtual isocentre in concurrence to PTV-shaped collimators in standard distance–a planning study. *Radiat Oncol J.* 2017;12(1):1-9.
312. Bortfeld T, Oelfke U, Nill S. What is the optimum leaf width of a multileaf collimator? *Med Phys.* 2000;27(11):2494-2502.
313. Earl MA, Shepard DM, Naqvi S, Li XA, Yu CX. Inverse planning for intensity-modulated arc therapy using direct aperture optimization. *Phys Med Biol.* 2003;48(8):1075.

APPENDIX A COPYRIGHT PERMISSION

A.1. PERMISSION FOR: INVESTIGATING THE IMPACTS OF INTRAFRACTION MOTION ON DOSIMETRIC OUTCOMES WHEN TREATING SMALL TARGETS WITH VIRTUAL CONES

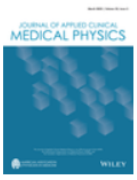

Investigating the impacts of intrafraction motion on dosimetric outcomes when treating small targets with virtual cones

Author: Cody Church, David Parsons, Alasdair Syme

Publication: Journal of Applied Clinical Medical Physics

Publisher: John Wiley and Sons

Date: Jul 17, 2021

APPENDIX B SUPPLEMENTARY DATA

B.1. SUPPLEMENTARY DATA FOR CHAPTER 6

Table 8: Arc geometries and weighting for each patient analyzed.

Number of Lesions = 1				
Patient	Collimator Angle	Couch Angle	Gantry Span	MU per Arc
1	330	0	180.1 - 179.9 CW	2683
	30	30	179.9 - 0.0 CCW	1757
	330	330	180.1 - 0.0 CW	1417
2	330	0	180.1 - 179.9 CW	1535
	30	45	179.9 - 0.0 CCW	1691
	330	315	180.1 - 340.0 CW	1436
3	330	0	180.1 - 179.9 CW	2695
	30	45	179.9 - 0.0 CCW	1466
	330	315	180.1 - 0.0 CW	1544
4	330	0	180.1 - 179.9 CW	2492
	30	45	179.9 - 0.0 CCW	1240
	330	315	180.1 - 0.0 CW	1273
5	330	0	180.1 - 179.9 CW	2190
	30	45	179.9 - 0.0 CCW	1148
	330	315	180.1 - 0.0 CW	1118
6	90	0	180.1 - 179.9 CW	2180
	90	90	179.9 - 350.0 CCW	1169
	90	45	179.9 - 30.0 CCW	901
	90	315	180.1 - 330.0 CW	878
7	330	0	0.0 - 179.9 CW	1224
	30	45	179.9 - 0.0 CCW	1248
	330	315	0 - 180.1 CCW	1269
8	90	0	180.1 - 179.9 CW	2678
	90	90	179.9 - 350.0 CCW	2093
	90	45	179.9 - 350.0 CCW	1838
	90	315	180.1 - 10.0 CW	1384
9	330	0	180.1 - 179.9 CW	1342
	30	45	170.0 - 20.0 CCW	2190
	330	315	205.0 - 350.0 CW	2142
10	330	0	180.1 - 0.0 CW	1213
	330	315	180.1 - 0.0 CW	1199
	30	270	0.0 - 180.1 CCW	1375
11	330	0	180.1 - 179.9 CW	990

	30	45	179.9 - 0.0 CCW	1777
	330	315	180.1 - 0.0 CW	1743
	90	0	180.1 - 179.9 CW	2731
12	30	45	179.9 - 30.0 CCW	2498
	330	90	150.0 - 30.0 CCW	2158
	330	0	180.1 - 179.9 CW	646
13	30	90	179.9 – 40.0 CCW	1067
	330	315	340.0 - 180.1 CCW	1184

Number of Lesions = 2

Patient	Collimator Angle	Couch Angle	Gantry Span	MU per Arc
	10	0	20.0 - 179.9 CW	1068
1	90	90	179.9 - 20.0 CCW	1116
	90	45	179.9 - 20.0 CCW	1085
	330	315	180.1 - 310.0 CW	856
	90	0	180.1 - 179.9 CW	3941
2	90	90	150.0 - 30.0 CCW	1333
	90	45	150.0 - 40.0 CCW	1250
	90	315	225.0 - 330.0 CW	1204
	330	0	180.1 - 179.9 CW	1102
3	0	45	179.9 - 10.0 CCW	1608
	90	90	170.0 - 15.0 CCW	1552
	90	0	180.1 - 179.9 CW	2151
4	90	45	179.9 - 350.0 CCW	1430
	90	90	180.0 - 10.0 CCW	1194
	90	0	180.1 - 179.9 CW	2308
5	90	90	170.0 - 25.0 CCW	1007
	90	45	170.0 - 25.0 CCW	957
	90	315	190.0 - 325.0 CW	956
	90	0	180.1 - 179.9 CW	2053
6	90	90	179.9 - 35.0 CCW	825
	90	45	179.9 - 45.0 CCW	779
	90	315	180.1 - 10.0 CW	1196
	300	0	180.1 - 0.0 CW	1103
7	60	0	0.0 - 179.9 CW	1159
	80	45	179.9 - 0.0 CCW	1212
	90	90	170.0 - 10.0 CW	1003
8	90	0	180.1 - 179.9 CW	1476
	0	45	155.0 -25.0 CCW	1880
	0	90	150.0 - 15.0 CCW	1941
9	350	0	240.0 - 120.0 CW	1755
	70	45	150.0 - 0.0 CCW	1085
	30	90	150.0 - 0.0 CCW	963

	350	315	210.0 - 0.0 CW	959
10	10	0	180.1 - 179.9 CW	2380
	90	45	179.9 - 350.0 CCW	1542
	350	315	180.1 - 10.0 CW	1264
11	350	0	180.1 - 179.9 CW	1053
	0	45	179.9 - 15.0 CCW	1651
	0	315	180.1 - 345.0 CW	1674

Number of Lesions = 3

Patient	Collimator Angle	Couch Angle	Gantry Span	MU per Arc
1	90	0	180.1 - 179.9 CW	2536
	90	90	179.9 - 350.0 CCW	1310
	90	45	179.9 - 350.0 CCW	1364
	90	315	180.1 - 10.0 CW	1475
2	90	0	180.1 - 179.9 CW	1991
	90	90	179.9 - 350.0 CCW	1453
	90	45	179.9 - 350.0 CCW	1564
	90	315	180.1 - 10.0 CW	1428
3	20	45	20.0 - 179.9 CW	1778
	10	325	180.1- 340.0 CW	1822
	5	289	340.0 - 180.1 CCW	1795
4	345	0	180.1 - 179.9 CW	3054
	30	45	179.9 - 10.0 CCW	1906
	330	315	180.1 - 350.0 CW	1441